Springer Tracts in Modern Physics

Volume 251

For further volumes:
http://www.springer.com/series/426

Springer Tracts in Modern Physics

Springer Tracts in Modern Physics provides comprehensive and critical reviews of topics of current interest in physics. The following fields are emphasized: Elementary Particle Physics, Condensed Matter Physics, Light Matter Interaction, Atomic and Molecular Physics, Complex Systems, Fundamental Astrophysics.

Suitable reviews of other fields can also be accepted. The Editors encourage prospective authors to correspond with them in advance of submitting a manuscript. For reviews of topics belonging to the above mentioned fields, they should address the responsible Editor as listed below.

Special offer: For all clients with a print standing order we offer free access to the electronic volumes of the Series published in the current year.

Hiroshi Kontani

Transport Phenomena in Strongly Correlated Fermi Liquids

Springer

Hiroshi Kontani
Department of Physics
Nagoya University
Nagoya-shi, Aichi
Japan

ISSN 0081-3869 ISSN 1615-0430 (electronic)
ISBN 978-3-642-35364-2 ISBN 978-3-642-35365-9 (eBook)
DOI 10.1007/978-3-642-35365-9
Springer Heidelberg New York Dordrecht London

Library of Congress Control Number: 2012954624

Printed on acid-free paper

Springer is part of Springer Science+Business Media (www.springer.com)

To my parents, Masaaki and Sachiko
To my family, Mai and Yuriko

Preface

We present a recent advancement in the theory of transport phenomena based on the Fermi liquid theory. In conventional metals, various transport coefficients are scaled by the quasiparticles relaxation time, τ, which implies that the relaxation time approximation (RTA) holds well. However, such a simple scaling does not hold in many strongly correlated electron systems, reflecting their unique electronic states. The most famous example would be cuprate high-T_c superconductors (HTSCs), where almost all the transport coefficients exhibit a significant deviation from the RTA results. Similar anomalous transport phenomena have been observed in metals near their antiferromagnetic (AF) quantum critical points (QCPs). Now, we have to demonstrate whether the anomalous transport phenomena in HTSC is the evidence of non-Fermi liquid ground state, or it is just the violation of the RTA in strongly correlated Fermi liquids. For these purpose, we develop a method for calculating various transport coefficients beyond the RTA by employing field theoretical techniques.

In a Fermi liquid, collisions between excited quasiparticles induce a finite current in the Fermi sea, which is called current vertex correction (CVC). The existence of CVC was first noticed by Landau. On the basis of the Fermi liquid theory, we develop a transport theory involving resistivity and Hall coefficient by including the CVC to satisfy the conservation laws. We find that the CVC exhibits singular momentum dependence in a nearly AF Fermi liquid, which is induced by the strong backward scattering due to AF fluctuations. Evidently, this fact explains the significant enhancement in the Hall coefficient, magnetoresistance, thermoelectric power, and Nernst coefficient in nearly AF metals. This fact strongly suggests the validity of the Fermi liquid description of HTSCs for a wide range of doping; from over-doped to slightly under-doped regime. Further, the present theory can explain very similar anomalous transport phenomena occurring in CeMIn5 (M = Co or Rh), which is a heavy-fermion system near the AF QCP, and in the organic superconductor κ-(BEDT-TTF).

In this text, we also discuss the interesting spin-related transport phenomena that are widely observed in various d- and f-electron systems. In multiband systems with spin–orbital interaction, the Bloch electron acquires the trajectory- and

spin-dependent Berry phase, which works as the spin-dependent outer magnetic field. This mechanism presents the anomalous Hall effect (AHE) in ferromagnetic metals and spin Hall effect (SHE) in paramagnetic metals. The Hall conductivity due to this mechanism is independent of τ, in highly contrast to the ordinary Hall conductivity $\sigma_{xy}^{\mathrm{ord}} \propto \tau^2$. Due to this fact, the SHC and AHE are called the quantum transport phenomena. In Part I, we explain how to calculate these quantum transport phenomena based on the Nakano-Kubo formula. In Part II, we study the "giant SHE" that are recently observed in various transition metals, which attracts great attention for the application of the spintronics. We also study the "spin-structure-driven AHE" realized in several pyrochlore compounds.

Recently, various new strongly correlated compounds with spin and orbital degrees of freedoms had been synthesized intensively, by which the condensed matter physics acquires rich variety. One of the example is the Fe-based HTSC discovered by Kamihara and Hosono in 2008. We hope that the present text would be helpful in developing the modern transport theory for these new materials.

I had started the study of transport phenomena in correlated metals during the master course in the Department of Physics of Kyoto University, under the supervision of Prof. Kosaku Yamada. I would like to deeply acknowledge Prof. Kosaku Yamada, Prof. Kazuo Ueda, Prof. Dai S. Hirashima, Prof. Jun-ichiro Inoue, Prof. Masatoshi Sato, Prof. Yuji Matsuda, Prof. H. D. Drew, Prof. Tetsuro Saso, Dr. Kazuki Kanki, Dr. Seiichiro Onari, Dr. Yasuyuki Nakajima, and all other collaborators for fruitful guidances and collaborations.

Nagoya, Japan, September 2012 Hiroshi Kontani

Contents

Part I
Basic Concept

Chapter 1
Introduction

1.1 Relaxation Time Approximation (RTA) and Current Vertex Correction (CVC)

Due to the study of transport phenomena in metals, we can extract various important information with regard to the electronic states. In conventional metals, various transport phenomena are governed by a single parameter, namely, the quasiparticle relaxation time τ. That is, the relaxation-time-approximation (RTA) holds in conventional metals [1]. For example, resistivity ρ is proportional to τ^{-1}, and $\tau^{-1} \propto T^2$ in conventional Fermi liquids. The Hall coefficient $R_{\rm H}$ is independent of τ, and the magnetoresistance $\Delta\rho/\rho_0$ is proportional to τ^{-2}. The thermoelectric power S is proportional to T whereas independent of τ for a wide range of temperatures. The signs of $R_{\rm H}$ and S represent the type of carrier (i.e., electrons or holes). These Fermi liquid behaviors are well explained by the RTA.

In strongly correlated electron systems, however, abovementioned conventional Fermi liquid behaviors are frequently violated. For example, in cuprate high-$T_{\rm c}$ superconductors (HTSCs), both $R_{\rm H}$ and S/T show strong T-dependence and strongly enhanced at low temperatures [2–13]. For example, $1/e|R_{\rm H}|$ is considerably greater than the electron density in optimally- or under-doped systems. Similar "non-Fermi-liquid-like behaviors" are also observed in organic superconductors [14–17] and heavy-fermion systems (f-electron systems) [18–21]. Apparently, a simple RTA does not work well in these metals. To obtain significant information from the transport phenomena in strongly correlated systems, we had to develop the theory beyond the RTA.

In this textbook, we try to understand the origin of the non-Fermi-liquid-like transport properties in cuprate HTSCs, which have been intensively studied as one of the central issues. To understand transport anomaly, various non-Fermi-liquid ground states had been proposed. For example, P. W. Anderson considered the resonating-valence-bond (RVB) state, in which the elementary excitations are described by spinons and holons. It is considered that holons, whose density is small in under-doped systems, are responsible for the anomalous transport [6, 22, 23]. Also,

H. Kontani, *Transport Phenomena in Strongly Correlated Fermi Liquids*,
Springer Tracts in Modern Physics 251, DOI: 10.1007/978-3-642-35365-9_1,

a lot of efforts have been payed to understand the transport anomaly based on the assumption of the Fermi-liquid ground state. Within the RTA, transport coefficients were calculated based on the nearly antiferromagnetic (AF) Fermi liquid picture [24–27]. However, only a limited experimental results could been understood in both kinds of studies, so the true ground state had been unclear.

In interacting electron systems, a quasiparticle excitation is decayed by creating particle-hole excitations by collisions, and the current given by the latter excitations are represented by the current vertex correction (CVC). The CVC is closely related to the conservation laws, which is described by the Ward identity in the field theory [28–33]. The significance of the CVC had been recognized historically, although the CVC is dropped in the RTA. For example, Landau discussed the CVC in a spherical model, which is called the backflow in the phenomenological Fermi liquid theory [28–30]. In general, the CVC can be significant in strongly correlated systems. However, its effect in cuprate HTSCs has not been studied well until recently.

In this textbook, we develop the transport theory based on the Fermi-liquid ground picture: We discuss the role of CVC in nearly AF Fermi liquids, such as HTSCs, organic metals, and heavy-fermion systems near the magnetic quantum critical point (QCP), and find that *the prominently developed CVC entirely modifies the RTA results* [34–41]. In a Fermi liquid, the transport coefficients are described by the total current $\boldsymbol{J}_{\mathbf{k}}$, which is expressed as a sum of quasiparticle velocity $\boldsymbol{v}_{\mathbf{k}}$ and CVC [42–49]. In the present study, we find that the $\boldsymbol{J}_{\mathbf{k}}$ *in nearly AF metals shows anomalous* $\mathbf{k}$*-dependence due to the CVC*. This is the origin of the transport anomalies in nearly AF metals, such as R_{H}, $\Delta\rho/\rho_0$, S, and the Nernst coefficient (ν). We confirm this idea by performing a numerical study based on the FLEX + CVC theory. In this approximation, the Coulomb interaction U is the only fitting parameter.

Here, we demonstrate the physical meaning of CVC in an isotropic model [28–30]. In the RTA, we consider an excited quasiparticle at $\mathbf{k}$ in Fig. 1.1 as if it *annihilates* after the relaxation time. In this approximation, the conductivity due to a quasiparticle at $\mathbf{k}$ is proportional to the mean free path $v_{\mathbf{k}}\tau_{\mathbf{k}}$. Since $\tau_{\mathbf{k}} \propto T^{-2}$ in a Fermi liquid [28–30], the resistivity according to the RTA, $\rho^{\mathrm{RTA}} \propto \tau^{-1}$, is finite. However, this result is *not true* since the momentum conservation law ensures zero resistivity in the absence of Umklapp processes [44]. The correct answer (zero resistivity) is recovered by considering all the relevant normal scattering process as shown in Fig. 1.1: When a quasiparticle at $\mathbf{k}$ is scattered to $\mathbf{k}+\mathbf{q}$ after the relaxation time $\tau_{\mathbf{k}}$, a particle-hole pair (at $\mathbf{k}'-\mathbf{q}$ and $\mathbf{k}'$) should be created according to the momentum and energy conservation laws. *The CVC represents the current conveyed by the particles at* $(\mathbf{k}+\mathbf{q}, \mathbf{k}'-\mathbf{q})$ *and a hole at* $\mathbf{k}'$, *which emerge during the scattering process*. Therefore, the zero-resistivity in the absence of the Umklapp process are explained by considering the CVC [44].

Therefore, the conservation law is a very important constraint on the transport properties. In the RTA, however, the conservation law is violated because of neglecting the CVC [44, 47]. In this textbook, we find that the CVC is very significant in nearly AF metals, since it is the origin of a variety of anomalous transport phenomena in such metals.

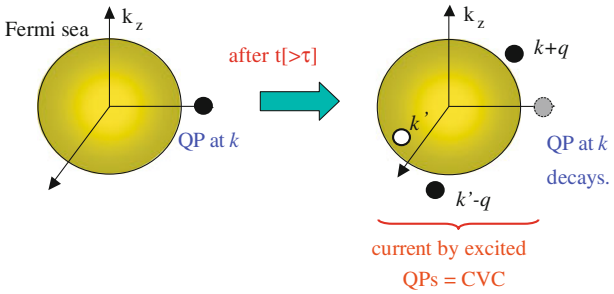

Fig. 1.1 Decay process of a quasiparticle (QP) at $\mathbf{k}$. After the relaxation time τ, the quasiparticle at $\mathbf{k}$ collides with another quasiparticle at $\mathbf{k}'$ in the Fermi sea. As a result, the two quasiparticles ($\mathbf{k}+\mathbf{q}$ and $\mathbf{k}'-\mathbf{q}$) and one quasi-hole ($\mathbf{k}'$) are created. The total momentum is conserved in this process

1.2 Non-Fermi-Liquid-Like Transport Phenomena in Cuprate High-T_c Cuprates

In cuprate HTSCs, almost all the transport phenomena deviate from the conventional behaviors in Fermi liquids, referred to as the non-Fermi liquid behaviors [50, 51]. These phenomena have been studied intensively in order to reveal the true ground state in HTSCs.

The Fermi liquid theory has been developed and applied to cuprate HTSCs by many authors [52]. By using the self-consistent renormalization (SCR) theory, Moriya, Takahashi and Ueda explained that the correct superconducting (SC) order parameter $d_{x^2-y^2}$ as well as T-linear resistivity are derived from the strong AF fluctuations [53–56]. Based on a phenomenological spin fluctuation model, Monthoux and Pines performed a quantitative analysis for optimally-doped YBCO [57].

As for the study based on the Hubbard model, several authors revealed the appearance of d-wave SC state based on the random-phase-approximation (RPA) [58, 59]. Later, Bickers et al. studied the square-lattice Hubbard model according to a self-consistent RPA, called the fluctuation-exchange (FLEX) approximation [35, 60–62]. These spin fluctuation theories have succeeded in reproducing various non-Fermi-liquid behaviors in HTSCs, such as the nuclear spin-lattice relaxation rate given by NMR/NQR measurements, $1/T_1T \propto \sum_{\mathbf{q}} \mathrm{Im}\chi^s_{\mathbf{q}}(\omega)/\omega|_{\omega=0} \propto T^{-1}$. Moreover, reflecting the T-dependence of spin fluctuations, the relation $1/\tau \propto T$ is realized in 2D systems. Therefore, famous T-linear resistivity in HTSC,

$$\rho \propto 1/\tau \propto T, \tag{1.1}$$

is also explained. (The Fermi liquid behavior $1/\tau \propto T^2$ will recover at very low T if we can suppress the superconductivity.) These spin fluctuation theories successfully reproduce various non-Fermi-liquid-like behaviors in HTSCs except for the under-doped region $|1-n| < 0.1$, where n is the number of electrons per site

[63–67]. A schematic phase diagram of HTSC is shown in Fig. 1.2. The $d_{x^2-y^2}$-wave symmetry in the SC state was confirmed by phase-sensitive measurements [68–70], and tunneling spectroscopy [71]. $d_{x^2-y^2}$-wave SC state was also derived according to the third-order-perturbation theory with respect to U [72].

Regardless of the success of the Fermi liquid theory during the 1990s, the anomalous transport phenomena in HTSCs remained unresolved (except for the resistivity) for a long time. The failure the RTA results was frequently considered as a hallmark of the breakdown of the Fermi liquid state in cuprates. In HTSCs, $|R_H|$ increases below $T_0 \sim 600\,\mathrm{K}$ as

$$R_H \propto 1/T \tag{1.2}$$

above the pseudo-gap temperature $T^* \sim 200\,\mathrm{K}$, and $|R_H| \gg 1/ne$ at T^* [2, 3, 73]. The sign of R_H is positive in hole-doped systems such as $La_{2-\delta}Sr_\delta CuO_4$ (LSCO) [2–4], $YBa_2Cu_3O_{7-\delta}$ (YBCO) [5, 6] and $Tl_2Ba_2CuO_{6+\delta}$ (TBCO) [7]; however, it is negative in electron-doped systems such as $Nd_{2-\delta}Ce_\delta CuO_4$ (NCCO) [8] and $Pr_{2-\delta}Ce_\delta CuO_4$ (PCCO) [9], even though the angle resolved photoemission (ARPES) measurements resolved hole-like Fermi surfaces [74, 75]. The experimental T-dependences of R_H for LSCO and NCCO are shown in Fig. 1.3. The magnetoresistance of HTSCs also shows strong temperature dependence as

$$\Delta\rho/\rho_0 \propto T^{-4} \tag{1.3}$$

for a wide range of temperatures in LSCO [13, 76, 77], YBCO [76] and TBCO [78]. These results completely contradict with Kohler's rule ($R_H \propto$ const. and $\Delta\rho/\rho_0 \propto \rho_0^{-2}$) given by the RTA for a single-band model. Interestingly, the following "modified Kohler's rule" holds well for optimally-doped LSCO [13, 76], 90 and 60 K YBCO [76] and TBCO [78]:

$$\Delta\rho/\rho_0 \propto \tan^2\Theta_H, \tag{1.4}$$

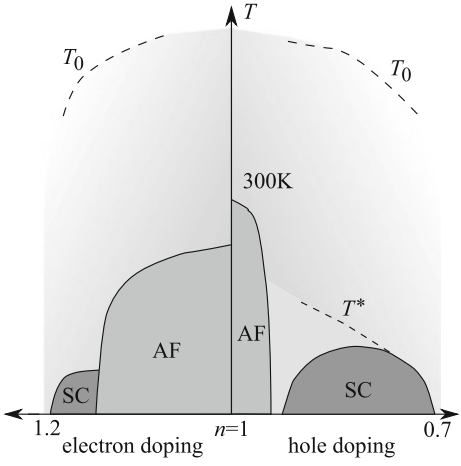

Fig. 1.2 Schematic phase diagram of HTSC. AF spin fluctuations start to increase below T_0. At the same time, R_H starts to increase. Below T^* (in the pseudo-gap region), the AF fluctuations are suppressed since the strong SC fluctuations reduce the density of states at the Fermi level, which is called the pseudo-gap

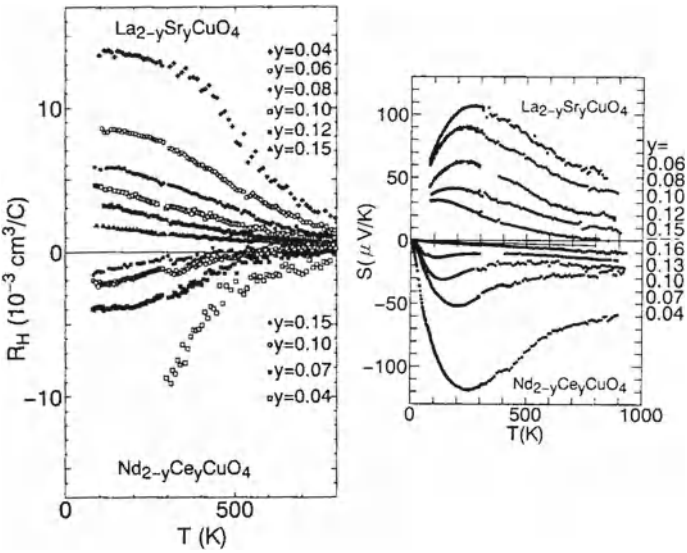

Fig. 1.3 Experimental Hall coefficient and the thermoelectric power for LSCO and NCCO. (Ref. [2, 3])

where $\tan \Theta_{\rm H} = \sigma_{xy}/\sigma_{xx}$ is the Hall angle. This rule strongly suggests that the anomalous behaviors of the Hall effect and the magnetoresistance have the same origin. Below T^*, however, $R_{\rm H}$ decreases whereas $\Delta\rho/\rho_0$ increases further [79]. Thus, the modified Kohler's rule is not well applicable below T^* [80–82].

For a long time, anomalous transport phenomena have been considered as one of the strongest objection against the Fermi liquid description of HTSCs. For example, to explain Eqs. (1.1)–(1.4), Anderson introduced the Tomonaga-Luttinger model with two types of relaxation times. However, it is not obvious how to describe the crossover from the Tomonaga-Luttinger liquid state to the Landau-Fermi liquid state with doping. On the other hand, we should verify the reliability of the RTA before abandoning the Fermi liquid picture, since the RTA sometimes yields unphysical results in correlated metals because of the violation of conservation laws [44]. In this text, we study the Fermi liquid description for HTSC, starting from the well-established Fermi liquid state in the over-doped region [52]. We explain that the anomalous transport phenomena in cuprate HTSCs are understood based on the Fermi liquid theory by including the CVC.

Here, we discuss the pseudo-gap phenomena in slightly under-doped systems below $T^* \sim 200$ K, which is also one of the most important issues in HTSC. $1/T_1T$ starts to decrease below T^*, which means that the AF fluctuations are suppressed in the pseudo-gap region [83–87]. According to ARPES measurements, prominent deep pseudo-gap appears in the density of states (DOS) below T^* [88–91]. A simple spin fluctuation theory cannot explain the various anomalous phenomena in the pseudo-gap region. One possible origin would be the strong SC fluctuations [92–94],

which are induced by the AF fluctuations [95–97]. In Chap. 6, we study the transport phenomena below T^* by taking account of the CVC due to both spin and SC fluctuations. However, recent STM/STS and ARPES measurements indicate the occurrence of a novel density order in heavily under-doped compounds [98–101]. Therefore, we have not yet achieved the whole understanding of the pseudo-gap phenomena.

1.3 Non-Fermi Liquid Transport Phenomena in CeMIn$_5$ (M = Co, Rh, or Ir) and κ-(BEDT-TTF)

In twenty-first century, it has been found that transport coefficients frequently exhibit striking deviations from the Fermi liquid behaviors in strongly correlated metals. In particular, anomalous transport properties similar to Eqs. (1.1)–(1.4) have been observed in many systems with strong magnetic fluctuations such as κ-(BEDT-TTF)$_2$X [X = Cu[N(CN)$_2$]Br [14], X = Cu[N(CN)$_2$]Cl [15, 16], X = Cu(NCS)$_2$ [16, 17]], κ-(BEDT-TTF)$_4$Hg$_{2.89}$Br$_8$ [16], and CeMIn$_5$ (M = Co, Rh) [18, 19]. BEDT-TTF is an abbreviation of bis(ethylenedithio)tetrathiafulvalene. These experimental facts strongly suggest that the anomalous transport phenomena are not specific to HTSCs, but universal in nearly AF Fermi liquids [19].

κ-(BEDT-TTF) is a layered organic compound made of BEDT-TTF molecules. The d-wave superconductivity can be realized in a wide region of the pressure-temperature (P-T) phase diagram, adjacent to the AF insulating states [102]. For example, Cu[N(CN)$_2$]Cl salt at ambient pressure is an AF insulator, with its Néel temperature $T_N = 27$ K. Under pressure, T_N decreases and superconductivity appears via a weak first order transition; The maximum T_c is 13 K at 200 bar. An effective theoretical model is given by the anisotropic triangular lattice Hubbard model at half-filling [103]. Using the FLEX approximation, the phase diagram of κ-(BEDT-TTF) is well reproduced, and the d-wave superconductivity is expected to be realized [104–106]. In addition, anomalous transport phenomena in κ-(BEDT-TTF) [14–17] are quantitatively reproduced by the FLEX + CVC theory [107].

CeMIn$_5$ is a quasi two-dimensional (2D) heavy-fermion compound with weak in-plane anisotropy $\rho_c/\rho_{a,b} \sim 2$ [108–110]. At ambient pressure, CeCoIn$_5$ is a superconductor with $T_c = 2.3$ K. The electronic specific heat coefficient γ has been measured to be 300 mJ/K^2 mol at $T \gtrsim T_c$. In CeIrIn$_5$, $T_c = 0.4$ K and $\gamma = 680$ mJ/K^2 mol. At ambient pressure, CeRhIn$_5$ is an AF metal with $T_N = 3.8$ K, and it undergoes a SC transition at $P_c = 2$ GPa, indicating that the AF quantum critical point (QCP) is located at P_c. The T-dependence of the NMR relaxation rate T_1^{-1} indicate the presence of quasi 2D AF spin fluctuations in the normal state [111, 112]. The measurements of the angle resolved thermal conductivity [113, 114] and specific heat [115, 116] revealed that the symmetry of the SC state exhibits d-wave symmetry. Furthermore, the Fulde-Ferrell-Larkin-Ovchinnikov (FFLO) SC state has been observed [117–121].

In $CeMIn_5$, Eqs. (1.1)–(1.4) are satisfied very well, and $|R_H/ne| \sim 50$ is satisfied in $CeRhIn_5$ near the AF QCP [18, 19]. The Nernst coefficient ν is also strongly enhanced [122].[1] In addition, modified Kohler's rule (1.4) is well satisfied for $0 < H \lesssim 3$ Tesla, irrespective that both σ_{xy}/H and $(\Delta\rho/\rho_0)/H^2$ are drastically suppressed by a very weak magnetic field ($H > 0.1$ Tesla) near the AF QCP [18, 19]. These results can be understood by considering the (field-dependence of) CVC based on the quasi 2D Hubbard model [124].

1.4 Fermi Liquid or Non-Fermi Liquid?

In this text, we assume that the Fermi liquid ground state is realized in a wide range of the phase diagram in cuprate HTSCs. Based on this idea, we study the anomalous transport phenomena by taking the CVC into account, which is a main-body effect overlooked in previous studies. Our final aim is to explain the anomalous transport phenomena in various nearly AF Fermi liquids *in a unified way*, including HTSC, heavy fermions and organic metals.

However, it is a nontrivial question whether the Fermi liquid state is realized in two-dimensional strongly correlated electron systems near the half-filling. In fact, the Fermi liquid state seems to be broken in heavily under-doped HTSCs. In the infinite dimension Hubbard model, the Fermi liquid state with heavy mass is realized next to the Mott insulating state [125, 126]. In 2D Hubbard models [127], it was rigorously proved that the limit value of the interaction U, below which the Fermi liquid state might be realized, is finite. However, in strongly correlated 2D systems, an exotic non-Fermi liquid ground state may be realized next to the Mott insulating state due to the strong thermal and quantum fluctuations.

To study the strong correlation effect in HTSCs, the $t-J$ model has been frequently analyzed. The $t-J$ model is derived from the Hubbard model (or $d-p$ model) by a canonical transformation, by excluding the double occupancy of holes to represent the strong Coulomb interaction. It is given by

$$H^{t-J} = \sum_{\langle i,j\rangle,\sigma} P_G(t_{i,j}c^{\dagger}_{i\sigma}c_{j\sigma} + \text{h.c})P_G + J\sum_{\langle i,j\rangle}^{\text{n.n}} \mathbf{S}_i \cdot \mathbf{S}_j \tag{1.5}$$

where P_G represents the exclusion of the doubly occupied state, $t_{i,j}$ is the hopping integral between (i, j) sites, and J is the superexchange energy between the neighboring spins. $J = 0.10 \sim 0.14$ meV in real HTSCs. In the t-J model, the Hilbert space with high-energy state is eliminated by P_G, which enables us to perform numeral calculations easier or to invent new approximations. Based on the t-J model, various versions of the new fluid have been proposed, with novel kinds of excitation,

[1] Note that the sign of ν in $CeCoIn_5$ is *positive* according to the definition of the present paper [Eq. (6.5)]. See also Ref. [123].

many involving gauge theories of spin-charge separated spinons and holons [22, 23, 128–130]. The exact diagonalization technique [131, 132] has been applied to the square-lattice t-J model. The ground state phase diagram of the t-J model has been studied using the variational Monte Carlo method [133–135], and it was found that the $d_{x^2-y^2}$-wave SC state is realized in a wide range of the phase diagram. Unfortunately, quantum Monte Carlo (QMC) simulation for t-J model is difficult because of a serious negative sign problem. Instead, QMC simulation for the Hubbard model with moderate value of U [136, 137] have been performed intensively.

On the other hand, some authors have considered non-Fermi liquid ground states due to novel quantum criticalities, other than a conventional spin QCP [64, 138, 139]. For example, Varma et al. proposed that the marginal Fermi liquid state is realized in HTSCs, where the **k**-independent self-energy is given by [138]

$$\Sigma(\omega + i\delta) = \lambda(\omega \ln(\omega_c/x) - ix), \tag{1.6}$$

where $x = \max(|\omega|, \pi T)$, λ is a coupling constant, and ω_c is a cutoff energy. This state is not a Fermi liquid since the quasiparticle renormalization factor $z = (1 - \partial \mathrm{Re}\Sigma/\partial\omega)^{-1} = (1 + \lambda \ln(\omega_c/x))^{-1}$ vanishes logarithmically as $(\omega, T) \to 0$. The self-energy in Eq. (1.6) can be derived if electrons couple to the following **k**-independent charge and spin fluctuations that are singular at $T = 0$:

$$\mathrm{Im}P(\omega + i\delta) \propto \min(|\omega|/T, 1). \tag{1.7}$$

In this model, $\rho \propto -\mathrm{Im}\Sigma(i\delta) = \lambda\pi T$, $1/T_1T \propto \mathrm{Im}P(\omega)/\omega|_{\omega=0} \propto 1/T$, and the optical conductivity is $\sigma(\omega) \propto (\omega - i\lambda x)^{-1}$. They are typical non-Fermi liquid behaviors in HTSCs. A microscopic derivation of the **k**-independent quantum critical fluctuations is an important issue.

References

1. H.M. Ziman, *Electrons and Phonons: The Theory of Transport Phenomena in Solids* (Oxford Classic Texts in the Physical Sciences, Oxford, 1960)
2. J. Takeda, T. Nishikawa, M. Sato, Phys. C **231**, 293 (1994)
3. T. Nishikawa, J. Takeda, M. Sato, J. Phys. Soc. Jpn. **63**, 1441 (1994)
4. H.Y. Hwang, B. Batlogg, H. Takagi, H.L. Kao, J. Kwo, R.J. Cava, J.J. Krajewski, W.F. Peck Jr, Phys. Rev. Lett. **72**, 2636 (1994)
5. P. Xiong, G. Xiao, X.D. Wu, Phys. Rev. B **47**, 5516 (1993)
6. T.R. Chien, Z.Z. Wang, N.P. Ong, Phys. Rev. Lett. **67**, 2088 (1991)
7. Y. Kubo, Y. Shimakawa, T. Manako, H. Igarashi, Phys. Rev. B **43**, 7875 (1991)
8. P. Fournier, X. Jiang, W. jiang, S.N. Mao, T. Venkatesan, C.J. Lobb, R.L. Greene. Phys. Rev. B **56**, 14149 (1997)
9. Y. Dagan, M.M. Qazilbash, C.P. Hill, V.N. Kulkarni, R.L. Greene, Phys. Rev. Lett. **92**, 167001 (2004)
10. Y. Abe, K. Segawa, Y. Ando, Phys. Rev. B **60**, R15055 (1999)
11. Y. Hanaki, Y. Ando, S. Ono, J. Takeya, Phys. Rev. B **64**, 172514 (2001)
12. G. Xiao, P. Xiong, M.Z. Cieplak, Phys. Rev. B **46**, 8687 (1992)

13. A. Malinowski, M.Z. Cieplak, S. Guha, Q. Wu, B. Kim, A. Krickser, A. Perali, K. Karpinska, M. Berkowski, C.H. Shang, P. Lindenfeld, Phys. Rev. B **66**, 104512 (2002)
14. K. Katayama, T. Nagai, H. Taniguchi, K. Satoh, N. Tajima, R. Kato, J. Phys. Soc. Jpn. 76 (2007) Suppl. A, 194.
15. Yu. V. Sushko, N. Shirakawa, K. Murata, Y. Kubo, N.D. Kushch, E.B. Yagubskii, Synth. Met. **85**, 1541 (1997)
16. H. Taniguchi, Unpublished.
17. K. Murata, M. Ishibashi, Y. Honda, N.A. Fortune, M. Tokumoto, N. Kinoshita, H. Anzai, Solid State Comm. **76**, 377 (1990)
18. Y. Nakajima, K. Izawa, Y. Matsuda, S. Uji, T. Terashima, H. Shishido, R. Settai, Y. Onuki, H. Kontani, J. Phys. Soc. Jpn. **73**, 5 (2004)
19. Y. Nakajima, H. Shishido, H. Nakai, T. Shibauchi, K. Behnia, K. Izawa, M. Hedo, Y. Uwatoko, T. Matsumoto, R. Settai, Y. Onuki, H. Kontani, Y. Matsuda, J. Phys. Soc. Jpn. **76**, 027403 (2007)
20. T. Namiki, H. Sato, H. Sugawara, Y. Aoki, R. Settai, Y. Onuki, Preprint.
21. S. Paschen, T. Luhmann, S. Wirth, P. Gegenwart, O. Trovarelli, C. Geibel, F. Steglich, P. Coleman, Q. Si, Nature **432**, 881 (2004)
22. P.W. Anderson, Phys. Rev. Lett. **67**, 209 (1997)
23. P.W. Anderson, *The Theory of Superconductivity in the High-Tc Cuprates* (Princeton Series in Physics, New Jersey, 1991)
24. R. Hlubina, T.M. Rice, Phys. Rev. B **51**, 9253–9260 (1995)
25. B.P. Stojkovic, D. Pines, Phys. Rev. B **55**, 8576 (1997)
26. L.B. Ioffe, A.J. Millis, Phys. Rev. B **58**, 11631 (1998)
27. Y. Yanase, K. Yamada, J. Phys. Soc. Jpn. **68**, 548 (1999)
28. L. Landau, Sov. Phys. JETP **3**, 920 (1957)
29. L. Landau, Sov. Phys. JETP **5**, 101 (1957)
30. L. Landau, Sov. Phys. JETP **8**, 70 (1959)
31. P. Noziéres, D. Pines, *Theory of Quantum Liquids* (Addison Wesley, New York, 1989)
32. P. Noziéres, *Theory of Interaction Fermion Systems* (Benjamin, New York, 1964)
33. A.A. Abricosov, L.P. Gor'kov, I.E. Dzyaloshinskii, *Methods of Quantum Field Theory in Statistical Physics* (Dover, New York, 1975)
34. H. Kontani, K. Yamada, J. Phy, Soc. Jpn. **74**, 155 (2005)
35. H. Kontani, K. Kanki, K. Ueda, Phys. Rev. B **59**, 14723 (1999)
36. K. Kanki, H. Kontani, J. Phys. Soc. Jpn. **68**, 1614 (1999)
37. H. Kontani, Phys. Soc. Jpn. **70**, 1873 (2001)
38. H. Kontani, Phys. Soc. Jpn. **70**, 2840 (2001)
39. H. Kontani, Phys. Rev. Lett. **89**, 237003 (2002)
40. H. Kontani, Phys. Rev. B **64**, 054413 (2001)
41. H. Kontani, Phys. Rev. B **67**, 014408 (2003)
42. G.M. Eliashberg, Sov. Phys. JETP **14**, 886 (1962)
43. J.S. Langer, Phys. Rev. **120**, 714 (1960)
44. K. Yamada, K. Yosida, Prog. Theor. Phys. **76**, 621 (1986)
45. H. Kohno, K. Yamada, Prog. Theor. Phys. **80**, 623 (1988)
46. H. Fukuyama, H. Ebisawa, Y. Wada, Prog. Theor. Phys. **42**, 494 (1969)
47. S. Fujimoto, H. Kohno, K. Yamada, Phys. Soc. Jpn. **60**, 2724 (1991)
48. H. Maebashi, H. Fukuyama, Phys. Soc. Jpn. **66**, 3577 (1997)
49. H. Maebashi, H. Fukuyama, Phys. Soc. Jpn. **67**, 242 (1998)
50. Y. Iye, in Physical Properties of High Temperature Superconductors, vol. 3, ed. by D.M. Ginsberg (World Scientific, Singapore, 1992).
51. K. Asayama, Y. Kitaoka, G.-q. Zheng, K. Ishida, Prog. NMR. Spectrosc. **28**, 221 (1996)
52. K. Yamada, *Electron Correlation in Metals* (Cambridge University Press, Cambridge, 2004)
53. T. Moriya, Y. Takahashi, K. Ueda, J. Phys. Soc. Jpn **59**, 2905 (1990)
54. K. Ueda, T. Moriya, Y. Takahashi, J. Phys. Chem. Solids **53**, 1515 (1992)
55. T. Moriya, K. Ueda, Adv. Phys. **49**, 555 (2000)

56. K. Miyake, O. Narikiyo, J. Phys. Soc. Jpn. **63**, 3821 (1994)
57. P. Monthoux, D. Pines, Phys. Rev. B **47**, 6069 (1993)
58. D.J. Scalapino, E. Loh Jr, J.E. Hirsch, Phys. Rev. B **34**, 8190 (1986)
59. K. Miyake, S. Schmitt-Rink, C.M. Varma, Phys. Rev. B **34**, 6554 (1986)
60. N.E. Bickers, S.R. White, Phys. Rev. B **43**, 8044 (1991)
61. K. Kuroki, R. Arita, H. Aoki, Phys. Rev. B **60**, 9850 (1999)
62. H. Yoshimura, D.S. Hirashima, J. Phys. Soc. Jpn. **73**, 2057 (2004)
63. P. Coleman, C. Pépin, Q. Si, R. Ramazashvili, J. Phys. Condens. Matter. **13**, R723 (2001)
64. S. Sachdev, *Quantum Phase Transitions* (Cambridge University Press, Cambridge UK, 1999)
65. A.V. Chubukov, D. Pines, J. Schmalian, The Physics of Superconductors, vol. 1, ed. by K.-H. Bennemann, J.B. Ketterson (Springer, Berlin, 2002).
66. A. Abanov, A.V. Chubukov, J. Schmalian, Adv. Phys. 52, 119 (2003) and references therein.
67. D. Manske, *Theory of Unconventional Superconductors: Cooper-Pairing Mediated By Spin Excitations* (Springer, Berlin, 2004)
68. M. Sigrist, T.M. Rice, J. Phys. Soc. Jpn. **61**, 4283 (1992)
69. D.A. Wollmann, D.J. Van Harlingen, W.C. Lee, D.M. Ginsberg, A.J. Leggett, Phys. Rev. Lett. **71**, 2134 (1993)
70. C.C. Tsuei, J.R. Kirtley, C.C. Chi, L.S. Yu-Jahnes, A. Gupta, T. Shaw, J.Z. Sun, M.B. Ketchen, Phys. Rev. Lett. **73**, 593 (1994)
71. S. Kashiwaya, Y. Tanaka, Rep. Prog. Phys. **63**, 1641 (2000)
72. T. Hotta, J. Phys. Soc. Jpn. **63**, 4126 (1994)
73. N.P. Ong, Physical Properties of High Temperature Superconductors, vol. 2, ed. by D.M. Ginsberg (World Scientific, Singapore, 1992).
74. N.P. Armitage, D.H. Lu, C. Kim, A. Damascelli, K.M. Shen, F. Ronning, D.L. Feng, P. Bogdanov, Z.-X. Shen, Phys. Rev. Lett. **87**, 147003 (2001)
75. N.P. Armitage, F. Ronning, D.H. Lu, C. Kim, A. Damascelli, K.M. Shen, D.L. Feng, H. Eisaki, Z.-X. Shen, P.K. Mang, N. Kaneko, M. Greven, Y. Onose, Y. Taguchi, Y. Tokura, Phys. Rev. Lett. **88**, 257001 (2002)
76. J.M. Harris, Y.F. Yan, P. Mati, N.P. Ong, P.W. Anderson, T. Kimura, K. Kitazawa, Phys. Rev. Lett. **75**, 1391 (1995)
77. S. Uchida, K. Kitazawa, M. Hiroi, M. Sera, N. Kobayashi, Phy. Rev. B **53**, 8733 (1996)
78. A.W. Tyler, Y. Ando, F.F. Balakirev, A. Passner, G.S. Boebinger, A.J. Schofield, A.P. Mackenzie, O. Laborde, Phys. Rev. B **57**, R728 (1998)
79. Z.A. Xu, Y. Zhang, N.P. Ong, cond-mat/9903123.
80. Y. Ando, T. Murayama, Phys. Rev. B **60**, R6991 (1999)
81. Y. Abe, Y. Ando, J. Takeya, H. Tanabe, T. Watauchi, I. Tanaka, H. Kojima, Phys. Rev. B **59**, 14753 (1999)
82. F.F. Balakirev, I.E. Trofimov, S. Guha, M.Z. Cieplak, P. Lindenfeld, Phys. Rev. B **57**, R8083 (1998)
83. H. Yasuoka, T. Imai, T. Shimizu, *Strong Correlation and Superconductivity* (Springer-Verlag, Berlin, 1989), p. 254
84. W.W. Warren, R.E. Walstedt, G.F. Brennert, R.J. Cava, R. Tycko, R.F. Bell, G. Dabbagh, Phys. Rev. Lett. **62**, 1193 (1989)
85. M. Takigawa, A.P. Reyes, P.C. Hammel, J.D. Thompson, R.H. Heffner, Z. Fisk, K.C. Ott, Phys. Rev. B **43**, 247 (1991)
86. Y. Itoh, H. Yasuoka, Y. Fujiwara, Y. Ueda, T. Machi, I. Tomeno, K. Tai, N. Koshizuka, S. Tanaka, J. Phys. Soc. Jpn. **61**, 1287 (1992)
87. M.H. Julien, P. Carretta, M. Horvatić, Phys. Rev. Lett. **76**, 4238 (1996)
88. H. Ding, T. Yokoya, J.C. Campuzano, T. Takahashi, M. Randeria, M.R. Norman, T. Mochiku, K. Kadowaki, J. Giapintzakis, Nature **382**, 51 (1996)
89. A.G. Loeser, Z.X. Shen, D.S. Dessau, D.S. Marshall, C.H. Park, P. Fournier, A. Kapitulnik, Science **273**, 325 (1996)
90. M.R. Norman, H. Ding, M. Randeria, J.C. Campuzano, T. Yokoya, T. Takeuchi, T. Takahashi, T. Mochiku, K. Kadowaki, P. Guptasarma, D.G. Hinks, Nature **392**, 157 (1998)

91. A. Damascelli, Z. Hussain, Z.-X. Shen, Rev. Mod. Phys. **75**, 473 (2003)
92. Q. Chen, I. Kosztin, B. Jankó, K. Levin, Phys. Rev. Lett. **81**, 4708 (1998)
93. Q. Chen, I. Kosztin, B. Janko, K. Levin, Phys. Rev. B **59**, 7083 (1999)
94. J. Maly, B. Janko, K. Levin, Phys. Rev. B **59**, 1354 (1999)
95. T. Dahm, D. Manske, L. Tewordt, Europhys. Lett. **55**, 93 (2001)
96. Y. Yanase, K. Yamada, J. Phys. Soc. Jpn. **70**, 1659 (2001)
97. A. Kobayashi, A. Tsuruta, T. Matsuura, Y. Kuroda, J. Phys. Soc. Jpn. **70**, 1214 (2001)
98. T. Hanaguri, C. Lupien, Y. Kohsaka, D.-H. Lee, M. Azuma, M. Takano, H. Takagi, J.C. Davis, Nature **430**, 1001 (2004)
99. T. Yoshida et al., J. Phys. Soc. Jpn. **81**, 011006 (2012)
100. T. Yoshida, M. Hashimoto, I.M. Vishik, Z.-X. Shen, A. Fujimori, J. Phys. Soc. Jpn. **81**, 011006 (2012)
101. T. Kondo et al., Nat. Phys. **7**, 21 (2011)
102. K. Kanoda, Phys. C **282–287**, 299 (1997)
103. H. Kino, H. Fukuyama, J. Phys. Soc. Jpn. **65**, 2158 (1996)
104. H. Kino, H. Kontani, J. Phys. Soc. Jpn. **67**, 3691 (1998)
105. H. Kondo, T. Moriya, J. Phys. Soc. Jpn. **67**, 3695 (1998)
106. J. Schmalian, Phys. Rev. Lett. **81**, 4232 (1998)
107. H. Kontani, H. Kino, Phys. Rev. B **63**, 134524 (2001)
108. C. Petrovic, P.G. Pagliuso, M.F. Hundley, R. Movshovich, J.L. Sarrao, J.D. Thompson, Z. Fisk, P. Monthoux, J. Phys. Condens. Matter. **13**, L337 (2001)
109. H. Hegger, C. Petrovic, E.G. Moshopoulou, M.F. Hundley, J.L. Sarrao, Z. Fisk, J.D. Thompson, Phys. Rev. Lett. **84**, 4986 (2000)
110. C. Petrovic, R. Movshovich, M. Jaime, P.G. Pagliuso, M.F. Hundley, J.L. Sarrao, Z. Fisk, J.D. Thompson, Europhys. Lett. **53**, 354 (2001)
111. G.-q. Zeng, K. Tanabe, T. Mito, S. Kawasaki, Y. Kitaoka, D. Aoki, Y. Haga, Y. Onuki, Phys. Rev. Lett. 86, 4664 (2001).
112. Y. Kawasaki, S. Kawasaki, M. Yashima, T. Mito, G.-q Zheng, Y. Kitaoka, H. Shishido, R. Settai, Y. Haga, Y. Onuki. J. Phys. Soc. Jpn. **72**, 2308 (2003)
113. K. Izawa, H. Yamaguchi, Y. Matsuda, H. Shishido, R. Settai, Y. Onuki, Phys. Rev. Lett. **87**, 057002 (2001)
114. Y. Matsuda, K. Izawa, I. Vekhter, J. Phys. Condens. Matter. **18**, R705 (2006)
115. R. Movshovich, M. Jaime, J.D. Thompson, C. Petrovic, Z. Fisk, P.G. Pagliuso, J.L. Sarrao, Phys. Rev. Lett. **86**, 5152 (2001)
116. H. Aoki, T. Sakakibara, H. Shishido, R. Settai, Y. Onuki, P. Miranovic, K. Machida, J. Phys. Condens. Matter. **16**, L13 (2004)
117. H.A. Radovan, N.A. Fortune, T.P. Murphy, S.T. Hannahs, E.C. Palm, S.W. Tozer, D. Hall, Nature **425**, 51 (2003)
118. A. Bianchi, R. Movshovich, C. Capan, P.G. Pagliuso, J.L. Sarrao, Phys. Rev. Lett. **91**, 187004 (2003)
119. T. Watanabe, Y. Kasahara, K. Izawa, T. Sakakibara, Y. Matsuda, C.J. van der Beek, T. Hanaguri, H. Shishido, R. Settai, Y. Onuki, Phys. Rev. B **70**, 020506 (2004)
120. K. Kakuyanagi, M. Saitoh, K. Kumagai, S. Takashima, M. Nohara, H. Takagi, Y. Matsuda, Phys. Rev. Lett. **94**, 047602 (2005)
121. Y. Matsuda, H. Shimahara, J. Phys. Soc. Jpn. **76**, 051005 (2007)
122. R. Bel, K. Behnia, Y. Nakajima, K. Izawa, Y. Matsuda, H. Shishido, R. Settai, Y. Onuki, Phys. Rev. Lett. **92**, 217002 (2004)
123. K. Izawa, K. Behnia, Y. Matsuda, H. Shishido, R. Settai, Y. Onuki, J. Flouquet, Phys. Rev. Lett. **99**, 147005 (2007)
124. S. Onari, H. Kontani, Y. Tanaka, Phys. Rev. B **73**, 224434 (2006)
125. A. Georges, G. Kotliar, W. Krauth, M.J. Rozenberg, Rev. Mod. Phys. **68**, 13 (1996)
126. G. Kotliar, D. Vollhardt, Phys. Today **57**, 53 (2004)
127. J. Feldman, D. Lehmann, H. Knorrer, E. Trubowitz, Constructive Physics, ed. by V. Rivasseau (Springer, Berlin, 1995).

128. Y. Suzumura, Y. Hasegawa, H. Fukuyama, J. Phys. Soc. Jpn. **57**, 2768 (1988)
129. G. Kotliar, Phys. Rev. B **37**, 3664 (1988)
130. P.A. Lee, N. Nagaosa, X.-G. Wen, Rev. Mod. Phys. **78**, 17 (2006)
131. T. Tohyama, Phys. Rev. B **70**, 174517 (2004)
132. E. Dagotto, Rev. Mod. Phys. **66**, 763 (1994)
133. T. Yanagisawa, S. Koike, K. Yamaji, Phys. Rev. B **64**, 184509 (2001)
134. H. Yokoyama, M. Ogata, J. Phys. Soc. Jpn. **65**, 3615 (1996)
135. H. Yokoyama, M. Ogata, Y. Tanaka, J. Phys. Soc. Jpn. **75**, 114706 (2006)
136. F.F. Assaad, M. Imada, J. Phys. Soc. Jpn. **65**, 189 (1996)
137. R. Preuss, W. Hanke, C. Grober, H.G. Evertz, Phys. Rev. Lett. **79**, 1122–1125 (1997)
138. C.M. Varma, P.B. Littlewood, S. Schmitt-Rink, E. Abrahams, A.E. Ruckenstein, Phys. Rev. Lett. **63**, 1996 (1989)
139. C.M. Varma, Phys. Rev. B **55**, 14554 (1997)

Chapter 2
Fluctuation Theory

2.1 Phenomenological Spin Fluctuation Model

Here, we discuss the phenomenological dynamical spin susceptibility $\chi^s_{\mathbf{q}}(\omega)$ in nearly AF metals. We use the unit $c = \hbar = k_B = 1$ hereafter. This is the most important physical quantity in such metals since it is the origin of various non-Fermi liquid behaviors in HTSCs. The functional form of $\chi^s_{\mathbf{q}}(\omega)$ is given by [1–5]

$$\chi^s_{\mathbf{q}}(\omega) = \sum_{\mathbf{Q}} \frac{\chi_Q}{1 + \xi^2_{\mathrm{AF}}(\mathbf{q} - \mathbf{Q})^2 - \mathrm{i}\omega/\omega_{\mathrm{sf}}}, \tag{2.1}$$

where $\mathbf{Q} = (\pm\pi, \pm\pi)$ is the antiferromagnetic (AF) wavevector, and ξ_{AF} is the AF correlation length. This is referred to as the Millis-Monien-Pines model [4]. These parameters can be obtained by using NMR/NQR spectroscopy and the neutron diffraction measurement. In HTSCs above the pseudo-gap temperature T^*, both χ_Q and $1/\omega_{\mathrm{sf}}$ are scaled by ξ^2_{AF} as follows [6]:

$$\xi^2_{\mathrm{AF}} \approx \alpha_0/(T + \Theta), \tag{2.2}$$

$$\chi_Q \approx \alpha_1 \cdot \xi^2_{\mathrm{AF}}, \quad 1/\omega_{\mathrm{sf}} \approx \alpha_2 \cdot \xi^2_{\mathrm{AF}}, \tag{2.3}$$

where Θ, α_0, α_1 and α_2 are constants. Since $\chi_Q \omega_{\mathrm{sf}} \propto \xi^0_{\mathrm{AF}}$ in Eq. (2.3), the dynamical exponent z is 2. Just above the superconducting transition temperature T_c [7], $\xi_{\mathrm{AF}} \sim 2\,a$ in optimally-doped YBCO, whereas it exceeds 100 a in slightly under-doped NCCO. (a is the unit-cell length; we put $a = 1$ hereafter.) The relationship $\omega_{\mathrm{sf}} \gtrsim T$ ($\omega_{\mathrm{sf}} \lesssim T$) is satisfied in the over-doped (under-doped) YBCO. Using this phenomenological model, T_c is well reproduced by solving the strong-coupling Eliashberg equation [3].

Theoretically, the relationships in Eqs. (2.2) and (2.3) are explained by the SCR theory, due to both self-energy correction and vertex correction to the dynamical susceptibility, referred to as the "mode-mode coupling effect" [8]. These

H. Kontani, *Transport Phenomena in Strongly Correlated Fermi Liquids*,
Springer Tracts in Modern Physics 251, DOI: 10.1007/978-3-642-35365-9_2,

relationships are also reproduced by the FLEX approximation [9–15], in which only the mode-mode coupling effect due to the self-energy correction is considered: In the FLEX approximation, $\chi^s_{\mathbf{q}}(0)$ in the mean-field approximation (or RPA) is strongly suppressed by the imaginary part of the self-energy. In pure 2D systems, T_N is suppressed to zero by the self-energy, so the Mermin-Wagner theorem is satisfied in the FLEX approximation [16, 17]. Similar results are obtained by the SCR and FLEX approximation.

2.2 Model Hamiltonian and FLEX Approximation

Here, we introduce the effective Hamiltonian of strongly correlated metals. It is given by the kinetic term and the interaction term. The kinetic term is frequently represented by the tight-binding model, given by the set of hopping integrals between different Wannier functions. The interaction term is usually approximated as the local Coulomb interaction, considering the screening effect. In many transition metal oxides or heavy fermions, Fermi surfaces are composed of more than one d- or f-orbitals. In the case of cuprate HTSCs, however, orbital degrees of freedom are absent. The corresponding single-orbital Hubbard model is given as

$$H = \sum_{\mathbf{k}\sigma} \epsilon^0_{\mathbf{k}} c^\dagger_{\mathbf{k}\sigma} c_{\mathbf{k}\sigma} + U \sum_{\mathbf{k}\mathbf{k}'\mathbf{q}} c^\dagger_{\mathbf{k}+\mathbf{q}\uparrow} c^\dagger_{\mathbf{k}'-\mathbf{q}\downarrow} c_{\mathbf{k}'\downarrow} c_{\mathbf{k}\uparrow}, \tag{2.4}$$

where U is the Coulomb interaction, and $\epsilon^0_{\mathbf{k}}$ is the spectrum of the conduction electron. In a square lattice, $\epsilon^0_{\mathbf{k}}$ is given by

$$\epsilon^0_{\mathbf{k}} = 2t_0(\cos k_x + \cos k_y) + 4t_1 \cos k_x \cos k_y + 2t_2(\cos 2k_x + \cos 2k_y), \tag{2.5}$$

where $c^\dagger_{\mathbf{k}\sigma}$ is the creation operator of an electron with momentum $\mathbf{k}$ and spin σ. We represent the electron filling by n, and $n = 1$ corresponds to the half-filling. n is smaller (larger) than unity in YBCO and LSCO (NCCO). To fit the band structures given by the local density approximation (LDA) for YBCO [18], NCCO [19], and LSCO [20, 21] and by the angle resolved photoemission (ARPES) experiments for YBCO [22], NCCO [23, 24] and LSCO [25], we select the following set of parameters [26, 27].

(I) YBCO (hole-doping) and NCCO (electron-doping):

$$t_0 = -1, \quad t_1 = 1/6, \quad \text{and} \quad t_2 = -1/5. \tag{2.6}$$

(II) LSCO (hole-doping):

$$t_0 = -1, \quad t_1 = 1/10, \quad \text{and} \quad t_2 = -1/10. \tag{2.7}$$

The Fermi surfaces for YBCO and NCCO without interaction are shown in Fig. 2.1a. The deformation of the Fermi surface in the presence of U has been discussed in Ref. [27]. Note that the Fermi surface in $Bi_2Sr_2CaCu_2O_8$ (BSCCO) is similar to that in YBCO [28]. Since $|t_0| \sim 4000\,\mathrm{K}$ in HTSCs, $T = 0.1$ in the present study corresponds to 400 K.

In the RPA, the dynamical spin and charge susceptibilities are given by

$$\chi_{\mathbf{q}}^{s(c),\mathrm{RPA}}(i\omega_l) = \chi_{\mathbf{q}}^{00} \cdot \left\{1 - (+)U\chi_{\mathbf{q}}^{00}(i\omega_l)\right\}^{-1}, \tag{2.8}$$

$$\chi_{\mathbf{q}}^{00}(i\omega_l) = -T\sum_{\mathbf{k},n} G_{\mathbf{q}+\mathbf{k}}^{0}(i\omega_l + i\epsilon_n)G_{\mathbf{k}}^{0}(i\epsilon_n), \tag{2.9}$$

where $G_{\mathbf{k}}^{0}(i\epsilon_n) = (i\epsilon_n + \mu - \epsilon_{\mathbf{k}}^{0})^{-1}$ is the non-interaction Green function.

Using the complex integration, Eq. (2.9) is given as

$$\chi_{\mathbf{q}}^{00}(i\omega_l) = \sum_{\mathbf{k}} \int_C \frac{d\epsilon}{2\pi i} f(\epsilon) \frac{1}{(\epsilon - i\omega_l + \epsilon_{\mathbf{k}+\mathbf{q}})(\epsilon - \epsilon_k)}, \tag{2.10}$$

where $f(\epsilon) = (1 + e^{\beta\epsilon})^{-1}$, which has poles at $\epsilon = i(2n+1)\pi T$ on the imaginary axis, and the corresponding residue is $-T$. The complex integration path C is shown in Fig. 2.2a. By changing the integration path to Fig. 2.2b, we have only to pick up two residues at $\epsilon = \epsilon_{\mathbf{k}}$ and $\epsilon = -i\omega_l + \epsilon_{\mathbf{k}+\mathbf{q}}$:

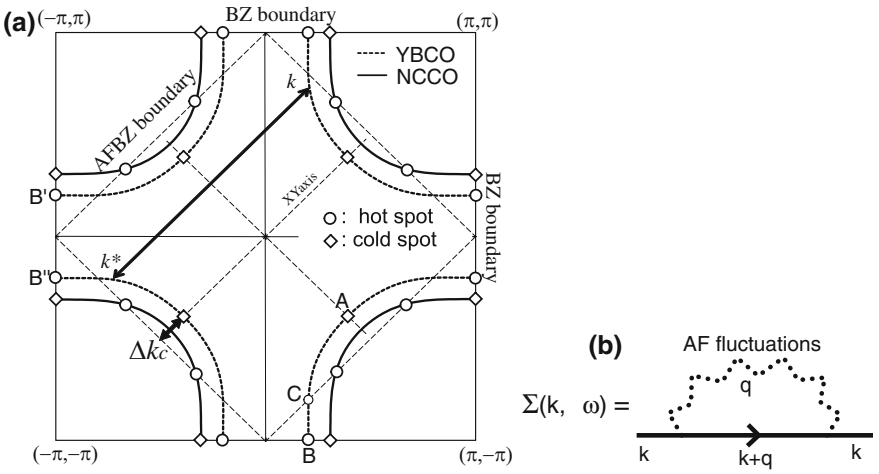

Fig. 2.1 **a** The Fermi surfaces for YBCO ($n < 1$) and NCCO ($n > 1$). The location of the hot spots and the cold spots are shown. In the FLEX approximation, the hot spot in YBCO shifts to point B, by reflecting the large DOS at $(\pi, 0)$. **b** Diagrammatic representation of the self-energy in the one-loop (FLEX) approximation

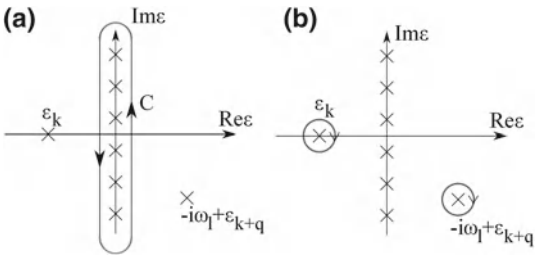

Fig. 2.2 **a** The complex integration path C in the complex ϵ plane. **b** A modified complex integration path C'

$$\chi_{\mathbf{q}}^{00}(i\omega_l) = \sum_{\mathbf{k}} \left\{ \frac{-f(\epsilon_{\mathbf{k}})}{i\omega_l + \epsilon_{\mathbf{k}} - \epsilon_{\mathbf{k}+\mathbf{q}}} + \frac{-f(-i\omega_l + \epsilon_{\mathbf{k}+\mathbf{q}})}{-i\omega_l - \epsilon_{\mathbf{k}} + \epsilon_{\mathbf{k}+\mathbf{q}}} \right\}$$
$$= \sum_{\mathbf{k}} \frac{f(\epsilon_{\mathbf{k}+\mathbf{q}}) - f(\epsilon_{\mathbf{k}})}{i\omega_l + \epsilon_{\mathbf{k}} - \epsilon_{\mathbf{k}+\mathbf{q}}} \tag{2.11}$$

It is easy to verify that $\chi_{\mathbf{q}}^{00}(i\omega_l)$ is a real function. However, it becomes a complex function after the analytic continuation $i\omega_l (l > 0) \to \omega + i\delta$ or $i\omega_l (l < 0) \to \omega - i\delta$.

By expanding $\chi_{\mathbf{q}}^{00}(i\omega_l) \approx \chi_{\mathbf{Q}}^{00}(0) - b(\mathbf{q}-\mathbf{Q})^2 + c|\omega_l|$, we obtain $\chi_{\mathbf{q}}^{s(c),\mathrm{RPA}}(i\omega_l) \approx \chi_{\mathbf{Q}}^{00}(0)[1 - U\chi_{\mathbf{Q}}^{00}(0) + Ub(\mathbf{q}-\mathbf{Q})^2 - Uc|\omega_l|]^{-1}$. After the analytic continuation $i\omega_l (l > 0) \to \omega_l + i\delta$, we obtain the MMP model in Eq. (2.1) with $\xi_{\mathrm{AF}}^2 = Ub/(1 - \alpha_{\mathrm{St}})$, $\omega_{\mathrm{sf}} = (1 - \alpha_{\mathrm{St}})/Uc$, and $\chi_Q = \chi_{\mathbf{Q}}^{00}(0)/(1 - \alpha_{\mathrm{St}})$, where $\alpha_{\mathrm{St}} = U\chi_{\mathbf{Q}}^{00}(0)$ is the Stoner factor. α_{St} is close to unity near AF-QCP.

In the FLEX approximation [9], the Green functions in Eq. (2.9) are replaced with the Green functions with self-energy:

$$G_{\mathbf{k}}(i\epsilon_n) = (i\epsilon_n + \mu - \epsilon_{\mathbf{k}}^0 - \Sigma_{\mathbf{k}}(i\epsilon_n))^{-1}, \tag{2.12}$$

The FLEX is classified as a conserving approximation whose framework was constructed by Baym and Kadanoff [29] and by Baym [30]. For this reason, we can calculate the CVC without ambiguity, by following the Ward identity $\Gamma^I = \delta\Sigma/\delta G$. Here, the Green function and the self-energy are given by

$$\Sigma_{\mathbf{k}}(i\epsilon_n) = T \sum_{\mathbf{q},l} G_{\mathbf{k}-\mathbf{q}}(i\epsilon_n - i\omega_l) \cdot V_{\mathbf{q}}(i\omega_l), \tag{2.13}$$

$$V_{\mathbf{q}}(i\omega_l) = U^2 \left(\frac{3}{2}\chi_{\mathbf{q}}^s(i\omega_l) + \frac{1}{2}\chi_{\mathbf{q}}^c(i\omega_l) - \chi_{\mathbf{q}}^0(i\omega_l) \right) + U, \tag{2.14}$$

$$\chi_{\mathbf{q}}^{s(c)}(i\omega_l) = \chi_{\mathbf{q}}^0 \cdot \left\{ 1 - (+)U\chi_{\mathbf{q}}^0(i\omega_l) \right\}^{-1}, \tag{2.15}$$

$$\chi_{\mathbf{q}}^0(i\omega_l) = -T \sum_{\mathbf{k},n} G_{\mathbf{q}+\mathbf{k}}(i\omega_l + i\epsilon_n) G_{\mathbf{k}}(i\epsilon_n), \tag{2.16}$$

where $\epsilon_n = (2n+1)\pi T$ and $\omega_l = 2l\pi T$, respectively. The self-energy in Eq. (2.13) is schematically shown by Fig. 2.1b. $\chi^{s(c)}_{\mathbf{q}}(i\omega_l)$ is the spin (charge) susceptibility, and $\chi^0_{\mathbf{q}}(i\omega_l)$ is the irreducible susceptibility. We solve the Eqs. (2.13)–(2.16) self-consistently, choosing μ so as to satisfy $n = T\sum_{\mathbf{k},n} G_{\mathbf{k}}(i\epsilon_n)\cdot e^{i\epsilon_n 0_+}$.

The FLEX approximation is suitable for the analysis of nearly AF Fermi liquids. Many authors have applied this approximation to the square-lattice Hubbard model [9–12]. Although it is an approximation, the obtained results are in good agreement with the results obtained from the quantum Monte Carlo simulations for a moderate U [9]. The FLEX approximation has also been applied to the ladder compound $Sr_{14-x}Ca_xCu_{24}O_{41}$ [13], organic κ-(BEDT-TTF) compounds [31–35], and various extended Hubbard models [36].

Note that the FLEX approximation can not reproduce the pseudo-gap behaviors below $T^* \sim 200$K in slightly under-doped systems. In Chap. 6, we improve this approximation by taking both spin and SC fluctuations into account (FLEX+T-matrix approximation), and reproduce experimental pseudo-gap behaviors.

Figure 2.3 shows $\chi^s_{\mathbf{q}}(\omega = 0)$ given by the FLEX approximation, both for YBCO ($n = 0.85$; optimum doping) at $T = 0.02$ and for NCCO ($n = 1.20$, slightly over-doping) at $T = 0.04$, respectively [27]. In optimum YBCO, the Stoner factor $U\chi^0_{\mathbf{Q}}(0) \sim 0.98$ at $T = 0.02$, and the AF correlation length ξ_{AF} is approximately $2\sim3\,a$ (a denotes the lattice spacing). On the other hand, ξ_{AF} in NCCO ($n = 1.20$) exceeds 10 a at $T = 0.02$. (The broadness of $\chi(\mathbf{q})$ in YBCO originates from the closeness of the Fermi surface to the van-Hove singular point at $(\pi, 0)$.) We stress that, in both cases, $\chi^s_{\mathbf{q}}(\omega = 0)$ becomes incommensurate in the RPA, inconsistently with neutron experiments. Therefore, the self-energy correction given by the FLEX approximation is important to reproduce appropriate dynamical spin susceptibilities.

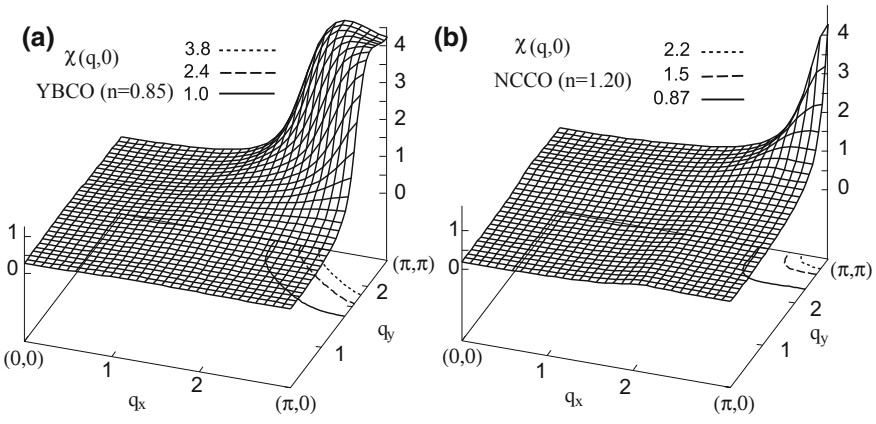

Fig. 2.3 $\chi(\mathbf{q}, \omega = 0)$ for **a** YBCO ($n = 0.85$) at $T = 0.02$ and **b** for NCCO ($n = 1.20$) at $T = 0.04$, given by the FLEX approximation. In YBCO, $\xi_{\mathrm{AF}} = 2a{-}3a$, whereas ξ_{AF} for NCCO exceeds $\sim 10a$ at $T = 0.02$. a is the lattice spacing [27]

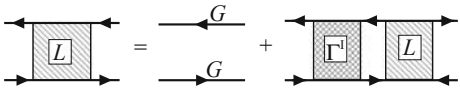

Fig. 2.4 Bethe-Salpeter equation for two-particle Green function $L(k,k')$. $\Gamma^I(k,k')$ is the irreducible four point vertex with respect to the particle-hole channel $G_{k''+q}G_{k''}$

We also stress that the NMR results are quantitatively reproducible in the FLEX approximation.[1]

In the FLEX approximation, the Mermin-Wagner theorem is satisfied as proved in Appendix A of Ref. [16, 17]. Hence, the critical region ($U\chi^0_{\mathbf{Q}}(0) \gtrsim 0.99$) is stable in 2D systems since the SDW order ($U\chi^0_Q(0) = 1$) is prevented by the Mermin-Wagner theorem. That is, $U_{\rm cr} = \infty$ in 2D systems.

In the next stage, we derive the two-particle Green function $L(k,k')$, by which transport coefficients are represented in the linear response theory. According to the microscopic Fermi liquid theory [37, 38], $L(k,k')$ can be obtained by the solution of the following Bethe-Salpeter equation:

$$\begin{aligned} L(k,k';q) &= -G_{k+q}G_k\delta_{k,k'}/T - G_{k+q}G_k\Gamma(k,k';q)G_{k'+q}G_{k'} \\ &= -G_{k+q}G_k\delta_{k,k'}/T \\ &\quad - T\sum_{k''} G_{k+q}G_k\Gamma^I(k,k'';q)G_{k''+q}G_{k''}L(k'',k';q), \end{aligned} \tag{2.17}$$

which is expressed by Fig. 2.4. Here $k = (\mathbf{k}, i\epsilon_n)$, $\Gamma(k,k';q)$ is the full four-point vertex, and $\Gamma^I(k,k';q)$ is the irreducible four-point vertex. In the conserving approximation (like the FLEX approximation), it is given by the Fourier transformation of the Ward identity in real space; $\hat{\Gamma}^I = \delta\hat{\Sigma}/\delta\hat{G}$. Then, transport coefficient obtained by $L(k,k')$ automatically satisfies conservation laws, proved in Refs. [29, 30]. This is a great advantage of the conserving approximation for the study of transport phenomena. In the FLEX approximation, irreducible four-point vertex is given in Eq. (5.1) in Sect. 5.1.

2.3 Hot/Cold-Spot Structure and T-Linear Resistivity in Nearly AF Metals

One of the important aspects in nearly AF Fermi liquids is the "hot/cold-spot structure" of the quasiparticle damping rate, $\gamma_{\mathbf{k}} = {\rm Im}\Sigma_{\mathbf{k}}(-i\delta)$ [3, 5, 9, 39–41]. That is, $\gamma_{\mathbf{k}}$ becomes anisotropic in the presence of AF fluctuations. Note that $\tau_{\mathbf{k}} = \hbar/2\gamma_{\mathbf{k}}$,

[1] I calculated the $1/T_1T$ of Cu nuclei for $n = 0.85$ using the FLEX approximation. I used Eq. (2.12) in Ref. [4] by correcting misprints, assuming that $A_\perp = B = 3.3 \times 10^{-7}$ eV. The obtained $1/T_1T$ under $\mathbf{H} \perp \hat{c}$ is 1–2 (m/s) at ∼200 K, which is consistent with experiments.

and we put $\hbar = 1$ in the textbook. The portions of the Fermi surface at which $\gamma_{\mathbf{k}}$ takes the maximum and minimum values are referred to as *hot spots* and *cold spots*, respectively [5, 41]. According to the spin fluctuation theory, the hot spots usually exist around the crossing points with the AF Brillouin zone (AFBZ)-boundary, whereas the cold spot is at the points where the distance from the AFBZ-boundary is the largest. Their positions are shown in Fig. 2.1a. The electronic states around the cold spots play the major role for various transport phenomena. Note that the hot spot in YBCO shifts to the Brillouin zone boundary (point B), by reflecting the large DOS at $(\pi, 0)$.

Figure 2.5 shows the $\mathbf{k}$-dependence of $\gamma_{\mathbf{k}}$ on the Fermi surface given by the FLEX approximation [27]. In YBCO, the hot spot moves to the BZ-boundary [point B] in Fig. 2.1a, by reflecting the large DOS at the van-Hove singularity point $(\pi, 0)$. Therefore, the spectral weight at the Fermi energy, $\rho_{\mathbf{k}}(\omega) = \gamma_{\mathbf{k}}/((\omega+\mu-\epsilon_{\mathbf{k}})^2+\gamma_{\mathbf{k}}^2)$ at $\omega = 0$, is strongly reduced around $(\pi, 0)$ due to large $\gamma_{\rm hot}$, consistently with the ARPES experiments [42]. In NCCO, in contrast, the hot and cold spots are located at point C and B, respectively. The location of the cold spot in NCCO was first predicted by the FLEX approximation in Ref. [27] in 1999, and it was later confirmed by ARPES [23, 24]. According to the spin fluctuation theories [5], $\gamma_{\rm hot} \propto \sqrt{T}$, and $\gamma_{\rm cold} \propto T$ except that $\xi_{\rm AF} \gg (\Delta k_c)^{-1}$; Δk_c is shown in Fig. 2.1a.

The critical value of U for a spin density wave (SDW) transition in the RPA (i.e., the mean-field approximation) is $U_{\rm cr}^{\rm RTA} \sim 2.3$ in LSCO ($n = 0.9$). In YBCO and NCCO, $U_{\rm cr}^{\rm RTA} \sim 3.5$ for both YBCO ($n = 0.9$) and NCCO ($n = 1.1$), since the nesting is not good due to the large next-nearest and third-nearest hopping integrals (t_1 and t_2). In YBCO, the dimensionless coupling constant $UN(0)$ is large, since the van-Hove singular point is close to the Fermi level. Here, $N(0)$ is the DOS at the Fermi level. Therefore, $\mathrm{Im}\,\Sigma_{\mathbf{k}}(0)$ takes a large value, which significantly reduces the interacting DOS at $(\pi, 0)$ as well as $\chi_{\mathbf{q}}^s(0)$ at $\mathbf{q} = (\pi, \pi)$ [27]. This effect is smaller in NCCO since the saddle point is far below the Fermi level. For this reason, $\xi_{\rm AF}$ for NCCO is much larger than that for YBCO in the FLEX approximation, consistently with experiments.

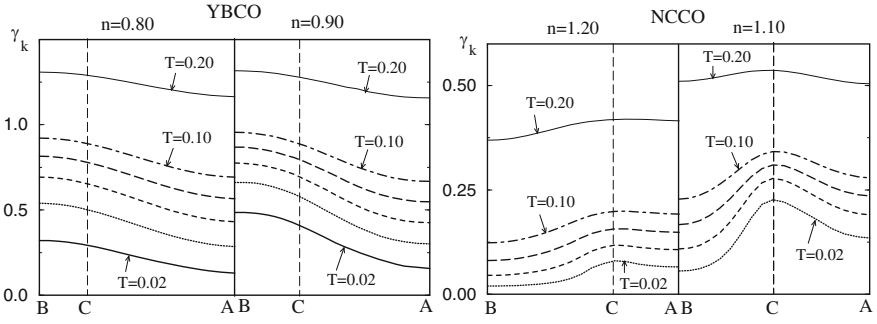

Fig. 2.5 The $\mathbf{k}$-dependence of $\gamma_{\mathbf{k}}$ on the Fermi surface at various temperatures given by the FLEX approximation. The cold spot in YBCO (NCCO) is point A (B)

The real-frequency Green function is given by the analytic continuation of $G_{\mathbf{k}}(i\epsilon_n)$ in Eq. (2.12). In a Fermi liquid, the advanced (retarded) Green function $G_{\mathbf{k}}^{A(R)}(\epsilon) = G_{\mathbf{k}}(\epsilon - (+)i\delta)$ for $\epsilon \sim 0$ and $|\mathbf{k}| \sim k_{\mathrm{F}}$ is represented as

$$G_{\mathbf{k}}^{A(R)}(\epsilon) = z_{\mathbf{k}}/(\epsilon - E_{\mathbf{k}}^{*} - (+)\mathrm{i}\gamma_{\mathbf{k}}^{*}), \tag{2.18}$$

$$E_{\mathbf{k}} = \epsilon_{\mathbf{k}}^{0} + \Sigma_{\mathbf{k}}(0) - \mu, \quad E_{\mathbf{k}}^{*} = z_{\mathbf{k}} E_{\mathbf{k}}, \tag{2.19}$$

$$\gamma_{\mathbf{k}} = \mathrm{Im}\Sigma_{\mathbf{k}}^{A}(0), \quad \gamma_{\mathbf{k}}^{*} = z_{\mathbf{k}}\gamma_{\mathbf{k}}, \tag{2.20}$$

where $z_{\mathbf{k}}$ is the renormalization factor $z_{\mathbf{k}} = 1/(1 - \partial \mathrm{Re}\,\Sigma_{\mathbf{k}}(\epsilon)/\partial\epsilon)_{\epsilon=0}$ and $E_{\mathbf{k}}^{*}$ is the renormalized quasi-particle spectrum, which is the solution of $\mathrm{Re}G_{\mathbf{k}}^{-1}(E_{\mathbf{k}}^{*}) = 0$. The quasiparticle spectrum is given by

$$\rho_{\mathbf{k}}(\epsilon) = \frac{1}{\pi}\mathrm{Im}G_{\mathbf{k}}^{A}(\epsilon). \tag{2.21}$$

The DOS is expressed as $N(\epsilon) = \sum_{\mathbf{k}} \rho_{\mathbf{k}}(\epsilon)$. In the case of $z_{\mathbf{k}}\gamma_{\mathbf{k}} \ll \mu$,

$$\rho_{\mathbf{k}}(\epsilon) = z_{\mathbf{k}}\delta(\epsilon - E_{\mathbf{k}}^{*}) \tag{2.22}$$

for $\epsilon \approx 0$.

In the FLEX approximation, $\gamma_{\mathbf{k}}$ is given by the analytic continuation of Eq. (2.13):

$$\gamma_{\mathbf{k}} = \frac{1}{2}\sum_{\mathbf{q}}\int d\epsilon \left[\mathrm{cth}\frac{\epsilon}{2T} - \mathrm{th}\frac{\epsilon}{2T}\right]\mathrm{Im}V_{\mathbf{q}}(\epsilon + i\delta)\rho_{\mathbf{k}+\mathbf{q}}(\epsilon) \tag{2.23}$$

where $V_{\mathbf{q}}(\omega + i\delta)$ is given by the analytic continuation of Eq. (2.14). Using the spin fluctuation model in Eq. (2.1), $\mathrm{Im}V_{\mathbf{q}}(0)$ in Eq. (2.23) is replaced with $(3U^2/2)\mathrm{Im}\chi_{\mathbf{q}}^{s}(\omega) = (3U^2/2)\omega\chi_Q\omega_{\mathrm{sf}}/(\omega_{\mathbf{q}}^2 + \omega^2)$, where $\omega_{\mathbf{q}} = \omega_{\mathrm{sf}} + \omega_{\mathrm{sf}}\xi_{\mathrm{AF}}^2(\mathbf{q} - \mathbf{Q})^2$. According to Refs. [5, 27], Eq. (2.23) is approximately transformed to

$$\gamma_{\mathbf{k}} \approx \frac{3U^2}{4\pi}\int_{\mathrm{FS}}\frac{dk'_{\parallel}}{v_{\mathbf{k}'}}\chi_Q\omega_{\mathrm{sf}}\frac{(\pi T)^2}{4\omega_{\mathbf{k}-\mathbf{k}'}(\omega_{\mathbf{k}-\mathbf{k}'} + \pi T/2)}, \tag{2.24}$$

so $\gamma_{\mathbf{k}}$ at the hot spot in 2D systems is given by [5]:

$$\gamma_{\mathrm{hot}} \propto T\xi_{\mathrm{AF}} \quad \text{for } \pi T/2\omega_{\mathrm{sf}} \gg 1 \tag{2.25}$$

$$\gamma_{\mathrm{hot}} \propto T^2\xi_{\mathrm{AF}}^3 \quad \text{for } \pi T/2\omega_{\mathrm{sf}} \ll 1. \tag{2.26}$$

Since $\xi_{\mathrm{AF}}^2 \propto T^{-1}$, $\gamma_{\mathrm{hot}} \propto \sqrt{T}$ for any value of ω_{sf}/T: This result is recognized in the numerical study in Fig. 2.5. Also, γ_{cold} in 2D systems is obtained as [5]:

$$\gamma_{\rm cold} \propto T \quad \text{for } \pi T/2\omega_{\rm sf} \sim (\xi_{\rm AF}\Delta k_c)^2, \tag{2.27}$$

$$\gamma_{\rm cold} \propto T^2 \quad \text{for } \pi T/2\omega_{\rm sf} \ll (\xi_{\rm AF}\Delta k_c)^2. \tag{2.28}$$

According to Eqs. (2.2) and (2.3), $\pi T/2\omega_{\rm sf}$ is constant if $\Theta \approx 0$, and it is of order unity in optimally-doped HTSCs. Therefore, $\gamma_{\rm cold} \propto T$ when $\xi_{\rm AF}\Delta k_c \sim O(1)$, and $\gamma_{\rm cold} \propto T^2$ when $\xi_{\rm AF}\Delta k_c \gg 1$: Δk_c represents the "deviation from the nesting condition at the cold spot" shown in Fig. 2.1. Note that the measure part of the Fermi surface becomes cold when $\xi_{\rm AF}\Delta k_c \gg 1$.

Now, we consider the T-dependence of resistivity by dropping the CVC. In the SCR theory [39], the resistivity is derived from the Born approximation $\rho \propto \langle\gamma_{\mathbf{k}}\rangle_{\rm FS} \equiv \sum_{\mathbf{k}} \gamma_{\mathbf{k}}\rho_{\mathbf{k}}(0)$. In the case of $\omega_{\rm sf} \gg T$, Eq. (2.24) is simplified as

$$\gamma_{\mathbf{k}} \approx \sum_{\mathbf{q}} \frac{(\pi T)^2}{2} {\rm Im}\,\dot{V}_{\mathbf{q}}(0)\rho_{\mathbf{k}+\mathbf{q}}(0), \tag{2.29}$$

where $\dot{V}_{\mathbf{q}}(0) = dV_{\mathbf{q}}(\omega + i\delta)/d\omega|_{\omega=0}$. Using Eqs. (2.1) and (2.29), the resistivity is given as [39, 43]

$$\begin{aligned} \rho_{\rm SCR} &\propto \langle\gamma_{\mathbf{k}}\rangle_{\rm FS} \\ &\propto T^2 \sum_{\mathbf{q}} {\rm Im}\,\dot{V}_{\mathbf{q}}(0) \sum_{\mathbf{k}} \rho_{\mathbf{k}}(0)\rho_{\mathbf{k}+\mathbf{q}}(0) \\ &\propto T^2 \xi_{\rm AF}^{4-d}, \end{aligned} \tag{2.30}$$

where d is the dimension of the system. In deriving Eq. (2.30), we utilized the fact that the $\mathbf{q}$-dependence of ${\rm Im}\dot{\chi}^0_{\mathbf{q}}(0) = (\pi/2)\sum_{\mathbf{k}} \rho_{\mathbf{k}}(0)\rho_{\mathbf{k}+\mathbf{q}}(0)$ is moderate. Since $\xi_{\rm AF} \propto \sqrt{\chi_Q} \propto T^{-0.5}$ near the AF-QCP [39], $\rho_{\rm SCR}$ is proportional to $T^{d/2}$ ($d = 2, 3$). Note that the Fermi liquid behavior $\rho_{\rm SCR} \propto T^2$ is recovered when $\xi_{\rm AF}$ =constant away from the AF-QCP, like in over-doped systems at low temperatures.

However, Eq. (2.30) would be appropriate only when $\gamma_{\mathbf{k}}$ is moderately anisotropic [41, 44]: According to the linear response theory, the correct resistivity is give by

$$\rho \propto 1/\langle\gamma_{\mathbf{k}}^{-1} v_{\mathbf{k}x}^2\rangle_{\rm FS} \sim \gamma_{\rm cold}. \tag{2.31}$$

According to Eqs. (2.27) and (2.28), T-linear behavior of ρ would be realized for $\xi_{\rm AF}\Delta k_c \sim O(1)$ (moderately anisotropic $\gamma_{\mathbf{k}}$ case). This would be the case of optimally doped or slightly under-doped YBCO and LSCO. On the other hand, $\rho \propto T^2$ for $\xi_{\rm AF}\Delta k_c \gg 1$ (highly anisotropic $\gamma_{\mathbf{k}}$ case), since the dominant part of the Fermi surface becomes the cold spot.

In Sect. 5.2, we will calculate the resistivity using the FLEX approximation including the CVC. The obtained ρ follows an approximate T-linear behavior in under-doped LSCO and NCCO, and it shows a T^2-like behavior in the over-doped NCCO. As for the resistivity, the CVC is quantitatively important.

In real systems with finite randomness, impurity scattering rate $\gamma_{\rm imp}$, which gives the residual resistivity, dominates the elastic scattering rate $\gamma_{\mathbf{k}}$ at sufficiently low temperatures. In this case, the "T^2-resistivity in the close vicinity of the AF-QCP" is not observed: In fact, for $\gamma_{\rm imp} \gg \gamma_{\mathbf{k}}$, Eq. (2.31) is given by

$$\rho \propto 1/\langle(\gamma_{\mathbf{k}} + \gamma_{\rm imp})^{-1}\rangle_{\rm FS} \propto \gamma_{\rm imp} + \langle\gamma_{\mathbf{k}}\rangle_{\rm FS}. \tag{2.32}$$

Therefore, according to Eq. (2.30), $\rho = \rho_0 + aT^{d/2}$ $(d = 2, 3)$ holds near the AF-QCP in the presence of impurities. In most cases, $a > 0$ is assured even if the CVC is taken into account. ($a = 0$ is realized only in a special case where the Fermi surface is completely isotropic and the Umklapp process is absent; see Sect. 3.2.)

2.4 Validity of the Spin Fluctuation Theories

In Sect. 2.2, we explained that the FLEX approximation explains characteristic electronic properties in optimally-doped HTSC. For example, it can reproduce experimental behavior of the dynamical spin susceptibility $\chi^s_{\mathbf{q}}(\omega)$, which is given in Eq. (2.1). Experimentally, AF correlation starts to increase below $T_0 \sim 600$ K. Using the obtained $\chi^s_{\mathbf{q}}(\omega)$, both the damping rate $\gamma_{\mathbf{k}}$ and CVC are appropriately calculated. For example, the hot/cold spot structure of $\gamma_{\mathbf{k}}$ (Fig. 2.1a) is reproduced well for both hole-doped and electron-doped systems, and the anomalous transport are well reproduced. These facts assure the validity of the FLEX approximation.

Now, we discuss the "weak pseudo-gap behavior" below T_0: Below T_0, the AF fluctuations suppress the DOS [45–48], Knight shift [49–51] and uniform susceptibility [52, 53]. The weak pseudo-gap in the DOS is shallow and wide in energy. The obtained weak pseudo-gap behaviors in the FLEX approximation are too moderate, after the self-consistent determination of the self-energy and Green function. In fact, a large weak pseudo-gap in the DOS is reproduced at the first iteration stage of the FLEX. Similar tendency is reported in the GW approximation: This is a first principle calculation for the self-energy, which is given by the convolution of the Green function G and the screened interaction W within the RPA. Although the descriptions of the bandwidth reduction and satellite structure in the quasiparticle spectrum are satisfactory in a partially self-consistent GW method, they are smeared out in the fully self-consistent GW due to strong feedback effect [54–56]. Mathematically, this too strong feedback effect should be canceled by the vertex correction in the self-energy.

Therefore, to produce a weak pseudo-gap, it is better to apply the (i) fully self-consistent calculation with vertex corrections or (ii) partially (or no) self-consistent calculation. Along the lines of method (i), Schmalian and Pines calculated the self-energy with all the vertex corrections in the $(\mathbf{k}, \mathbf{k} + \mathbf{Q})$ model by applying a high-temperature approximation [57, 58]. Using a similar technique, the pseudo-gap due to strong SC fluctuations had been calculated [59]. It is noteworthy that the

fourth-order-perturbation theory with respect to U well reproduces the weak pseudo-gap since the vertex corrections for the self-energy are considered [60]. This method also reproduces the difference of T_c between YBCO and LSCO [61, 62], and the p-wave SC state in Sr_2RuO_4 [63, 64].

Along the lines of method (ii), Vilk and Tremblay proposed a two-particle self-consistent (TPSC) method [65], where full self-consistency is not imposed on the self-energy. Therein, the renormalized spin susceptibility is given by the RPA, by using the effective Coulomb interaction $U_{\rm eff}$ ($< U$) that is determined so as to satisfy the sum rule for the susceptibility. This philosophy has been applied to extend the dynamical mean field theory (DMFT) by including self-energy correction due to spin fluctuations [66, 67]. These theories can explain the weak pseudo-gap in the DOS. However, they are not suitable for the study of the transport phenomena since the conservation laws are not satisfied. To calculate the transport phenomena with satisfying the conservation laws, the FLEX approximation is very useful.

References

1. T. Moriya, Y. Takahashi, K. Ueda, J. Phys. Soc. Jpn. **59**, 2905 (1990)
2. K. Ueda, T. Moriya, Y. Takahashi, J. Phys. Chem. Solids **53**, 1515 (1992)
3. P. Monthoux, D. Pines, Phys. Rev. B **47**, 6069 (1993)
4. A.J. Millis, H. Monien, D. Pines, Phys. Rev. B **42**, 167 (1990)
5. B.P. Stojkovic, D. Pines, Phys. Rev. B **55**, 8576 (1997)
6. V. Barzykin, D. Pines, Phys. Rev. B **52**, 13585 (1995)
7. E.M. Motoyama, G. Yu, I.M. Vishik, O.P. Vajk, P.K. Mang, M. Greven, Nature **445**, 186 (2007)
8. T. Moriya, *Spin Fluctuations in Itinerant Electron Magnetism* (Springer, Berlin, 1985)
9. N.E. Bickers, S.R. White, Phys. Rev. B **43**, 8044 (1991)
10. T. Dahm, L. Tewordt, Phys. Rev. B **52**, 1297 (1995)
11. T. Takimoto, T. Moriya, J. Phys. Soc. Jpn. **67**, 3570 (1994)
12. S. Koikegami, S. Fujimoto, K. Yamada, J. Phys. Soc. Jpn. **66**, 1438 (1997)
13. H. Kontani, K. Ueda, Phys. Rev. Lett. **80**, 5619 (1998)
14. S. Wermbter, Phys. Rev. B **55**, R10149 (1997)
15. D. Manske, I. Eremin, K.H. Bennemann, Phys. Rev. B **67**, 134520 (2003)
16. H. Kontani, M. Ohno, Phys. Rev. B **74**, 014406 (2006)
17. H. Kontani, M. Ohno, J. Magn. Magn. Mater. **310**, 483 (2007)
18. J. Yu, S. Massidda, A.J. Freeman, D.D. Koelling, Phys. Lett. A **122**, 203 (2012)
19. S. Massidda, N. Hamada, J. Yu, A.J. Freeman, Phys. C **157**, 571 (1989)
20. A.J. Freeman, J. Yu, Phys. B **150**, 50 (1988)
21. J.-H. Xu, T.J. Watson-Yang, J. Yu, A.J. Freeman, Phys. Lett. A **120**, 489 (1987)
22. J.C. Campuzano, G. Jennings, M. Faiz, L. Beaulaigue, B.W. Veal, J.Z. Liu, A.P. Paulikas, K. Vandervoort, H. Claus, R.S. List, A.J. Arko, R.J. Bartlett, Phys. Rev. Lett. **64**, 2308 (1990)
23. N.P. Armitage, D.H. Lu, C. Kim, A. Damascelli, K.M. Shen, F. Ronning, D.L. Feng, P. Bogdanov, Z.-X. Shen, Phys. Rev. Lett. **87**, 147003 (2001)
24. N.P. Armitage, F. Ronning, D.H. Lu, C. Kim, A. Damascelli, K.M. Shen, D.L. Feng, H. Eisaki, Z.-X. Shen, P.K. Mang, N. Kaneko, M. Greven, Y. Onose, Y. Taguchi, Y. Tokura, Phys. Rev. Lett. **88**, 257001 (2002)
25. A. Ino, C. Kim, M. Nakamura, T. Yoshida, T. Mizokawa, A. Fujimori, Z.-X. Shen, T. Kakeshita, H. Eisaki, S. Uchida, Phys. Rev. B **65**, 094504 (2002)
26. T. Tanamoto, H. Kohno, H. Fukuyama, J. Phys. Soc. Jpn. **61**, 1886 (1992)

27. H. Kontani, K. Kanki, K. Ueda, Phys. Rev. B **59**, 14723 (1999)
28. M. Lindroos, S. Sahrakorpi, V. Arpiainen, R.S. Markiewicz, A. Bansil, J. Phys. Chem. Solids **67**, 244 (2006)
29. G. Baym, L.P. Kadanoff, Phys. Rev. **124**, 287 (1961)
30. G. Baym, Phys. Rev. **127**, 1391 (1962)
31. H. Kino, H. Kontani, J. Phys. Soc. Jpn. **67**, 3691 (1998)
32. H. Kondo, T. Moriya, J. Phys. Soc. Jpn. **67**, 3695 (1998)
33. J. Schmalian, Phys. Rev. Lett. **81**, 4232 (1998)
34. H. Kino, H. Kontani, T. Miyazaki, J. Phys. Soc. Jpn. **73**, 25 (2004)
35. H. Kino, H. Kontani, T. Miyazaki, J. Phys. Soc. Jpn. **75**, 104702 (2006)
36. S. Onari, R. Arita, K. Kuroki, H. Aoki, Phys. Rev. B **68**, 024525 (2003)
37. P. Noziéres, *Theory of Interaction Fermion Systems* (Benjamin, New York, 1964)
38. A.A. Abricosov, L.P. Gor'kov, I.E. Dzyaloshinskii, *Methods of Quantum Field Theory in Statistical Physics* (Dover, New York, 1975)
39. T. Moriya, K. Ueda, Adv. Phys. **49**, 555 (2000)
40. K. Yamada, *Electron Correlation in Metals* (Cambridge University Press, Cambridge, 2004)
41. R. Hlubina, T.M. Rice, Phys. Rev. B **51**, 9253–9260 (1995)
42. A. Damascelli, Z. Hussain, Z.-X. Shen, Rev. Mod. Phys. **75**, 473 (2003)
43. H. Kohno, K. Yamada, Prog. Theor. Phys. **85**, 13 (1991)
44. A. Rosch, Phys. Rev. Lett. **82**, 4280 (1999)
45. Ch. Renner, B. Revaz, J.-Y. Genoud, K. Kadowaki, Ø. Fischer, Phys. Rev. Lett. **80**, 149 (1998)
46. N. Miyakawa, P. Guptasarma, J.F. Zasadzinski, D.G. Hinks, K.E. Gray, Phys. Rev. Lett. **80**, 157 (1998)
47. R.M. Dipasupil, M. Oda, N. Momono, M. Ido, J. Phys. Soc. Jpn. **71**, 1535 (2002)
48. T. Sato, T. Yokoya, Y. Naitoh, T. Takahashi, K. Yamada, Y. Endoh, Phys. Rev. Lett. **83**, 2254 (1999)
49. M. Takigawa, A.P. Reyes, P.C. Hammel, J.D. Thompson, R.H. Heffner, Z. Fisk, K.C. Ott, Phys. Rev. B **43**, 247–1991 (1991)
50. H. Alloul, T. Ohno, P. Mendels, Phys. Rev. Lett. **63**, 1700 (1989)
51. K. Ishida, Y. Kitaoka, G-q Zheng, J. Phys. Soc. Jpn. **60**, 3516 (1991)
52. D.C. Johnston, Phys. Rev. Lett. **62**, 957 (1989)
53. M. Oda, H. Matsuki, M. Ido, Solid State Commun. **74**, 1321 (1990)
54. B. Holm, F. Aryasetiawan, Phys. Rev. B **56**, 12825 (1997)
55. B. Holm, U. von Barth, Phys. Rev. B **57**, 2108 (1998)
56. P. Garcia-Gonzalez, R.W. Godby, Phys. Rev. B **63**, 075112 (2001)
57. J. Schmalian, D. Pines, B. Stojkovi, Phys. Rev. B **60**, 667 (1999)
58. J. Schmalian, D. Pines, B. Stojkovi, Phys. Rev. Lett. **80**, 3839 (1998)
59. S. Fujimoto, J. Phys. Soc. Jpn. **71**, 1230 (2002)
60. H. Ikeda, S. Shinkai, K. Yamada, submitted to J. Phys. Soc. Jpn. (2007)
61. S. Shinkai, H. Ikeda, K. Yamada, J. Phys. Soc. Jpn. **74**, 2592 (2005)
62. S. Shinkai, H. Ikeda, K. Yamada, J. Phys. Soc. Jpn. **75**, 104712 (2006)
63. T. Nomura, K. Yamada, J. Phys. Soc. Jpn. **69**, 3678 (2000)
64. T. Nomura, K. Yamada, J. Phys. Soc. Jpn. **71**, 1993 (2002)
65. M. Vilk, A.-M.S. Tremblay, J. Phys. I France **7**, 1309 (1997)
66. H. Kusunose, J. Phys. Soc. Jpn. **75**, 054713 (2006)
67. T. Saso, J. Phys. Soc. Jpn. **68**, 3941 (1999)

Chapter 3
Anomalous Transport Phenomena in Nearly AF Fermi Liquids

3.1 Boltzmann Transport Theory and RTA

Before investigating the transport coefficients using the microscopic Fermi liquid theory, we briefly review the relaxation time approximation (RTA) based on the Bloch-Boltzmann theory [1]. The CVC provides correction for the RTA, and we will see that the CVC becomes crucial near the AF QCP in later sections.

Here, we consider a non-equilibrium steady state under weak electronic field $\boldsymbol{E}$, magnetic field $\boldsymbol{H}$, and the temperature gradient ∇T. In a quasi-classical treatment, the distribution function is given as $f_{\mathbf{k}}(\mathbf{r})$. According to Liouville theorem, $f_{\mathbf{k}(t)}(\mathbf{r}(t)) = f_{\mathbf{k}(t+\Delta t)}(\mathbf{r}(t+\Delta t))$ in the absence of impurity and electron-electron scattering. Therefore, the Boltzmann equation in a nonequilibrium steady state is expressed as [1]

$$\frac{df_{\mathbf{k}}}{dt} = \nabla_{\mathbf{k}} f_{\mathbf{k}} \cdot \dot{\mathbf{k}} + \nabla_{\mathbf{r}} f_{\mathbf{k}} \cdot \dot{\mathbf{r}} = 0, \tag{3.1}$$

where $\dot{\mathbf{k}} = -e(\boldsymbol{E} + \boldsymbol{v} \times \boldsymbol{E})$ and $\dot{\mathbf{r}} = \boldsymbol{v}_{\mathbf{k}}$. Here, we put $c = \hbar = 1$, and $-e$ ($e > 0$) is the charge of electron.

In the presence of electron scattering, Eq. (3.1) is modified as

$$\nabla_{\mathbf{k}} f_{\mathbf{k}} \cdot \dot{\mathbf{k}} + \nabla_{\mathbf{r}} f_{\mathbf{k}} \cdot \dot{\mathbf{r}} = \left(\frac{\partial f_{\mathbf{k}}}{\partial t}\right)_{\text{scatt.}}, \tag{3.2}$$

where the right-hand-side term represents the rate of change in $f_{\mathbf{k}}$ due to scattering between quasiparticles, which is called the collision integral. Using the scattering amplitude from the quasiparticle pair $(\mathbf{k}, \mathbf{k}')$ to $(\mathbf{k}+\mathbf{q}, \mathbf{k}'-\mathbf{q})$, $I(\mathbf{k}, \mathbf{k}'; \mathbf{q})$, it is given by [1]

H. Kontani, *Transport Phenomena in Strongly Correlated Fermi Liquids*,
Springer Tracts in Modern Physics 251, DOI: 10.1007/978-3-642-35365-9_3,

$$\left(\frac{\partial f_{\mathbf{k}}}{\partial t}\right)_{\text{scatt.}} = -\sum_{\mathbf{k}'\mathbf{q}} I(\mathbf{k},\mathbf{k}';\mathbf{q})\left[f_{\mathbf{k}} f_{\mathbf{k}'}(1-f_{\mathbf{k}+\mathbf{q}})(1-f_{\mathbf{k}'-\mathbf{q}}) - (1-f_{\mathbf{k}})(1-f_{\mathbf{k}'}) f_{\mathbf{k}+\mathbf{q}} f_{\mathbf{k}'-\mathbf{q}}\right], \tag{3.3}$$

where the first (second) term represents the outgoing (incoming) scattering process.

When both $\mathbf{E}$ and $\nabla_{\mathbf{r}} T$ are small, it is convenient to analyze the linearized Boltzmann equation with respect to $\mathbf{E}$ and $\nabla_{\mathbf{r}} T$. Here, we introduce the displacement function $g_{\mathbf{k}} = f_{\mathbf{k}} - f^0_{\mathbf{k}}$, where $f^0 = (e^{(\epsilon_{\mathbf{k}}-\mu)/T}+1)^{-1}$ is the Fermi-Dirac function at $T = T(\mathbf{r})$. Considering that $g_{\mathbf{k}}$ is linear in $\mathbf{E}$ and ∇T, Eq. (3.2) is linearized as

$$\left(-\frac{\partial f^0_{\mathbf{k}}}{\partial \epsilon_{\mathbf{k}}}\right)\mathbf{v}_{\mathbf{k}} \cdot \left\{\frac{\epsilon_{\mathbf{k}}-\mu}{T}\nabla_{\mathbf{r}} T + e\mathbf{E}\right\} = \left(\frac{\partial f_{\mathbf{k}}}{\partial t}\right)_{\text{scatt.}} + e\,(\mathbf{v}_{\mathbf{k}} \times \mathbf{H}) \cdot \nabla_{\mathbf{k}} g_{\mathbf{k}}. \tag{3.4}$$

In the same way, the collision integral in Eq. (3.3) is given by

$$\left(\frac{\partial f_{\mathbf{k}}}{\partial t}\right)_{\text{scatt.}} = -\frac{1}{T}\sum_{\mathbf{k}',\mathbf{q}} \tilde{I}(\mathbf{k},\mathbf{k}';\mathbf{q})\left\{\Phi_{\mathbf{k}} + \Phi_{\mathbf{k}'} - \Phi_{\mathbf{k}+\mathbf{q}} - \Phi_{\mathbf{k}'-\mathbf{q}}\right\}, \tag{3.5}$$

where $g_{\mathbf{k}} = \left(-\frac{\partial f^0_{\mathbf{k}}}{\partial \epsilon_{\mathbf{k}}}\right)\Phi_{\mathbf{k}}$ and $\tilde{I}(\mathbf{k},\mathbf{k}';\mathbf{q}) = I(\mathbf{k},\mathbf{k}';\mathbf{q}) f^0_{\mathbf{k}} f^0_{\mathbf{k}'}(1-f^0_{\mathbf{k}+\mathbf{q}})(1-f^0_{\mathbf{k}'-\mathbf{q}})$. In deriving Eq. (3.5), we have used the relation $\tilde{I}(\mathbf{k},\mathbf{k}';\mathbf{q}) = \tilde{I}(\mathbf{k}+\mathbf{q},\mathbf{k}'-\mathbf{q};-\mathbf{q})$ and $\left(-\frac{\partial f^0_{\mathbf{k}}}{\partial \epsilon_{\mathbf{k}}}\right) = \frac{f^0_{\mathbf{k}}(1-f^0_{\mathbf{k}})}{T}$ [1]. The displacement function $g_{\mathbf{k}}$ is given by solving Eqs. (3.4) and (3.5). Using the obtained $g_{\mathbf{k}}$, the conductivity is given by

$$\sigma_{\mu\nu} = -2e\sum_{\mathbf{k}} v_{\mathbf{k}\mu} g_{\mathbf{k}}/E_{\nu}, \tag{3.6}$$

where the factor 2 is attributed to the spin degeneracy.

In Sect. 3.2, we will analyze the Boltzmann equations (3.4) and (3.5) based on the variational principle, which is very powerful in the case of $\mathbf{H} = \nabla_{\mathbf{r}} T = 0$ [1]. Unfortunately, it is still difficult to solve the linearized Boltzmann equation in general cases. Therefore, the RTA is frequently applied to simplify the collision term:

$$\left(\frac{\partial f_{\mathbf{k}}}{\partial t}\right)_{\text{scatt.}} = \left(\frac{\partial g_{\mathbf{k}}}{\partial t}\right)_{\text{scatt.}} = -\frac{g_{\mathbf{k}}}{\tau_{\mathbf{k}}}, \tag{3.7}$$

which means that $g_{\mathbf{k}}(t)$ decays in proportion to $e^{-t/\tau_{\mathbf{k}}}$ in the absence of outer fields. Note that $\tau_{\mathbf{k}} = 1/2\gamma_{\mathbf{k}}$ is the quasiparticle lifetime. Within the RTA, the linearized Boltzmann equation is simplified as

$$-\frac{g_{\mathbf{k}}}{\tau_{\mathbf{k}}} = \left(e\mathbf{E} + \frac{\epsilon_{\mathbf{k}} - \mu}{T}\nabla_{\mathbf{r}} T\right) \cdot \boldsymbol{v}_{\mathbf{k}} \left(-\frac{\partial f_{\mathbf{k}}^0}{\partial \epsilon_{\mathbf{k}}}\right) - e\,(\boldsymbol{v}_{\mathbf{k}} \times \mathbf{H}) \cdot \nabla_{\mathbf{k}} g_{\mathbf{k}}. \tag{3.8}$$

The solution of Eq. (3.8) is given by

$$-g_{\mathbf{k}} = (1 - e\tau_{\mathbf{k}}\,(\boldsymbol{v} \times \mathbf{H}) \cdot \nabla_{\mathbf{k}})^{-1} \left(e\mathbf{E} + \frac{\epsilon_{\mathbf{k}} - \mu}{T}\nabla_{\mathbf{r}} T\right) \cdot \tau_{\mathbf{k}} \boldsymbol{v}_{\mathbf{k}} \left(-\frac{\partial f_{\mathbf{k}}^0}{\partial \epsilon_{\mathbf{k}}}\right). \tag{3.9}$$

Although it is a crude approximation, the RTA can explain the various transport phenomena in metals with weak correlation.

According to Eq. (3.9), $\left.\frac{\partial^n g_{\mathbf{k}}}{\partial H^n}\right|_{H=0} \propto \tau^{n-1}$ when the $\mathbf{k}$-dependence of $\tau_{\mathbf{k}}$ is moderate. In this case, $\sigma_{\mu\nu}$ under the magnetic field, which is given by Eq. (3.6), has the following functional form: $\sigma_{\mu\nu} = \tau F_{\mu\nu}(\tau H)$. This relation given by the RTA is known as the "Kohler's rule", which is well satisfied in many (single band) simple metals.

Here, we assume $\mathbf{H} \parallel \hat{\mathbf{z}}$. Then, $(\boldsymbol{v} \times \mathbf{H}) \cdot \nabla_{\mathbf{k}} = -H_z(\boldsymbol{v}_{\mathbf{k}} \times \nabla_{\mathbf{k}})_z$. Using Eq. (3.9), the longitudinal conductivity, Hall conductivity, and magnetoconductivity in the RTA are given by

$$\sigma_{xx}^{\mathrm{RTA}} = 2e^2 \sum_{\mathbf{k}} \left(-\frac{df^0}{d\epsilon_{\mathbf{k}}}\right) v_{\mathbf{k}x} \cdot \tau_{\mathbf{k}} v_{\mathbf{k}x}, \tag{3.10}$$

$$\sigma_{xy}^{\mathrm{RTA}} = -2e^3 H_z \sum_{\mathbf{k}} \left(-\frac{df^0}{d\epsilon_{\mathbf{k}}}\right) v_{\mathbf{k}x} (\tau_{\mathbf{k}} \boldsymbol{v}_{\mathbf{k}} \times \nabla_{\mathbf{k}})_z \tau_{\mathbf{k}} v_{\mathbf{k}y}, \tag{3.11}$$

$$\Delta\sigma_{xx}^{\mathrm{RTA}} = 2e^4 H_z^2 \sum_{\mathbf{k}} \left(-\frac{df^0}{d\epsilon_{\mathbf{k}}}\right) v_{\mathbf{k}x} (\tau_{\mathbf{k}} \boldsymbol{v}_{\mathbf{k}} \times \nabla_{\mathbf{k}})_z^2 \tau_{\mathbf{k}} v_{\mathbf{k}x}, \tag{3.12}$$

where $(\tau_{\mathbf{k}} \boldsymbol{v}_{\mathbf{k}} \times \nabla_{\mathbf{k}})_z = \tau_{\mathbf{k}}(v_x \partial_y - v_y \partial_x)$. Apparently, the Kohler's rule

$$\sigma_{xx} \propto \tau, \quad \sigma_{xy} \propto \tau^2 H_z, \quad \Delta\sigma_{xx}^{\mathrm{RTA}} \propto \tau^3 H_z^2, \tag{3.13}$$

is satisfied when $\tau_{\mathbf{k}}$ is rather isotropic.

The RTA works only in heavily over-doped samples ($T_{\mathrm{c}} \approx 10\,\mathrm{K}$) [2–4], where the Hall coefficient is small and its temperature dependence is tiny. Hussey et al. determined the anisotropy of $\tau_{\mathbf{k}}$ in heavily over-doped Tl2201 by measuring the Angle-dependent Magnetoresistance Oscillation (AMRO) along c-axis [5, 6], and calculated transport coefficients using Eqs. (3.10)–(3.12). The derived $R_{\mathrm{H}}^{\mathrm{RTA}}$ agrees with the experimental Hall coefficient $R_{\mathrm{H}}^{\mathrm{exp}}$, whose magnitude is of order $1/ne$.

In optimally doped HTSCs, however, the RTA does not work: Stojkovic and Pines [7] attempted to explain the violation of Kohler's rule in HTSCs based on the RTA. They assumed the highly anisotropic $\tau_{\mathbf{k}}$ model (hot/cold-spot model), where only the quasiparticles near the cold spot contribute to the transport phenomena. In this

model, $R_{\rm H}$ can take a large value since the "effective carrier density for the transport phenomena" is reduced. They calculated $\tau_{\mathbf{k}}$ based on the Millis-Monien-Pines model; the anisotropy of $\tau_{\mathbf{k}}$ reaches 100 in the optimally doped YBCO, which is too large to be consistent with the ARPES measurements. (The reason for this overestimation is that self-consistency is not imposed in their calculations.) In spite of the large anisotropy of $\tau_{\mathbf{k}}$, the obtained enhancement ratio of $R_{\rm H}$ is about two according to Ref. [8], which is too small to explain experiments. More disadvantageously, the magnetoresistance becomes 100 times greater than the experimental value when the anisotropy of $\tau_{\mathbf{k}}$ is of the order of 100 [9]. Therefore, the highly anisotropic $\tau_{\mathbf{k}}$ model is not applicable for optimally-doped HTSCs. In the next section, we explain the various anomalous transport phenomena in HTSCs "all together", by considering the CVC.

Finally, we discuss the thermoelectric transport phenomena in the presence of thermal gradient $\nabla_{\mathbf{r}} T \neq 0$: When $\mathbf{H} = 0$ in Eq. (3.9), both the electric current J_μ and thermal current J_μ^Q are given as

$$J_\mu = -2e \sum_{\mathbf{k}} v_{\mathbf{k},\mu} g_{\mathbf{k}} = e^2 K^0_{\mu\nu} E_\nu + \frac{-e}{T} K^1_{\mu\nu} (-\nabla_{\mathbf{r}} T)_\nu, \tag{3.14}$$

$$J^Q_\mu = 2 \sum_{\mathbf{k}} (\epsilon_{\mathbf{k}} - \mu) v_{\mathbf{k},\mu} g_{\mathbf{k}} = -e K^1_{\mu\nu} E_\nu + \frac{1}{T} K^2_{\mu\nu} (-\nabla_{\mathbf{r}} T)_\nu, \tag{3.15}$$

where $\mu, \nu = x, y, z$. The coefficient $K^n_{\mu\nu}$ is given as

$$K^n_{\mu\nu} = \sum_{\mathbf{k}} (\epsilon_{\mathbf{k}} - \mu)^n \tau_{\mathbf{k}} v_{\mathbf{k},\mu} v_{\mathbf{k},\nu} \left(-\frac{\partial f^0}{\partial \epsilon} \right) \tag{3.16}$$

Using the Sommerfeld expansion $\int \Phi(\epsilon) \left(-\frac{\partial f^0}{\partial \epsilon} \right) d\epsilon = \Phi(\mu) + \frac{(\pi T)^2}{6} \left[\frac{\partial^2 \Phi}{\partial \epsilon^2} \right]_{\epsilon=\mu}$ $+ O(T^4)$, we obtain the relationships

$$K^2 = \frac{1}{3} (\pi T)^2 K^0, \; K^1 = \frac{1}{3} (\pi T)^2 \left[\frac{\partial}{\partial \mu} K^0 \right]. \tag{3.17}$$

Now, we consider an open circuit ($J = 0$) in the presence of the electric field and temperature gradient. Then, the relation $E_\mu = (eT)^{-1} (K^1/K^0)(-\nabla_{\mathbf{r}} T)_\mu$ is derived from Eq. (3.14). Therefore, the thermoelectric power $S = E/|\nabla_{\mathbf{r}} T|$ is given as

$$\begin{aligned} S &= \frac{-1}{eT} \frac{K^1}{K^0} = \frac{-1}{eT} \frac{\frac{(\pi T)^2}{3} \frac{\partial}{\partial \mu} \sigma}{\sigma} \\ &= \frac{-\pi^2 T}{3e} \frac{\partial}{\partial \mu} \ln \sigma(\mu) \end{aligned} \tag{3.18}$$

which is called the Mott formula. Here, $\sigma(\mu)$ is the electric conductivity for the chemical potential μ.

The thermal current J^Q is finite even in an open circuit. It is derived from Eq. (3.14) as $J^Q = eK^1 \dfrac{-1}{eT}\dfrac{K^1}{K^0}(-\nabla_{\mathbf{r}} T) + \dfrac{1}{T}K^2(-\nabla_{\mathbf{r}} T)$. Therefore, the thermal conductivity $\kappa = J^Q/(-\nabla_{\mathbf{r}} T)$ is given by

$$\kappa = \frac{1}{T}\left(K^2 - \frac{(K^1)^2}{K^0}\right)(-\nabla_{\mathbf{r}} T) \tag{3.19}$$

Since $K^2 \propto \tau T^2$ and $(K^1)^2/K^0 \propto \tau T^4$, we obtain $\kappa = K^2/T$ at low temperatures. Since $\sigma = e^2 K^0$, we obtain the Wiedemann-Franz law:

$$\kappa = \frac{\pi^2}{3}\frac{T}{e^2}\sigma \tag{3.20}$$

Note that this relationship is exact beyond the RTA, if the elastic scattering dominates the inelastic scattering at sufficiently low temperatures.

3.2 The Variational Principle and CVC

In the RTA where $\dot{g}_k = -g_{\mathbf{k}}/\tau_{\mathbf{k}}$ is assumed, the deviation from the equilibrium distribution function $g_{\mathbf{k}}$ dissipates with time since $g_{\mathbf{k}} \propto e^{-t/\tau_{\mathbf{k}}}$ in the absence of outer fields. However, $g_{\mathbf{k}}$ should remain finite when the Umklapp scattering process is absent, because of the momentum conservation laws [1, 10]. On the other hand, the quasiparticle lifetime $\tau_{\mathbf{k}} = 1/2\gamma_{\mathbf{k}}$, which is given by Eq. (2.29), is always finite, and therefore the conservation laws are violated in the RTA. To recover the conservation laws, we have to take account of the CVCs introduced in Fig. 1.1, which correspond to $\Phi_{\mathbf{k}'}$, $\Phi_{\mathbf{k}+\mathbf{q}}$ and $\Phi_{\mathbf{k}'-\mathbf{q}}$ in the collision integral in Eq. (3.3).

To include the CVC into the calculation, we analyze the Boltzmann equations (3.4) and (3.5) by applying the variational principle. This method had been studied by Umeda [11, 12], Kohler [13, 14] and Sondheimer [15], and it is explained in Ref. [1] in detail. When $\mathbf{H} = \nabla_{\mathbf{r}} T = 0$, the left-hand-side of Eq. (3.4) becomes $X \equiv \left(-\dfrac{\partial f^0_{\mathbf{k}}}{\partial \epsilon_{\mathbf{k}}}\right)\mathbf{v}_{\mathbf{k}} \cdot e\mathbf{E}$. If we write the right-hand-side of Eq. (3.5) as $-P\Phi$, the Boltzmann equations is expressed as

$$X = -P\Phi \tag{3.21}$$

Now, we consider that $\Phi_{\mathbf{k}}$ as the *trial function* with $\langle \Phi_{\mathbf{k}} \rangle = 0$. Then, the lower limit of the resistivity ρ is given by the following variational formula:

$$\rho \leq \frac{\langle \Phi, P\Phi \rangle}{[\langle \Phi, X(E=1) \rangle]^2} \tag{3.22}$$

where $\langle \Phi, \Psi \rangle \equiv \sum_{\mathbf{k}} \Phi_{\mathbf{k}} \Psi_{\mathbf{k}}$ is the inner product. The equal sign in Eq. (3.22) is realized when the trial function Φ is the solution of the Boltzmann equation (3.21). The variational formula (3.22) will be proved in Appendix A.

Equation (3.22) is easily rewritten as

$$\rho \leq \frac{\frac{1}{8T} \sum_{\mathbf{k},\mathbf{k}',\mathbf{q}} \tilde{I}(\mathbf{k},\mathbf{k}';\mathbf{q}) \left\{ \Phi_{\mathbf{k}} + \Phi_{\mathbf{k}'} - \Phi_{\mathbf{k}+\mathbf{q}} - \Phi_{\mathbf{k}'-\mathbf{q}} \right\}^2}{\left[e \sum_{\mathbf{k}} v_{\mathbf{k}x} \Phi_{\mathbf{k}} \left(-\frac{\partial f^0_{\mathbf{k}}}{\partial \epsilon_{\mathbf{k}}} \right) \right]^2} \tag{3.23}$$

The physical meaning of the variational principle is that the current in the nonequilibrium steady state under E is realized so as to maximize the production of entropy due to scattering processes (= Joule heat E^2/ρ) [1]. The trial function is generally constructed as $\Phi_{\mathbf{k}} = \mathrm{Re} \sum_{l,m} \eta_l^m Y_l^m(\hat{\mathbf{k}})$, where $Y_l^m(\hat{\mathbf{k}})$ is the spherical harmonics. In crystals, $Y_l^m(\hat{\mathbf{k}})$ can be replaced with the Fermi surface harmonics [16].

Now, we put $\Phi_{\mathbf{k}} \propto [\mathbf{k}]_{\mathrm{c}} \cdot \mathbf{E}/E$, where $[\mathbf{k}]_{\mathrm{c}}$ is the crystal momentum in the first Brillouin zone for general $\mathbf{k}$. When the Umklapp scattering process is absent, both $\mathbf{k}+\mathbf{q}$ and $\mathbf{k}'-\mathbf{q}$ are always inside of the first Brillouin zone, and therefore $\Phi_{\mathbf{k}} + \Phi_{\mathbf{k}'} - \Phi_{\mathbf{k}+\mathbf{q}} - \Phi_{\mathbf{k}'-\mathbf{q}} = 0$. In this case, the right hand side of Eq. (3.22) vanishes identically. Therefore, electron-electron correlation does not cause the resistivity ($\rho = 0$) if the Umklapp scattering is absent, irrespective of the shape of Fermi surfaces. [Exactly speaking, ρ is finite due to the higher Umklapp scattering processes.] Therefore, the role of the CVC discussed in Sect. 1.1 is described by solving the Boltzmann equation.

In the presence of Umklapp scattering processes, ρ becomes finite since $\Phi_{\mathbf{k}} + \Phi_{\mathbf{k}'} - \Phi_{\mathbf{k}+\mathbf{q}} - \Phi_{\mathbf{k}'-\mathbf{q}} \neq 0$ for Umklapp scattering; see Fig. 3.4b. In this case, it is empirically known that a simple trial function $\Phi_{\mathbf{k}} \propto \mathbf{v}_{\mathbf{k}} \cdot \mathbf{E}/E$ presents a reasonable value of ρ. Then, we obtain $\rho \propto T^2$ in three dimensional systems after performing the momentum integrations in Eq. (3.23), if the scattering amplitude I (not $\tilde{I}$) is temperature independent.

In addition, we consider the system with dilute impurities. Then, the Matthiesen's rule tells that the resistivity is given as

$$\rho = \rho_0 + \rho_{\mathrm{el-el}}, \tag{3.24}$$

where ρ_0 is the residual resistivity due to impurities. At sufficiently low temperatures where $\rho \sim \rho_0$, $\Phi_{\mathbf{k}}$ is almost determined by the impurity scattering. The variational principle for ρ_0 is given as

$$\rho_0 \leq \frac{\frac{1}{4T} \sum_{\mathbf{k},\mathbf{k}'} \tilde{I}_{\mathrm{imp}}(\mathbf{k},\mathbf{k}') \{\Phi_{\mathbf{k}} - \Phi_{\mathbf{k}'}\}^2}{\left[e \sum_{\mathbf{k}} v_{\mathbf{k}x} \Phi_{\mathbf{k}} \left(-\frac{\partial f^0_{\mathbf{k}}}{\partial \epsilon_{\mathbf{k}}} \right) \right]^2}. \tag{3.25}$$

When the impurity potential is delta functional, the scattering amplitude becomes $\tilde{I}_{\rm imp}(|\mathbf{k}|, |\mathbf{k}'|)$. Then, because of the relation $|\langle x|y\rangle|^2 \leq \langle x|x\rangle\langle y|y\rangle$, the right-hand-side of Eq. (3.25) is minimized when $\Phi_{\mathbf{k}}$ is proportional to $\mathbf{v}_{\mathbf{k}} \cdot \mathbf{E}/E$. That is, the relaxation time approximation $\Phi_{\mathbf{k}}^{\rm imp} = -e\tau_{\rm imp} v_{\mathbf{k}x} E$ becomes exact, where $\tau_{\rm imp}$ is the relaxation time by impurity scattering. In this case, $\rho_{\rm el-el}$ ($\ll \rho_0$) in Eq. (3.24) is given by Eq. (3.22) with $\Phi_{\mathbf{k}}^{\rm imp} = -e\tau_{\rm imp} v_{\mathbf{k}x} E$. Then, $\rho_{\rm el-el}$ is finite even if the Umklapp process is absent, because $\Phi_{\mathbf{k}}^{\rm imp} + \Phi_{\mathbf{k}'}^{\rm imp} - \Phi_{\mathbf{k}+\mathbf{q}}^{\rm imp} - \Phi_{\mathbf{k}'-\mathbf{q}}^{\rm imp}$ is non-zero except when the Fermi surface is completely spherical [17].

Although the effect of the CVC can be calculated by using the variational method, its applicability is limited. Therefore, in later sections, we analyze the CVC based on the microscopic Fermi liquid theory. Therein, the CVC is included in the total current $\mathbf{J}_{\mathbf{k}}$, which is obtained by solving the Bethe-Salpeter equation. Using $\mathbf{J}_{\mathbf{k}}$, the solution of the Boltzmann equation, $\Phi_{\mathbf{k}}$, is expressed as

$$\Phi_{\mathbf{k}} = -e\tau_{\mathbf{k}} \mathbf{J}_{\mathbf{k}} \cdot \mathbf{E}, \tag{3.26}$$

where $\tau_{\mathbf{k}}$ is the lifetime of quasiparticle at $\mathbf{k}$; $\tau_{\mathbf{k}} = 1/2\gamma_{\mathbf{k}} = 1/2{\rm Im}\Sigma_{\mathbf{k}}(-i\delta)$.

3.3 Analysis of the CVC Based on the Fermi Liquid Theory

Here, we calculate the CVC based on the linear response theory, utilizing the powerful field theoretical techniques. In principle, the CVC can be derived from the Boltzmann equation (3.3) by applying the variational principle [1]. However, a systematic calculation of the CVC is very difficult, particularly in the presence of a magnetic field.

We shortly derive the Nakano-Kubo linear response theory [18–21]. Therein, we discuss the first-order perturbation theory with respect to the time-dependent potential:

$$V(t) = -e \int dx P_{\mu}(x) E_{\mu}(t) \tag{3.27}$$

where $P_{\mu} = \int dx x_{\mu} n(x)$ is the polarization operator and E_{μ} is the electronic field. Then, the time-dependent Schroedinger equation is

$$i\frac{\partial}{\partial t}|\phi(t)\rangle = [H_0 + V(t)]|\phi(t)\rangle \tag{3.28}$$

where H_0 represents the Hamiltonian without outer fields. Now, we express the eigenstate of Eq. (3.28) as

$$|\phi(t)\rangle = e^{-iH_0 t} A(t)|0\rangle \tag{3.29}$$

where $|0\rangle$ is the initial eigenstate without V, and $A(t)$ is an unknown function. When $V \equiv 0$, $A(t) \equiv 1$. By inputting it into Eq. (3.28), we obtain $\dot{A}(t) = -iV_H(t)A(t)$,

where $V_H(t) = e^{iH_0t}V(t)e^{-iH_0t}$. Since $A(t) = 1 - i\int_0^t V_H(t')dt' + O(V^2)$, we obtain

$$|\phi(t)\rangle = e^{-iH_0t}|0\rangle - ie^{-iH_0t}\int_0^t dt' V_H(t')|0\rangle + O(V^2). \tag{3.30}$$

Thus, the induced current under the electronic field is

$$\begin{aligned}\langle j_\mu(x,t)\rangle &\equiv \langle\phi(t)|j_\mu(x)|\phi(t)\rangle \\ &= \int dx' \int_{-\infty}^{\infty} dt'(-i)\langle\phi_0(0)|[j_\mu(x,t),\, P_\nu(x',t')]|\phi_0(0)\rangle \\ &\times \theta(t-t')eE_\nu(t')\end{aligned} \tag{3.31}$$

At finite temperatures, this formula is expressed as

$$\langle j_\mu(x,t)\rangle = \int dx' \int_{-\infty}^{\infty} dt'(-i)\langle[j_\mu(x,t),\, P_\nu(x',t')]\rangle_0\theta(t-t')eE_\nu(t') \tag{3.32}$$

where $\langle\cdots\rangle_0 = \mathrm{Tr}\{e^{-\beta H_0}\cdots\}/\mathrm{Tr}\{e^{-\beta H_0}\}$.

As following Nakano [18]. we put $E_\nu(t) = E_\nu e^{-i\omega t+\eta t}$ ($\eta > 0$). Noticing the relation $\dot{P}_\nu(x,t) = j_\nu(x,t)$ and performing the partial integration, we obtain

$$\begin{aligned}\langle j_\mu(x,t)\rangle = \int dx' \int_{-\infty}^{\infty} dt'(-i)\langle[j_\mu(x,t),\, j_\nu(x',t')]\rangle_0 \\ \times\left[\theta(t-t')\frac{e^{-i\omega t'}}{i\omega} + \theta(t'-t)\frac{e^{-i\omega t}}{i\omega}\right]eE_\mu\end{aligned} \tag{3.33}$$

After performing the Fourier transformation with respect to (x,t), we obtain the Nakano-Kubo formula for the conductivity [18–21]:

$$\sigma_{\mu\nu}(\omega) = \frac{e^2}{i\omega}\left[K^R_{\mu\nu}(\omega) - K^R_{\mu\nu}(0)\right], \tag{3.34}$$

where $K^R_{\mu\nu}(\omega) = K_{\mu\nu}(\omega + i\delta)$ is the retarded current-current correlation function, given by the Fourier transformation of

$$K^R_{\mu\nu}(t) = -i\int_{-\infty}^{\infty} dt'\langle[j_{\mathbf{q},\mu}(t),\, j_{-\mathbf{q},\nu}(t')]\rangle\theta(t-t'). \tag{3.35}$$

Since it is difficult to calculate $K^R_{\mu\nu}(\omega)$ directly, we first calculate the following thermal correlation function

$$K_{\mu\nu}(i\omega_l) = \int_0^{1/T} d\tau e^{-i\omega_l\tau}\left\langle T_\tau j_{\mathbf{q},\mu^A}(0)j_{-\mathbf{q},\nu}(\tau)\right\rangle \tag{3.36}$$

where $\omega_l \equiv 2\pi T l$ is the Matsubara frequency; here we promise l represents an integer and n is a half-integer, respectively. Then, the retarded function is obtained by performing the analytic continuation $i\omega_l (\geq 0) \to \omega + i\delta$.

Next, we consider the conductivities in the presence of the uniform magnetic field. Then, the hopping integral between site i and j exhibits the Peierls phase:

$$t_{m,j} = t^0_{m,j} \exp[-ie(\mathbf{A}_m + \mathbf{A}_j) \cdot (\mathbf{r}_m - \mathbf{r}_j)/2], \tag{3.37}$$

where $t^0_{m,j}$ is the original hopping integral, and $\mathbf{A}_m$ is the vector potential at site m. Then, the Hamiltonian and the velocity operator under the magnetic field, H_A and j^A_μ respectively, are given by

$$H_A = \sum_{(m,j),\sigma} t_{m,j} c^\dagger_{m\sigma} c_{j\sigma} + \frac{U}{2} \sum_m n_{m\uparrow} n_{m\downarrow}, \tag{3.38}$$

$$j^A_\mu(\mathbf{r}_m) = \sum_\sigma i[H_A, \mathbf{r}_m c^\dagger_{m\sigma} c_{m\sigma}] \tag{3.39}$$

Here, we assume that the vector potential is given by $\mathbf{A}_j = \mathbf{A} e^{i\mathbf{q}\cdot\mathbf{r}_j}$, and take the limit $\mathbf{q} \to 0$ at the final stage of the calculation [22]. (The magnetic field is $\mathbf{H} = i\mathbf{q} \times \mathbf{A}$.) After the Fourier transformation, both the Hamiltonian and the velocity operator of the order of $O(A)$ are given by [23]

$$H_A = H - \mathbf{A} \cdot \mathbf{j}(-\mathbf{q}) + O(A^2), \tag{3.40}$$

$$j^A_\mu(\mathbf{q}') = j_\mu(\mathbf{q}') - \sum_\alpha^{x,y} A_\alpha j_{\alpha\mu}(\mathbf{q}' - \mathbf{q}) + O(A^2), \tag{3.41}$$

where $j_\mu(\mathbf{q}) = -e \sum_{\mathbf{k},\sigma} \partial_\mu \epsilon^0_{\mathbf{k}} \cdot c^\dagger_{\mathbf{k}-\mathbf{q}/2,\sigma} c_{\mathbf{k}+\mathbf{q}/2,\sigma}$, and $j_{\alpha\mu}(\mathbf{q}) = e^2 \sum_{\mathbf{k}} \partial_{\alpha\mu} \epsilon^0_{\mathbf{k}} \cdot c^\dagger_{\mathbf{k}-\mathbf{q}/2,\sigma} c_{\mathbf{k}+\mathbf{q}/2,\sigma}$. ($\partial_\mu = \partial/\partial k_\mu$ and $\partial_{\mu\alpha} = \partial^2/\partial k_\mu \partial k_\alpha$.) Then, the current-current correlation function under $\mathbf{H} \neq 0$ is given as [22–24]

$$K_{\mu\nu}(i\omega_l) = \sum_{m=0,1,\cdots} \int_0^{1/T} d\tau e^{-i\omega_l \tau} \langle T_\tau j^A_\mu(m\mathbf{q}, 0) j^A_\nu(0, \tau) \rangle_A \tag{3.42}$$

$$= \int_0^{1/T} d\tau e^{-i\omega_l \tau} \langle T_\tau j_\mu(0,0) j_\nu(0,\tau) \rangle \tag{3.43}$$

$$+ \sum_\alpha^{x,y} A_\alpha \int\int_0^{1/T} d\tau d\tau' e^{-i\omega_l \tau} \left\{ -T \cdot \langle T_\tau j_\mu(\mathbf{q}, 0) j_{\alpha\nu}(-\mathbf{q}, \tau) \rangle \right.$$

$$\left. + \langle T_\tau j_\mu(\mathbf{q}, 0) j_\nu(0, \tau) j_\alpha(-\mathbf{q}, \tau') \rangle \right\} + O(A^2). \tag{3.44}$$

Hereafter, we ignore the spin indices to simplify expressions. According to Eq. (3.43), $K_{xx}(i\omega_l)$ without the magnetic field is given by [25]

$$K_{xx}(i\omega_l) = -2e^2T \sum_{n,m,\mathbf{k},\mathbf{k}'} v^0_{\mathbf{k}x} v^0_{\mathbf{k}'x} L(\mathbf{k}n, \mathbf{k}'m; i\omega_l)$$
$$= -2e^2T \sum_{n,\mathbf{k}} v^0_{\mathbf{k}x} g^{n;l}_{\mathbf{k}} \Lambda^{n;l}_{\mathbf{k}x}, \tag{3.45}$$

where $g^{n;l}_{\mathbf{k}} \equiv G^n_{\mathbf{k}} G^{n+l}_{\mathbf{k}}$. $G^n_{\mathbf{k}} \equiv G_{\mathbf{k}}(i\epsilon_n)$ is the Green function where n is a half-integer, and $L(\mathbf{k}n, \mathbf{k}'m; i\omega_l)$ is the two-particle Green function in Eq. (2.27). $v^0_{\mathbf{k}\mu} \equiv \partial\epsilon^0_{\mathbf{k}}/\partial k_\mu$ is the velocity of the free electron, and

$$\mathbf{\Lambda}^{n;l}_{\mathbf{k}} = \mathbf{v}^0_{\mathbf{k}} + T \sum_{\mathbf{k}',m} L(\mathbf{k}n, \mathbf{k}'m; i\omega_l) g^{m;l}_{\mathbf{k}'} \mathbf{v}^0_{\mathbf{k}'} \tag{3.46}$$

is the three-point vertex.

In the same way, Kohno and Yamada [24] derived the H-linear term of $K_{xy}(i\omega_l)$ from Eq. (3.44) as

$$K_{xy}(i\omega_l) = i \cdot e^3 HT \sum_{n,\mathbf{k}} \sum_{\mu,\nu}^{x,y} \left[\partial_\mu G^{n+l}_{\mathbf{k}} \cdot G^n_{\mathbf{k}} - G^{n+l}_{\mathbf{k}} \cdot \partial_\mu G^n_{\mathbf{k}}\right] \left[\Lambda^{n;l}_{\mathbf{k}x} \cdot \partial_\nu \Lambda^{n;l}_{\mathbf{k}y}\right] \cdot \epsilon_{\mu\nu z}$$
$$+ [6 \text{ point VC term}], \tag{3.47}$$

where $\epsilon_{\mu\nu\lambda}$ is an antisymmetric tensor with $\epsilon_{xyz} = 1$. In deriving Eq. (3.47), we used the relation $H_z = i(q_x A_y - q_y A_x)$ and took the limit $\mathbf{q} \to 0$ at the final stage of calculation [22]. Several kinds of Ward identities have to be correctly applied to maintain the gauge invariance [24].

In order to derive the conductivity $\sigma_{\mu\nu}(\omega)$, we have to perform the analytic continuations of Eqs. (3.45) and (3.47); $i\omega_l$ $(l > 0)$ $\to$ $\omega + i\delta$. For the practice of the analytic continuation, we analyze $K_{xx}(i\omega_l)$ without vertex correction:

$$K^{\text{noVC}}_{xx}(i\omega_l) = -2e^2T \sum_{n,\mathbf{k}} (v^0_{\mathbf{k}x})^2 G_{\mathbf{k}}(i\epsilon_n) G_{\mathbf{k}}(i\epsilon_n + i\omega_l)$$
$$= -2e^2 \sum_{\mathbf{k}} \oint_C \frac{d\epsilon}{4\pi i} \text{th}\frac{\epsilon}{2T} (v^0_{\mathbf{k}x})^2 g^{n;l}_{\mathbf{k}} \tag{3.48}$$

where the complex integration path C is shown in Fig. 3.1a. In deriving the second line of Eq. (3.48), we utilized the fact that $\text{th}\dfrac{\epsilon}{2T}$ has poles at $\epsilon = i(2n+1)\pi T$ on the imaginary axis, and the corresponding residue is $2T$. By changing the integration path to Fig. 3.1b, Eq. (3.48) is modified as

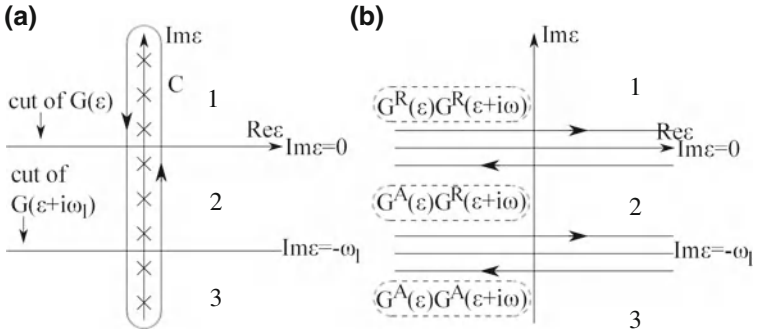

Fig. 3.1 **a** The analytic regions 1–3 as a function of a complex variable ϵ. Here, we put $\mathrm{Im}\,\omega > 0$. From each region, $g^{n;l}_{\mathbf{k}}$ and $\Lambda^{n;l}_{\mathbf{k}x}$ are analytically continued to become $g^{(i)}_{\mathbf{k}}(\epsilon;\omega)$ and $J^{(i)}_{\mathbf{k}x}(\epsilon;\omega)$ ($i = 1$–3), respectively. (b) The path C of the complex integration in Eq. (3.48)

$$K^{\mathrm{noVC}}_{xx}(i\omega_l) = -2e^2 \int_{-\infty}^{\infty} \frac{d\epsilon}{4\pi i} (v^0_{\mathbf{k}x})^2 \Big[\mathrm{th}\frac{\epsilon}{2T} (G^R_{\mathbf{k}}(\epsilon) - G^A_{\mathbf{k}}(\epsilon)) G_{\mathbf{k}}(\epsilon + i\omega_l) + \mathrm{th}\frac{\epsilon - i\omega_l}{2T} G_{\mathbf{k}}(\epsilon - i\omega_l) \big(G^R_{\mathbf{k}}(\epsilon) - G^A_{\mathbf{k}}(\epsilon)\big) \Big], \tag{3.49}$$

where $G^{R(A)}_{\mathbf{k}}(\epsilon) = G_{\mathbf{k}}(\epsilon \pm i\delta)$, and its functional form is given in Eq. (2.18). Finally, we perform the analytic continuation $i\omega_l (l \geq 0) \to w + i\delta$:

$$K^{\mathrm{noVC}}_{xx}(\omega + i\delta) = -2e^2 \int_{-\infty}^{\infty} \frac{d\epsilon}{4\pi i} (v^0_{\mathbf{k}x})^2 \sum_{i=1}^{3} \lambda^{(i)}(\epsilon;\omega) g^{(i)}_{\mathbf{k}}(\epsilon;\omega) \tag{3.50}$$

where $g^{(i)}_{\mathbf{k}}(\epsilon;\omega)$ ($i = 1, 2, 3$) is given by the analytic continuation of $G_{\mathbf{k}}(i\epsilon) G_{\mathbf{k}}(i\epsilon + i\omega)$ from the region i shown in Fig. 3.1a to real frequencies. It is expressed as $g^{(1)}_{\mathbf{k}}(\epsilon;\omega) \equiv G^R_{\mathbf{k}}(\epsilon) G^R_{\mathbf{k}}(\epsilon + \omega)$, $g^{(2)}_{\mathbf{k}}(\epsilon;\omega) \equiv G^A_{\mathbf{k}}(\epsilon) G^R_{\mathbf{k}}(\epsilon + \omega)$, and $g^{(3)}_{\mathbf{k}}(\epsilon;\omega) \equiv G^A_{\mathbf{k}}(\epsilon) G^A_{\mathbf{k}}(\epsilon + \omega)$. The corresponding thermal factors for region i is $\lambda^{(1)}(\epsilon;\omega) \equiv \mathrm{th}\frac{\epsilon}{2T}$, $\lambda^{(2)}(\epsilon;\omega) \equiv (\mathrm{th}\frac{\epsilon+\omega}{2T} - \mathrm{th}\frac{\epsilon}{2T})$, and $\lambda^{(3)}(\epsilon;\omega) \equiv -\mathrm{th}\frac{\epsilon+\omega}{2T}$. According to Eqs. (2.18)–(2.20), the relation $|G^R_{\mathbf{k}}(\epsilon)|^2 = \frac{\pi\rho_{\mathbf{k}}(\epsilon)}{\gamma^*_{\mathbf{k}}} \approx \frac{\pi\delta(E_{\mathbf{k}})}{\gamma_{\mathbf{k}}}$ holds for $\gamma_{\mathbf{k}} \ll E_F$, so $g^{(2)}$ in Eq. (3.50) gives the dominant contribution. On the other hand, $g^{(1,3)}$ is less significant since two poles locate on the same upper- or lower-complex plane [25]. For this reason, only $g^{(2)}_{\mathbf{k}}$ presents the dominant contribution to the DC conductivity:

$$\begin{aligned}\sigma_{xx}^{\mathrm{noVC}} &= \frac{1}{\omega}\mathrm{Im}K_{xx}^{\mathrm{noVC}}(\omega+i\delta)|_{\omega=0} \\ &= e^2\sum_{\mathbf{k}}\int_{-\infty}^{\infty}\frac{d\epsilon}{\pi}(v_{\mathbf{k}x}^0)^2\left(-\frac{\partial f}{\partial\epsilon}\right)|G_{\mathbf{k}}^R(\epsilon)|^2 \\ &\approx e^2\sum_{\mathbf{k}} z_{\mathbf{k}}\left(-\frac{\partial f}{\partial\epsilon}\right)_{E_{\mathbf{k}}^*}\frac{(v_{\mathbf{k}x}^0)^2}{\gamma_{\mathbf{k}}} \end{aligned} \tag{3.51}$$

where $f(\epsilon) = (e^{\epsilon/T}+1)^{-1}$, and the relation $z_{\mathbf{k}}(-\partial f^0/\partial\epsilon)_{E_{\mathbf{k}}^*} = (-\partial f^0/\partial\epsilon)_{E_{\mathbf{k}}} = \delta(E_{\mathbf{k}})$ holds at low temperatures. Thus, we obtain $\sigma_{xx}^{\mathrm{noVC}} \propto \gamma^{-1}$, which diverges when $\gamma \to 0$.

In the presence of CVCs, the procedure of the analytic continuation becomes more complicated: The expression of $K_{xx}(\omega+i\delta)$ is [25]

$$K_{xx}(\omega+i\delta) = -2e^2\int_{-\infty}^{\infty}\frac{d\epsilon}{4\pi i}\sum_{l=1,2,3}\lambda^{(1)}(\epsilon;\omega)K_{xx}^{(1)}(\epsilon;\omega), \tag{3.52}$$

$$K_{xx}^{(i)}(\epsilon;\omega) = \sum_{\mathbf{k}} v_{\mathbf{k}x}^0 g_{\mathbf{k}}^{(i)}(\epsilon;\omega)J_{\mathbf{k}x}^{(i)}(\epsilon;\omega), \tag{3.53}$$

where $i = 1,2,3$. $J_{\mathbf{k}x}^{(i)}(\epsilon;\omega)$ is given by the analytic continuation of $\Lambda_{\mathbf{k}x}^{n;l} = \Lambda_{\mathbf{k}x}(i\epsilon_n, i\omega_l)$ in Eq. (3.46), from region i shown in Fig. 3.1a to real frequencies. It is expressed as

$$J_{\mathbf{k}x}^{(i)}(\epsilon,\omega) = v_{\mathbf{k}x}^0 + \sum_{\mathbf{k}',j=1,2,3}\int_{-\infty}^{\infty}\frac{d\epsilon'}{4\pi i}\mathcal{T}_{\mathbf{k},\mathbf{k}'}^{i,j}(\epsilon,\epsilon';\omega)g_{\mathbf{k}'}^{(j)}(\epsilon';\omega)v_{\mathbf{k}'x}^0, \tag{3.54}$$

where $\mathcal{T}_{\mathbf{k},\mathbf{k}'}^{i,j}(\epsilon,\epsilon';\omega)$ is the four point vertex correction connected with $g^{(i)}(\epsilon;\omega)$ and $g^{(j)}(\epsilon';\omega)$: It is given by the analytic continuation of the full four-point vertex $\Gamma(i\epsilon_n, i\epsilon_m; iw_l)$ in Eq. (2.17), from the region i (j) for $i\epsilon_n$ ($i\epsilon_m$) in Fig. 3.1a to real frequencies. Thermal factors are included in the definition of $\mathcal{T}_{\mathbf{k},\mathbf{k}'}^{i,j}$, and its functional form will be given in Appendix B.

According to Eq. (3.54), $\mathcal{T}^{i,j}$ satisfies the following Bethe-Salpeter equation:

$$\begin{aligned}\mathcal{T}^{i,j}(\epsilon,\epsilon';\omega) &= \mathcal{T}^{(I)i,j}(\epsilon,\epsilon';\omega) \\ &+ \sum_{l=1,2,3}\int\frac{d\epsilon''}{4\pi i}\mathcal{T}^{(I)i,l}(\epsilon,\epsilon'';\omega)g^{(l)}(\epsilon'';\omega)\mathcal{T}^{l,j}(\epsilon'',\epsilon';\omega)\end{aligned} \tag{3.55}$$

where we dropped the momentum suffices for simplicity, and $\mathcal{T}^{(I)}$ represent the irreducible vertex without any particle-hole pairs $g^{(l)}$. We can also construct the following Bethe-Salpeter equation according to Eliashberg [25]:

$$\mathcal{T}^{i,j}(\epsilon,\epsilon';\omega)=\mathcal{T}^{(0)i,j}(\epsilon,\epsilon';\omega)+\int\frac{d\epsilon''}{4\pi i}\mathcal{T}^{(0)i,2}(\epsilon,\epsilon'';\omega)g^{(2)}(\epsilon'';\omega)\mathcal{T}^{2,j}(\epsilon'',\epsilon';\omega) \tag{3.56}$$

where $\mathcal{T}^{(0)}$ is the irreducible vertex without any $g^{(2)}$, whereas $g^{(1)}$ and $g^{(3)}$ can be included: $\mathcal{T}^{(0)i,j}=\mathcal{T}^{(I)i,j}+\sum_{l=1,3}\int\frac{d\epsilon''}{4\pi i}\mathcal{T}^{(I)i,l}g^{(l)}\mathcal{T}^{(0)l,j}$.

In the same way, we can divide $K_{xx}(\omega+i\delta)$ in Eq. (3.52) into $K^a_{xx}+K^b_{xx}$; the former does not contain any $g^{(2)}$ and the latter includes more than one $g^{(2)}$. We neglect K^a_{xx} since the dominant contribution of $\sigma_{xx}\propto\gamma^{-1}$ comes from $g^{(2)}$. Then, K^b_{xx} is rewritten as

$$K_{xx}(\omega+i\delta)=-2e^2\int_{-\infty}^{\infty}\frac{d\epsilon}{4\pi i}\tilde{J}^{(0)}_{\mathbf{k}x}(\epsilon;\omega)\lambda^{(2)}(\epsilon;\omega)g^{(2)}_{\mathbf{k}}(\epsilon;\omega)J_{\mathbf{k}x}(\epsilon;\omega) \tag{3.57}$$

The left-hand-side current $\tilde{J}^{(0)}_{\mathbf{k}x}$, which is irreducible with respect to $g^{(2)}$, is given by

$$\tilde{J}^{(0)}_{\mathbf{k}x}(\epsilon;\omega)=v^0_{\mathbf{k}x}+\int_{-\infty}^{\infty}\frac{d\epsilon'}{4\pi i}\sum_{\mathbf{k}',l=1,3}\lambda^{(l)}(\epsilon';\omega)v^0_{\mathbf{k}'x}g^{(2)}_{\mathbf{k}'}(\epsilon';\omega)\times\mathcal{T}^{(0)l,2}_{\mathbf{k}',\mathbf{k}}(\epsilon',\epsilon;\omega)/\lambda^{(2)}(\epsilon;\omega) \tag{3.58}$$

Also, the right-hand-side current $J_{\mathbf{k}x}$ is given by

$$J_{\mathbf{k}x}(\epsilon;\omega)=J^{(0)}_{\mathbf{k}x}(\epsilon;\omega)+\int_{-\infty}^{\infty}\frac{d\epsilon'}{4\pi i}\mathcal{T}^{2,2}_{\mathbf{k},\mathbf{k}'}(\epsilon,\epsilon';\omega)g^{(2)}_{\mathbf{k}'}(\epsilon';\omega)J^{(0)}_{\mathbf{k}'x}(\epsilon';\omega) \tag{3.59}$$

$$J^{(0)}_{\mathbf{k}x}(\epsilon;\omega)=v^0_{\mathbf{k}x}+\int_{-\infty}^{\infty}\frac{d\epsilon'}{4\pi i}\sum_{\mathbf{k}',l=1,3}\mathcal{T}^{(0)2,l}_{\mathbf{k},\mathbf{k}'}(\epsilon,\epsilon';\omega)g^{(l)}_{\mathbf{k}'}(\epsilon';\omega)v^{(0)}_{\mathbf{k}'x} \tag{3.60}$$

Note that $\mathcal{T}^{2,2}(\epsilon,\epsilon';\omega=0)$ does not contain any $g^{(1,3)}$ because of the relation $\mathcal{T}^{(I)i,2}(\epsilon,\epsilon';\omega)\propto\lambda^{(2)}(\epsilon';\omega)=0$ at $\omega=0$. That is, $\mathcal{T}^{2,2}(\epsilon,\epsilon';0)=\mathcal{T}^{(I)2,2}(\epsilon,\epsilon';0)+\int\frac{d\epsilon''}{4\pi i}\mathcal{T}^{(I)2,2}(\epsilon,\epsilon'';0)g^{(2)}(\epsilon'';0)\mathcal{T}^{2,2}(e'',\epsilon';0)$. Using the Ward identity, both $J^{(0)}_{\mathbf{k}x}(\epsilon,0)$ and $\tilde{J}^{(0)}_{\mathbf{k}x}(\epsilon,0)$ are replaced with the quasiparticle velocity $v_{\mathbf{k}x}=v^0_{\mathbf{k},x}+\partial\mathrm{Re}\Sigma_{\mathbf{k}}(\epsilon)/\partial k_x$ [25]. $J_{\mathbf{k}x}$ is called the total current since it contains the CVC discussed in previous sections.

In deriving the DC-conductivity $\sigma_{xx}=\partial\mathrm{Im}K_{xx}/\partial\omega|_{\omega=0}$ from Eq. (3.57), we have to take the ω-linear term from $\lambda^{(2)}(\epsilon;\omega)$ since $\lambda^{(2)}(\epsilon;0)=0$. Because of the relation $\lambda^{(2)}(\epsilon;\omega)=2(-\partial f(\epsilon)/\partial\epsilon)\cdot\omega+O(\omega^2)$, the expression of σ_{xx} with CVC is given as [25]

$$\sigma_{xx}=e^2\sum_{\mathbf{k}}z_{\mathbf{k}}\left(-\frac{\partial f^0}{\partial\epsilon}\right)_{E^*_{\mathbf{k}}}v_{\mathbf{k}x}\frac{J_{\mathbf{k}x}(E^*_{\mathbf{k}};0)}{\gamma_{\mathbf{k}}}, \tag{3.61}$$

which is exact when $\gamma \ll E_F$. This expression is given by replacing one of the velocity $v_{\mathbf{k}x}$ in the RTA in Eq. (3.10) with the total current $J_{\mathbf{k}x}$. Since $J_{\mathbf{k}x}$ is not singular with respect to γ^{-1}, Eq. (3.61) is proportional to γ^{-1}.

Next, we discuss the Hall conductivity due to the Lorentz force: The analytic continuation of $K_{xy}(i\omega_l)$ had been performed in Refs. [22, 24]. The obtained expression, which is exact within the most divergent term of order $O(\gamma^{-2})$, is given by

$$\sigma_{xy} = -\frac{e^3}{2} H \sum_{\mathbf{k}} z_{\mathbf{k}} \left(-\frac{\partial f^0}{\partial \epsilon} \right)_{E^*_{\mathbf{k}}} \frac{J_{\mathbf{k}x}}{\gamma_{\mathbf{k}}} (\boldsymbol{v}_{\mathbf{k}} \times \boldsymbol{\nabla}_{\mathbf{k}})_z \frac{J_{\mathbf{k}y}}{\gamma_{\mathbf{k}}}. \tag{3.62}$$

which is given by replacing $v_{\mathbf{k}x}$ and $v_{\mathbf{k}y}$ in the RTA in Eq. (3.11) with $J_{\mathbf{k}x}$ and $J_{\mathbf{k}y}$: $J_{\mathbf{k}\mu}$ is given by Eq. (3.59) by replacing $J^{(0)}_{\mathbf{k}\mu}$ with $v_{\mathbf{k}\mu}$. This expression was derived by Fukuyama et al. within the Born approximation [22], and it was proved to be correct in Fermi liquids [24]. We have dropped the [6 point VC term] in Eq. (3.47) since they are less singular with respect to $\gamma^{-1}_{\mathbf{k}}$ [24]. In particular, its contribution to σ_{xy} vanishes in the FLEX approximation.

Apparently, Eqs. (3.61) and (3.62) become equal to the RTA results given in Eqs. (3.10) and (3.11) if we replace the total current $\boldsymbol{J}_{\mathbf{k}}$ with the quasiparticle velocity $\boldsymbol{v}_{\mathbf{k}}$, that is, if we drop the CVC by $\mathcal{T}^{2,2}$. The RTA had been frequently used in analyzing transport anomaly in high-T_c cuprates. However, we will explain that the neglect of the CVC causes various unphysical results.

In the same way, the present author has derived the exact expressions for the magneto-conductivity $\Delta\sigma_{xx} \equiv \sigma_{xx}(H_z) - \sigma_{xx}(0)$ [23]. The expression will be shown in Eqs. (5.13) and (5.14) in Sect. 5.3: $\Delta\sigma^a_{xx}$ is given by replacing two $v_{\mathbf{k}x}$'s in the RTA result in Eq. (3.12) with the total currents, whereas $\Delta\sigma^b_{xx}$ is totally absent in the RTA. Also, the exact expression for the Peltier coefficient $\alpha_{xy} = E_y/(-\nabla_x T)$ under the magnetic field is also derived in Ref. [26].

3.4 CVC and Ward Identity

In later analytical and numerical studies, it is convenient to transform Eq. (3.59) into the following Bethe-Salpeter equation [25]:

$$J_{\mathbf{k}x}(\epsilon) = v_{\mathbf{k}x} + \sum_{\mathbf{k}'} \int_{-\infty}^{\infty} \frac{d\epsilon'}{4\pi i} \mathcal{T}^{(0)}_{\mathbf{k},\mathbf{k}'}(\epsilon, \epsilon') g^{(2)}_{\mathbf{k}'}(\epsilon'; 0) J_{\mathbf{k}'x}(\epsilon'), \tag{3.63}$$

where $\mathcal{T}^{(0)} \equiv \mathcal{T}^{(0)2,2}$, and the total current $J_{\mathbf{k}x}$ appears in both sides of the equations. Here, $v_{\mathbf{k}x} = v^0_{\mathbf{k}x} + \partial \mathrm{Re}\,\Sigma_{\mathbf{k}}(0)/\partial k_x$, and we put $\epsilon = 0$ in $J_{\mathbf{k}x}(\epsilon)$ for simplicity. Equation (3.63) is expressed in Fig. 3.2a. It is given by

$$\mathcal{T}^{(0)}_{\mathbf{k},\mathbf{k}'}(0, \epsilon') = \left(\mathrm{cth}\frac{\epsilon'}{2T} - \mathrm{th}\frac{\epsilon'}{2T} \right) \left(\Gamma^{(0);II}_{\mathbf{k},\mathbf{k}'}(0, \epsilon') - \Gamma^{(0);IV}_{\mathbf{k},\mathbf{k}'}(0, \epsilon') \right) \tag{3.64}$$

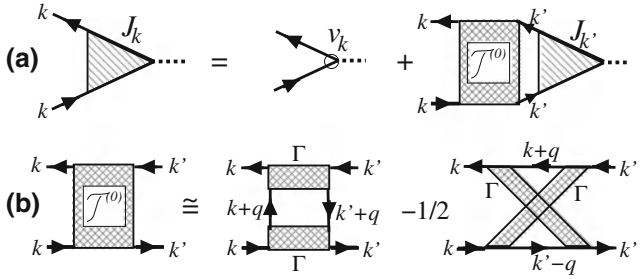

Fig. 3.2 **a** Bethe-Salpeter equation (Eq. (3.63)) for the total current $\boldsymbol{J}_{\mathbf{k}}$. **b** Expression for $\mathcal{T}^{(0)}_{\mathbf{k},\mathbf{k}'}(0,\epsilon')$ in the microscopic Fermi liquid theory. The factor $-1/2$ is necessary to avoid double counting

where $\Gamma^{(0);X}$ $(X = II, IV)$ is given by the analytic continuation from each region $(2, 2; X)$ in Fig. B.1 in Appendix B. At $\omega = 0$, $\mathcal{T}^{(0)}_{\mathbf{k},\mathbf{k}'}$ in Eq. (3.64) is irreducible with respect to any particle-hole pair $g^{(1,2,3)}$, because of the relations in Eqs. (B.5) and (B.11).

Here, we have discussed the transport phenomena under the outer field $Ee^{ikx-i\omega t}$. The DC-conductivity is given under the condition $kv_F/\omega \ll 1$ and $\omega \to 0$, which is called the ω-limit case or hydrostatic case. Landau discussed the transport phenomena in the opposite condition $kv_F/\omega \gg 1$, which is called the k-limit case or hydrodynamic case. He found the significant role of the CVC, which is called the backflow in the phenomenological Fermi liquid theory.

We analyze the Bethe-Salpeter equation (3.63) in the ω-limit and $\omega \to 0$: Its solution is real since $\mathcal{T}^{(0)}_{\mathbf{k},\mathbf{k}'}(0,\epsilon')$ in Eq. (3.64) is pure imaginary. Since $\mathrm{Im}\Gamma^{X}_{\mathbf{k},\mathbf{k}'}(0,0) = 0$ $(X = II, IV)$, we have to extract the ϵ'-linear term of $\mathrm{Im}\Gamma^{(0);X}_{\mathbf{k},\mathbf{k}'}(0,\epsilon')$. Since it originates from the cut of the particle-hole pair or that of the particle-particle pair [27], $\Gamma^{II,IV}$ is divided into two Γ's after taking the derivative of ϵ'. Using the relations such as $\mathrm{Im}\dot{\chi}^{0}_{\mathbf{q}}(0) = (\pi/2)\sum_{\mathbf{k}} \rho_{\mathbf{k}}(0)\rho_{\mathbf{k}+\mathbf{q}}(0)$, the ϵ'-linear term of $\mathrm{Im}\Gamma^{(0);X}(0,\epsilon')$ is given by [10]

$$\mathrm{Im}\Gamma^{(0);II}_{\mathbf{k},\mathbf{k}'}(0,\epsilon') = \pi\epsilon' \sum_{\mathbf{q}} \Gamma^{2}(\mathbf{k},\mathbf{k}';\mathbf{k}'-\mathbf{q},\mathbf{k}+\mathbf{q}) \times \left(\rho_{\mathbf{k}+\mathbf{q}}(0)\rho_{\mathbf{k}'+\mathbf{q}}(0) - \frac{1}{2}\rho_{\mathbf{k}+\mathbf{q}}(0)\rho_{\mathbf{k}'-\mathbf{q}}(0)\right), \tag{3.65}$$

where $\Gamma(\mathbf{k},\mathbf{k}';\mathbf{k}'-\mathbf{q},\mathbf{k}+\mathbf{q})$ is the full four-point vertex at the Fermi level, which is a real function of $(\mathbf{k},\mathbf{k}',\mathbf{q})$. The factor $\frac{1}{2}$ in front of the second term in the curly bracket in Eq. (3.65) is necessary to avoid double counting. Equation (3.65) is schematically shown in Fig. 3.2b.

After changing momentum variables, the Bethe-Salpeter equation (3.63) is transformed into [10]

$$\boldsymbol{J}_{\mathbf{k}} = \boldsymbol{v}_{\mathbf{k}} + \Delta\boldsymbol{J}_{\mathbf{k}}, \tag{3.66}$$

$$\Delta\boldsymbol{J}_{\mathbf{k}} = \sum_{\mathbf{k}'\mathbf{q}} \bar{\mathcal{T}}^{(0a)}_{\mathbf{k},\mathbf{k}+\mathbf{q}} \frac{\rho_{\mathbf{k}+\mathbf{q}}(0)}{2\gamma_{\mathbf{k}+\mathbf{q}}} \boldsymbol{J}_{\mathbf{k}+\mathbf{q}} + \sum_{\mathbf{k}'\mathbf{q}} \bar{\mathcal{T}}^{(0b)}_{\mathbf{k},\mathbf{k}'-\mathbf{q}} \frac{\rho_{\mathbf{k}'-\mathbf{q}}(0)}{2\gamma_{\mathbf{k}'-\mathbf{q}}} \boldsymbol{J}_{\mathbf{k}'-\mathbf{q}} + \sum_{\mathbf{k}'\mathbf{q}} \bar{\mathcal{T}}^{(0c)}_{\mathbf{k},\mathbf{k}'} \frac{\rho_{\mathbf{k}'}(0)}{2\gamma_{\mathbf{k}'}} \boldsymbol{J}_{\mathbf{k}'}, \tag{3.67}$$

where we used the relation $\int_{-\infty}^{\infty} d\epsilon[\mathrm{cth}(\epsilon/2T) - \mathrm{th}(\epsilon/2T)]\epsilon = (\pi T)^2$. $\bar{\mathcal{T}}^{(0\alpha)}$ ($\alpha = a, b, c$) are functions of $(\mathbf{k}, \mathbf{k}', \mathbf{q})$, and they represent the forward scattering amplitude [25, 27]. The expressions for $\bar{\mathcal{T}}^{(0\alpha)}$ ($\alpha = a, b, c$) at sufficiently low temperatures are given by [10]

$$\bar{\mathcal{T}}^{(0a)}_{\mathbf{k},\mathbf{k}+\mathbf{q}} = \frac{\pi(\pi T)^2}{2} \frac{1}{2} \Gamma^2(\mathbf{k}, \mathbf{k}'; \mathbf{k}' - \mathbf{q}, \mathbf{k} + \mathbf{q}) \rho_{\mathbf{k}'}(0) \rho_{\mathbf{k}'-\mathbf{q}}(0), \tag{3.68}$$

$$\bar{\mathcal{T}}^{(0b)}_{\mathbf{k},\mathbf{k}'-\mathbf{q}} = \frac{\pi(\pi T)^2}{2} \frac{1}{2} \Gamma^2(\mathbf{k}, \mathbf{k}'; \mathbf{k}' - \mathbf{q}, \mathbf{k} + \mathbf{q}) \rho_{\mathbf{k}'}(0) \rho_{\mathbf{k}+\mathbf{q}}(0), \tag{3.69}$$

$$\bar{\mathcal{T}}^{(0c)}_{\mathbf{k},\mathbf{k}'} = -\frac{\pi(\pi T)^2}{2} \frac{1}{2} \Gamma^2(\mathbf{k}, \mathbf{k}'; \mathbf{k}' - \mathbf{q}, \mathbf{k} + \mathbf{q}) \rho_{\mathbf{k}+\mathbf{q}}(0) \rho_{\mathbf{k}'-\mathbf{q}}(0). \tag{3.70}$$

Since the CVC due to $\bar{\mathcal{T}}^{(0c)}$ represents the hole current, the minus sign appears in Eq. (3.70). In Eqs. (3.68)–(3.70), we dropped spin indices in Γ to simplify equations: If spin indices are taken into account, $\frac{1}{2}\Gamma^2$ in each equation is replaced with $\frac{1}{2}\Gamma^2_{\uparrow,\uparrow;\uparrow,\uparrow} + \Gamma^2_{\uparrow,\downarrow;\downarrow,\uparrow} + \Gamma^2_{\uparrow,\downarrow;\uparrow,\downarrow}$ as explained in Ref. [10]. Equations (3.68)–(3.70) are expressed in Fig. 3.3(i). Note that Eqs. (3.68) and (3.69) are equivalent since $\Gamma(\mathbf{k}, \mathbf{k}'; \mathbf{k}' - \mathbf{q}, \mathbf{k} + \mathbf{q})$ is fully antisymmetrized as a consequence of the Pauli principle.

In the same way, $\mathrm{Im}\Sigma_{\mathbf{k}}(-i\delta) = \gamma_{\mathbf{k}}$ at sufficiently low temperatures can be expressed as [10, 27]

$$\begin{aligned} \gamma_{\mathbf{k}} &= \frac{1}{2} \sum_{\mathbf{k}'} \int \frac{d\epsilon'}{4\pi i} \mathcal{T}^{(0)}_{\mathbf{k},\mathbf{k}'}(0, \epsilon') \cdot \pi \rho_{\mathbf{k}'}(\epsilon') \\ &= \frac{1}{2} \sum_{\mathbf{k}'\mathbf{q}} \bar{\mathcal{T}}^{(0a)}_{\mathbf{k},\mathbf{k}+\mathbf{q}} \rho_{\mathbf{k}+\mathbf{q}}(0), \end{aligned} \tag{3.71}$$

which is proportional to T^2 at the zero-temperature limit, if the dimension is slightly higher than two. [In pure 2D systems, $\gamma_{\mathbf{k}} \propto -T^2 \ln T$.] Equation (3.71) is shown in Fig. 3.3(ii). We note that $\gamma_{\mathbf{k}}$ is also given by $\gamma_{\mathbf{k}} = \frac{1}{2}\sum_{\mathbf{k}'\mathbf{q}} \bar{\mathcal{T}}^{(0b)}_{\mathbf{k},\mathbf{k}'-\mathbf{q}} \rho_{\mathbf{k}'-\mathbf{q}}(0) = -\frac{1}{2}\sum_{\mathbf{k}'\mathbf{q}} \bar{\mathcal{T}}^{(0c)}_{\mathbf{k},\mathbf{k}'} \rho_{\mathbf{k}'}(0)$.

Here, we calculate the CVC in a free dispersion model in the absence of Umklapp scattering according to Yamada and Yosida [10]. In this case, both $\gamma_{\mathbf{k}}$ and $\boldsymbol{J}_{\mathbf{k}}$ on the Fermi surface are isotropic, that is, $\gamma_{\mathbf{k}} = \gamma_{k_{\mathrm{F}}}$ and $\boldsymbol{J}_{\mathbf{k}} = J \cdot \mathbf{k}/k_{\mathrm{F}}$. By noticing the

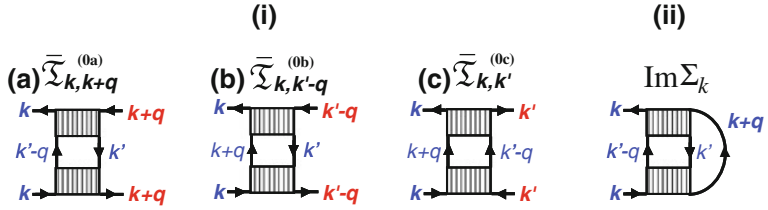

Fig. 3.3 (i) Diagrammatic representation of Eqs. (3.68)–(3.70). Each *hatched part* represents the real part of the full antisymmetrized four point vertex $\Gamma(\mathbf{k}, \mathbf{k}'; \mathbf{k}+\mathbf{q}, \mathbf{k}'-\mathbf{q})$. Each *line with arrow* represents the imaginary part of the Green function. Note that **a** becomes different from **b** if we violate the antisymmetric nature of $\Gamma(\mathbf{k}, \mathbf{k}'; \mathbf{k}+\mathbf{q}, \mathbf{k}'-\mathbf{q})$ in the course of approximation. (ii) Diagrammatic representation of Eq. (3.71)

relationship $\boldsymbol{J}_{\mathbf{k}+\mathbf{q}} + \boldsymbol{J}_{\mathbf{k}'-\mathbf{q}} - \boldsymbol{J}_{\mathbf{k}'} = \boldsymbol{J}_{\mathbf{k}}$ and using Eqs. (3.68)–(3.71), it is easy to verify that the CVC in Eq. (3.67) is exactly given by

$$\Delta \boldsymbol{J}_{\mathbf{k}} = \boldsymbol{J}_{\mathbf{k}}, \tag{3.72}$$

in a free dispersion model. If we put $\Delta \boldsymbol{J}_{\mathbf{k}} = c\boldsymbol{J}_{\mathbf{k}}$ (c is a constant), the solution of Eq. (3.66) is given by $\boldsymbol{J}_{\mathbf{k}} = \boldsymbol{v}_{\mathbf{k}}/(1-c)$, which diverges when $c \to 1$. Therefore, the conductivity given by Eq. (3.61) diverges, which is a natural consequence of the momentum conservation law [10]. Yamada and Yosida also showed that $\boldsymbol{J}_{\mathbf{k}}$ remains finite in the presence of the Umklapp processes [10].

Next, we discuss the case where $\epsilon^0_{\mathbf{k}}$ is anisotropic. Then, the formal solution of Eq. (3.63) is given by

$$\boldsymbol{J}_{\mathbf{k}} = \sum_{\mathbf{k}'} (\hat{1} - \hat{C})^{-1}_{\mathbf{k},\mathbf{k}'} \boldsymbol{v}_{\mathbf{k}'}, \tag{3.73}$$

where $C_{\mathbf{k},\mathbf{k}'} = \int \frac{d\epsilon'}{4\pi i} \mathcal{T}^{(0)}_{\mathbf{k},\mathbf{k}'}(0,\epsilon') \cdot \rho_{\mathbf{k}'}(0)/2\gamma_{\mathbf{k}'}$. When $\epsilon^0_{\mathbf{k}}$ is anisotropic, quasiparticle current is not conserved in the normal scattering process; $\mathbf{v}_{\mathbf{k}} + \mathbf{v}_{\mathbf{k}'} \neq \mathbf{v}_{\mathbf{k}+\mathbf{q}} + \mathbf{v}_{\mathbf{k}'-\mathbf{q}}$. Nonetheless of the fact, one can show that $\det\{\hat{1} - \hat{C}\} = 0$ as a result of the momentum conservation [28, 29]. Therefore, $\boldsymbol{J}_{\mathbf{k}}$ in Eq. (3.73) and σ_{xx} diverge in any anisotropic model without normal Umklapp processes. The same result was already obtained by the variational principle in Sect. 3.2. [Exactly speaking, $\rho_{xx} = 1/\sigma_{xx}$ is proportional to T^{2N-2} when the N-particle Umklapp scattering processes are present [30].]

The FLEX approximation reproduces the divergence of the conductivity in the absence of the Umklapp scattering, if one consider the CVC given by the Ward identity $\Gamma^I = \delta\Sigma/\delta G$ [31, 32]. Therefore, the FLEX approximation will be appropriate for the study of transport phenomena in correlated electron systems.

3.5 CVC in Nearly AF Fermi Liquids

We consider the role of the CVC in nearly AF Fermi liquids in the presence of Umklapp scattering, where the scattering processes are mainly given by the strong AF fluctuations with $\mathbf{q} \sim \mathbf{Q}$. First, we intuitively discuss the CVC in nearly AF metals, where the quasiparticles are scattered by strong AF fluctuations with $\mathbf{q} \sim \mathbf{Q} = (\pi, \pi)$. As shown in Fig. 3.4a, the quasiparticle at $\mathbf{k}'$ is scattered to $\mathbf{k}' - \mathbf{q}$ because of the momentum conservation. The current due to the quasiparticle at $\mathbf{k}' - \mathbf{q}$ and the hole at $\mathbf{k}'$ is given by $\boldsymbol{v}_{\mathbf{k}'-\mathbf{q}} - \boldsymbol{v}_{\mathbf{k}'}$. This current almost cancels after performing the $\mathbf{k}'$-summation: In fact, the current of the particle-hole pair $(\mathbf{k}'' - \mathbf{q}, \mathbf{k}'')$ for $\mathbf{k}'' = -\mathbf{k}'$, which is shown in Fig. 3.4b, is $\boldsymbol{v}_{-\mathbf{k}'-\mathbf{q}} - \boldsymbol{v}_{-\mathbf{k}'} \approx -\boldsymbol{v}_{\mathbf{k}'-\mathbf{q}} + \boldsymbol{v}_{\mathbf{k}'}$ since $2\mathbf{q} \approx 2\mathbf{Q}$ is a reciprocal lattice vector. Therefore, the CVC is given only by the quasiparticle at $\mathbf{k} + \mathbf{q}$. Then, the conductivity does not diverge because of the existence of the Umklapp processes in Fig. 3.4b.

Since the total current $\boldsymbol{J}_{\mathbf{k}}$ is approximately parallel to $\boldsymbol{v}_{\mathbf{k}} + \boldsymbol{v}_{\mathbf{k}+\mathbf{Q}}$ in nearly AF metals, $\boldsymbol{J}_{\mathbf{k}}$ is not perpendicular to the Fermi surface. Thus, $\boldsymbol{J}_{\mathbf{k}}$ has strong $\mathbf{k}$-dependence near the AF QCP due to the multiple backscattering between $\mathbf{k}$ and $\mathbf{k} + \mathbf{Q}$. [The schematic behavior of $\boldsymbol{J}_{\mathbf{k}}$ is shown in Fig. 3.7.] This fact is the origin of the enhancement of R_{H} [33]. Thus far, we discussed only the two-body scattering process, and ignored the higher-order processes. This is justified when $\gamma / E_{\mathrm{F}} \ll 1$, which is well satisfied in optimally-doped cuprate HTSCs [34–36].

Now, we return to the microscopic analysis. When the scattering processes are mainly given by the strong AF fluctuations with $\mathbf{q} \sim \mathbf{Q}$, we can approximate the full

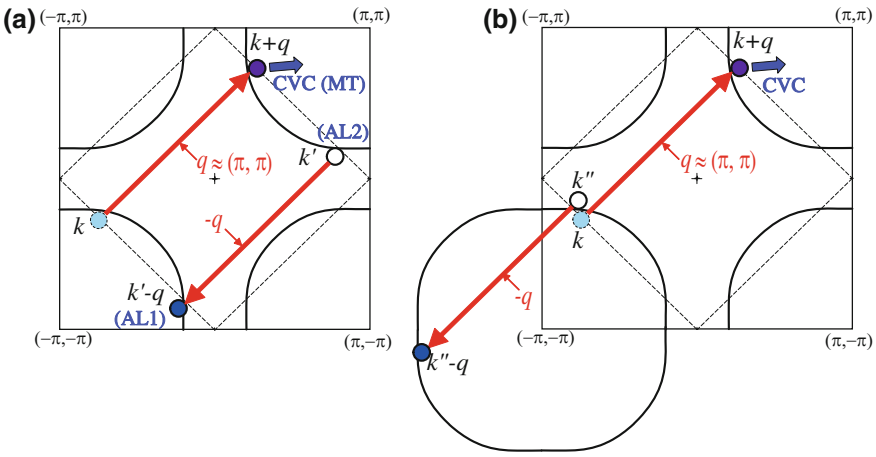

Fig. 3.4 Decay process of a quasiparticle at $\mathbf{k}$ in HTSCs. **a** Due to strong AF fluctuations, this quasiparticle at $\mathbf{k}$ is scattered to $\mathbf{k} + \mathbf{q}$ ($\mathbf{q} \sim \mathbf{Q}$), creating a particle-hole pair ($\mathbf{k}'$, $\mathbf{k}' - \mathbf{q}$). **b** The current of the particle-hole excitation in **a** is almost canceled by another particle-hole excitation ($\mathbf{k}''$, $\mathbf{k}'' - \mathbf{q}$) for $\mathbf{k}'' = -\mathbf{k}'$. Therefore, the CVC is given by the quasiparticle at $\mathbf{k} + \mathbf{Q}$ alone (=Maki-Thompson term). The process (**b**) is the Umklapp scattering

four-point vertex in Eqs. (3.68)–(3.70) as

$$\Gamma_{s_1,s_2;s_3,s_4}(\mathbf{k},\mathbf{k}';\mathbf{k}'-\mathbf{q},\mathbf{k}+\mathbf{q}) \approx \frac{\bar{U}^2}{2}\left\{\chi^s_{\mathbf{q}}(0)\boldsymbol{\sigma}_{s_1,s_4}\cdot\boldsymbol{\sigma}_{s_2,s_3} - \chi^s_{\mathbf{k}-\mathbf{k}'+\mathbf{q}}(0)\boldsymbol{\sigma}_{s_1,s_3}\cdot\boldsymbol{\sigma}_{s_2,s_4}\right\}, \tag{3.74}$$

which satisfies the antisymmetric nature of Γ that is the consequence of the Pauli principle. The diagrammatic representation of Eq. (3.74) is shown in Fig. 3.5a. Here, s_i ($i = 1\,4$) represents the spin index and $\boldsymbol{\sigma}$ is the Pauli matrix vector. $\bar{U}$ in Eq. (3.74) is the effective interaction between the electrons and spin fluctuations, given by the three-point vertex shown in Fig. 3.5b.

In the present subsection, however, we analyze the CVC using the following more simplified approximation for Γ:

$$\Gamma_{s_1,s_2;s_3,s_4}(\mathbf{k},\mathbf{k}';\mathbf{k}'-\mathbf{q},\mathbf{k}+\mathbf{q}) \approx \frac{\bar{U}^2}{2}\chi^s_{\mathbf{q}}(0)\boldsymbol{\sigma}_{s_1,s_4}\cdot\boldsymbol{\sigma}_{s_2,s_3}. \tag{3.75}$$

Although Eq. (3.75) violates the Pauli principle, this approximation produces the dominant CVC (Maki-Thompson term) near AF-QCP. In Ref. [37], we analyzed the CVC using Eq. (3.74), and showed that the analysis based on Eq. (3.75) is justified.

Using the approximation in Eq. (3.75), $\bar{\mathcal{T}}^{(0\alpha)}$ ($\alpha = a, b, c$) in Eqs. (3.68)–(3.70) are expressed by (a)–(c) in Fig. 3.6(i), respectively, where wavy lines represent the spin fluctuations. The CVCs expressed in (a) and (b) correspond to the current due to the quasiparticles at $\mathbf{k}+\mathbf{q}$ and $\mathbf{k}'-\mathbf{q}$, respectively, and the CVC in (c) corresponds to the current due to the quasi-hole at $\mathbf{k}'$ in Fig. 3.4. In the field theory, (a) is called the Maki-Thompson term, and (b) and (c) are called the Aslamazov-Larkin terms. As explained in Fig. 3.4, the Aslamazov-Larkin terms approximately disappears [33] whereas the Maki-Thompson term plays an important role when $\xi_{\mathrm{AF}} \gg 1$ and $\mathbf{Q} \approx (\pi, \pi)$.

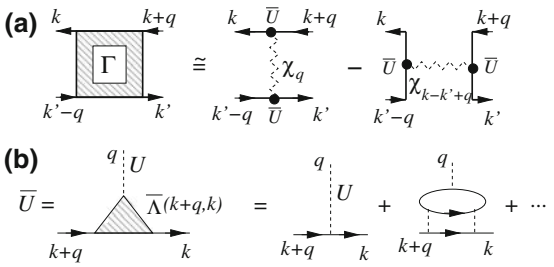

Fig. 3.5 **a** Diagrammatic representation of Eq. (3.74). The *wavy lines* represent the spin fluctuations, $\chi^s_{\mathbf{q}}(0)$. **b** Diagrammatic representation of $\bar{U}$ in Eq. (3.74). U is the bare Coulomb interaction in the Hubbard model and $\bar{\Lambda}(\mathbf{k}+\mathbf{q},\mathbf{q})$ is the three-point vertex that is irreducible with respect to U

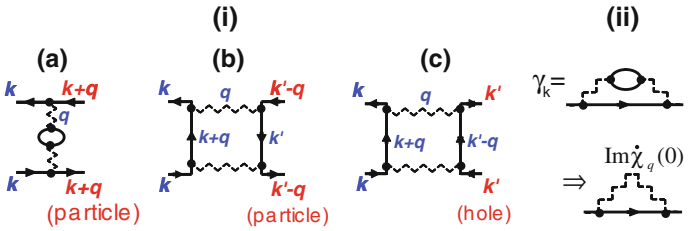

Fig. 3.6 (i) The CVC within the one-loop approximation due to Eq. (3.75). Here, $\bar{\mathcal{T}}^{(0a)}_{\mathbf{k},\mathbf{k}+\mathbf{q}}$, $\bar{\mathcal{T}}^{(0b)}_{\mathbf{k},\mathbf{k}'-\mathbf{q}}$, and $\bar{\mathcal{T}}^{(0c)}_{\mathbf{k},\mathbf{k}'}$ in Fig. 3.3a–c are approximated as **a**-**c**, respectively. **a** corresponds to the Maki-Thompson term in the FLEX approximation, which represents the CVC (MT) in Fig. 3.4. **b** and **c** correspond to the Aslamazov-Larkin terms, which represent the (AL1) and (AL2) in Fig. 3.4. (ii) The expression for $\gamma_{\mathbf{k}}$ in the same approximation

According to Eq. (3.75), $\frac{1}{2}\Gamma^2$ in $\bar{\mathcal{T}}^{(0a)}$ becomes $(3U^4/4)[\chi^s_q(0)]^2$ after taking the summation of spin indices. However, we replace $\frac{1}{2}\Gamma^2$ with $(3U^4/2)[\chi^s_q(0)]^2$ since the term (a) in Fig. 3.6 is also derived from $\bar{\mathcal{T}}^{(0b)}$ if we use Eq. (3.74). Then, the CVC in Eq. (3.67) and $\gamma_{\mathbf{k}}$ given in Eq. (3.71) near the AF QCP are obtained as

$$\Delta \boldsymbol{J}_{\mathbf{k}} = \sum_{\mathbf{q}} (\pi T)^2 \frac{3\bar{U}^4}{4} [\chi^s_{\mathbf{q}}(0)]^2 \mathrm{Im}\dot{\chi}^0_q(0) \frac{\rho_{\mathbf{k}+\mathbf{q}}(0)}{\gamma_{\mathbf{k}+\mathbf{q}}} \boldsymbol{J}_{\mathbf{k}+\mathbf{q}}, \tag{3.76}$$

$$\gamma_{\mathbf{k}} = \sum_{\mathbf{q}} (\pi T)^2 \frac{3\bar{U}^4}{4} [\chi^s_{\mathbf{q}}(0)]^2 \mathrm{Im}\dot{\chi}^0_q(0) \rho_{\mathbf{k}+\mathbf{q}}(0), \tag{3.77}$$

where we used the relation $\mathrm{Im}\dot{\chi}^0_{\mathbf{q}}(0) = (\pi/2)\sum_{\mathbf{k}} \rho_{\mathbf{k}}(0)\rho_{\mathbf{k}+\mathbf{q}}(0)$. Since $\mathrm{Im}\dot{\chi}^s_q(0) = \mathrm{Im}\dot{\chi}^0_{\mathbf{q}}(0)[\bar{U}\chi^s_{\mathbf{q}}(0)]^2$, Eqs. (3.76) and (3.77) are rewritten as

$$\boldsymbol{J}_{\mathbf{k}} = \boldsymbol{v}_{\mathbf{k}} + \sum_{\mathbf{q}} \frac{3\bar{U}^2}{4} (\pi T)^2 \mathrm{Im}\dot{\chi}^s_{\mathbf{q}}(0) \frac{\rho_{\mathbf{k}+\mathbf{q}}(0)}{\gamma_{\mathbf{k}+\mathbf{q}}} \boldsymbol{J}_{\mathbf{k}+\mathbf{q}}. \tag{3.78}$$

$$\gamma_{\mathbf{k}} = \sum_{\mathbf{q}} \frac{3\bar{U}^2}{4} (\pi T)^2 \mathrm{Im}\dot{\chi}^s_{\mathbf{q}}(0) \rho_{\mathbf{k}+\mathbf{q}}(0). \tag{3.79}$$

Note that Eq. (3.79) is equivalent to $\gamma_{\mathbf{k}}$ in the spin fluctuation theory in Eq. (2.29).

In this section, we have neglected the energy-dependence of the four-point vertices [in Eqs. (3.68)–(3.70)] and that of the spin susceptibilities [in Eqs. (3.76)–(3.79)] to simplify the discussion. For this reason, Eqs. (3.78) and (3.79) are appropriate only for $\omega_{\mathrm{sf}} \gtrsim T$ where ω-dependence of $\chi^s_{\mathbf{q}}(\omega)$ can be ignored. In the case of $\omega_{\mathrm{sf}} \ll T$, $(\pi T)^2$ in Eqs. (3.78) and (3.79) should be replaced with $\int_{-\omega_{\mathrm{sf}}}^{\omega_{\mathrm{sf}}} [\mathrm{cth}(\epsilon/2T) - \mathrm{th}(\epsilon/2T)]\epsilon d\epsilon = 4T\omega_{\mathrm{sf}}$. For any value of ω_{sf}/T, they are expressed by Eqs. (36) and (33) in Ref. [33], respectively.

Here, we approximately solve Eq. (3.78) when $\xi_{\rm AF} \gg 1$ and $\xi_{\rm AF}\Delta k_c \sim O(1)$. We assume $\mathbf{k}$ is close to point A in Fig. 2.1a. Since $\chi^s_{\mathbf{q}}(0)$ is large only when $|\mathbf{q}-\mathbf{Q}| \lesssim \xi_{\rm AF}^{-1}$, the CVC term in Eq. (3.78) is expressed as $\Delta \boldsymbol{J}_{\mathbf{k}} \approx (\boldsymbol{J}_{\mathbf{k}^*}/\gamma_{\mathbf{k}^*}) \sum_{\mathbf{q}} (3\bar{U}^2/4)(\pi T)^2 \, {\rm Im}\chi^s_{\mathbf{q}}(0)$, where $(k_x^*, k_y^*) = (-k_y, -k_x)$ for $k_x k_y > 0$, and $(k_x^*, k_y^*) = (k_y, k_x)$ for $k_x k_y < 0$ as shown in Fig. 2.1a. Considering Eq. (3.79), $\Delta \boldsymbol{J}_{\mathbf{k}} \approx \boldsymbol{J}_{\mathbf{k}^*}$ in the case of $\xi_{\rm AF} \gg 1$. The more detailed expression for the CVC term $\Delta \boldsymbol{J}_{\mathbf{k}}$ is given by [33]

$$\begin{aligned} \Delta \boldsymbol{J}_{\mathbf{k}} &\approx \langle\, \boldsymbol{J}_{\mathbf{k}'} \,\rangle_{|\mathbf{k}'-\mathbf{k}^*|<1/\xi_{\rm AF}} \\ &\approx \boldsymbol{J}_{\mathbf{k}^*} \cdot \langle\, \cos(\theta^J_{\mathbf{k}'} - \theta^J_{\mathbf{k}^*}) \,\rangle_{|\mathbf{k}'-\mathbf{k}^*|<1/\xi_{\rm AF}} \approx \alpha_{\mathbf{k}} \boldsymbol{J}_{\mathbf{k}^*}, \end{aligned} \tag{3.80}$$

where $\alpha_{\mathbf{k}} \approx (1 - c/\xi^2_{\rm AF}) < 1$ and $c \sim O(1)$ is a constant. The $\mathbf{k}$-dependence of $\alpha_{\mathbf{k}}$ will be moderate if $\xi_{\rm AF}\Delta k_c \gtrsim 1$. By this simplification, Eq. (3.78) becomes

$$\boldsymbol{J}_{\mathbf{k}} = \boldsymbol{v}_{\mathbf{k}} + \alpha_{\mathbf{k}} \boldsymbol{J}_{\mathbf{k}^*}, \tag{3.81}$$

and the solution is given by [33]

$$\boldsymbol{J}_{\mathbf{k}} = \frac{1}{1-\alpha^2_{\mathbf{k}}} \left(\boldsymbol{v}_{\mathbf{k}} + \alpha_{\mathbf{k}} \boldsymbol{v}_{\mathbf{k}^*}\right). \tag{3.82}$$

Here, we examine the $\mathbf{k}$-dependence of $\boldsymbol{J}_{\mathbf{k}}$ given in Eq. (3.82): (a) near points A and B, $\boldsymbol{J}_{\mathbf{k}}$ is almost parallel to $\boldsymbol{v}_{\mathbf{k}}$ by symmetry. At point A, $\boldsymbol{J}_{\mathbf{k}} = \boldsymbol{v}_{\mathbf{k}}/(1+\alpha_{\mathbf{k}}) \sim \frac{1}{2}\boldsymbol{v}_{\mathbf{k}}$ since $\boldsymbol{v}_{\mathbf{k}} = -\boldsymbol{v}_{\mathbf{k}^*}$. (b) Near point C, $\boldsymbol{J}_{\mathbf{k}} \approx (\xi^2_{\rm AF}/2c)(\boldsymbol{v}_{\mathbf{k}} + \boldsymbol{v}_{\mathbf{k}^*})$, which is nearly parallel to the AFBZ. These behaviors of $\boldsymbol{J}_{\mathbf{k}}$ together with $\boldsymbol{v}_{\mathbf{k}}$ are schematically shown in Fig. 3.7a. Here, we have assumed that $\xi_{\rm AF}\Delta k_c \sim O(1)$, where Δk_c represents the deviation from the nesting condition at the cold spot in Fig. 2.1a. This condition is

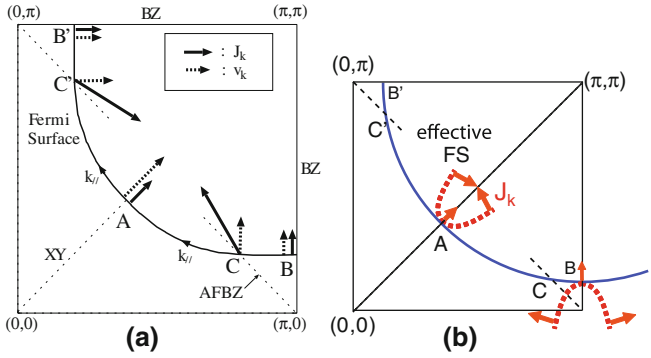

Fig. 3.7 **a** Schematic total current $\boldsymbol{J}_{\mathbf{k}}$ and the quasiparticle velocity $\boldsymbol{v}_{\mathbf{k}}$ on the Fermi surface. The cold spot is around the point *A* (*B*) in hole-doped (electron-doped) HTSCs. **b** Effective Fermi surface for σ_{xy}. The large curvature of the effective Fermi surface around the cold spot presents the enhancement (and the sign-change) of $R_{\rm H}$

satisfied in slightly under-doped YBCO and LSCO above T_c, as discussed in Sect. 2.3. In Fig. 2.1b, we show an "effective Fermi surface" that it is orthogonal to $\boldsymbol{J}_{\mathbf{k}}$ around the cold spot [38]. Based on this concept, we discuss the role of the CVC in the Hall coefficient in Sect. 5.2.

When $\xi_{\rm AF}\Delta k_c \gg 1$, one may think that the CVC is small around the cold spot, so the increment in $R_{\rm H}$ by CVC is small. However, this expectation is not true since $\gamma_{\mathbf{k}}$ is also small by the same reason, and therefore $\alpha_{\mathbf{k}}$ in Eq. (3.80) is close to unity. We have verified that the CVC around the cold spot is significant even if $\xi_{\rm AF}\Delta k_c \gg 1$, by using a phenomenological $\chi^s_{\mathbf{q}}(\omega)$ model given in Eq. (2.1) [39]. Later, we demonstrate that $R_{\rm H}$ is strongly enhanced by the CVC using the FLEX approximation, which yields a realistic functional form of $\chi^s_{\mathbf{q}}(\omega)$. We will show that the CVC is important in NCCO, although $\xi_{\rm AF}\Delta k_c \gg 1$ is realized at low temperatures.

Here, we have analyzed the CVC by assuming Eq. (3.75), which corresponds to the one-loop approximation for the self-energy like the FLEX approximation. When AF fluctuations are strong, only Maki-Thompson term is important. Moreover, Eqs. (3.76) and (3.77) contain the same Kernel function $[\chi^s_{\mathbf{q}}(0)]^2 {\rm Im}\dot{\chi}^s_q(0)\rho_{\mathbf{k}+\mathbf{q}}(0)]$ owing to the Ward identity between CVC and $\gamma_{\mathbf{k}}$. For this reason, the factor $\alpha_{\mathbf{k}}$ in Eq. (3.82) approaches unity near AF-QCP, which assures the anomalous $\mathbf{k}$-dependence of $\boldsymbol{J}_{\mathbf{k}}$ near AF-QCP that shown in Fig. 3.7. In Ref. [37], we have analyzed the self-energy and the CVC beyond the one-loop approximation by assuming Eq. (3.74). It is confirmed that the CVC near the AF QCP is important even if the higher-loop diagrams are taken into account.

References

1. H.M. Ziman, *Electrons and Phonons: The Theory of Transport Phenomena in Solids* (Oxford Classic Texts in the Physical Sciences, Oxford, 1960)
2. M. Abdel-Jawad, M.P. Kennett, L. Balicas, A. Carrington, A.P. Mackenzie, R.H. McKenzie, N.E. Hussey, Nat. Phys. **2**, 821 (2006)
3. M. Abdel-Jawad, J.G. Analytis, L. Balicas, A. Carrington, J.P.H. Charmant, M.M.J. French, N.E. Hussey, Phys. Rev. Lett. **99**, 107002 (2007)
4. A. Narduzzo, G. Albert, M.M.J. French, N. Mangkorntong, M. Nohara, H. Takagi, N.E. Hussey: Phys. Rev. B **77**, 220502(R) (2008)
5. K. Yamaji, J. Phys. Soc. Jpn. **58**, 1520 (1989)
6. R. Yagi, Y. Iye, T. Osada, S. Kagoshima, J. Phys. Soc. Jpn. **59**, 3069 (1990)
7. B.P. Stojkovic, D. Pines, Phys. Rev. B **55**, 8576 (1997)
8. Y. Yanase, K. Yamada, J. Phys. Soc. Jpn. **68**, 548 (1999)
9. L.B. Ioffe, A.J. Millis, Phys. Rev. B **58**, 11631 (1998)
10. K. Yamada, K. Yosida, Prog. Theor. Phys. **76**, 621 (1986)
11. K. Umeda, Sci. Pap. Inst. Phys. Chem. Res. Tokyo **39**, 342 (1942)
12. K. Umeda, T. Toya, J. Fac. Sci. Hokkaido Univ. [2] **3**, 257 (1949)
13. M. Kohler, Z. Phys. **124**, 772 (1948)
14. M. Kohler, Z. Phys. **125**, 679 (1949)
15. E.H. Sondheimer, Proc. R. Soc. A **203**, 75 (1960)
16. P.B. Allen, Phys. Rev. B **13**, 1416 (1976)
17. J.M. Langer, Phys. Rev. **127**, 5 (1962)
18. H. Nakano, Int. J. Mod. Phys. B **7**, 2397 (1993)

19. R. Kubo, J. Phys. Soc. Jpn. **12**, 570 (1957)
20. M.S. Green, J. Chem. Phys. **20**, 1281 (1952)
21. M.S. Green, J. Chem. Phys. **22**, 398 (1954)
22. H. Fukuyama, H. Ebisawa, Y. Wada, Prog. Theor. Phys. **42**, 494 (1969)
23. H. Kontani, Phys. Rev. B **64**, 054413 (2001)
24. H. Kohno, K. Yamada, Prog. Theor. Phys. **80**, 623 (1988)
25. G.M. Eliashberg, Sov. Phys. JETP **14**, 886 (1962)
26. H. Kontani, Phys. Rev. B **67**, 014408 (2003)
27. A.A. Abricosov, L.P. Gor'kov, I.E. Dzyaloshinskii, *Methods of Quantum Field Theory in Statistical Physics* (Dover, New York, 1975)
28. H. Maebashi, H. Fukuyama, Phys. Soc. Jpn. **66**, 3577 (1997)
29. H. Maebashi, H. Fukuyama, Phys. Soc. Jpn. **67**, 242 (1998)
30. A. Rosch, Ann. Phys. (Leipzig) **15**, 526 (2006)
31. G. Baym, L.P. Kadanoff, Phys. Rev. **124**, 287 (1961)
32. G. Baym, Phys. Rev. **127**, 1391 (1962)
33. H. Kontani, K. Kanki, K. Ueda, Phys. Rev. B **59**, 14723 (1999)
34. L. Landau, Sov. Phys. JETP **3**, 920 (1957)
35. L. Landau, Sov. Phys. JETP **5**, 101 (1957)
36. L. Landau, Sov. Phys. JETP **8**, 70 (1959)
37. H. Kontani, Rep. Prog. Phys. **71**, 026501 (2008)
38. Y. Nakajima, H. Shishido, H. Nakai, T. Shibauchi, K. Behnia, K. Izawa, M. Hedo, Y. Uwatoko, T. Matsumoto, R. Settai, Y. Onuki, H. Kontani, Y. Matsuda, J. Phys. Soc. Jpn. **76**, 027403 (2007)
39. K. Kanki, H. Kontani, J. Phys. Soc. Jpn. **68**, 1614 (1999)

Chapter 4
Anomalous Hall Effect (AHE) and Spin Hall Effect (SHE)

4.1 Relation Between AHE and SHE

In this chapter, we study the interesting spin-related transport phenomena that are widely observed in various d- and f-electron systems. For example, in the presence of the magnetization $\mathbf{M}$, charge current is induced by an electric field $\mathbf{E}$ in parallel to $\mathbf{M} \times \mathbf{E}$. This phenomenon, which is called the anomalous Hall effect (AHE), has been studied for a long time, and recently attracted renewed interest. The spin Hall effect (SHE) in paramagnetic metals has received considerable attention due to its fundamental as well as technological interest. The SHE is the phenomenon that an electric field induces a spin current (not a charge current) in a tranverse direction. The SHE occurs even if the time reversal symmetry is not violated since the spin current does not change by time reversal. By using the spin Hall effect, one can create a pure spin current by applying an electric field to a paramagnetic metal. Inversely, spin current is converted to the electric field in the perpendicular direction via the inverse SHE.

In 1954, Karplus and Luttinger [1] showed that in multiband ferromagnetic systems with spin-orbit interaction, a conduction electron feels a force perpendicular to the electric field even in the absence of magnetic field: For an electron with $s_z = \pm\hbar/2$, the spin-orbit interaction $\lambda \boldsymbol{l} \cdot \boldsymbol{\sigma}$ is reduced to be $\pm\lambda\hbar l_z/2$. This term affects the motion of the electron like a "magnetic field" in a multiorbital system where the atomic angular momentum is not quenched; we will discuss in detail in later sections. This is the origin of AHE as shown in Fig. 4.1a. When the magnetization is reversed, the charge current due to the AHE, j_y^{AHE}, also changes its sign. In a paramagnetic state where $N_\uparrow = N_\downarrow$, $j_{y\uparrow} = -j_{y\downarrow}$ as shown in Fig. 4.1b. Then, spin current $j_y^s = (-\hbar/2e)(j_{y\uparrow} - j_{y\downarrow})$ flows along y-direction where $-e$ (< 0) is the electron charge, whereas charge current $j_y = j_{y\uparrow} + j_{y\downarrow}$ cancels out identically. Therefore, origin of the SHE and that of the AHE are the same. [In above explanation, we disregarded the fact that the electron spin can be reversed by the x, y components of the spin-orbit interaction $\lambda(l_x s_x + l_y s_y)$ to simplify the explanation.]

H. Kontani, *Transport Phenomena in Strongly Correlated Fermi Liquids*,
Springer Tracts in Modern Physics 251, DOI: 10.1007/978-3-642-35365-9_4,

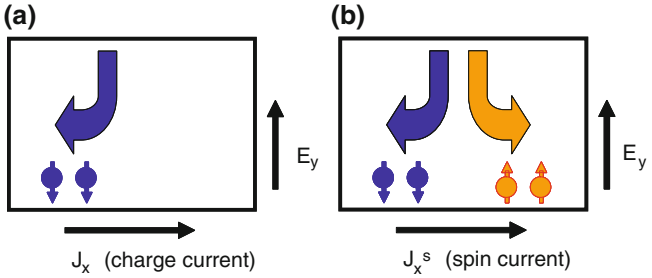

Fig. 4.1 **a** AHE in a ferromagnetic metal. **b** SHE in a paramagnetic metal. In (**b**), finite AHE appears when the magnetic field is applied along z-axis

The KL theory is called the "intrinsic Hall effect" since this is an universal phenomenon in multiband systems in the presence of spin-orbit interaction (SOI), free from the impurity scattering. Since the intrinsic Hall conductivity under E_y ($\sigma^a_{xy} = j_x/E_y$ or $\sigma^s_{xy} = j^s_x/E_y$) is independent of the quasiparticle damping rate γ, it cannot be described by the conventional RTA. For this reason, the intrinsic Hall effect is called the "quantum transport phenomenon". After the KL theory [1, 2], it was revealed that the SHE and AHE are also induced by impurity scattering, which is called the "extrinsic Hall effect". There are two kinds of the extrinsic mechanism; the skew scattering [3] and side-jump [4] mechanisms. The former (latter) Hall conductivity is proportional to γ (γ^0). In this chapter, we concentrate on the intrinsic Hall effect.

Recent experimental efforts have revealed that many metallic compounds show sizable spin Hall conductivity (SHC). In particular, Pt shows a very huge SHC at room temperature [5, 6]: The observed SHC in Pt is about 10^4 times larger than the SHC reported in n-type semiconductors [7, 8]. To elucidate the origin of the huge SHE in transition metals, authors in Ref. [9] presented the first report on the theoretical study of SHE in transition metal compound Sr_2RuO_4. It was found that the d-orbital degree of freedom is crucial to realize the huge SHE in various transition metals. Later, several authors have studied the SHC based on the multiorbital tight-binding models [10–12].

4.2 AHE in Two-Orbital Tight-Binding Model

For a long time, the intrinsic Hall effect proposed by KL had been underestimated. This would be because the theoretical model assumed in Ref. [2] was too oversimplified, and therefore quantitative analysis of σ^a_{xy} could not be achieved. In 1994, authors in Refs. [13, 14] derived a simple expression of the intrinsic AHE in the periodic Anderson model, which is a frequently-used canonical model for heavy fermion systems. This study strongly indicates that the large AHE in heavy fermion systems

originates from the intrinsic mechanism. Based on the similar method, intrinsic AHE had been studied in various metals.

In this section, we study the intrinsic AHC in a simple tight-binding model with (d_{xz}, d_{yz})-orbitals. The band structure of this model corresponds to α and β bands of Sr_2RuO_4. Here, we represent the creation operator of an electron on xz (yz) orbital as $c_{\mathbf{k}}^{x\dagger}$ $(c_{\mathbf{k}}^{y\dagger})$. The Hamiltonian without ls-coupling is given by $H^0 = \sum_{\mathbf{k}} \hat{c}_{\mathbf{k}}^{\dagger} \hat{h}_{\mathbf{k}}^0 \hat{c}_{\mathbf{k}}$, where

$$\hat{h}_{\mathbf{k}}^0 = \begin{pmatrix} \xi_{\mathbf{k}}^x & \xi_{\mathbf{k}}^{xy} \\ \xi_{\mathbf{k}}^{xy} & \xi_{\mathbf{k}}^y \end{pmatrix}, \tag{4.1}$$

and $\hat{c}_{\mathbf{k}}^{\dagger} = (c_{\mathbf{k}}^{x\dagger}, c_{\mathbf{k}}^{y\dagger})$. $\xi_{\mathbf{k}}^x = -2t \cos k_x$, $\xi_{\mathbf{k}}^y = -2t \cos k_y$ and $\xi_{\mathbf{k}}^{xy} = 4t' \sin k_x \sin k_y$. Here, $-t$ and $\pm t'$ are the hopping integrals between nearest-neighbors and next-nearest-neighbors, respectively. They are shown in Fig. 4.2.

Then, the velocity is given by $\hat{v}_\mu = \partial \hat{h}_{\mathbf{k}}^0 / \partial k_\mu$, where $\mu = x, y$. They are given by

$$\hat{v}_x = \begin{pmatrix} 2t \sin k_x & 4t' \cos k_x \sin k_y \\ 4t' \cos k_x \sin k_y & 0 \end{pmatrix}, \tag{4.2}$$

$$\hat{v}_y = \begin{pmatrix} 0 & 4t' \sin k_x \cos k_y \\ 4t' \sin k_x \cos k_y & 2t \sin k_y \end{pmatrix}. \tag{4.3}$$

Thus, the inter-orbital velocity v_x^{xy} (v_y^{xy}) is an odd-function of k_y (k_x), which is called the "anomalous velocity".

Finally, we introduce the atomic ls-coupling $2\lambda \boldsymbol{l} \cdot \boldsymbol{s}$: We put the coupling constant as 2λ in this section. It is expressed as $H^\lambda = \sum_{\mathbf{k}} \hat{c}_{\mathbf{k}}^{\dagger} \hat{h}^\lambda \hat{c}_{\mathbf{k}}$. Because $|xz\rangle = -(|l_z = +1\rangle - |l_z = -1\rangle)/\sqrt{2}$ and $|yz\rangle = i(|l_z = +1\rangle + |l_z = -1\rangle)/\sqrt{2}i$, $\hat{h}^\lambda$ in the present orbital basis is given by

$$\hat{h}^\lambda = \mathrm{sgn}(s_z) \lambda \hat{\tau}_y, \tag{4.4}$$

where $\hat{\tau}_y$ is the Pauli matrix for the orbital space. Note that $\hat{l}_y = \hat{l}_z = 0$ in the present basis. Hereafter, we put $\mu_B = 1$ for the simplicity of calculation.

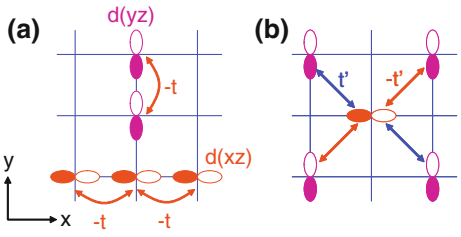

Fig. 4.2 Hopping integrals between the **a** same orbitals and **b** different orbitals. The sign of the inter-orbital hopping integral changes by $\pi/2$ rotation. This fact gives rise to the anomalous velocity

The Green function in the presence of atomic ls-coupling, $\hat{G}_{\mathbf{k}}(\omega) = (\omega + \mu - \hat{h}^0_{\mathbf{k}} - \hat{h}^{\lambda})^{-1}$, is given by

$$\begin{pmatrix} G_{xx} & G_{xy} \\ G_{yx} & G_{yy} \end{pmatrix} = \frac{1}{d(\omega)} \begin{pmatrix} \omega + \mu - \xi^y_{\mathbf{k}} & \alpha_{\mathbf{k}} \\ \alpha^*_{\mathbf{k}} & \omega + \mu - \xi^x_{\mathbf{k}} \end{pmatrix}, \tag{4.5}$$

where $\alpha_{\mathbf{k}} = \xi^{xy}_{\mathbf{k}} + i\lambda \mathrm{sgn}(s_z)$ and $d(\omega) = (\omega + \mu - \xi^x_{\mathbf{k}})(\omega + \mu - \xi^y_{\mathbf{k}}) - |\alpha_{\mathbf{k}}|^2$, which is expressed as

$$d(\omega) = (\omega + \mu - E^+_{\mathbf{k}})(\omega + \mu - E^-_{\mathbf{k}}), \tag{4.6}$$

$$E^{\pm}_{\mathbf{k}} = \frac{1}{2}\left(\xi^x_{\mathbf{k}} + \xi^y_{\mathbf{k}} \pm \sqrt{(\xi^x_{\mathbf{k}} - \xi^y_{\mathbf{k}})^2 + 4|\alpha_{\mathbf{k}}|^2}\right), \tag{4.7}$$

where $E^{\pm}_{\mathbf{k}}$ represents the quasiparticle dispersion. Figure 4.3 shows the Fermi surfaces for $(t, t') = (1, 0.1)$. In Sr_2RuO_4, $t'/t \sim 0.1$. The splitting $\Delta^{\pm}$ represents the minimum band-splitting ($|E^+_{\mathbf{k}} - E^-_{\mathbf{k}}|$) measured from the Fermi surface of $E^{\pm}_{\mathbf{k}}$-band. In Fig. 4.3, $\mathbf{k}^*$ represents the position of the minimum band-splitting, $\Delta \equiv \min\{\Delta^+, \Delta^-\}$.

Assuming the orbital diagonal quasiparticle damping γ, the retarded (advanced) Green function is given by

$$G^{R(A)}_{\alpha\beta'}(\omega) = G_{\alpha\beta'}(\omega + (-)i\gamma), \tag{4.8}$$

where $\alpha, \beta = xz, yz$.

The expression of the intrinsic AHC is derived from the Kubo formula, Eq. (3.48), for multiorbital systems. Its diagrammatic expression is shown in Fig. 4.4. Then, we have to perform the analytic continuation exactly to obtain the expression of the intrinsic term that is of order γ^0. According to Refs. [15] and [16], the exact expression of the intrinsic AHC without vertex correction is

$$\sigma^a_{\mu\nu} = \sigma^{a,I}_{\mu\nu} + \sigma^{a,II}_{\mu\nu}, \tag{4.9}$$

$$\sigma^{a,I}_{\mu\nu} = \sum_{\mathbf{k},\alpha\alpha'\beta\beta'} \int \frac{d\epsilon}{2\pi} v^{\alpha'\alpha}_{\mu} v^{\beta'\beta}_{\nu} \left(-\frac{\partial f}{\partial \epsilon}\right) \times \left[G^R_{\alpha\beta'} G^A_{\beta\alpha'} - \frac{1}{2}\left(G^R_{\alpha\beta'} G^R_{\beta\alpha'} + G^A_{\alpha\beta'} G^A_{\beta\alpha'}\right)\right], \tag{4.10}$$

$$\sigma^{a,II}_{\mu\nu} = -\frac{1}{2} \sum_{\mathbf{k},\alpha\alpha'\beta\beta'} \int \frac{d\epsilon}{2\pi} v^{\alpha'\alpha}_{\mu} v^{\beta'\beta}_{\nu} f(\omega) \times \left[\frac{\partial}{\partial \epsilon} G^R_{\alpha\beta'} \cdot G^R_{\beta\alpha'} - G^R_{\alpha\beta'} \frac{\partial}{\partial \epsilon} G^R_{\beta\alpha'} - \frac{\partial}{\partial \epsilon} G^A_{\alpha\beta'} \cdot G^A_{\beta\alpha'} + G^A_{\alpha\beta'} \frac{\partial}{\partial \epsilon} G^A_{\beta\alpha'}\right], \tag{4.11}$$

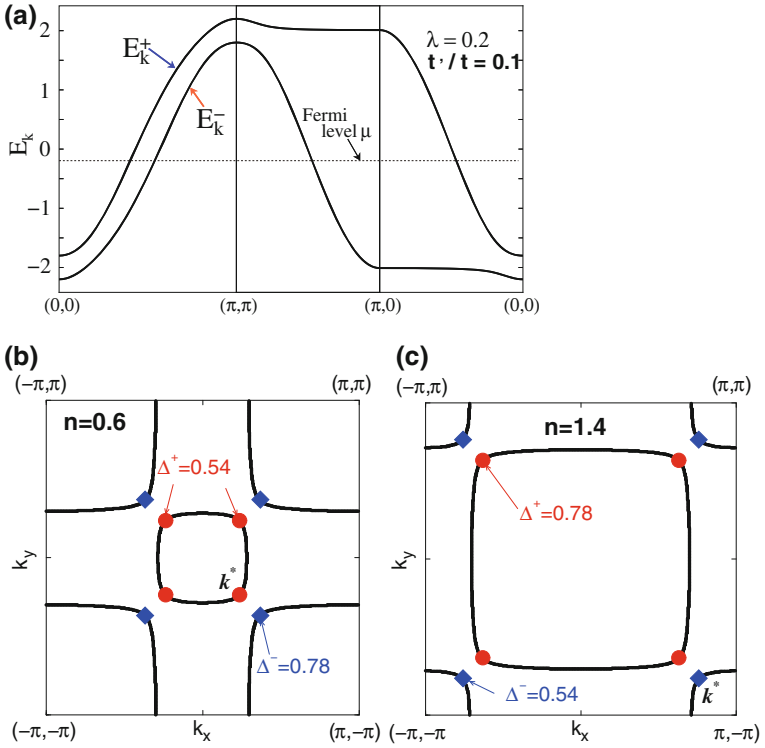

Fig. 4.3 **a** The bandstructure of the two-orbital model for $(t, t') = (1, 0.1)$, which corresponds to Sr_2RuO_4. **b**, **c** Fermi surfaces for $n = 0.6$ and $n = 1.4$

where $f(\epsilon)$ is the Fermi distribution function. Note that Eq. (4.10) [Eq. (4.11)] is derived from Eq. (3.50), with the factor $\lambda^{(2)}$ ($\lambda^{(1,3)}$). We call $\sigma_{\mu\nu}^{a,I}$ and $\sigma_{\mu\nu}^{a,II}$ the "Fermi surface term" and the "Fermi sea term", respectively, according to literature.

From now on, we calculate the intrinsic AHC in the present model. Using the square lattice symmetry of the present model, we obtain that

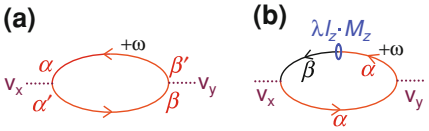

Fig. 4.4 **a** Green function from orbital α to orbital β, **b** velocity orbital α to orbital β, and **c** diagrammatic expression for the AHC without CVC

$$\sigma_{xy}^{a,I} = \lambda \sum_{\mathbf{k}} \int \frac{d\epsilon}{2\pi} v_x^{xx} v_y^{xy} \left(-\frac{\partial f}{\partial \epsilon}\right) \frac{4\gamma}{d^R d^A}, \tag{4.12}$$

$$\sigma_{xy}^{a,II} = 2i\lambda \sum_{\mathbf{k}} \int \frac{d\epsilon}{2\pi} v_x^{xx} v_y^{xy} f(\omega) \left[\left(\frac{1}{d^R}\right)^2 - \left(\frac{1}{d^A}\right)^2 \right], \tag{4.13}$$

where $v_x^{xx} v_y^{xy} = 8tt' \sin^2 k_x \cos k_y$. Here, it is essential that $v_x^{xx} v_y^{xy}$ is the totally symmetric representation (A_{1g}), and it does not vanish after the $\mathbf{k}$-summation. Note that the term proportional to $G^R G^R + G^A G^A$ in $\sigma_{xy}^{a,I}$ vanishes identically.

Here, we derive the expressions for $\sigma_{xy}^{a,I}$ and $\sigma_{xy}^{a,II}$ at $T = 0$. Then, the ω-integration in Eq. (4.13) can be performed using the relation

$$\int_{-\infty}^{\mu} \frac{dx}{(x-a)^2(x-b)^2} = \frac{-(2\mu - a - b)}{(a-b)^2(\mu - a)(\mu - b)} - \frac{2}{(a-b)^3} \ln\left(\frac{a-\mu}{b-\mu}\right). \tag{4.14}$$

The final result for the intrinsic AHC is given by

$$\sigma_{xy}^{a} = \sigma_{xy}^{a,I} + \sigma_{xy}^{a,IIa} + \sigma_{xy}^{a,IIb}, \tag{4.15}$$

$$\sigma_{xy}^{a,I} = \frac{2\lambda}{\pi} \sum_{\mathbf{k}} v_x^{xx} v_y^{xy} \frac{\gamma}{((\mu - E_{\mathbf{k}}^+)^2 + \gamma^2)((\mu - E_{\mathbf{k}}^-)^2 + \gamma^2)}, \tag{4.16}$$

$$\sigma_{xy}^{a,IIa} = \frac{2\lambda}{\pi} \sum_{\mathbf{k}} v_x^{xx} v_y^{xy} \frac{1}{(E_{\mathbf{k}}^+ - E_{\mathbf{k}}^-)^2} \times \mathrm{Im}\left\{ \frac{2\mu - E_{\mathbf{k}}^+ - E_{\mathbf{k}}^- + 2i\gamma}{(\mu - E_{\mathbf{k}}^+ + i\gamma)(\mu - E_{\mathbf{k}}^- + i\gamma)} \right\}, \tag{4.17}$$

$$\sigma_{xy}^{a,IIb} = \frac{4\lambda}{\pi} \sum_{\mathbf{k}} v_x^{xx} v_y^{xy} \frac{1}{(E_{\mathbf{k}}^+ - E_{\mathbf{k}}^-)^3} \times \mathrm{Im}\left\{ \ln\left(\frac{E_{\mathbf{k}}^+ - \mu - i\gamma}{E_{\mathbf{k}}^- - \mu - i\gamma} \right) \right\}. \tag{4.18}$$

Later, we perform numerical calculation of the AHC using these expressions. (The expressions of the AHC for general multiorbital models had been derived in Ref. [11].) When the number of bands is infinite and $\gamma \to 0$, $\sigma_{xy}^{a,IIb}$ is written as the integration of the Berry curvature over the Brillouin zone as explained in Sect. 11.5, known as the Thouless-Kohmoto-Nightingale-den Nijs (TKKN) formula [17].

Before performing the numerical study, we analyze Eqs. (4.16), (4.17) and (4.18) when γ is very small. According to Ref. [16], Eqs. (4.16)–(4.18) are rewritten as follows for $\gamma \to 0$:

$$\sigma_{xy}^{a,I} \approx 2\lambda \sum_{\mathbf{k}} v_x^{xx} v_y^{xy} \frac{\delta(\mu - E_{\mathbf{k}}^+) + \delta(\mu - E_{\mathbf{k}}^-)}{(E_{\mathbf{k}}^+ - E_{\mathbf{k}}^-)^2}, \tag{4.19}$$

$$\sigma_{xy}^{a,IIa} \approx -\sigma_{xy}^{I}, \tag{4.20}$$

$$\sigma_{xy}^{a,IIb} \approx 4\lambda \sum_{\mathbf{k}} v_x^{xx} v_y^{xy} \frac{-\theta(\mu - E_{\mathbf{k}}^+) + \theta(\mu - E_{\mathbf{k}}^-)}{(E_{\mathbf{k}}^+ - E_{\mathbf{k}}^-)^3}. \tag{4.21}$$

According to Eq. (4.21), the main contribution to $\sigma_{xy}^{a,IIb}$ comes from an area near $\mathbf{k}^*$ in Fig. 4.3, if $E_{\mathbf{k}}^+ > 0$ and $E_{\mathbf{k}}^- < 0$ are satisfied. When $d_{\mathbf{k}} \equiv E_{\mathbf{k}}^+ - E_{\mathbf{k}}^-$ is small, then $(-\theta(\mu - E_{\mathbf{k}}^+) + \theta(\mu - E_{\mathbf{k}}^-))/d_{\mathbf{k}} \approx 2\delta(\mu - (E_{\mathbf{k}}^+ + E_{\mathbf{k}}^-)/2)$. In this case, we obtain

$$\begin{aligned} \sigma_{xy}^{a,IIb} &\approx 4\lambda \sum_{\mathbf{k}} v_x^{xx} v_y^{xy} \frac{\delta(\mu - (E_{\mathbf{k}}^+ + E_{\mathbf{k}}^-)/2)}{(E_{\mathbf{k}}^+ - E_{\mathbf{k}}^-)^2} \\ &\approx \sigma_{xy}^{a,I}. \end{aligned} \tag{4.22}$$

In case of $\gamma \to 0$, $\sigma_{xy}^{a,IIb}$ is written as the Berry curvature formula, as shown in Sect. 11.5.

From now on, we perform the numerical calculation for both σ_{xy}^{a} and σ_{xx} at $T = 0$, assuming a complete ferromagnetic state where $n_\downarrow = n$ and $n_\uparrow = 0$. In this case, $m_z = \mu_B n$. (We put $\mu_B = 1$ hereafter.) The unit of conductivity in this section is e^2/ha, where h is the Plank constant and a is the unit cell length (inter-layer distance in 2D systems). If we assume the length of unit cell a is 4 Angstrom, $e^2/ha \approx 10^3\ \Omega^{-1}\mathrm{cm}^{-1}$.

Figure 4.5a shows the n-dependence of σ_{xy} for $n = 0.2 \sim 1.8$. $n = 2$ is a ferromagnetic band insulators. In this model, $\sigma_{xy}(n) = -\sigma_{xy}(2 - n)$. Here, we put

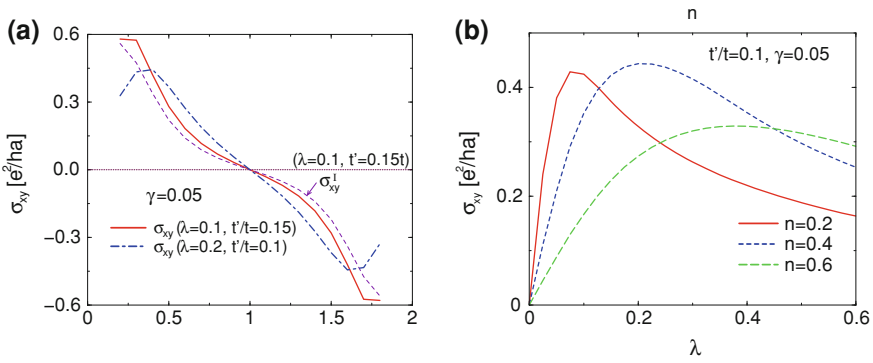

Fig. 4.5 **a** Obtained total AHC (σ_{xy}) and σ_{xy}^I as a function of $n = m_z$. It is verified that $\sigma_{xy} \approx \sigma_{xy}^I$ is well satisfied. $e^2/ha \approx 10^3\ \Omega^{-1}\mathrm{cm}^{-1}$ if we put the unit cell length $a = 4$ Angstrom. σ_{xy} is not a monotonic function of m_z, and changes its sign at $m_z \sim 1$. **b** λ-dependence of σ_{xy} for $n = 1.4$ and 0.6

$\gamma = 0.05$, which is sufficiently smaller than Δ shown in Fig. 4.3. If we assume $t = 4000$ K, the bandwidth is approximately $4|t| = 16000$ K. At $n \sim 1.8$, $|\sigma_{xy}|$ exceeds $0.5 \times 10^3\,\Omega^{-1}\mathrm{cm}^{-1}$, which is comparable with experimental value in Fe [18] and in Sr_2RuO_3 [19]. Figure 4.5b shows the λ-dependence of $|\sigma_{xy}|$ for $n = 0.6$ and 1.4. $|\sigma_{xy}|$ is approximately proportional to λ below $\lambda \sim 0.2$, whereas it tends to saturate when λ is as large as $\Delta_{\lambda=0}$ since $\Delta = E^+_{\mathbf{k}^*} - E^-_{\mathbf{k}^*}$ increases with λ [18].

Next, we examine the γ-dependence of the AHC. Figure 4.6a shows the total AHC (σ_{xy}), σ^I_{xy}, $-\sigma^{IIa}_{xy}$ and σ^{IIb}_{xy} for $n = 1.4$. We see that all of them are γ-independent when $\gamma \ll \Delta$. On the other hand, they start to decrease with γ when $\gamma \gg \Delta$: This is easily recognized from the functional forms of Eqs. (4.16)–(4.18). We see that σ^I_{xy} is almost equal to $-\sigma^{IIa}_{xy}$ and $\sigma_{xy} \approx \sigma^{IIb}_{xy}$ when $\gamma \ll \Delta$, as discussed in the previous section. On the other hand, $\sigma_{xy} \approx \sigma^I_{xy}$ whereas σ_{xy} is quite different from σ^{IIb}_{xy} for $\gamma \gg \Delta$. As a result, the Fermi surface term σ^I_{xy} succeeds in reproducing the overall behavior of the AHC for a wide range of γ.

We also study the relation between the AHC and the resistivity $\rho = 1/\sigma_{xx}$. Figure 4.6b shows that σ_{xy} is independent of ρ when $\rho \lesssim 0.1$ [$\sim 100\,\mu\Omega\,\mathrm{cm}$]. On the other hand, σ_{xy} starts to decrease for $\rho \gtrsim 0.1$ in proportion to ρ^{-2}. This crossover behavior of σ_{xy} at $\rho \sim 100\,\mu\Omega\,\mathrm{cm}$ is observed universally by recent experiments on various transition metal ferromagnets by Asamitsu et al. [20].

In summary, we derived a general expression for the intrinsic AHC σ_{xy} valid for any quasiparticle damping rate γ, by performing the analytic continuation carefully. Using the general expression, we analyzed the AHE in the two orbital model, which presents the α and β bands of Sr_2RuO_4, and it is convenient for the study of the intrinsic Hall effect. In case of $\gamma \ll \Delta$, σ_{xy} is independent of γ. In this case, $\sigma_{xy} \approx \sigma^{IIb}_{xy}$ since σ^{IIa}_{xy} almost cancels with σ^I_{xy}. The relationship $\sigma_{xy} \approx \sigma^I_{xy}$ also

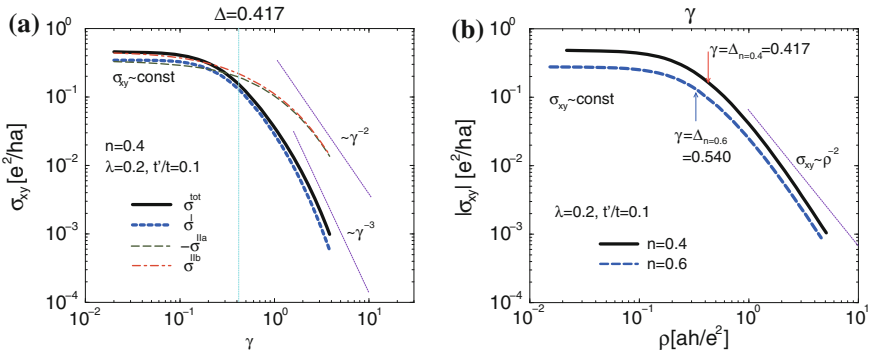

Fig. 4.6 **a** γ-dependences of σ_{xy}, σ^I_{xy}, $-\sigma^{IIa}_{xy}$ and σ^{IIb}_{xy}, respectively. σ_{xy} shows a crossover behavior at $\gamma \sim \Delta$. It is verified that σ^I_{xy} reproduces a overall behavior of the total σ_{xy} for a wide range of γ. **b** Obtained relation between σ_{xy} and $\rho = 1/\sigma_{xx}$ for $n = 1.6$ and 0.4. $\rho = 0.1$ corresponds to $100\,\mu\Omega\,\mathrm{cm}$. Experimentally, $\sigma_{xy} = 10^2 \sim 10^3\,\Omega^{-1}\mathrm{cm}^{-1}$ for $\rho = 1 \sim 100\,\mu\Omega\,\mathrm{cm}$, whereas $\sigma_{xy} \propto \rho^{-2}$ for $\rho \gg 100\,\mu\Omega\,\mathrm{cm}$

holds in metallic states. In the opposite case $\gamma \gg \Delta, \sigma_{xy}$ is proportional to γ^{-2}. In this case, the relation $\sigma_{xy} = \sigma_{xy}^{IIb}$ is no more valid whereas the relation $\sigma_{xy} \approx \sigma_{xy}^{I}$ holds well. Therefore, the AHC shows a crossover behavior from $\sigma_{xy} \propto \gamma^0$ ($R_{\rm H} \propto \rho^2$) to $\sigma_{xy} \propto \gamma^{-2}$ ($R_{\rm H} \propto \rho^0$) as the quasiparticle damping γ increases. This crossover behavior was first discovered in Ref. [13].

Therefore, for a wide range of γ, the relation

$$\sigma_{xy} \approx \sigma_{xy}^{I} \quad \text{(Fermi surface term)} \tag{4.23}$$

would be realized universally in real metallic systems, since the Fermi sea terms almost cancel each other except for a special situation where μ lies inside a narrow anticrossing band gap.

In Fig. 4.7, we present an intuitive explanation for the intrinsic Hall effect based on the two-orbital model. Here, we consider the motion of a $\downarrow$-spin electron along a triangle of a half unit cell. An electron in the d_{xz}-orbital can transfer to the d_{yz}-orbital and vice versa using the SOI for $\downarrow$-electron $-\hbar\lambda\hat{l}_z$, $\langle yz|\hat{l}_z|xz\rangle = -\langle xz|\hat{l}_z|yz\rangle = i$. These relations are derived from the fact that the $(\pi/2)$-rotation operator about the z-axis is given by $\exp(-i\pi\hat{l}_z/2) = \cos(\pi/2) - i\hat{l}_z \sin(\pi/2) = -i\hat{l}_z$ for $\hat{l}_z^2 = 1$. By considering the sign of the interorbital hopping integral ($\pm t'$) and the matrix elements of the SOI, it can be shown that a clockwise (anti-clockwise) motion along any triangle of the half unit cell causes the factor $+i$ ($-i$). This phase factor is called the "orbital Berry phase".

This factor can be interpreted as the Aharonov-Bohm phase factor $e^{2\pi i\phi/\phi_0}$ [$\phi_0 = hc/e$], where $\phi = \oint \mathbf{A}d\mathbf{r} = \phi_0/4$ represents the "effective magnetic flux" through the triangle of the half unit cell. Since the effective magnetic flux for $\uparrow$-electron is

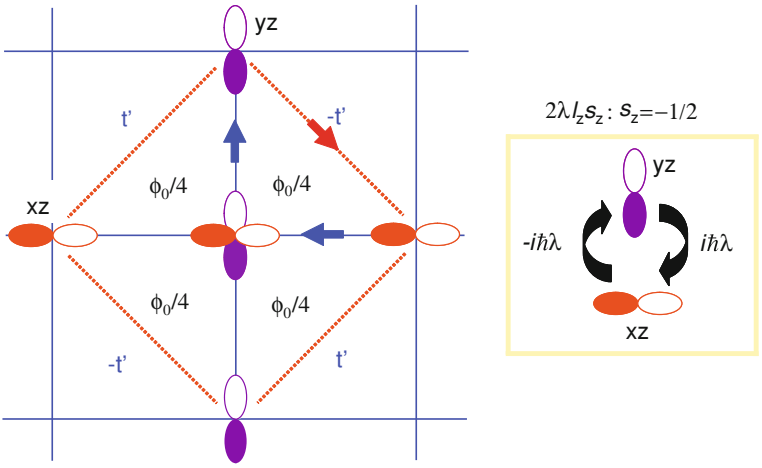

Fig. 4.7 The orbital Berry phase for $\downarrow$-electron through triangles of half unit cells in the two-orbital model. The "effective magnetic flux" for $\uparrow$-electron is $-\phi_0/4$ ($\phi_0 = hc/e$)

opposite in sign, ↑-electrons and ↓-electrons move in opposite directions. Thus, the effective magnetic flux in Fig. 4.7 gives rise to a AHE when $n_\uparrow \neq n_\downarrow$. Therefore, large AHE due to such "orbital Berry phase" will be ubiquitous in multiorbital systems.

We comment that the present (d_{xz}, d_{yz})-tight binding model in a paramagnetic state shows a finite SHC σ^z_{xy}. Since s_z is conserved in the present model, σ^z_{xy} is simply given by $(-\hbar/e)$ times Eq. (4.15). As shown in Fig. 4.5, σ^z_{xy} reaches $0.6\ [(\hbar/e)(e^2/ha)] \sim 600\ [\hbar e^{-1}\,\Omega^{-1}\mathrm{cm}^{-1}]$ for $a = 4$ Angstrom, which is almost one order of magnitude larger than typical SHC in semimetals.

Although s_z is conserved in the present two-orbital model, s_z is no more conserved in real Ru-oxides because of the existence of the d_{xy}-orbital Fermi surface. This is also true in various transition metals. Because of this reason, the two-orbital model is inappropriate for the realistic study of the SHE. Thus, to understand the origin of the recently observed giant SHC in transition metals [5, 6], authors in Ref. [9] analyzed the SHC in the t_{2g}-orbital (d_{xz}, d_{yz}, d_{xy}) tight-binding model with SOI, which well represents the band structure of Sr_2RuO_4. It was revealed that the spin-dependent orbital Berry phase in Fig. 4.7 causes giant SHC in various paramagnetic transition metal compounds.

4.3 General Expression for the AHC and SHC

In this section, we derive the expression for the AHC for the general multiorbital models. We consider a tight-binding model given by the set of hopping integrals between different Wannier functions:

$$H_0 = \sum_{\mathbf{k},\alpha\beta} c^\dagger_{\alpha\mathbf{k}} H^{0\alpha\beta}_{\mathbf{k}} c_{\beta\mathbf{k}}, \tag{4.24}$$

where α and β are atomic orbital and spin indices. When the quasiparticle damping γ is diagonal and independent of orbital, the Green function is given as $\hat{G}^{R(A)}_{\mathbf{k}}(\omega) = (\omega + \mu - \hat{H}^0_{\mathbf{k}} + (-)i\gamma)^{-1}$. Under the vector potential, the momentum $\mathbf{k}$ in the kinetic term is replaced with $\mathbf{k} + e\mathbf{A}$. $(-e$ is the electron charge.) Therefore, the velocity in the orbital basis is given by

$$\hat{v}_{\mathbf{k}\mu} = \left.\frac{\partial \hat{H}^0_{\mathbf{k}+e\mathbf{A}}}{\partial e A_\mu}\right|_{\mathbf{A}=0} = \frac{\partial \hat{H}^0_{\mathbf{k}}}{\partial k_\mu} \tag{4.25}$$

Here, we derive the general expression for the AHC in the orbital basis, which is convenient for numerical calculations. There is a $\mathbf{k}$-dependent unitary matrix $\hat{U}_{\mathbf{k}}$ which diagonalize the Hamiltonian as

$$\sum_{\alpha\beta} U^\dagger_{\mathbf{k},l\alpha} H^{0\alpha\beta}_{\mathbf{k}} U_{\mathbf{k},\beta m} = E^l_{\mathbf{k}} \delta_{lm}, \tag{4.26}$$

where α, β are orbital indices, and l, m are band indices. $E^l_{\mathbf{k}}$ gives the dispersion of the lth band. When the quasiparticle damping γ is diagonal and independent of orbital,

$$\sum_{\alpha\beta} U^{\dagger}_{\mathbf{k},l\alpha} G^{R(A)}_{\mathbf{k},\alpha\beta} U_{\mathbf{k},\beta m} = \frac{\delta_{l,m}}{\omega + \mu - E^l_{\mathbf{k}} + (-)i\gamma}, \tag{4.27}$$

Then, Eqs. (4.10) and (4.11) are rewritten as

$$\begin{aligned}
\sigma^{a,I}_{xy} &= \frac{1}{2\pi N} \sum_{\mathbf{k},l\neq m} (J_{\mathbf{k}x})^{ml} (J_{\mathbf{k}y})^{lm} \frac{1}{(E^l_{\mathbf{k}} - \mu - i\gamma)(E^m_{\mathbf{k}} - \mu - i\gamma)} \\
&= \frac{-1}{2\pi N} \sum_{\mathbf{k},l\neq m} \mathrm{Im}\left\{(J_{\mathbf{k}x})^{ml} (J_{\mathbf{k}y})^{lm}\right\} \\
&\quad \times \mathrm{Im}\left\{\frac{1}{(E^l_{\mathbf{k}} - \mu - i\gamma)(E^m_{\mathbf{k}} - \mu + i\gamma)}\right\}, \qquad (4.28) \\
\sigma^{a,II}_{xy} &= -\frac{1}{2\pi N} \sum_{\mathbf{k},l\neq m} \int_{-\infty}^{0} d\omega \mathrm{Im}\left\{(J_{\mathbf{k}x})^{ml} (J_{\mathbf{k}y})^{lm}\right\} \\
&\quad \times \mathrm{Im}\left\{\frac{1}{(\omega + \mu - E^l_{\mathbf{k}} + i\gamma)^2} \frac{1}{(\omega + \mu - E^m_{\mathbf{k}} + i\gamma)}\right. \\
&\quad \left. - \frac{1}{(\omega + \mu - E^l_{\mathbf{k}} + i\gamma)} \frac{1}{(\omega + \mu - E^m_{\mathbf{k}} + i\gamma)^2}\right\}, \qquad (4.29)
\end{aligned}$$

where $(J_{\mathbf{k}\mu})^{ml}$ is given by $\sum_{\alpha\beta} U^{\dagger}_{\mathbf{k},m\alpha} (v_{\mathbf{k}\mu})^{\alpha\beta} U_{\mathbf{k},\beta l}$, which is not diagonal even in the band-diagonal basis. Note that we dropped the diagonal terms $l = m$ in the summations in Eqs. (4.28) and (4.29) since they vanish identically. We also note that the transformation from the first row to the second row in Eq. (4.28) was performed since $\sum_{l,m} \mathrm{Re}\left\{(J_{\mathbf{k}x})^{ml} (J_{\mathbf{k}y})^{lm}\right\}$ vanishes identically after $\mathbf{k}$-summation. After performing the ω-integration in Eq. (4.29), the Fermi sea term is given by $\sigma^{a,II}_{xy} = \sigma^{a,IIa}_{xy} + \sigma^{a,IIb}_{xy}$, where

$$\begin{aligned}
\sigma^{a,IIa}_{xy} &= \frac{-1}{2\pi N} \sum_{\mathbf{k},l\neq m} \mathrm{Im}\left\{(J_{\mathbf{k}x})^{ml} (J_{\mathbf{k}y})^{lm}\right\} \frac{1}{E^l_{\mathbf{k}} - E^m_{\mathbf{k}}} \\
&\quad \times \mathrm{Im}\left\{\frac{E^l_{\mathbf{k}} + E^m_{\mathbf{k}} - 2\mu - 2i\gamma}{(E^l_{\mathbf{k}} - \mu - i\gamma)(E^m_{\mathbf{k}} - \mu - i\gamma)}\right\}, \qquad (4.30) \\
\sigma^{a,IIb}_{xy} &= \frac{1}{\pi N} \sum_{\mathbf{k},l\neq m} \mathrm{Im}\left\{(J_{\mathbf{k}x})^{ml} (J_{\mathbf{k}y})^{lm}\right\} \frac{1}{(E^l_{\mathbf{k}} - E^m_{\mathbf{k}})^2} \\
&\quad \times \mathrm{Im}\left\{\ln\left(\frac{E^l_{\mathbf{k}} - \mu - i\gamma}{E^m_{\mathbf{k}} - \mu - i\gamma}\right)\right\}. \qquad (4.31)
\end{aligned}$$

Here, we used the following relation to perform the ω-integration:

$$\int_{-\infty}^{\mu} dx \left\{ \frac{1}{(x-a)^2(x-b)} - \frac{1}{(x-a)(x-b)^2} \right\} = \frac{a+b-2\mu}{(a-b)(a-\mu)(b-\mu)} - \frac{2}{(a-b)^2} \ln\left(\frac{a-\mu}{b-\mu}\right). \tag{4.32}$$

In the same way, we can obtain the SHC by replacing $(J_{\mathbf{k}x})^{ml}$ in Eqs. (4.28)–(4.31) with the spin velocity

$$(J^s_{\mathbf{k}x})^{ml} = \sum_{\alpha\beta} U^{\dagger}_{\mathbf{k},m\alpha} (v^s_{\mathbf{k}x})^{\alpha\beta} U_{\mathbf{k},\beta l}, \tag{4.33}$$

where $\hat{v}^s_{\mathbf{k}x} = \{\hat{v}_{\mathbf{k}x}, \hat{s}_z\}/2$. In Chap. 11, we will calculate the AHC and SHC in various multiorbital models using Eqs. (4.28)–(4.31) and Eq. (4.33).

References

1. R. Karplus, J.M. Luttinger, Phys. Rev. **95**, 1154 (1954)
2. J.M. Luttinger, Phys. Rev. **112**, 739 (1958)
3. J. Smit, Physica **24**, 39 (1958)
4. L. Berger, Phys. Rev. B **2**, 4559 (1970)
5. T. Kimura, Y. Otani, T. Sato, S. Takahashi, S. Maekawa, Phys. Rev. Lett. **98**, 156601 (2007)
6. E. Saitoh, M. Ueda, H. Miyajima, G. Tatara, Appl. Phys. Lett. **88**, 182509 (2006)
7. S. Murakami, N. Nagaosa, S.C. Zhang, Phys. Rev. B **69**, 235206 (2004)
8. J. Sinova, D. Culcer, Q. Niu, N.A. Sinitsyn, T. Jungwirth, A.H. MacDonald, Phys. Rev. Lett. **92**, 126603 (2004)
9. H. Kontani, T. Tanaka, D.S. Hirashima, K. Yamada, J. Inoue, Phys. Rev. Lett. **100**, 096601 (2008)
10. M. Kontani, D.S. Naito, K. Hirashima, Yamada, and J. Inoue. J. Phys. Soc. Jpn. **76**, 103702 (2007)
11. T. Tanaka, H. Kontani, M. Naito, T. Naito, D.S. Hirashima, K. Yamada, J. Inoue, Phys. Rev. B **77**, 165117 (2008)
12. G.Y. Guo, S. Murakami, T.-W. Chen, N. Nagaosa, Phys. Rev. Lett. **100**, 096401 (2008)
13. H. Kontani, K. Yamada, J. Phys. Soc. Jpn. **63**, 2627 (1994)
14. H. Kontani, K. Yamada, J. Phys. Soc. Jpn. **66**, 2252 (1997)
15. P. Streda, J. Phys. C: Solid State Phys. **15**, L717 (1982)
16. H. Kontani, T. Tanaka, K. Yamada, Phys. Rev. B **75**, 184416 (2007)
17. D. Thouless, M. Kohmoto, M. Nightingale, M. den Nijs, Phys. Rev. Lett. **49**, 405 (1982)
18. Y. Yao, L. Kleinman, A.H. MacDonald, J. Sinova, T. Jungwirth, D. Wang, E. Wang, Q. Niu, Phys. Rev. Lett. **92**, 37204 (2004)
19. Z. Fang et al., Science **302**, 92 (2003)
20. T. Miyasato, N. Abe, T. Fujii, A. Asamitsu, S. Onoda, Y. Onose, N. Nagaosa, Y. Tokura, Phys. Rev. Lett. **99**, 086602 (2007)

Part II
Recent Advances

Chapter 5
Transport Phenomena in Cuprate HTSCs Above T^*

5.1 FLEX + CVC Approximation

In this chapter, we discuss the transport phenomena in cuprate HTSCs above the pseudo-gap temperature T^* where the SC fluctuations would be negligible. Here we concentrate on the FLEX + CVC approximation: The self-energy is given by Eq. (2.13), and the kernel function in the Bethe-Salpeter equation, $\mathcal{T}^{(0)}_{\mathbf{k},\mathbf{k}'}$, is given by Eq. (3.64). The total current $\boldsymbol{J}_{\mathbf{k}}$ is obtained by solving the Bethe-Salpeter equation [1].

In the FLEX approximation, the self-energy is given by the convolution of G and V as in Eq. (2.13). Then, $\Gamma^I = \delta\Sigma/\delta G$ (Ward identity) contains one Maki-Thompson term that is given by taking derivative of G, and two Aslamazov-Larkin terms that are given by taking derivative of V. These three terms corresponds to (a)–(c) in Fig. 3.6 [1, 2] given by the simplification in Eq. (3.75). Considering the relation $\delta\chi^0_{\mathbf{q}}/\delta G_{\mathbf{k}'} = -(G_{\mathbf{k}'+\mathbf{q}} + G_{\mathbf{k}'-\mathbf{q}})$, we can derive $\Gamma^I_{\mathbf{k},\mathbf{k}'} = \delta\Sigma_{\mathbf{k}}/\delta G_{\mathbf{k}'}$ in the FLEX approximation as

$$\begin{aligned}\Gamma^I_{\mathbf{k},\mathbf{k}'}(\epsilon_n,\epsilon_{n'}) &= V_{\mathbf{k}'-\mathbf{k}}(\epsilon_{n'}-\epsilon_n)\\ &\quad - T\sum_{\mathbf{q},l} U^2\left[\frac{3}{2}(U\chi^s_{\mathbf{q}}(\omega_l)+1)^2 + \frac{1}{2}(U\chi^c_{\mathbf{q}}(\omega_l)-1)^2 - 1\right]\\ &\quad \times G_{\mathbf{k}-\mathbf{q}}(\epsilon_n-\omega_l)G_{\mathbf{k}'-\mathbf{q}}(\epsilon_{n'}-\omega_l)\\ &\quad - T\sum_{\mathbf{q},l} U^2\left[\frac{3}{2}(U\chi^s_{\mathbf{q}}(\omega_l)+1)^2 + \frac{1}{2}(U\chi^c_{\mathbf{q}}(\omega_l)-1)^2 - 1\right]\\ &\quad \times G_{\mathbf{k}+\mathbf{q}}(\epsilon_n+\omega_l)G_{\mathbf{k}'-\mathbf{q}}(\epsilon_{n'}-\omega_l),\end{aligned} \tag{5.1}$$

where the first term is the Maki-Thompson term, and the last two terms are the Aslamazov-Larkin terms. Hereafter, we drop the Aslamazov-Larkin terms since they are negligible in nearly AF Fermi liquids ($\chi^s_Q \gg \chi^c_Q, \chi^0_Q$), as discussed in Sect. 3.5.

H. Kontani, *Transport Phenomena in Strongly Correlated Fermi Liquids*,
Springer Tracts in Modern Physics 251, DOI: 10.1007/978-3-642-35365-9_5,

Then, the kernel function of the Bethe-Salpeter equation (3.63) is obtained by the analytic continuation of $V_{\mathbf{k}'-\mathbf{k}}(\epsilon_{n'} - \epsilon_n)$. It is given by Eq. (B.8) at $\omega = 0$, where $\Gamma^{II}_{2,2}(\epsilon, \epsilon') = V(\epsilon' - \epsilon + i\delta)$ and $\Gamma^{III}_{2,2}(\epsilon, \epsilon') = \Gamma^{IV}_{2,2}(\epsilon, \epsilon') = V(\epsilon' - \epsilon - i\delta)$ for the Maki-Thompson term (see Fig. B.1a). The obtained kernel function is $\mathcal{T}^{(0)}(\epsilon, \epsilon') = \left(\mathrm{cth}\frac{\epsilon' - \epsilon}{2T} - \mathrm{th}\frac{\epsilon'}{2T}\right)\big(V(\epsilon' - \epsilon + i\delta) - V(\epsilon' - \epsilon - i\delta)\big)$. Thus, the Bethe-Salpeter equation in the FLEX + CVC theory is given by [1],

$$\boldsymbol{J}_{\mathbf{k}}(\epsilon) = \boldsymbol{v}_{\mathbf{k}}(\epsilon) + \sum_{\mathbf{q}} \int \frac{d\epsilon'}{2\pi} \left[\mathrm{cth}\frac{\epsilon' - \epsilon}{2T} - \mathrm{th}\frac{\epsilon'}{2T}\right] \times \mathrm{Im} V_{\mathbf{q}-\mathbf{k}}(\epsilon' - \epsilon + i\delta) \cdot |G_{\mathbf{q}}(\epsilon' + i\delta)|^2 \cdot \boldsymbol{J}_{\mathbf{q}}(\epsilon') \tag{5.2}$$

where $\boldsymbol{v}_{\mathbf{k}}(\epsilon) = \nabla_{\mathbf{k}}(\epsilon^0_{\mathbf{k}} + \mathrm{Re}\Sigma_{\mathbf{k}}(\epsilon))$. By using the relation $\int[\mathrm{cth}(\epsilon/2T) - \mathrm{th}(\epsilon/2T)]\epsilon d\epsilon = (\pi T)^2$, and assuming the relation $\omega_{\mathrm{sf}} \gg T$, Eq. (5.2) is simplified as

$$\boldsymbol{J}_{\mathbf{k}}(\epsilon) \approx \boldsymbol{v}_{\mathbf{k}} + \sum_{\mathbf{q}} \frac{(\pi T)^2}{2} \mathrm{Im}\dot{V}_{\mathbf{q}}(0) \frac{\rho_{\mathbf{k}+\mathbf{q}}(0)}{\gamma_{\mathbf{k}+\mathbf{q}}} \boldsymbol{J}_{\mathbf{k}+\mathbf{q}}, \tag{5.3}$$

which is equivalent to Eq. (3.78) if we approximate $V_{\mathbf{q}} \approx 3U^2\chi^s_{\mathbf{q}}/2$. [Note that $\bar{U} = U$ in the FLEX approximation.] The numerical solution of Eq. (5.2) is shown in Fig. 5.1, which confirms the behavior of $\mathbf{J}_{\mathbf{k}}$ in Fig. 3.7a. This singular $\mathbf{k}$-dependence of $\mathbf{J}_{\mathbf{k}}$ is realized because $\alpha_{\mathbf{k}}$ in Eq. (3.80) approaches unity for $\xi_{\mathrm{AF}} \to \infty$. This result is not specific to the FLEX approximation since the same vertex function $[\mathcal{T}^{(0)}_{\mathbf{k},\mathbf{k}'}]$ appears in both (3.63) and (3.71) in the microscopic Fermi liquid theory, because of the Ward identity. For this reason, singular $\mathbf{k}$-dependence of $\mathbf{J}_{\mathbf{k}}$ for $\xi_{\mathrm{AF}} \gg 1$, which is shown in Fig. 5.1 given by the FLEX approximation, is a universal behavior in Fermi liquids near the AF QCP.

In hole-doped systems, $\gamma_{\mathbf{k}}$ attains its minimum (maximum) at point A (B) as shown in Fig. 2.5 [3, 4]. At low T, the local minimum of $|\boldsymbol{J}_{\mathbf{k}}|$ is located at points A and B, and its maximum is located at point C, schematically shown in Fig. 3.7a. Further, Fig. 5.1b shows that the mean free path with CVC, $|\boldsymbol{L}_{\mathbf{k}}| = |\boldsymbol{J}_{\mathbf{k}}/\gamma_{\mathbf{k}}|$, attains its local minimum at point A for $T \leq 0.02$, since $|\boldsymbol{J}_{\mathbf{k}}|$ rapidly increases as $\mathbf{k}$ deviates from the point A. In fact, Eq. (3.82) suggests that $|\boldsymbol{J}_{\mathbf{k}}| \propto \xi^2_{\mathrm{AF}}|\boldsymbol{v}_{\mathbf{k}} + \boldsymbol{v}_{\mathbf{k}^*}|$, which will takes a large value near the AF QCP except at points A and B. In later sections, we explain that the local minimum structure of $|\boldsymbol{L}_{\mathbf{k}}|$ at point A becomes prominent below T^*, which causes the significant increases in the Nernst coefficient and magnetoresistance.

In Ref. [1], we solved the Bethe-Salpeter equation by considering both Maki-Thompson term and the Aslamazov-Larkin terms, and calculated both ρ and R_{H}. It is verified numerically that the Aslamazov-Larkin terms are negligible in nearly AF metals.

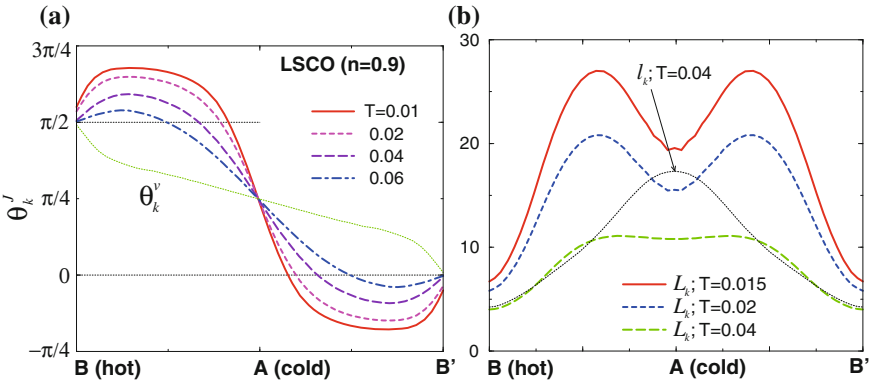

Fig. 5.1 **a** $\theta^J_{\mathbf{k}} = \tan^{-1}(J_{\mathbf{k}x}/J_{\mathbf{k}y})$ and **b** mean free path with CVC obtained by the FLEX + CVC method. $|\boldsymbol{L}_{\mathbf{k}}| = |\boldsymbol{J}_{\mathbf{k}}/\gamma_{\mathbf{k}}|$. $-d\theta^J_{\mathbf{k}}/dk_{\parallel}$ at the cold spot (A) increases as T decreases. $|\boldsymbol{L}_{\mathbf{k}}|$ attains its local minimum at the cold spot for $T \leq 0.02$, which induces increases in the Nernst coefficient and magnetoresistance. We also plot the mean free path without CVC; $|\boldsymbol{l}_{\mathbf{k}}| = |\boldsymbol{v}_{\mathbf{k}}/\gamma_{\mathbf{k}}|$. The Fermi surface is shown in Fig. 3.7

5.2 Resistivity and Hall Coefficient

First, we analyze the conductivity σ_{xx} using Eq. (3.61). According to the approximate expression for $\boldsymbol{J}_{\mathbf{k}}$ in Eq. (3.82),

$$[v_{\mathbf{k}x} J_{\mathbf{k}x}]_{\rm cold} = \left[\frac{v^2_{\mathbf{k}x}}{1+\alpha_{\mathbf{k}}}\right]_{\rm cold} \tag{5.4}$$

at the cold spot of YBCO [point A], at which the relationship $\mathbf{k} = -\mathbf{k}^*$ is satisfied. Since $1/(1+\alpha_{\mathbf{k}}) \sim 1/2$ when $\xi_{\rm AF} \gg 1$, it is obtained as $\sigma_{xx} \sim \sigma^{\rm RTA}_{xx}/2$. Therefore, the resistivity ρ is slightly increased by the CVC [1]. Since the effect of the CVC on ρ is not large, the RTA result is qualitatively correct.

Figure 5.2a shows the numerical results of ρ for LSCO ($n = 0.92$ and $U = 4.5$) given by the FLEX and FLEX+T-matrix approximations. In the FLEX approximation without CVC, ρ shows an approximate T-linear behavior for $T \geq 0.02$ ($\sim$80 K). Because of the CVC, ρ is slightly enhanced for wide range of temperatures, and ρ shows a tiny "kink" structure at $\sim T_0$, below which AF fluctuations strongly grow. This result is consistent with experiments [5]. The kink becomes more prominent in the FLEX+T-matrix approximation, which will be discussed in Sect. 6.2. In Fig. 5.2a, $\rho = 1-250\,\mu\Omega\,$cm at $T = 0.08-320\,$K: The resistivity increases with U, and $\rho \sim 450\,\mu\Omega\,$cm for YBCO with $U = 8$ and $n = 0.9$ [1]. Consistently, $\rho \approx 200-300\,\mu\Omega\,$cm at 300 K in optimally-doped YBCO and LSCO, and it increases to $400-600\,\mu\Omega\,$cm in slightly under-doped compounds ($n \sim 0.1$) [6]. However, the FLEX + CVC method cannot reproduce the huge resistivity in heavily under-doped compounds.

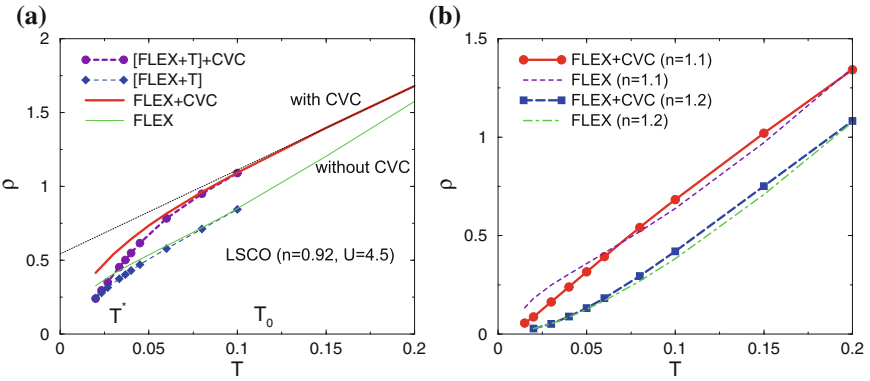

Fig. 5.2 **a** ρ for LSCO obtained by the FLEX (without CVC) and FLEX + CVC approximations. ρ is slightly enhanced because of the CVC. We also plot ρ obtained by the FLEX + T-matrix (without CVC) and [FLEX + T-matrix] + CVC approximations. The FLEX + T-matrix approximation coincides with the FLEX approximation for $T \gg T^*$, where SC fluctuations disappear. $T = 0.2$ corresponds to 800 K. **b** ρ for NCCO obtained by the FLEX (without CVC) and FLEX + CVC approximations

Figure 5.2b shows the ρ for NCCO ($U = 5.5$) obtained by the FLEX approximation (within the RTA) and the FLEX + CVC approximation. In the case of $n = 1.20$ (over-doped), ρ shows a T^2-like behavior below $T = 0.1-400$ K, which is consistent with experiments. In the case of $n = 1.10$ (under-doped), ρ shows an approximate T-linear behavior when the CVC is included in the calculation. Interestingly, $\rho_{\mathrm{FLEX+CVC}} < \rho_{\mathrm{FLEX(RTA)}}$ for $n = 1.10$ below $T = 0.06$, since $|\boldsymbol{J}_{\mathbf{k}}| \gg |\boldsymbol{v}_{\mathbf{k}}|$ due to the CVC in NCCO at low temperatures.

Next, we discuss the Hall coefficient. Using the Onsager's relation $\sigma_{xy} = -\sigma_{yx}$, the general expression for σ_{xy} in Eq. (3.62) and $\sigma_{xy}^{\mathrm{RTA}}$ in Eq. (3.11) in 2D systems can be rewritten as [1]

$$\sigma_{xy}/H_z = \frac{e^3}{4}\oint_{\mathrm{FS}} \frac{dk_\parallel}{(2\pi)^2}\left(\boldsymbol{L}_{\mathbf{k}} \times \frac{\partial \boldsymbol{L}_{\mathbf{k}}}{\partial k_\parallel}\right)_z$$
$$= \frac{e^3}{4}\oint_{\mathrm{FS}} \frac{dk_\parallel}{(2\pi)^2}|\boldsymbol{J}_{\mathbf{k}}|^2\left(\frac{-d\theta_{\mathbf{k}}^J}{dk_\parallel}\right)\cdot\frac{1}{\gamma_{\mathbf{k}}^2}, \tag{5.5}$$

$$\sigma_{xy}^{\mathrm{RTA}}/H_z = \frac{e^3}{4}\oint_{\mathrm{FS}} \frac{dk_\parallel}{(2\pi)^2}|\boldsymbol{v}_{\mathbf{k}}|^2\left(\frac{-d\theta_{\mathbf{k}}^v}{dk_\parallel}\right)\cdot\frac{1}{\gamma_{\mathbf{k}}^2}, \tag{5.6}$$

where $\boldsymbol{L}_{\mathbf{k}} = \boldsymbol{J}_{\mathbf{k}}/\gamma_{\mathbf{k}}$, $\theta_{\mathbf{k}}^J = \tan^{-1}(J_{\mathbf{k}x}/J_{\mathbf{k}y})$ and $\theta_{\mathbf{k}}^v = \tan^{-1}(v_{\mathbf{k}x}/v_{\mathbf{k}y})$. $dk_\parallel$ is the momentum tangent to the Fermi surface, which is depicted in Fig. 3.7a. Note that $|\boldsymbol{L}_{\mathbf{k}}|$ represents the mean free path by considering the CVC. In deriving above equations, we used the relation $|v_{\mathbf{k}}|\partial/\partial k_\parallel = (\hat{z}\times\boldsymbol{v}_{\mathbf{k}})\cdot\nabla_{\mathbf{k}} = (\boldsymbol{v}_{\mathbf{k}}\times\nabla_{\mathbf{k}})_z$ in 2D systems. Using the relation $\sqrt{v_{\mathbf{k}x}^2 + v_{\mathbf{k}y}^2}\,\partial/\partial k_\parallel = (\boldsymbol{v}_{\mathbf{k}}\times\nabla_{\mathbf{k}})_z$, σ_{xy} in a 3D system is given by

$$\sigma_{xy}/H_z = \frac{e^3}{4}\int_{\rm FS}\frac{dS_{\mathbf{k}}}{(2\pi)^3}\frac{\sqrt{v_{\mathbf{k}x}^2+v_{\mathbf{k}y}^2}}{|\boldsymbol{v}_{\mathbf{k}}|}|\boldsymbol{J}_{\mathbf{k}}|^2\left(\frac{-d\theta_{\mathbf{k}}^J}{dk_\parallel}\right)\cdot\frac{1}{\gamma_{\mathbf{k}}^2}, \tag{5.7}$$

where $dS_{\mathbf{k}}$ represents the Fermi surface element, and $dk_\parallel$ is the momentum tangent to the Fermi surface and parallel to the xy-plane. We stress that the k-derivative of $\gamma_{\mathbf{k}}$ does not contribute to σ_{xy}, whereas it is important for $\Delta\sigma_{xx}$ and α_{xy}.

In the expression of $\sigma_{xy}^{\rm RTA}$, $(-d\theta_{\mathbf{k}}^v/dk_\parallel)$ represents the curvature of the Fermi surface [7, 8]; in both hole-doped and electron-doped HTSCs, $(-d\theta_{\mathbf{k}}^v/dk_\parallel) \sim 1/k_{\rm F}$ (>0) on the Fermi surface. On the other hand, $(-d\theta_{\mathbf{k}}^J/dk_\parallel)$ exhibits strong $\mathbf{k}$-dependence in nearly AF metals, as shown in Fig. 3.7a: It is positive (negative) around point A (B). Since the cold spot locates at point A in hole-doped systems [1], the present study predicts that $R_{\rm H} > 0$ in hole-doped systems. [Note that the charge of electron is $-e$ $(e>0)$.] On the other hand, $R_{\rm H} < 0$ in electron-doped systems with strong AF fluctuations since the cold spot in electron-doped systems is B [1]. To understand the role of the CVC within the scheme of the RTA, we have introduced an "effective Fermi surface" obtained by bending the true Fermi surface such that it is orthogonal to $\boldsymbol{J}_{\mathbf{k}}$ [9]. The effective Fermi surface in HTSCs is shown in Fig. 3.7b: Its curvature is equal to $(-d\theta_{\mathbf{k}}^J/dk_\parallel)$ by definition, and it takes a large positive (negative) value around the cold spot in hole-doped (electron-doped) systems. Therefore, $R_{\rm H}$ in hole-doped (electron-doped) systems exhibits a large positive (negative) value at low temperatures [1].

Figure 5.3a, c, and d shows the numerical results for $R_{\rm H}$ given by the FLEX + CVC approximations. In hole-doped systems $(n<1)$, $R_{\rm H}$ increases as the doping $\delta = |1-n|$ decreases. On the other hand, $R_{\rm H}$ for electron-doped systems $(n>1)$ becomes negative below $T = 0.09{-}400$ K. For a long time, it had been considered that the negative $R_{\rm H}$ in electron-doped systems is a strong evidence of the breakdown of the Fermi liquid state. However, it is naturally explained in terms of the Fermi liquid picture since the curvature of the "effective Fermi surface" becomes negative around point B, depicted in Fig. 3.7b [1].

As shown in Fig. 5.3a, c, and d, $R_{\rm H}$ in the RTA (without CVC) slightly decreases at low temperatures, because of the deformation of the interacting Fermi surface [1]: The curvature of the Fermi surface is reduced by the $\mathbf{k}$-dependence of the self-energy when AF fluctuations are strong. A tiny increment in $R_{\rm H}^{\rm RTA}$ in YBCO below $T = 0.02$ is caused by the strong anisotropy of $\gamma_{\mathbf{k}}$. In the present calculation, $\gamma_{\rm hot}/\gamma_{\rm cold} \approx 3$ at $T = 0.02$.

Figure 5.3b shows the $k_\parallel$-dependence of $\Delta\sigma_{xx}(k_\parallel) = \boldsymbol{v}_{\mathbf{k}}\cdot\boldsymbol{L}_{\mathbf{k}}/|\boldsymbol{v}_{\mathbf{k}}|$ and $\Delta\sigma_{xy}(k_\parallel) = |\boldsymbol{L}_{\mathbf{k}}|^2(-\partial\theta_{\mathbf{k}}^J/\partial k_\parallel)$, where $\sigma_{xx} = \oint_{\rm FS} dk_\parallel \Delta\sigma_{xx}(k_\parallel)$ and $\sigma_{xy} = \oint_{\rm FS} dk_\parallel \Delta\sigma_{xy}(k_\parallel)$. In both σ_{xx} and σ_{xy}, the electrons around the cold spot gives the dominant contributions. σ_{xx} is slightly reduced by including the CVC. On the other hand, σ_{xy} obtained from the FLEX + CVC theory is considerably larger than $\sigma_{xy}^{\rm RTA}$, since $|d\theta_{\mathbf{k}}^J/dk_\parallel| \gg |d\theta_{\mathbf{k}}^v/dk_\parallel|$ at the cold spot. $\Delta\sigma_{xy}(k_\parallel)$ is large only around the cold spot, and it becomes negative around the hot spot.

Here, we discuss the temperature dependence of $R_{\rm H}$ in detail using the approximate expression for $\boldsymbol{J}_{\mathbf{k}}$ in Eq. (3.82). Since $\partial\alpha_{\mathbf{k}}/\partial k_\parallel = 0$ at the cold spot [point A]

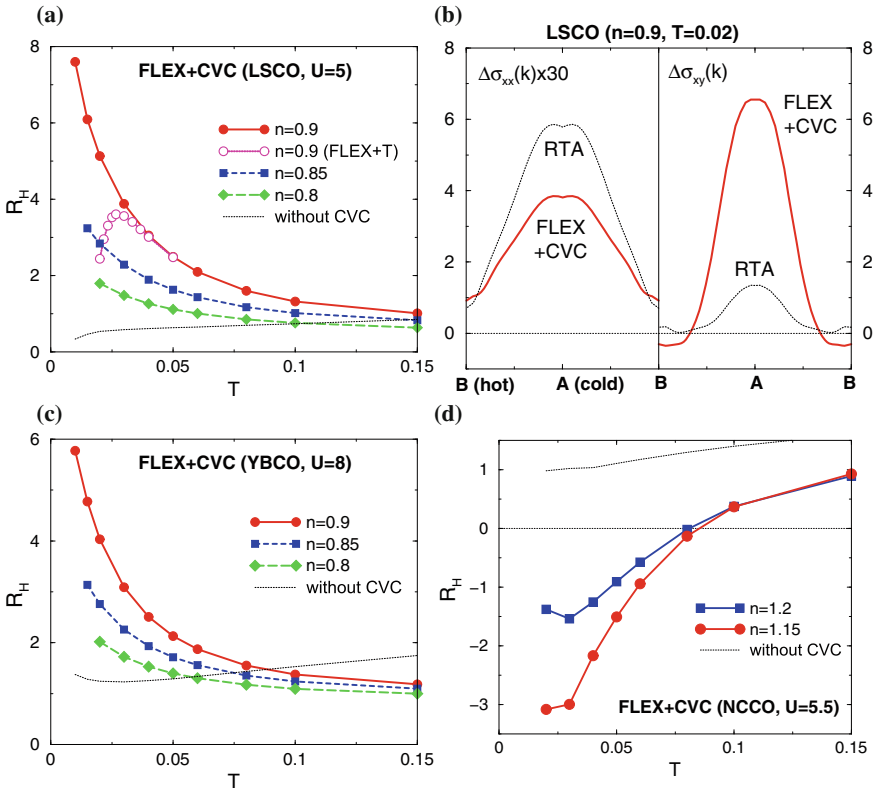

Fig. 5.3 **a** Strong T-dependence of $R_{\rm H}$ for LSCO obtained by the FLEX + CVC approximation. In contrast, $R_{\rm H}^{\rm RTA}$ given by the RTA (without CVC) is almost T-independent. $R_{\rm H}$ obtained using the FLEX + T-matrix approximation is also shown; it starts to decrease below $T^* \sim 0.04$ ($\sim$160) K (pseudo-gap behavior). **b** $k_\parallel$-dependence of $\Delta\sigma_{xx}(k_\parallel)$ and $\Delta\sigma_{xy}(k_\parallel)$ at $T = 0.02$. Note that $\sigma_{\mu\nu} = \int_{\rm FS} dk_\parallel \Delta\sigma_{\mu\nu}(k_\parallel)$. **c** $R_{\rm H}$ for YBCO in the FLEX + CVC method. **d** $R_{\rm H}$ for NCCO in the FLEX + CVC method

because of the symmetry,

$$\frac{d\boldsymbol{J}_{\mathbf{k}}}{dk_\parallel} = \frac{1}{1-\alpha_{\mathbf{k}}^2}\left(\frac{d\boldsymbol{v}_{\mathbf{k}}}{dk_\parallel} + \alpha_{\mathbf{k}}\frac{d\boldsymbol{v}_{\mathbf{k}^*}}{dk_\parallel}\right) \tag{5.8}$$

at the cold spot. Then, by noticing the relationships $(\boldsymbol{v}_{\mathbf{k}^*} \times d\boldsymbol{v}_{\mathbf{k}^*}/dk_\parallel)_z = -(\boldsymbol{v}_{\mathbf{k}} \times d\boldsymbol{v}_{\mathbf{k}}/dk_\parallel)_z$ and $(\boldsymbol{v}_{\mathbf{k}^*} \times d\boldsymbol{v}_{\mathbf{k}}/dk_\parallel)_z = -(\boldsymbol{v}_{\mathbf{k}} \times d\boldsymbol{v}_{\mathbf{k}^*}/dk_\parallel)_z$, we obtain that

$$\left(\boldsymbol{J}_{\mathbf{k}} \times \frac{d\boldsymbol{J}_{\mathbf{k}}}{dk_{\parallel}}\right)_z = |\boldsymbol{J}_{\mathbf{k}}|^2 \left(\frac{-d\theta^J_{\mathbf{k}}}{dk_{\parallel}}\right)_{\text{cold}} = \frac{1}{1-\alpha^2_{\mathbf{k}}} |\boldsymbol{v}_{\mathbf{k}}|^2 \left(\frac{-d\theta^v_{\mathbf{k}}}{dk_{\parallel}}\right)_{\text{cold}}, \tag{5.9}$$

which is proportional to $(1-\alpha_{\mathbf{k}})^{-1} \propto \xi^2_{\text{AF}}$ [1]. In fact, Fig. 5.1a shows that Eq. (5.9) increases as the temperature decreases. As a result, R_{H} behaves as [1]

$$|R_{\text{H}}| \propto \xi^2_{\text{AF}}. \tag{5.10}$$

Thus, both the sign and the T-dependence of R_{H} in hole-doped HTSC are successfully reproduced in the present approach.

Finally, we discuss electron-doped systems. At the point B in Fig. 2.1a, $|\mathbf{k}_{\text{B}} - \mathbf{k}_{\text{B}'} - \mathbf{Q}|$ is equal to $|\mathbf{k}_{\text{B}} - \mathbf{k}_{\text{B}''} - \mathbf{Q}|$ for $\mathbf{Q} = (\pi, -\pi)$. Then, the CVC at $\mathbf{k}_{\text{B}}$, which is given by the second term of Eq. (3.78), is approximately proportional to $\boldsymbol{J}_{B'} + \boldsymbol{J}_{B''} = 0$. Therefore, $\alpha_{\mathbf{k}} = 0$ in the simplified Bethe-Salpeter equation (3.81) and $\boldsymbol{J}_{\mathbf{k}} \approx \boldsymbol{v}_{\mathbf{k}}$ at point B. Since $\alpha_{\mathbf{k}}$ rapidly increases if $\mathbf{k}$ deviates from point B, $(-d\theta^J_{\mathbf{k}}/dk_{\parallel})$ attains a large negative value around the cold spot of NCCO. Therefore, the negative sign of R_{H} is realized by considering the CVC.

5.3 Magnetoresistance

Next, we study the orbital magnetoresistance $\Delta\rho/\rho_0$ in HTSCs by considering the CVC. According to the linear response theory [10], the magnetoresistance due to the Lorentz force ($\mathbf{k} \to \mathbf{k} + e\mathbf{A}$) is given by

$$\Delta\rho/\rho_0 \equiv -\Delta\sigma_{xx}/\sigma^0_{xx} - (\sigma_{xy}/\sigma^0_{xx})^2, \tag{5.11}$$

where σ^0_{xx} denotes the conductivity without a magnetic field, and $\Delta\sigma_{xx} \equiv \sigma_{xx}(H_z) - \sigma^0_{xx}$ is the magneto-conductivity due to the Lorentz force. This orbital magneto-conductivity is always negative and proportional to γ^{-3}, so it is significant in good metals with small γ. In the RTA, the first term in Eq. (5.11) is always dominant except when the Fermi surface is isotropic, so the orbital magnetoresistance $\Delta\rho/\rho_0$ is always positive [10]. This statement is true beyond the RTA, since the enhancement of $|\Delta\sigma_{xx}|$ due to the CVC is larger than that of $(\sigma_{xy})^2$.

In strongly correlated metals with large γ, on the other hand, the Zeeman effect causes a large field dependence of γ; $\gamma(H) = \gamma(0) \cdot (1 - aH^2)$. Usually, $a > 0$ and $|a| \propto (m^*/m)^2$ since the Zeeman splitting reduces the inelastic scattering. In heavy fermion systems, this Zeeman splitting mechanism causes the "negative" magnetoresistance at $T \sim T_{\text{K}}$, $(\Delta\rho/\rho_0)_{\text{Zeeman}} \propto (\gamma(H) - \gamma(0))/\gamma(0) \propto -aH^2$. However, positive orbital magnetoresistance given by Eq. (5.11), $\Delta\rho/\rho_0 \propto \gamma(0)^{-2}H^2$, is dominant for $T \ll T_{\text{K}}$ since $\gamma(0)$ is small in the coherent Fermi liquid regime.

Here, we concentrate on the orbital effect, and neglect the Zeeman effect on γ. By performing the partial integration, the magneto-conductivity in Eq. (3.12) is rewritten in 2D systems as

$$\Delta\sigma_{xx}^{\mathrm{RTA}} = -H_z^2 \cdot \frac{e^4}{8} \oint_{\mathrm{FS}} \frac{dk_\parallel}{(2\pi)^2} |\boldsymbol{v}_{\mathbf{k}}| \left[|\boldsymbol{l}_{\mathbf{k}}|^2 \left(\frac{\partial \theta_{\mathbf{k}}^v}{\partial k_\parallel} \right)^2 + \left(\frac{\partial |\boldsymbol{l}_{\mathbf{k}}|}{\partial k_\parallel} \right)^2 \right] \frac{1}{\gamma_{\mathbf{k}}}, \tag{5.12}$$

where $\boldsymbol{l}_{\mathbf{k}} = \boldsymbol{v}_{\mathbf{k}}/\gamma_{\mathbf{k}}$. Here, we used the relation $|v_{\mathbf{k}}|\partial/\partial k_\parallel = (\hat{z} \times \boldsymbol{v}_{\mathbf{k}}) \cdot \nabla_{\mathbf{k}} = (\boldsymbol{v}_{\mathbf{k}} \times \nabla_{\mathbf{k}})_z$ in 2D systems. When the Fermi surface is spherical, the second term in the bracket in Eq. (5.12) vanishes identically. In this case, $\sigma_{xx}^0 = e^2 k_{\mathrm{F}} v_{\mathrm{F}}/4\pi\gamma$, $\sigma_{xy} = (e v_{\mathrm{F}}/2\gamma)\sigma_{xx}^0$ and $\Delta\sigma_{xx} = -(e v_{\mathrm{F}}/2\gamma)^2 \sigma_{xx}^0$ according to the RTA, where k_{F} and v_{F} are the Fermi momentum and Fermi velocity, respectively. Therefore, $\Delta\rho/\rho_0$ given in Eq. (5.11) becomes zero. Except for this special case, the orbital magnetoresistance is always positive [10].

The general expression for the magneto-conductivity is derived by performing the analytic continuation of Eq. (3.42) for $m = 2$ [11]. This work enables us to calculate the magneto-conductivity along with satisfying the conservation laws. At low temperatures, the magneto-conductivity can be expressed by a simple form [11]: $\Delta\sigma_{xx} = \Delta\sigma_{xx}^a + \Delta\sigma_{xx}^b$, and

$$\Delta\sigma_{xx}^a = -H_z^2 \cdot \frac{e^4}{4} \sum_{\mathbf{k}} z_{\mathbf{k}} \left(-\frac{\partial f^0}{\partial \epsilon} \right)_{E_{\mathbf{k}}^*} \{d_{\mathbf{k}x}\}^2 \frac{1}{\gamma_{\mathbf{k}}}, \tag{5.13}$$

$$\Delta\sigma_{xx}^b = -H_z^2 \cdot \frac{e^4}{4} \sum_{\mathbf{k}} z_{\mathbf{k}} \left(-\frac{\partial f^0}{\partial \epsilon} \right)_{E_{\mathbf{k}}^*} d_{\mathbf{k}x} \{D_{\mathbf{k}x} - d_{\mathbf{k}x}\} \frac{1}{\gamma_{\mathbf{k}}}, \tag{5.14}$$

$$d_{\mathbf{k}x} = |v_{\mathbf{k}}| \frac{\partial L_{\mathbf{k}x}}{\partial k_\parallel}, \tag{5.15}$$

$$J_{\mathbf{k}x} = v_{\mathbf{k}x} + \sum_{\mathbf{k}'} \int_{-\infty}^{\infty} \frac{d\epsilon'}{4i} \mathcal{T}_{\mathbf{k},\mathbf{k}'}^{(0)}(0, \epsilon') \frac{\rho_{\mathbf{k}'}(0)}{\gamma_{\mathbf{k}'}} J_{\mathbf{k}'x},$$

$$D_{\mathbf{k}x} = d_{\mathbf{k}x} + \sum_{\mathbf{k}'} \int_{-\infty}^{\infty} \frac{d\epsilon'}{4i} \mathcal{T}_{\mathbf{k},\mathbf{k}'}^{(0)}(0, \epsilon') \frac{\rho_{\mathbf{k}'}(0)}{\gamma_{\mathbf{k}'}} D_{\mathbf{k}'x}, \tag{5.16}$$

where $\boldsymbol{L}_{\mathbf{k}} = \boldsymbol{J}_{\mathbf{k}}/\gamma_{\mathbf{k}}$ and $\mathcal{T}_{\mathbf{k},\mathbf{k}'}^{(0)}(0, \epsilon')$ is the irreducible four-point vertex in the particle-hole channel introduced in Eq. (3.63). $\Delta\sigma_{xx}^{\mathrm{RTA}}$ in Eq. (3.12) is given by Eqs. (5.13) and (5.15), by replacing $\boldsymbol{J}_{\mathbf{k}}$ with $\boldsymbol{v}_{\mathbf{k}}$. In the FLEX approximation, $\int \frac{d\epsilon'}{4\pi i} \mathcal{T}_{\mathbf{k},\mathbf{k}'}^{(0)}(0, \epsilon') \approx (3U^2/2)(\pi T)^2 \mathrm{Im}\partial\chi_{\mathbf{k}-\mathbf{k}'}^s(\omega)/\partial\omega|_{\omega=0}$, as shown in Eq. (3.78).

Using the relation $\Delta\sigma_{xx} = \Delta\sigma_{yy}$, we can rewrite $\Delta\sigma_{xx}^a$ as

$$\Delta\sigma_{xx}^a = -H_z^2 \cdot \frac{e^4}{8} \oint_{\mathrm{FS}} \frac{dk_\parallel}{(2\pi)^2} |\boldsymbol{v}_{\mathbf{k}}| \left[|\boldsymbol{L}_{\mathbf{k}}|^2 \left(\frac{\partial \theta_{\mathbf{k}}^J}{\partial k_\parallel} \right)^2 + \left(\frac{\partial |\boldsymbol{L}_{\mathbf{k}}|}{\partial k_\parallel} \right)^2 \right] \frac{1}{\gamma_{\mathbf{k}}}, \tag{5.17}$$

where $\boldsymbol{L}_{\mathbf{k}} = \boldsymbol{J}_{\mathbf{k}}/\gamma_{\mathbf{k}}$. According to Eq. (5.9), the first term in the bracket in Eq. (5.17) is proportional to $(d\theta^J_{\mathbf{k}}/dk_{\parallel})^2_{\rm cold}\gamma^{-3}_{\rm cold} \propto \xi^4_{\rm AF}\gamma^{-3}_{\rm cold}$ [12]. Further, remaining terms (the second term in Eq. (5.17) and $\Delta\sigma^b_{xx}$) are also proportional to $\xi^4_{\rm AF}\gamma^{-3}_{\rm cold}$ for a wide range of temperatures, since the $k_{\parallel}$-derivative of $\bar{\mathcal{T}}^{(0)}_{\mathbf{k},\mathbf{k}'}$ yields a factor proportional to $\xi^2_{\rm AF}$ [1, 12]. In Sect. 6.2, we will explain that $|\boldsymbol{L}_{\mathbf{k}}|$ becomes highly anisotropic below T^* due to AF+SC fluctuations. For this reason, due to the second term in Eq. (5.17), $\Delta\rho/\rho_0$ is drastically enhanced below T^* in under-doped HTSCs.

Therefore, the magnetoresistance in nearly AF metals behaves as

$$\Delta\rho/\rho_0 \propto H^2\xi^4_{\rm AF}\cdot\rho_0^{-2} \propto T^{-4} \tag{5.18}$$

above T^* due to the CVC since $\rho_0 \propto T$ and $\xi^2_{\rm AF} \propto T^{-1}$. Equation (5.18) is consistent with experimental results in LSCO [13–15], YBCO [14] and TBCO [16]. On the other hand, in a conventional Fermi liquid where $\xi_{\rm AF}$ is constant, Eq. (5.18) gives Kohler's rule $\Delta\rho/\rho_0 \propto H^2\rho_0^{-2}$. Equations (5.10) and (5.18) directly imply the "modified Kohler's rule" [12]

$$\Delta\rho/\rho_0 \propto H^2\tan^2\theta_{\rm H}, \tag{5.19}$$

where $\tan\theta_{\rm H} = \sigma_{xy}/\sigma^0_{xx} = HR_{\rm H}/\rho_0$. Experimentally, the modified Kohler's rule is well satisfied in various HTSC compounds [13, 14, 16] and in CeMIn$_5$(M = Co or Rh) [9, 17], whereas the conventional Kohler's rule is completely broken. The modified Kohler's rule implies the same origin of the enhancements of $R_{\rm H}$ and $\Delta\rho/\rho_0$; the CVC due to AF fluctuations.

Figure 5.4 shows the numerical results for (a) YBCO and (b) LSCO by using the FLEX + CVC method. The coefficient

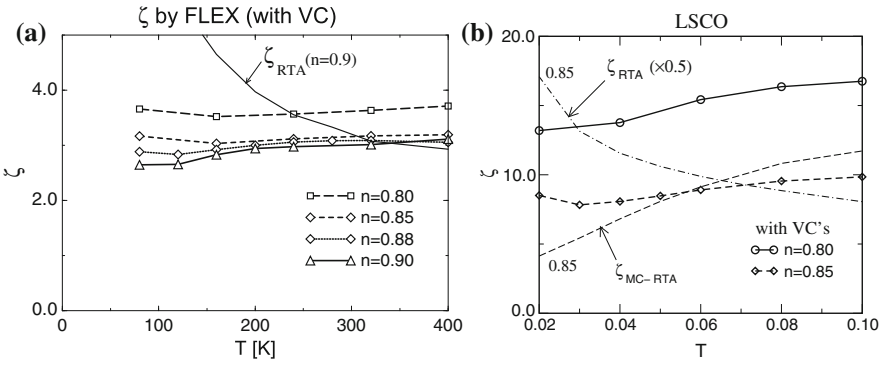

Fig. 5.4 $\zeta = (\Delta\rho/\rho_0)\cot^2\theta_{\rm H}$ for **a** YBCO and **b** LSCO calculated by the FLEX + CVC method for $0.02 \le T \le 0.1 (80 \sim 400\,{\rm K})$. The modified Kohler's rule (ζ =const.) holds well by considering the CVC. In contrast, $\zeta_{\rm RTA}$ obtained by the RTA exhibits a strong T-dependence. [Reference [12]]

$$\zeta = (\Delta\rho/\rho_0)\cot^2\theta_{\rm H} = -\frac{\Delta\sigma_{xx}\cdot\sigma_{xx}}{(\sigma_{xy})^2} - 1 \tag{5.20}$$

is nearly constant for a wide range of temperatures, only when the CVCs are correctly considered: In Fig. 5.4, we show that $\zeta_{\rm RTA} \equiv (\Delta\rho/\rho_0)_{\rm RTA}(\cot^2\theta_{\rm H})_{\rm RTA}$ and $\zeta_{\text{MC-RTA}} \equiv -\frac{\Delta\sigma_{xx}^{\rm RTA}\cdot\sigma_{xx}^{\rm CVC}}{(\sigma_{xy}^{\rm CVC})^2} - 1$. Here, $\zeta_{\rm RTA}$ increases as T decreases, since the anisotropy of $|\boldsymbol{l}_k| = |\boldsymbol{v}_{\mathbf{k}}/\gamma_{\mathbf{k}}|$ increases at low temperatures. In contrast, $\zeta_{\text{MC-RTA}}$ decreases at low temperatures since the $R_{\rm H}$ is strikingly enhanced by the CVC. Only when both σ_{xy} and $\Delta\sigma_{xx}$ are calculated using the FLEX + CVC method, the modified Kohler's rule $\zeta \approx$ const. is satisfied.

The experimental value is $\zeta \approx$ 1.5–1.7 for YBCO [14] and $\zeta \approx$ 2–3 for $Tl_2Ba_2CuO_{6+\delta}$ [16]. In contrast, ζ takes much larger value in LSCO: $\zeta \approx 13.6$ for a slightly over-doped sample ($x = 0.17$) [15], and it increases (decreases) as the doping increases (decreases) [13]. In both these systems, the modified Kohler's rule (5.19) is well reproduced by the FLEX + CVC method, as shown in Fig. 5.4. In YBCO, the dominant contribution is given by $\Delta\sigma_{xx}^{a}$, particularly by the first term in the bracket in Eq. (5.17) that includes $(\partial\theta_{\mathbf{k}}^{J}/\partial k_{\parallel})^2$. In the case of LSCO, the second term in Eq. (5.17) is very important. In LSCO, the Fermi surface is very close to the van-Hove singularity point $(\pi, 0)$ since both $|t'/t|$ and $|t''/t|$ in Eq. (2.5) are smaller than those in other systems. Since $\boldsymbol{v}_{\mathbf{k}} = 0$ at $(\pi, 0)$, the anisotropy of the velocity $|\boldsymbol{v}_{\mathbf{k}}|$ on the Fermi surface is larger in LSCO. Hence, the second term in Eq. (5.17) [or Eq. (5.12)] takes a large value in LSCO. In heavily over-doped LSCO at $\delta = 0.225$, where CVC is expected to be unimportant, ζ exceeds 100 [13]. This result is consistent with recent ARPES measurement [18], which shows that the Fermi surface in LSCO passes through $(\pi, 0)$ in the over-doped region $\delta = 0.2$–0.22.

Therefore, experimental value of ζ gives us a useful measure of the anisotropy of $\boldsymbol{L}_{\mathbf{k}} = \boldsymbol{J}_{\mathbf{k}}/\gamma_{\mathbf{k}}$. ($\boldsymbol{L}_{\mathbf{k}} \approx \boldsymbol{l}_{\mathbf{k}}$ in weakly correlated systems.) In $CeMIn_5$ (M = Rh, Co), ζ is of order $O(100)$ [9], which indicates that the anisotropy of $\boldsymbol{L}_{\mathbf{k}}$ is large in the main Fermi surface.

5.4 Thermoelectric Power

We also discuss the thermoelectric power, S. In cuprate HTSCs, S takes a large value in under-doped systems, and it increases as T decreases below the room temperature. Except for over-doped compounds, $S > 0$ in hole-doped systems [19–26] whereas $S < 0$ in electron-doped systems [27, 28] below the room temperature. We stress that the peak temperature of S is nearly equal to the pseudo-gap temperature T^* in many hole-doped compounds; in $HgBa_2CuO_{4+\delta}$ [23, 24], LSCO, YBCO [25] and $Bi_2Sr_2RCu_2O_8$ (R = Ca, Y, Pr, Dy or Er) [26]. By neglecting the CVC, Hildebrand et al. calculated the thermoelectric power for YBCO using the FLEX approximation [29]. Here, we study the thermoelectric power both for hole-doped and electron-doped systems using the FLEX + CVC method.

According to the linear response theory [30–33], the thermoelectric power in a Fermi liquid system is given by

$$S = \alpha_{xx}/\sigma_{xx}, \tag{5.21}$$

where α_{xx} is the diagonal Peltier conductivity; $j_x = \alpha_{xx}(-\nabla_x T)$. It is given by [30–33],

$$\alpha_{xx} = K^{\alpha}_{xx}(\omega + \mathrm{i}0)/\mathrm{i}\omega\big|_{\omega\to 0}, \tag{5.22}$$

where $K^{\alpha}_{xx}(\omega + \mathrm{i}0)$ is given by the analytic continuation of [33]

$$K^{\alpha}_{xx}(i\omega_\lambda) = \frac{1}{T}\int_0^\beta d\tau e^{-\omega_\lambda \tau}\langle T_\tau j^Q_x(0) j_x(\tau)\rangle, \tag{5.23}$$

where $\boldsymbol{j}$ and $\boldsymbol{j}^Q$ are charge and heat current operators, respectively. The heat current is defined by the following energy conservation law; $\partial_t(h(\mathbf{r}) - \mu n(\mathbf{r})) + \nabla\cdot\boldsymbol{j}^Q(\mathbf{r}) = 0$. Then, $\boldsymbol{j}^Q$ contains complex two-body terms in the presence of electron-electron correlation. Fortunately, the Ward identity allows us to rewrite the heat current as $\boldsymbol{j}^Q_{\mathbf{k}}(\epsilon) = \epsilon \boldsymbol{v}_{\mathbf{k}}$, where $\boldsymbol{v}_{\mathbf{k}} = \nabla_{\mathbf{k}}(\epsilon^0_{\mathbf{k}} + \mathrm{Re}\,\Sigma_{\mathbf{k}})$ [33]. By performing the analytic continuation of Eq. (5.23), we can derive the exact expression of α_{xx} of order $O(E_{\mathrm{F}}/\gamma)$ as [33]

$$\begin{aligned}\alpha_{xx} = \frac{-e}{T}\sum_{\mathbf{k}}\int\frac{d\epsilon}{\pi}\left(-\frac{\partial f^0}{\partial\epsilon}\right)\epsilon v_{\mathbf{k}x}(\epsilon) \\ \times\left(J_{\mathbf{k}x}(\epsilon)|G_{\mathbf{k}}(\epsilon)|^2 - 2v_{\mathbf{k}x}(\epsilon)\mathrm{Re}G_{\mathbf{k}}(\epsilon)^2\right),\end{aligned} \tag{5.24}$$

where $J_{\mathbf{k}x}(\epsilon)$ is the total current given in Eq. (3.63). At sufficiently low temperatures, α_{xx} is simplified as

$$\alpha_{xx} = -e\frac{\pi^2 T}{3}\int_{\mathrm{FS}}\frac{dk_\parallel}{(2\pi)^2}\frac{1}{z_{\mathbf{k}}|v_{\mathbf{k}}(E^*_{\mathbf{k}})|}\frac{\partial}{\partial k_\perp}\left(\frac{v_{\mathbf{k}x}(E^*_{\mathbf{k}})J_{\mathbf{k}x}(E^*_{\mathbf{k}})}{|v_{\mathbf{k}}(E^*_{\mathbf{k}})|\gamma_{\mathbf{k}}(E^*_{\mathbf{k}})}\right), \tag{5.25}$$

where $-e$ ($e > 0$) is the electron charge. $dk_\perp$ represents the momentum vertical to the Fermi surface. When γ is energy-independent, Eq. (5.25) yields $S = -e\pi T/6z\gamma\sigma_{xx} = -\pi T m^*/3en$ ($m^* = m/z$ is the effective mass) in the 2D isotropic system with $E_{\mathbf{k}} = k^2/2m - \mu$.

Figure 5.5 shows the damping rate $\gamma(\mathbf{k}, \epsilon^*_{\mathbf{k}}) = \mathrm{Im}\,\Sigma^A(\mathbf{k}, \epsilon^*_{\mathbf{k}})$ for YBCO and NCCO given by the FLEX approximation at $T = 0.02$, along $(0, 0) \to (\pi, \pi)$ and $(0, \pi) \to (\pi, \pi)$. This strong momentum-dependence of $\gamma_{\mathbf{k}}(E^*_{\mathbf{k}})$ causes large thermoelectric power in HTSC: In Fig. 5.6a, we show the numerical results of S for YBCO and NCCO given by the FLEX + CVC method. In LSCO, $S > 0$ in the optimally-doped case ($n = 0.85$) below the room temperature, and it increases in the under-doped case. In NCCO ($n = 1.10$), $S < 0$ and it takes a peak around 200 K. These results

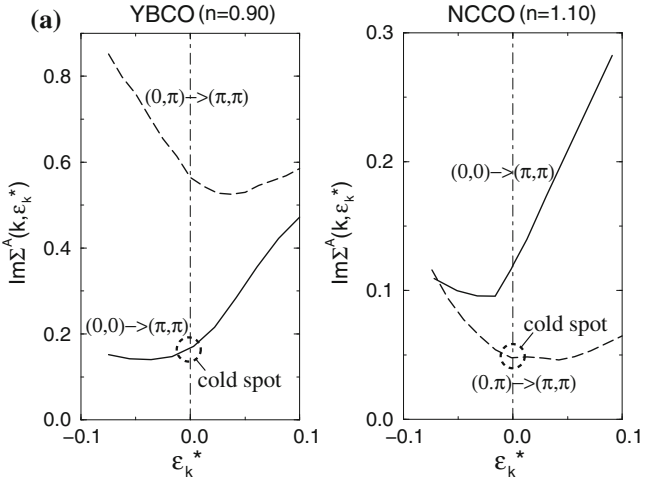

Fig. 5.5 $\gamma(\mathbf{k}, \epsilon_{\mathbf{k}}^*) = \mathrm{Im}\Sigma^A(\mathbf{k}, \epsilon_{\mathbf{k}}^*)$ for YBCO and NCCO, along $(0, 0) \rightarrow (\pi, \pi)$ and $(0, \pi) \rightarrow (\pi, \pi)$

are consistent with the experimental results [19–25]. The origin of the non-Fermi-liquid-like behavior is the strong $\mathbf{k}-$ and ϵ-dependences of $\gamma_{\mathbf{k}}(\epsilon)$ shown in Fig. 5.5. In nearly AF Fermi liquids, $\partial\gamma_{\mathbf{k}}(E_{\mathbf{k}}^*)/\partial k_\perp > 0$ at point A in Fig. 2.1a since $\gamma_{\mathbf{k}}$ increases near the AFBZ. Since point A is the cold spot of YBCO, Eq. (5.25) becomes positive in YBCO. Therefore, $S > 0$ in under-doped YBCO and LSCO. On the other hand, $S < 0$ in NCCO since $\partial\gamma_{\mathbf{k}}(E_{\mathbf{k}}^*)/\partial k_\perp < 0$ at point B. Numerical results of S are summarized in Fig. 5.6a.

In YBCO, S slightly decreases if the CVC is included, since $|\boldsymbol{J}_{\mathbf{k}}| < |\boldsymbol{v}_{\mathbf{k}}|$ around the cold spot. In NCCO, in contrast, absolute value of S is enhanced by the CVC. In both cases, the effect of the CVC on S is much smaller than that on R_{H}. Figure 5.6b shows the S for YBCO ($n = 0.90$), together with $S_{\mathrm{in}}(S_{\mathrm{out}})$ which denotes the contribution from the inside (outside) of the AFBZ. S_{in} is positive and it deviates from a conventional behavior ($S \propto T$) since the ϵ-dependence of $\gamma_{\mathbf{k}}(\epsilon)$ becomes large inside of the AFBZ at lower temperatures. On the other hand, S_{out} is negative and it approaches zero as T decreases. Therefore, the sign of $S = S_{\mathrm{in}} + S_{\mathrm{out}}$ becomes positive below $T = 0.075$ ($\sim$300 K).

5.5 Comments on Over-Doped HTSCs and Other Transport Coefficients

In this text, we have shown that the CVC is very important for various transport phenomena in optimally- or slightly under-doped HTSCs. Here, we shortly discuss on the transport coefficients in over-doped systems. In clean heavily over-doped

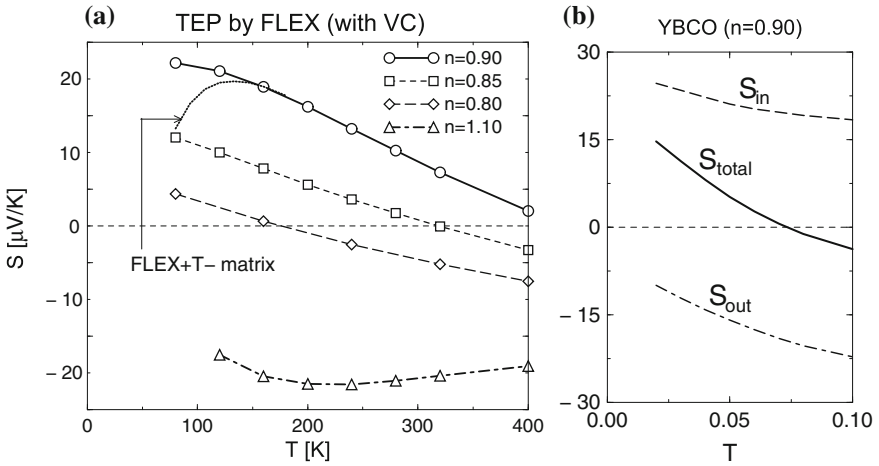

Fig. 5.6 **a** S for YBCO and NCCO given by the FLEX + CVC approximation, by including the CVC for $\boldsymbol{J}_{\mathbf{k}}$. Reflecting the reduction in AF fluctuations, S starts to decrease below $T^* \approx 0.04$ ($\sim$160) K in the FLEX $+T$-matrix method, which is consistent with the experimental pseudo-gap behavior in S. **b** $S_{\mathrm{in(out)}}$ denotes the thermoelectric power given by the *inside* (*outside*) of the AFBZ. $S_{\mathrm{total}} = S_{\mathrm{in}} + S_{\mathrm{out}}$. [Reference [34]]

LSCO samples, R_{H} is almost temperature-independent for $\delta \gtrsim 0.24$ [35]. Further, its sign smoothly changes from positive to negative between $\delta = 0.28$ and 0.32, corresponding to the change in the curvature of the Fermi surface. Hussey et al. also showed that the RTA analysis is successful in heavily over-doped Tl2201 [36, 37] and LSCO [38]. These experimental results are consistent with the present theory: According to the present analysis, the RTA works well in heavily over-doped systems since the CVC is unimportant when the AF fluctuations are very weak. This fact is well explained in Ref. [5].

We also comment on other important theoretical study involving the CVC in strongly correlated systems. In the interacting electron gas model, the electron cyclotron frequency ω_c is given by eH/mc, where m is the bare electron mass. In 1961, Kohn proved that ω_c is unchanged by electron-electron interaction due to the consequence of the angular momentum conservation law, which is called the "Kohn's theorem" [39]. The Kohn's theorem is also proved by the phenomenological Fermi liquid theory, by correctly considering the CVC [40]. Kanki and Yamada studied this problem based on the microscopic Fermi liquid theory, and found that ω_c is influenced by the electron-electron correlation if the Umklapp processes are present [41]. Moreover, the effect of the vertex correction on the Raman spectroscopy in HTSC was studied [42].

5.6 Summary of This Chapter

We have investigated the mechanism of non-Fermi-liquid-like transport phenomena in Fermi liquids with strong magnetic fluctuations. This problem had been widely recognized in the study of cuprate HTSC. The RTA for the anisotropic $\tau_{\mathbf{k}}$ model, which would be realized by strong AF fluctuations, is unable to reproduce relationships (1.1)–(1.4) consistently. These anomalous transport properties are not special phenomena in HTSC, but universal in Fermi liquids near AF QCP.

In the Fermi liquid theory, the total current $\boldsymbol{J}_{\mathbf{k}}$, which is responsible for the transport coefficients, is given by the summation of the quasiparticle velocity $\boldsymbol{v}_{\mathbf{k}}$ and the CVC $\Delta \boldsymbol{J}_{\mathbf{k}}$. In interacting electron systems, an excited quasiparticle induces other particle-hole excitations by collisions, and the CVC represents the current due to these particle-hole excitations. Since the CVC is ignored, the RTA frequently yields unphysical results, especially in strongly correlated systems. However, the CVC in HTSCs have not been analyzed in detail until 1999.

In the presence of strong AF fluctuations, (a) quasiparticle damping rate $\gamma_{\mathbf{k}} = 1/2\tau_{\mathbf{k}}$ becomes anisotropic, and the portion of the Fermi surface with small $\gamma_{\mathbf{k}}$ (cold spot) governs the transport phenomena [3, 4]. At the same time, (b) the total current $\mathbf{J}_{\mathbf{k}}$ becomes highly anisotropic due to large CVC [1]. Note that (a) and (b) occur simultaneously since both of them originate from the same origin; the strong backward scattering between $\mathbf{k}$ and $\mathbf{k}^*(\mathbf{k} - \mathbf{k}^* \approx \mathbf{Q})$ shown in Fig. 2.1a. Mathematically, $\gamma_{\mathbf{k}} = \mathrm{Im}\,\Sigma_{\mathbf{k}}(-i\delta)$ and the CVC are closely connected by the Ward identity near AF QCP, that is, the same vertex function $\mathcal{T}^{(0)}_{\mathbf{k},\mathbf{k}'}$ appears in Eqs. (3.71) and (3.63). Because of (a) and (b), anomalous transport phenomena in nearly AF metals are well explained in a unified way.

To demonstrate to the significance of the CVC, we calculated R_{H}, $\Delta\rho/\rho_0$, S and ν based on the FLEX (or FLEX+T-matrix) approximation by including CVCs. The obtained results semiquantitatively reproduce the various experimental facts in slightly under-doped HTSCs. The present study strongly suggests that *the striking deviation from the Fermi liquid behaviors* (*such as eqs.* (1.1)–(1.4)) *are ubiquitous in strongly correlated metals near the AF QCP, not specific to HTSCs.* Note that the increment in R_{H} is also observed in non-SC metals near AF phase, such as $V_{2-y}O_3$ [43] and $R_{2-x}Bi_xRu_2O_7$ (R = Sm or Eu) [44, 45].

We emphasize that the CVC-induced anomalous transport phenomena are also reproduced by several kinds of spin fluctuation theories. In fact, Kanki and Kontani [46] calculated $\boldsymbol{J}_{\mathbf{k}}$ based on the Millis-Monien-Pines model in Eq. (2.1), by assuming a realistic set of parameters for optimally-doped YBCO. The obtained $\boldsymbol{J}_{\mathbf{k}}$ represents the characteristic $\mathbf{k}$-dependence in nearly AF metals as shown in Fig. 3.7. As a result, it is general that R_{H} is prominently enhanced by the CVC when the AF fluctuations are strong, independent of the types of the spin fluctuation theories.

References

1. H. Kontani, K. Kanki, K. Ueda, Phys. Rev. B **59**, 14723 (1999)
2. N.E. Bickers, S.R. White, Phys. Rev. B **43**, 8044 (1991)
3. R. Hlubina, T.M. Rice, Phys. Rev. B **51**, 9253–9260 (1995)
4. B.P. Stojkovic, D. Pines, Phys. Rev. B **55**, 8576 (1997)
5. H. Kontani, K. Kanki, K. Ueda, J. Phys. Chem. Sol. **62**, 83 (2001)
6. Y. Fukuzumi, K. Mizuhashi, K. Takenaka, S. Uchida, Phys. Rev. Lett. **76**, 684 (1996)
7. M. Tsuji, J. Phys. Soc. Jpn. **13**, 979 (1958)
8. N.P. Ong, Phys. Rev. B **43**, 913 (1991)
9. Y. Nakajima, H. Shishido, H. Nakai, T. Shibauchi, K. Behnia, K. Izawa, M. Hedo, Y. Uwatoko, T. Matsumoto, R. Settai, Y. Onuki, H. Kontani, Y. Matsuda, J. Phys. Soc. Jpn. **76**, 027403 (2007)
10. J.M. Ziman, *Electrons and Phonons: The Theory of Transport Phenomena in Solids* (Oxford Classic Texts in the Physical Sciences) (Clarendon Press, Oxford, 1960)
11. H. Kontani, Phys. Rev. B **64**, 054413 (2001)
12. H. Kontani, J. Phys. Soc. Jpn. **70**, 1873 (2001)
13. A. Malinowski, Marta Z. Cieplak, S. Guha, Q. Wu, B. Kim, A. Krickser, A. Perali, K. Karpińska, M. Berkowski, C.H. Shang, P. Lindenfeld, Phys. Rev. B **66**, 104512 (2002)
14. J.M. Harris, Y.F. Yan, P. Mati, N.P. Ong, P.W. Anderson, T. Kimura, K. Kitazawa, Phys. Rev. Lett. **75**, 1391 (1995)
15. T. Kimura, S. Miyasaka, H. Takagi, K. Tamasaku, H. Eisaki, S. Uchida, K. Kitazawa, M. Hiroi, M. Sera, N. Kobayashi, Phys. Rev. B **53**, 8733 (1996)
16. A.W. Tyler, Y. Ando, F.F. Balakirev, A. Passner, G.S. Boebinger, A.J. Schofield, A.P. Mackenzie, O. Laborde, Phys. Rev. B **57**, R728 (1998)
17. Y. Nakajima, K. Izawa, Y. Matsuda, S. Uji, T. Terashima, H. Shishido, R. Settai, Y. Onuki, H. Kontani, J. Phys. Soc. Jpn. **73**, 5 (2004)
18. A. Ino, C. Kim, M. Nakamura, T. Yoshida, T. Mizokawa, A. Fujimori, Z.-X. Shen, T. Kakeshita, H. Eisaki, S. Uchida, Phys. Rev. B **65**, 094504 (2002)
19. J. Takeda, T. Nishikawa, M. Sato, Physica C **231**, 293 (1994)
20. T. Nishikawa, J. Takeda, M. Sato, J. Phys. Soc. Jpn. **63**, 1441 (1994)
21. S.D. Obertelli, J.R. Cooper, J.L. Tallon, Phys. Rev. B **46**, 14928 (1992)
22. C.P. Popoviciu, J.L. Cohn, Phys. Rev. B **55**, 3155 (1997)
23. A. Yamamoto, W.-Z. Hu, S. Tajima, Phys. Rev. B **63**, 024504 (2000)
24. A. Yamamoto, K. Minami, W.-Z. Hu, A. Miyakita, M. Izumi, S. Tajima, Phys. Rev. B **65**, 104505 (2002)
25. T. Honma, P.H. Hor, H.H. Hsieh, M. Tanimoto, Phys. Rev. B **70**, 214517 (2004)
26. T. Takemura, T. Kitajima, T. Sugaya, I. Terasaki, T. Takemura, T. Kitajima, T. Sugaya, J. Phys. Condens. Matter **12**, 6199 (2000)
27. P. Fournier, X. Jiang, W. jiang, S.N. Mao, T. Venkatesan, C.J. Lobb, R.L. Greene, Phys. Rev. B **56**, 14149 (1997)
28. G.V. Williams, R. Dupree, A. Howes, S. Kramer, H.J. Trodahl, C.U. Jung, M.-S. Park, S.-I. Lee, Phys. Rev. B **65**, 224520 (2002)
29. G. Hildebrand, T.J. Hagenaars, W. Hanke, S. Grabowski, J. Schmalian, Phys. Rev. B **56**, R4317 (1997)
30. J.M. Luttinger, Phys. Rev. A **135**, 1505 (1964)
31. M. Jonson, G.D. Mahan, Phys. Rev. B **42**, 9350 (1990)
32. G.D. Mahan, Solid State Phys. **51**, 81 (1998)
33. H. Kontani, Phys. Rev. B **67**, 014408 (2003)
34. H. Kontani, J. Phys. Soc. Jpn. **70**, 2840 (2001)
35. I. Tsukada, S. Ono, Phys. Rev. B **74**, 134508 (2006)
36. M. Abdel-Jawad, M.P. Kennett, L. Balicas, A. Carrington, A.P. Mackenzie, R.H. McKenzie, N.E. Hussey, Nat. Phys. **2**, 821 (2006)

37. M. Abdel-Jawad, J.G. Analytis, L. Balicas, A. Carrington, J.P.H. Charmant, M.M.J. French, N.E. Hussey, Phys. Rev. Lett. **99**, 107002 (2007)
38. A. Narduzzo, G. Albert, M.M.J. French, N. Mangkorntong, M. Nohara, H. Takagi, N.E. Hussey, Phys. Rev. B **77**, 220502(R) (2008)
39. W. Kohn, Phys. Rev. **123**, 1242 (1961)
40. Y. Takada, T. Ando, J. Phys. Soc. Jpn. **44**, 905 (1978)
41. K. Kanki, K. Yamada, J. Phys. Soc. Jpn. **66**, 1103 (1997)
42. T.P. Devereaux, A.P. Kampf, Phys. Rev. B **59**, 6411 (1999)
43. T.F. Rosenbaum, A. Husmann, S.A. Carter, J.M. Honig, Phys. Rev. B **5**(7), R13997 (1998)
44. S. Yoshii, K. Murata, M. Sato, J. Phys. Soc. Jpn. **69**, 17 (2000)
45. S. Yoshii, K. Murata, M. Sato, J. Phys. Chem. Solids **62**, 129 (2001)
46. K. Kanki, H. Kontani, J. Phys. Soc. Jpn. **68**, 1614 (1999)

Chapter 6
Transport Phenomena in HTSCs Below T^*

6.1 Mechanism of Pseudo-Gap Phenomena: Suppression of ρ, R_H and S Below T^*

In cuprate HTSCs, the DOS [1–4], Knight shift [5–7] and uniform susceptibility [8, 9] starts to decrease below $T_0 \sim 700\,\mathrm{K}$, corresponding to the growth of AF fluctuations. The weak pseudo-gap in the DOS is shallow and wide in energy. These "weak pseudo-gap behaviors" are reproducible in the FLEX approximation, although the obtained gap behaviors are rather moderate because of the fully self-consistent determination of the self-energy and the Green function. (The weak pseudo-gap in the DOS is prominent at the first iteration stage of the FLEX.) Mathematically, this too strong feedback effect in the fully self-consistent calculation should be canceled by the vertex correction in the self-energy.

In under-doped HTSCs, a deep pseudo-gap in the DOS emerges below $T^* \sim 200\,\mathrm{K}$; see Fig. 1.2. The origin of this "strong pseudo-gap" has been a central issue with regard to HTSCs. It does not originate from the spin fluctuations since the strength of the spin fluctuations decrease below T^* [5, 10–13]. According to early ARPES measurements [14–17], the $\mathbf{k}$-dependence of the pseudo-gap around the cold spot coincides with that of the $d_{x^2-y^2}$-wave SC gap function. This pseudo-gap structure in the quasiparticle spectrum $\rho(\mathbf{k},\omega) = \mathrm{Im}G(\mathbf{k},\omega - i\delta)/\pi$ starts to appear below T^*. Below T_c, the quasiparticle spectrum shows sharp peaks at the edge of the SC gap ($\omega \sim \Delta$) since the inelastic scattering is reduced by the SC gap. At the same time, a dip-hump structure is induced around ω_d ($\gtrsim \Delta$) by the strong resonance peak in $\mathrm{Im}\chi^s(\omega)$ at $\omega_r \sim 40\,\mathrm{meV}$ in YBCO and $Bi_2Sr_2CaCu_2O_8$ (BSCCO). Note that $\omega_d \approx \Delta + \omega_r$ and $\omega_r < 2\Delta$ (resonance condition).

Motivated by these experimental facts, various strong-coupling theories of SC fluctuations have been studied to reproduce the pseudo-gap phenomena [18–24]. Several groups developed the "FLEX + T-matrix theory", where the normal self-energy correction induced by the strong SC fluctuations, $\Sigma_{\mathbf{k}}^{\mathrm{SCF}}(\epsilon)$, has been self-consistently included into the FLEX approximation. The SC "amplitude" fluctuations are given by the ladder-type T-matrix (=particle-particle scattering amplitude by AF fluctuations),

H. Kontani, *Transport Phenomena in Strongly Correlated Fermi Liquids*,
Springer Tracts in Modern Physics 251, DOI: 10.1007/978-3-642-35365-9_6,

which greatly increase below T^*. The T-matrix due to the Thouless instability for the $d_{x^2-y^2}$-channel is given by

$$T_{\mathbf{k},\mathbf{k}';\mathbf{q}}(\epsilon_n,\epsilon_{n'};\omega_l) = V^{\mathrm{AFF}}_{\mathbf{k}-\mathbf{p}}(\epsilon_n-\epsilon_{n'}) + T\sum_{m,\mathbf{p}} V^{\mathrm{AFF}}_{\mathbf{k}-\mathbf{k}'}(\epsilon_n-\epsilon_m) \times G_{\mathbf{p}}(\epsilon_m)G_{-\mathbf{p}+\mathbf{q}}(-\epsilon_m+\omega_l)T_{\mathbf{p},\mathbf{k}';\mathbf{q}}(\epsilon_m,\epsilon_{n'};\omega_l), \tag{6.1}$$

which is shown in Fig. 6.1a. $V^{\mathrm{AFF}}_{\mathbf{k}}$ is given in Eq. (2.14). In the FLEX + T-matrix approximation, the Green function and the self-energy are given by

$$G_{\mathbf{k}}(\epsilon_n) = [i\epsilon_n+\mu-\epsilon^0_{\mathbf{k}}-\Sigma^{\mathrm{AFF}}_{\mathbf{k}}(\epsilon_n)-\Sigma^{\mathrm{SCF}}_{\mathbf{k}}(\epsilon_n)]^{-1}, \tag{6.2}$$

$$\Sigma^{\mathrm{AFF}}_{\mathbf{k}}(\epsilon_n) = \text{Eq. (2.13)},$$

$$\Sigma^{\mathrm{SCF}}_{\mathbf{k}}(\epsilon_n) = T\sum_{\mathbf{q},l} G_{-\mathbf{k}+\mathbf{q}}(-\epsilon_n+\omega_l)T_{\mathbf{k},\mathbf{k};\mathbf{q}}(\epsilon_n,\epsilon_n;\omega_l), \tag{6.3}$$

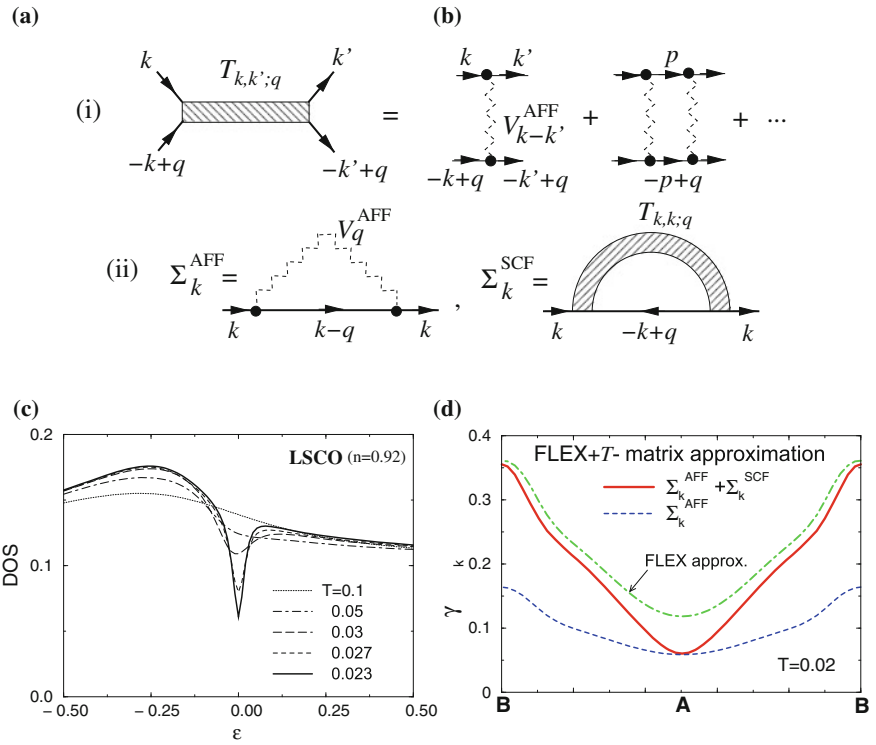

Fig. 6.1 **a** T-matrix induced by the AF fluctuations. **b** Self-energy $\Sigma_{\mathbf{k}}(\omega)$ in the FLEX + T-matrix approximation. **c** DOS given by the FLEX + T-matrix approximation. The pseudo-gap appears below $T^* \sim 0.04$ due to the strong SC fluctuations. d $\mathrm{Im}\Sigma^{\mathrm{AFF}}_{\mathbf{k}}(-i\delta)$ and $\mathrm{Im}\Sigma^{\mathrm{SCF}}_{\mathbf{k}}(-i\delta)$ given by the FLEX + T-matrix approximation at $T = 0.02$. For comparison, $\mathrm{Im}\Sigma_{\mathbf{k}}(-i\delta)$ in the FLEX approximation at $T = 0.02$ is also shown

where $\Sigma_{\mathbf{k}}^{\mathrm{AFF}}$ and $\Sigma_{\mathbf{k}}^{\mathrm{SCF}}$ are shown in Fig. 6.1b. The quasiparticle damping rate is $\gamma_{\mathbf{k}} = \mathrm{Im}\{\Sigma_{\mathbf{k}}^{\mathrm{AFF}}(-i\delta) + \Sigma_{\mathbf{k}}^{\mathrm{SCF}}(-i\delta)\}$. In the FLEX+$T$-matrix approximation, we solve Eqs. (2.13), (2.14), and (6.1)–(6.3) self-consistently. However, it is difficult to calculate Eq. (6.1) since a lot of memory in computer is required. Fortunately, Eq. (6.1) can be simplified by considering only the $d_{x^2-y^2}$-channel and drop other pairing channels as $T_{\mathbf{k},\mathbf{k}';\mathbf{q}}(\epsilon_n, \epsilon_{n'}; \omega_l) \approx \psi_{\mathbf{k}}(\epsilon_n)\psi_{\mathbf{k}'}(\epsilon_{n'})t_{\mathbf{q}}(\omega_l)$, where $\psi_{\mathbf{k}} \propto \cos k_x - \cos k_y$ [21, 23, 24]. This approximation would be reasonable for $T \gtrsim T_{\mathrm{c}}$ in HTSCs. Then, the $\mathbf{k}$-dependence of $\Sigma_{\mathbf{k}}^{\mathrm{SCF}}$ becomes $\Sigma_{\mathbf{k}}^{\mathrm{SCF}} \propto T_{\mathbf{k},\mathbf{k};\mathbf{q}} \propto \psi_{\mathbf{k}}^2$.

In the present approximation, T^* is defined as the temperature below which $\Sigma_{\mathbf{k}}^{\mathrm{SCF}}$ takes a considerable value. T^* is slightly greater than the $T_{\mathrm{c}}^{\mathrm{FLEX}}$ given in the FLEX approximation. Although FLEX + T-matrix theory satisfies the Mermin-Wagner-Hohenberg theorem, finite T_{c} is obtained when weak three-dimensionality is assumed. Sufficiently above T^*, the FLEX + T-matrix theory is equivalent to the FLEX approximation since $\Sigma_{\mathbf{k}}^{\mathrm{SCF}} \approx 0$. The obtained DOS and the self-energy are shown in Fig. 6.1c, d, respectively. Below $T^* \sim 0.04$, a strong pseudo-gap structure appears in the FLEX + T-matrix approximation, due to the cooperation of the real part and the imaginary part of $\Sigma_{\mathbf{k}}^{\mathrm{SCF}}$ [24]. Since AF fluctuations are suppressed below T^* due to the pseudo-gap in the DOS, the obtained $\mathrm{Im}\Sigma_{\mathbf{k}}^{\mathrm{AFF}}(0)$ is much smaller than $\mathrm{Im}\Sigma_{\mathbf{k}}(0)$ given by the FLEX approximation, as recognized in Fig. 6.1d. Below T_{c}, the strong pseudo-gap in the FLEX + T-matrix approximation smoothly changes to the SC gap [18].

Here, we discuss transport phenomena in the pseudo-gap region: In YBCO [25, 26], Bi2201 and Bi2212 [27], R_{H} shows a maximum around the pseudo-gap temperature T^*, at which $1/T_1T$ shows the maximum value. Also, the peak temperature of S is nearly equal to T^* in $HgBa_2CuO_{4+\delta}$ [28, 29], LSCO, YBCO [30] and $Bi_2Sr_2RCu_2O_8$ (R = Ca, Y, Pr, Dy and Er) [31]. As discussed in Ref. [32], these behaviors are naturally understood since both of them are strikingly enhanced by the AF fluctuations above T^*. Therefore, *both R_{H} and S should decrease below T^* in accordance with the reduction in the AF fluctuation* [32]. The obtained ρ, R_{H} and S for hole-doped systems by using the [FLEX + T-matrix]+CVC method are shown in Figs. 5.2a, 5.3a, and 5.6a, respectively. In this approximation, the Bethe-Salpeter equation is given as

$$\boldsymbol{J}_{\mathbf{k}}(\epsilon) = \boldsymbol{v}_{\mathbf{k}}(\epsilon) + \sum_{\mathbf{k}'} \int \frac{d\epsilon'}{4\pi i} \mathcal{T}_{\mathbf{k},\mathbf{k}'}^{(0)}(\epsilon, \epsilon')|G_{\mathbf{k}'}^{\mathrm{R}}(\epsilon')|^2 \boldsymbol{J}_{\mathbf{k}'}(\epsilon'), \tag{6.4}$$

where the kernel function is $\mathcal{T}_{\mathbf{k},\mathbf{k}'}^{(0)}(\epsilon, \epsilon') = i\left[\mathrm{cth}\frac{\epsilon'-\epsilon}{2T} + \mathrm{th}\frac{\epsilon'}{2T}\right]\mathrm{Im}\{V_{\mathbf{k}-\mathbf{k}'}(\epsilon - \epsilon') - T_{\mathbf{k},\mathbf{k};\mathbf{k}-\mathbf{k}'}(\epsilon, \epsilon; \epsilon - \epsilon')\}$, and $T_{\mathbf{k},\mathbf{k};\mathbf{k}-\mathbf{k}'}$ represents the T-matrix defined in Eq. (6.1). The detailed method of calculation is explained in Ref. [24].

As shown in Figs. 5.3a and 5.6a, both R_{H} and S start to decrease below $T^* \sim 0.04$ ($\sim$160 K), consistently with experiments [28–30]. Figure 5.2a shows the resistivity given by the FLEX approximation and the FLEX + T-matrix approximation, both of which are given by including CVCs. As pointed out in Ref. [33], ρ given by the

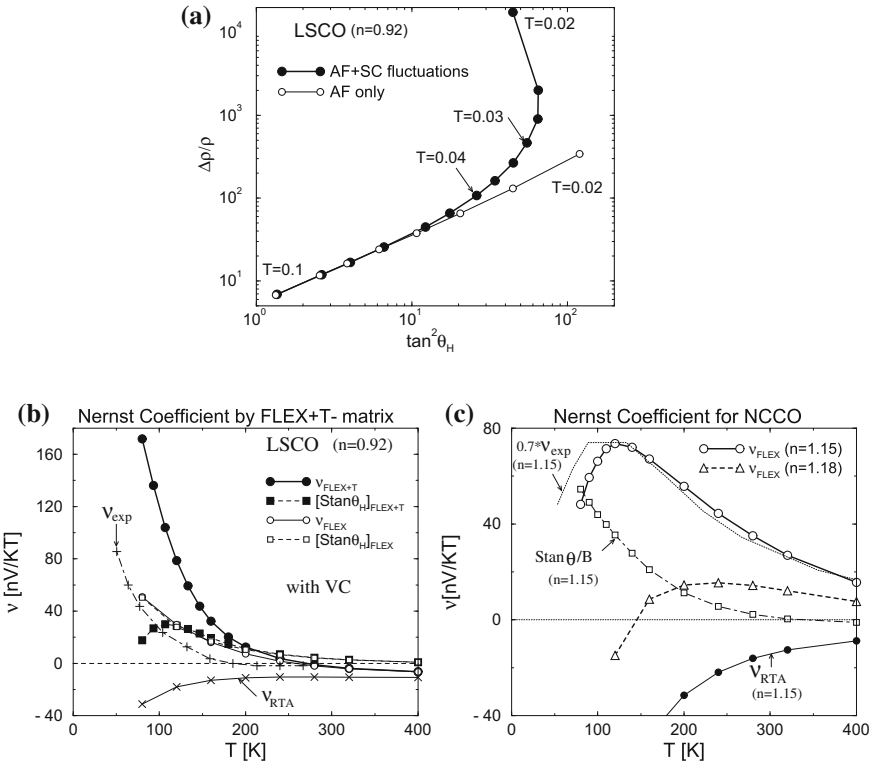

Fig. 6.2 **a** $\Delta\rho/\rho_0$ for LSCO in the [FLEX+T-matrix]+CVC; The modified Kohler's rule $\Delta\rho/\rho_0 \propto \tan^2\theta_H$ holds above T^*. Below $T^* \sim 0.04\,(\sim 160)$ K, modified Kohler's rule is violated since $\Delta\rho/\rho_0$ increases quite drastically that is caused by the CVC due to AF+SC fluctuations. **b** ν for LSCO in the [FLEX+T-matrix]+CVC; the abrupt increase in ν below T^* is caused by the CVC due to AF+SC fluctuations. Experimental data $\nu_{\rm exp}$ is cited from [38–40]. **c** ν for NCCO obtained by the FLEX+CVC approximation. Experimental data $\nu_{\rm exp}$ is cited from [41]. (Reference [42])

FLEX+CVC method shows a tiny "kink" structure at $T_0 \sim 0.12$, actually observed in LSCO [34] and YBCO [35]. In addition, large kink structure appears at T^* in the [FLEX + T-matrix]+CVC method, since the inelastic scattering is reduced by the formation of the strong pseudo-gap. As shown in Fig. 6.1d, $\mathrm{Im}\Sigma_{\mathbf{k}}^{\rm AFF}(0)$ decreases quickly below T^*, in accordance with the emergence of $\mathrm{Im}\Sigma_{\mathbf{k}}^{\rm SCF}(0)$. As a result, $\rho \sim T^2$ below T^*. To summarize, ρ, $R_{\rm H}$ and S are suppressed in the pseudo-gap region.

In the FLEX + T-matrix theory, the SC "amplitude" fluctuations is the origin of the pseudo-gap formation. Other than this scenario, various mechanisms of pseudo-gap formation have been proposed. For example, Kivelson and Emery proposed the SC "phase" fluctuation scenario [36]: they considered that the amplitude of the SC order-parameter develops in the pseudo-gap region, whereas the global phase coherence is absent. Moreover, several hidden-order scenarios, such as d-density

wave formation [37], have been proposed. To elucidate the correct scenario, study of anomalous transport phenomena in the pseudo-gap region is very significant. In the following, we show that the SC "amplitude" fluctuations scenario enables us to understand the anomalous transport phenomena below T^* in a unified way.

6.2 Enhancement of Nernst Coefficient and Magnetoresistance Below T^*

In contrast to $R_{\rm H}$ and S, the Nernst coefficient ν strongly increases in the pseudo-gap region by approximately 100 times than that in conventional metals [38–40, 43, 44]. The modified Kohler's rule in Eq. (5.19) violates in the pseudo-gap region, since the magnetoresistance $\Delta\rho/\rho_0$ increases faster than T^{-4} [45, 46]. Such nontrivial behaviors of ν and $\Delta\rho/\rho_0$ have attracted considerable attention as a key phenomenon closely related to the origin of the pseudo-gap.

Here, we study the Nernst coefficient. The definition of ν is $\nu \equiv S_{yx}/H_z = -E_y/H_z\nabla_x T$, which is the off-diagonal thermoelectric power under a magnetic field. According to the linear response theory [47–50], ν is given by

$$\nu = \left[\alpha_{xy}/\sigma_{xx} - S\sigma_{xy}/\sigma_{xx}\right]/H_z, \tag{6.5}$$

where $\alpha_{xx} = j_x/(-\nabla_x T)$, and $\alpha_{xy} = j_x/(-\nabla_y T)$ is the off-diagonal Peltier conductivity under the magnetic field H_z. (In the RTA, $\alpha_{xx} = (-e/T)K^1_{xx}$ in Eq. (3.14).) In conventional metals with simple Fermi surfaces, ν is small because of an approximate cancellation between the first and the second terms in Eq. (6.5), which is known as the Sondheimer cancellation. (This cancellation is perfect only when $\epsilon^0_{\mathbf{k}} = k^2/2m$.) In HTSCs, however, Sondheimer cancellation does not occur since α_{xy} is considerably enhanced. That is, α_{xy} is the origin of giant Nernst coefficient in LSCO below T^* and in NCCO below T_0 [38–40, 43].

In this study, we investigate α_{xy} due to the quasiparticle transport, and find that α_{xy} is prominently enhanced below T^* if we include the CVC caused by SC and AF fluctuations. As a result, $\nu \approx \alpha_{xy}/\sigma_{xx}$ takes a large value below T^*. Moreover, we show that all the transport anomalies below T^* are understood as the quasiparticle transport phenomena in a unified way. Although the Maki-Thompson-type CVC due to SC fluctuations is unimportant in d-wave superconductors when the elastic scattering is dominant [51], it plays significant roles when the inelastic scattering is dominant like in cuprates.

We note that Ussishkin et al. studied ν induced by short-lived Cooper pairs, which is independent of the quasiparticle lifetime and order $O(\gamma^0)$ [52]. However, the quasiparticle transport will be dominant in good metals where $k_{\rm F}l \sim E_{\rm F}/\gamma \gg 1$. Here, $l = v_{k_{\rm F}}\tau$ is the mean free path, and $k_{\rm F}l = 1$ corresponds to 1700 $\mu\Omega$cm in cuprate HTSCs. Therefore, the relation $k_{\rm F}l \gg 1$ is satisfied in slightly under-doped HTSC,

in which $\rho \lesssim 200\,\mu\Omega$cm above T_c. Hereafter, we calculate α_{xy} due to quasiparticle transport by considering the CVC.

In the microscopic Fermi liquid theory, a_{xy} is given by the correlation function between the heat and charge currents in the presence of $H_z \neq 0$. Therefore, a_{xy} is given by Eq. (3.44) by replacing j_μ with j_μ^Q. After the analytic continuation, the exact expression for α_{xy} of the order γ^{-2} is given by [50]

$$\alpha_{xy} = H_z \cdot \frac{e^2}{T} \sum_{\mathbf{k}} \int \frac{d\epsilon}{2\pi} \left(-\frac{\partial f^0}{\partial \epsilon} \right) |\mathrm{Im} G_{\mathbf{k}}^{\mathrm{R}}(\epsilon)| |G_{\mathbf{k}}^{\mathrm{R}}(\epsilon)|^2 \times |\boldsymbol{v}_{\mathbf{k}}(\epsilon)| \gamma_{\mathbf{k}}(\epsilon) A_{\mathbf{k}}(\epsilon), \tag{6.6}$$

$$A_{\mathbf{k}}(\epsilon) = \left(\boldsymbol{Q}_{\mathbf{k}}(\epsilon) \times \frac{\partial \boldsymbol{L}_{\mathbf{k}}(\epsilon)}{\partial k_\parallel} \right)_z, \tag{6.7}$$

$$\boldsymbol{Q}_{\mathbf{k}}(\epsilon) = \boldsymbol{q}_{\mathbf{k}}(\epsilon) + \sum_{\mathbf{k}'} \int \frac{d\epsilon'}{4\pi i} \mathcal{T}_{\mathbf{k},\mathbf{k}'}^{(0)}(\epsilon, \epsilon') |G_{\mathbf{k}'}^{\mathrm{R}}(\epsilon')|^2 \boldsymbol{Q}_{\mathbf{k}'}(\epsilon'), \tag{6.8}$$

where $\boldsymbol{L}_{\mathbf{k}}(\epsilon) = \boldsymbol{J}_{\mathbf{k}}(\epsilon)/\gamma_{\mathbf{k}}(\epsilon)$, $\boldsymbol{q}_{\mathbf{k}}(\epsilon) = \epsilon \cdot \boldsymbol{v}_{\mathbf{k}}$ is the quasiparticle heat velocity, and $\boldsymbol{Q}_{\mathbf{k}}(\epsilon)$ is the total heat current [24, 50]. Since the CVC term in Eq. (6.8) vanishes if we omit the energy dependence of $\mathcal{T}_{\mathbf{k},\mathbf{k}'}^{(0)}(\epsilon, \epsilon')$, the CVC for $\boldsymbol{Q}_{\mathbf{k}}(\epsilon)$ is expected to be unimportant. Therefore, $\boldsymbol{Q}_{\mathbf{k}}(\epsilon) \sim \boldsymbol{q}_{\mathbf{k}}(\epsilon)$ [24, 50]. In the FLEX + T-matrix approximation, $\mathcal{T}_{\mathbf{k},\mathbf{k}'}^{(0)}(\epsilon, \epsilon') = i \left[\mathrm{cth}\frac{\epsilon'-\epsilon}{2T} + \mathrm{th}\frac{\epsilon'}{2T} \right] \mathrm{Im}\{V_{\mathbf{k}-\mathbf{k}'}(\epsilon - \epsilon') - T_{\mathbf{k},\mathbf{k};\mathbf{k}-\mathbf{k}'}(\epsilon, \epsilon; \epsilon - \epsilon')\}$.

In contrast to R_{H} and S, the Nernst coefficient ν [38–40, 43] and $\Delta\rho/\rho_0$ [45, 46, 53] in LSCO rapidly increase below T^*. These facts are also explained by the [FLEX + T-matrix]+CVC method as shown in Fig. 6.2a, b. Since R_{H} decreases whereas $\Delta\rho/\rho_0$ increases drastically below T^*, the plot of $\Delta\rho/\rho_0$ as a function of $\tan^2\theta_{\mathrm{H}}$ forms an "inverse S-shape", which results in the violation of the modified Kohler's rule below T^*. This result is very similar to the experimental results provided in Ref. [53].

Next, we discuss ν in NCCO using the FLEX (not FLEX + T-matrix) approximation since the pseudo-gap is not observed in NCCO. The obtained ν is shown in Fig. 6.2c; it takes a large positive value only when the CVC are taken into account. In NCCO, ν increases gradually as T decreases, and it starts to decrease below ∼120 K. The obtained behaviors of ν are semiquantitatively consistent with experimental results [41]. Therefore, the present study can explain the experimental behaviors of ν and $\Delta\rho/\rho_0$ in HTSCs both above and below T^*.

Here, we explain a theoretical reason why ν is enhanced in both LSCO and NCCO: $A_{\mathbf{k}}$ in Eq. (6.7) can be rewritten as

$$A_{\mathbf{k}} = Q_{\mathbf{k}} L_{\mathbf{k}} (\partial\theta_{\mathbf{k}}^J/\partial k_\parallel) \cos(\theta_{\mathbf{k}}^J - \theta_{\mathbf{k}}^Q) + Q_{\mathbf{k}} (\partial L_{\mathbf{k}}/\partial k_\parallel) \sin(\theta_{\mathbf{k}}^J - \theta_{\mathbf{k}}^Q), \tag{6.9}$$

where $\theta_{\mathbf{k}}^J = \tan^{-1}(J_{\mathbf{k}y}/J_{\mathbf{k}x})$, $\theta_{\mathbf{k}}^Q = \tan^{-1}(Q_{\mathbf{k}y}/Q_{\mathbf{k}x})$, and $L_{\mathbf{k}} = J_{\mathbf{k}}/\gamma_{\mathbf{k}}$ is the mean free path with CVC. In the RTA, the heat current is given by $\boldsymbol{q}_{\mathbf{k}} = \epsilon \cdot \boldsymbol{v}_{\mathbf{k}}$. Since $\theta_{\mathbf{k}}^v = \theta_{\mathbf{k}}^q$, the second term is absent in the RTA. If the CVC is taken into account,

we obtain $\theta^J_{\mathbf{k}} \neq \theta^Q_{\mathbf{k}}$ since the CVC for $\boldsymbol{q}_{\mathbf{k}}$ is usually small (i.e., $\boldsymbol{Q}_{\mathbf{k}} \sim \boldsymbol{q}_{\mathbf{k}}$) [24, 50]: As we have explained, the CVC represents the current of the excited quasiparticles induced by electron-electron scatterings. The charge CVC can be large because of the momentum conservation law. However, the heat current $\boldsymbol{q}_{\mathbf{k}} = (\epsilon^0_{\mathbf{k}} - \mu)\boldsymbol{v}_{\mathbf{k}}$ is not conserved even in the free dispersion model, that is, $\boldsymbol{q}_{\mathbf{k}} + \boldsymbol{q}_{\mathbf{k}'} \neq \mathbf{q}_{\mathbf{k}+\mathbf{q}} + \mathbf{q}_{\mathbf{k}'-\mathbf{q}}$ even if $\epsilon^0_{\mathbf{k}} + \epsilon^0_{\mathbf{k}'} = \epsilon^0_{\mathbf{k}+\mathbf{q}} + \epsilon^0_{\mathbf{k}'-\mathbf{q}}$. For this reason, the heat CVC is small in general, and therefore the thermal conductivity κ is finite even if the Umklapp process is absent: In a 3D free dispersion model, $\kappa = (9/8)\kappa^{\mathrm{RTA}}$ within the second-order perturbation theory with respect to U [50].

Since $\theta^J_{\mathbf{k}} \neq \theta^Q_{\mathbf{k}}$, the second term gives rise to an enhancement of ν if $L_{\mathbf{k}}$ is highly anisotropic around the cold spot. Figure 5.1b shows $L_{\mathbf{k}}$ in LSCO given by the FLEX + CVC approximation, showing that $\partial L_{\mathbf{k}}/\partial k_{\parallel}$ takes a large value near the cold spot below $T = 0.02$. (Note that $\partial L_{\mathbf{k}}/\partial k_{\parallel} = 0$ just at point A.) This is the origin of increment in ν_{FLEX} in Fig. 6.2b. As shown in Fig. 6.2c, ν_{FLEX} for NCCO is much larger than ν_{FLEX} for LSCO, because of the large anisotropy of $L^{\mathrm{FLEX}}_{\mathbf{k}}$ in NCCO due to the relation $\xi_{\mathrm{AF}} \gg 1$ in NCCO.

Next, we consider the increment of ν in the pseudo-gap region in LSCO using the FLEX + T-matrix method, shown as ν_{FLEX} + T in Fig. 6.2b. The CVC due to SC fluctuations (Maki-Thompson term) represents the forward scattering caused by the short-lived Cooper pairs. The CVC due to the $d_{x^2-y^2}$-wave SC fluctuations magnifies $J_{\mathbf{k}}$ except at the nodal point (point A in Fig. 3.7). When the Ginzburg-Landau correlation length, which is proportional to $(T - T_{\mathrm{c}})^{-1/2}$, is longer than ξ_{AF}, the Bethe-Salpeter equation (6.4) in the FLEX + T-matrix approximation is approximately given as [24]

$$\boldsymbol{J}_{\mathbf{k}} \approx \boldsymbol{v}_{\mathbf{k}} + \sum_{\mathbf{k}'} \int \frac{d\epsilon'}{4\pi i} \mathcal{T}^{\mathrm{FLEX}}_{\mathbf{k},\mathbf{k}'}(0,\epsilon') |G^{\mathrm{R}}_{\mathbf{k}'}(\epsilon')|^2 \boldsymbol{J}_{\mathbf{k}'} + \frac{\mathrm{Im}\,\Sigma^{\mathrm{SCF}}_{\mathbf{k}}(-i\delta)}{\gamma_{\mathbf{k}}} \boldsymbol{J}_{\mathbf{k}} \tag{6.10}$$

where $\mathcal{T}^{\mathrm{FLEX}}_{\mathbf{k},\mathbf{k}'}(0,\epsilon')$ represents the Maki-Thompson term due to AF fluctuations. The last term comes from the Maki-Thompson term due to SC fluctuations, which produces the forward scattering. Then, the total current is approximately obtained as

$$\boldsymbol{J}_{\mathbf{k}} \approx (1 + h_{\mathbf{k}})\, \boldsymbol{J}^{\mathrm{no-SCF}}_{\mathbf{k}} \tag{6.11}$$

$$h_{\mathbf{k}} \equiv \mathrm{Im}\,\Sigma^{\mathrm{SCF}}_{\mathbf{k}}(0)/\mathrm{Im}\,\Sigma^{\mathrm{AFF}}_{\mathbf{k}}(0), \tag{6.12}$$

where $\boldsymbol{J}^{\mathrm{no-SCF}}_{\mathbf{k}}$ is given by the FLEX approximation without $\Sigma^{\mathrm{SCF}}_{\mathbf{k}}$ and $\mathcal{T}^{\mathrm{SCF}}$. That is, $\boldsymbol{J}^{\mathrm{no-SCF}}_{\mathbf{k}} \approx \dfrac{\boldsymbol{v}_{\mathbf{k}} + \alpha_{\mathbf{k}}\boldsymbol{v}_{\mathbf{k}^*}}{1 - \alpha^2_{\mathbf{k}}}$, where $\alpha_{\mathbf{k}} = (1 - c\xi^{-2}_{\mathrm{AF}})$ had been introduced in Eq. (3.80). $h_{\mathbf{k}}$ represents the enhancement factor due to SC fluctuations. Due to $h_{\mathbf{k}}$, the anisotropy of $L_{\mathbf{k}} = |\boldsymbol{J}_{\mathbf{k}}/\gamma_{\mathbf{k}}|$ becomes very large below T^* near the cold spot, because of the development of $\mathrm{Im}\,\Sigma^{\mathrm{SCF}}_{\mathbf{k}}(0) \propto \psi^2_{\mathbf{k}}$ below T^* shown in Fig. 6.1d. For this reason,

the second term in Eq. (6.9) takes a large value in the neighborhood of the point A [24]. Therefore, the rapid increment in ν below T^* is well understood based on the [FLEX + T-matrix]+CVC theory.

If the AF fluctuations are absent, $\theta_{\mathbf{k}}^J = \theta_{\mathbf{k}}^Q = \theta_{\mathbf{k}}^v$ even if the CVC due to SC fluctuations are taken into account. Therefore, to explain the enhancement in ν in the pseudo-gap region, we have to include CVCs due to both spin and SC fluctuations. In contrast, R_{H} decreases below T^* in proportion to ξ_{AF}^2 since the second term in Eq. (6.9) is absent if we replace $\boldsymbol{Q}_{\mathbf{k}}$ with $\boldsymbol{J}_{\mathbf{k}}$.

6.3 Fermi Arc Picture and Transport Phenomena

Figure 6.3 shows the intensity of the spectrum $\rho_{\mathbf{k}}(\omega) = \mathrm{Im}G_{\mathbf{k}}(\omega - i\delta)/\pi$ at $\omega = 0$ given by the FLEX and FLEX+T-matrix approximations for LSCO ($n = 0.9$), at $T = 0.02 \sim 80\,\mathrm{K}$. The intensity of $\rho_{\mathbf{k}}(0)$ at around $(\pi, 0)$ is suppressed in the FLEX approximation, which is called the *Fermi arc structure*. This structure becomes more prominent in the FLEX + T-matrix approximation, because the quasiparticle damping rate due to strong $d_{x^2-y^2}$-wave SC fluctuations, which is given in Eq. (6.3) in the FLEX + T-matrix approximation, takes large values around $(\pi, 0)$. The Fermi arc structure is observed by ARPES measurements in many compounds, such as Bi2212 [16, 54–56] and LSCO [57].

The Fermi arc structure is also observed in under-doped NCCO: In the ARPES measurements [58, 59], the intensity of $\rho_{\mathbf{k}}(0)$ for a portion of the Fermi surface near the AFBZ (see Fig. 2.1) is strongly suppressed below $T_{\mathrm{N}} \sim 150$ K by the SDW order. Below T_{N}, R_{H} is negative by reflecting the small electron-like Fermi surface around $(\pi, 0)$, which is caused by the reconstruction of the Fermi surface due to the SDW order. Surprisingly, R_{H} remains negative even above T_{N}, although SDW-induced Fermi surface reconstruction is absent. Moreover, no anomaly in R_{H} is observed at T_{N}. This highly nontrivial fact is explained by the Fermi liquid theory by considering

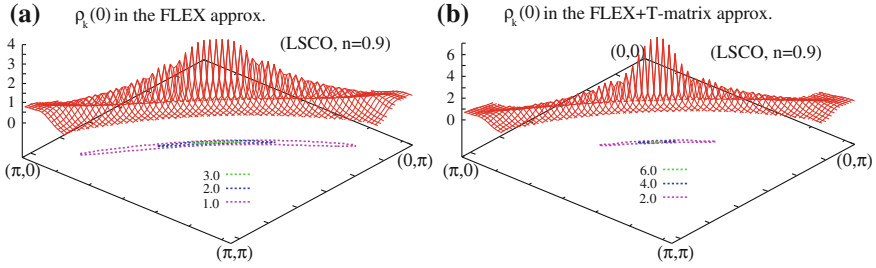

Fig. 6.3 **a** Quasiparticle spectrum $\rho_{\mathbf{k}}(0) = \mathrm{Im}G_{\mathbf{k}}(-i\delta)/\pi$ for LSCO at $T = 0.02$ given by the FLEX approximation. $\rho_{\mathbf{k}}(0)$ is shown only when $\rho_{\mathbf{k}}(0) > 0.1$. The contour is shown on the basal plane. **b** $\rho_{\mathbf{k}}(0)$ given by the FLEX + T-matrix approximation. The contour shows a "Fermi arc structure"

the CVC, as shown in Fig. 5.3d. In NCCO, pseudo-gap state due to AF fluctuations is observed above T_N by ARPES measurements [60].

It is sometimes claimed that the enhancement of R_H in HTSC can be explained by the reduction in the "effective carrier density at the Fermi level (n_{eff})" due to the emergence of the Fermi arc, since $R_H \propto 1/en_{eff}$ in the RTA. However, this argument is not true since R_H starts to decrease below T^*, whereas the length of the Fermi arc shrinks due to SC fluctuations. We have explained in Sect. 6.1 that the reduction in R_H in the pseudo-gap region is closely related to the reduction in the AF fluctuations.

If the distinct Fermi arc structure due to the highly anisotropic $\tau_{\mathbf{k}}$ is realized, it inevitably leads to a huge magnetoresistance within the RTA: in fact, $\Delta\sigma_{xx}$ diverges when the $\mathbf{k}$-dependence of the mean free path $l_{\mathbf{k}} = v_{\mathbf{k}}\tau_{\mathbf{k}}$ is not continuous on the Fermi surface; in this case, the second term in Eq. (5.12) diverges as pointed out in Ref. [61]. Therefore, the modified Kohler's rule given by Eq. (1.4) cannot be satisfied. In summary, a unified understanding of anomalous transport phenomena in HTSC cannot be achieved by the simple Fermi arc picture without the CVC.

6.4 Summary and Future Problems

We have studied ρ, R_H, $\Delta\rho/\rho_0$, S and ν in HTSCs using the FLEX + T-matrix approximation. The results are shown in Figs. 5.2a, 5.3a, 5.6a, and 6.2a–b. We can explain that (i) R_H and S start to decrease below T^*, (ii) ρ starts to deviate from the T-linear behavior at T_0, and it is approximately proportional to T^2 below T^*. Moreover, (iii) ν and $\Delta\rho/\rho$ further increase below T^*. [The RTA cannot explain the enhancement of ν since the second term in Eq. (6.9) vanishes identically in the RTA.] Therefore, the present study gives us a unified understanding of the various anomalous transport phenomena in both below and above T^*.

In NCCO (and CeMIn$_5$), ν starts to increase in proportion to T^{-1} below $T_0 \sim 600$ K, because of the CVC due to strong AF fluctuations; $\xi_{AF} \gg 1$. In LSCO, on the other hand, increment in ν below T_0 is small since ξ_{AF} is of order 1; ν in LSCO starts to increase rapidly below $T^* \ll T_0$, with the aid of the strong SC fluctuations. It should be noted that ν takes a very large value in the vortex-liquid state above H_{c1} in a clean 2D sample, reflecting the high mobility of the vortices. Therefore, ν is frequently used as a sensitive probe for the mixed state. Based on his observation, Ong *et al.* proposed that spontaneous vortex-antivortex pairs emerge in under-doped systems below T^*, and they govern the transport phenomena in the pseudo-gap region [38–40]. However, this assumption seems to contradict with the other transport coefficients; for example, the flux-flow resistance does not appear below T^*.

Finally, we comment on the recent experimental progress on the origin of the pseudo-gap phenomena. For example, Hanaguri et al. found the formation of the checker board pattern in lightly hole-doped $Ca_{2-x}Na_xCuO_2Cl_2$ by the STM/STS measurements [63] Also, Kondo et al. [64] and Yoshida et al. [62, 65] performed the ARPES measurement for under-doped cuprates, and found a strong deviation of

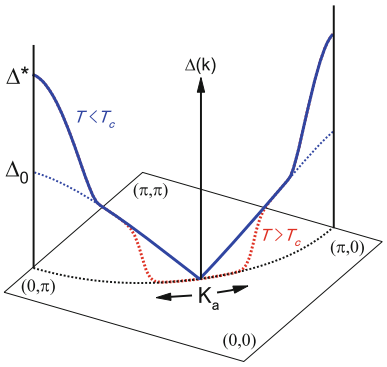

Fig. 6.4 Schematic picture of the energy gap on the Fermi surface of under-doped HTSCs. Near the nodal region, the **k**-dependence of the pseudo-gap is simple d-wave type, and it merges to the SC gap below T_c, validating the SC fluctuation scenario. Near the anti-nodal region, the pseudo-gap is much larger than the SC gap size, and it exist even below T_c. (Ref. [62])

the pseudo-gap from a simple d-wave form. It is found that the pseudo-gap near the node (Fermi arc) originates from the SC fluctuations, whereas that near the anti-nodal region is different in origin, since the energy-scale of the gap is very large, as shown in Fig. 6.4. Since the large pseudo-gap near the anti-nodal region exists even below T_c, its origin might be unconventional density order.

In summary, there are many evidences that the SC fluctuations play important roles in the pseudo-gap region, at least near the nodal region (or the cold spot). The transport phenomena are determined by the electronic states near the nodal region, whereas insensitive to the anti-nodal region. In this section, we have shown that characteristic anomalous transport phenomena in the pseudo-gap region can be reproduced by the FLEX + T-matrix approximation. We stress that the present study will be valid even in the coexistence of a different pseudo-gap mechanism that strongly modifies the electronic state in the anti-nodal region. We have to pay much more efforts to achieve the complete understanding of the pseudo-gap phenomena.

References

1. Ch. Renner, B. Revaz, J.-Y. Genoud, K. Kadowaki, Ø. Fischer, Phys. Rev. Lett. **80**, 149 (1998)
2. N. Miyakawa, P. Guptasarma, J.F. Zasadzinski, D.G. Hinks, K.E. Gray, Phys. Rev. Lett. **80**, 157 (1998)
3. R.M. Dipasupil, M. Oda, N. Momono, M. Ido, J. Phys. Soc. Jpn. **71**, 1535 (2002)
4. T. Sato, T. Yokoya, Y. Naitoh, T. Takahashi, K. Yamada, Y. Endoh, Phys. Rev. Lett. **83**, 2254 (1999)
5. M. Takigawa, A.P. Reyes, P.C. Hammel, J.D. Thompson, R.H. Heffner Z. Fisk, K.C. Ott, Phys. Rev. B **43**, 247 (1991)
6. H. Alloul, T. Ohno, P. Mendels, Phys. Rev. Lett. **63**, 1700 (1989)
7. K. Ishida, Y. Kitaoka, G.-q. Zheng, K. Asayama. J. Phys. Soc. Jpn. **60**, 3516 (1991)

8. D.C. Johnston, Phys. Rev. Lett. **62**, 957 (1989)
9. M. Oda, H. Matsuki, M. Ido, Solid State Commun. **74**, 1321 (1990)
10. H. Yasuoka, T. Imai, T. Shimizu, *Strong Correlation and Superconductivity* (Springer, Berlin, 1989)
11. W.W. Warren, R.E. Walstedt, G.F. Brennert, R.J. Cava, R. Tycko, R.F. Bell, G. Dabbagh, Phys. Rev. Lett. **62**, 1193 (1989)
12. Y. Itoh, H. Yasuoka, Y. Fujiwara, Y. Ueda, T. Machi, I. Tomeno, K. Tai, N. Koshizuka, S. Tanaka, J. Phys. Soc. Jpn. **61**, 1287 (1992)
13. M.H. Julien, P. Carretta, M. Horvatić. Phys. Rev. Lett. **76**, 4238 (1996)
14. H. Ding, T. Yokoya, J.C. Campuzano, T. Takahashi, M. Randeria, M.R. Norman, T. Mochiku, K. Kadowaki, J. Giapintzakis, Nature **382**, 51 (1996)
15. A.G. Loeser, Z.X. Shen, D.S. Dessau, D.S. Marshall, C.H. Park, P. Fournier, A. Kapitulnik, Science **273**, 325 (1996)
16. M.R. Norman, H. Ding, M. Randeria, J.C. Campuzano, T. Yokoya, T. Takeuchi, T. Takahashi, T. Mochiku, K. Kadowaki, P. Guptasarma, D.G. Hinks, Nature **392**, 157 (1998)
17. A. Damascelli, Z. Hussain, Z.-X. Shen, Rev. Mod. Phys. **75**, 473 (2003)
18. Q. Chen, I. Kosztin, B. Jankó, K. Levin, Phys. Rev. Lett. **81**, 4708 (1998)
19. Q. Chen, I. Kosztin, B. Janko, K. Levin, Phys. Rev. B **59**, 7083 (1999)
20. J. Maly, B. Janko, K. Levin, Phys. Rev. B **59**, 1354 (1999)
21. Y. Yanase, K. Yamada, J. Phys. Soc. Jpn. **70**, 1659 (2001)
22. A. Kobayashi, A. Tsuruta, T. Matsuura, Y. Kuroda, J. Phys. Soc. Jpn. **70**, 1214 (2001)
23. T. Dahm, D. Manske, L. Tewordt, Europhys. Lett. **55**, 93 (2001)
24. H. Kontani, Phys. Rev. Lett. **89**, 237003 (2002)
25. Y. Abe, K. Segawa, Y. Ando, Phys. Rev. B **60**, R15055 (1999)
26. Z.A. Xu, Y. Zhang, N.P. Ong, cond-mat/9903123.
27. Z. Konstantinovic, Z.Z. Li, H. Raffy, Phys. Rev. B **62**, R11989 (2000)
28. A. Yamamoto, W.-Z. Hu, S. Tajima, Phys. Rev. B **63**, 024504 (2000)
29. A. Yamamoto, K. Minami, W.-Z. Hu, A. Miyakita, M. Izumi, S. Tajima, Phys. Rev. B **65**, 104505 (2002)
30. T. Honma, P.H. Hor, H.H. Hsieh, M. Tanimoto, Phys. Rev. B **70**, 214517 (2004)
31. T. Takemura, T. Kitajima, T. Sugaya, I. Terasaki, T. Takemura, T. Kitajima, T. Sugaya, J. Phys.: Condens. Matter **12**, 6199 (2000)
32. H. Kontani, K. Kanki, K. Ueda, Phys. Rev. B **59**, 14723 (1999)
33. H. Kontani, K. Kanki, K. Ueda, J. Phy, Chem. Sol. **62**, 83 (2001)
34. T. Nakano, M. Oda, C. Manabe, N. Momono, Y. Miura, M. Ido, Phys. Rev. B **49**, 16000 (1994)
35. K. Takenaka et al., Phys. Rev. **B50**, 6534 (1994)
36. E.W. Carlson, V.J. Emery, S.A. Kivelson, D. Orgad, in *The Physics of Superconductors*, vol. 2, ed. by K.-H. Bennemann, J.B. Ketterson (Springer, Berlin, 2002)
37. S. Tewari, H.Y. Kee, C. Nayak, S. Chakravarty, Phys. Rev. B **64**, 224516 (2001)
38. Z.A. Xu, N.P. Ong, Y. Wang, T. Kakeshita, S. Uchida, Nature **406**, 486 (2000)
39. Y. Wang, Z.A. Xu, T. Kakeshita, S. Uchida, S. Ono, Y. Ando, N.P. Ong, Phys. Rev. B **64**, 224519 (2001)
40. Y. Wang, L. Li, N.P. Ong, Phys. Rev. B **73**, 024510 (2006)
41. P. Fournier, X. Jiang, W. jiang, S.N. Mao, T. Venkatesan, C.J. Lobb, R.L. Greene, Phys. Rev. **B56**, 14149 (1997)
42. H. Kontani, K. Yamada, J. Phy, Soc. Jpn. **74**, 155 (2005)
43. C.C. Capan et al., Phys. Rev. Lett. **88**, 056601 (2002)
44. F. Rullier-Albenque, R. Tourbot, H. Alloul, P. Lejay, D. Colson, A. Forget, Phys. Rev. Lett. **96**, 067002 (2006)
45. Y. Ando, T. Murayama, Phys. Rev. B **60**, R6991 (1999)
46. Y. Abe, Y. Ando, J. Takeya, H. Tanabe, T. Watauchi, I. Tanaka, H. Kojima, Phys. Rev. B **59**, 14753 (1999)
47. J.M. Luttinger, Phys. Rev. **135**, A1505 (1964)
48. M. Jonson, G.D. Mahan, Phys. Rev. B **42**, 9350 (1990)

49. G.D. Mahan, Solid State Phys. **51**, 81 (1998)
50. H. Kontani, Phys. Rev. B **67**, 014408 (2003)
51. S.-K. Yip, Phys. Rev. B **41**, 2612 (1990)
52. I. Ussishkin, S.L. Sondhi, D.A. Huse Phys, Rev. Lett. **89**, 287001 (2002)
53. A. Malinowski, M.Z. Cieplak, S. Guha, Q. Wu, B. Kim, A. Krickser, A. Perali, K. Karpiska, M. Berkowski, C.H. Shang, P. Lindenfeld, Phys. Rev. B **66**, 104512 (2002)
54. H. Ding, M.R. Norman, T. Yokoya, T. Takeuchi, M. Randeria, J.C. Campuzano, T. Takahashi, T. Mochiku, K. Kadowaki, Phys. Rev. Lett. **78**, 2628 (1997)
55. M.R. Norman, M. Randeria, H. Ding, J.C. Campuzano, Phys. Rev. B **57**, R11093 (1998)
56. U. Chatterjee, M. Shi, A. Kaminski, A. Kanigel, H.M. Fretwell, K. Terashima, T. Takahashi, S. Rosenkranz, Z.Z. Li, H. Raffy, A. Santander-Syro, K. Kadowaki, M.R. Norman, M. Randeria, J.C. Campuzano, Phys. Rev. Lett. **96**, 107006 (2006)
57. T. Yoshida, X.J. Zhou, T. Sasagawa, W.L. Yang, P.V. Bogdanov, A. Lanzara, Z. Hussain, T. Mizokawa, A. Fujimori, H. Eisaki, Z.-X. Shen, T. Kakeshita, S. Uchida, Phys. Rev. Lett. **91**, 027001 (2003)
58. N.P. Armitage, D.H. Lu, C. Kim, A. Damascelli, K.M. Shen, F. Ronning, D.L. Feng, P. Bogdanov, Z.-X. Shen, Phys. Rev. Lett. **87**, 147003 (2001)
59. N.P. Armitage, F. Ronning, D.H. Lu, C. Kim, A. Damascelli, K.M. Shen, D.L. Feng, H. Eisaki, Z.-X. Shen, P.K. Mang, N. Kaneko, M. Greven, Y. Onose, Y. Taguchi, Y. Tokura, Phys. Rev. Lett. **88**, 257001 (2002)
60. H. Matsui, K. Terashima, T. Sato, T. Takahashi, S.-C. Wang, H.-B. Yang, H. Ding, T. Uefuji, K. Yamada, Phys. Rev. Lett. **94**, 047005 (2005)
61. L.B. Ioffe, A.J. Millis, Phys. Rev. B **58**, 11631 (1998)
62. T. Yoshida, M. Hashimoto, I.M. Vishik, Z.-X. Shen, A. Fujimori, J. Phys. Soc. Jpn. **81**, 011006 (2012)
63. T. Hanaguri, C. Lupien, Y. Kohsaka, D.-H. Lee, M. Azuma, M. Takano, H. Takagi, J.C. Davis Nature **430**, 1001 (2004)
64. T. Kondo et al., Nat. Phys. **7**, 21 (2011)
65. T. Yoshida et al., J. Phys. Soc. Jpn. **81**, 011006 (2012)

Chapter 7
AC Transport Phenomena in HTSCs

In previous sections, we discussed the DC transport phenomena in nearly AF metals, and found that various non-Fermi-liquid-like behaviors originate from the same CVC. In principle, the AC transport phenomena can yield further useful and decisive information about the electronic status. Unfortunately, the measurements of the AC transport coefficients are not common because of the difficulty in their observations, except for the optical conductivity $\sigma_{xx}(\omega)$ measurements.

Fortunately, Drew's group has been reported reliable measurements of the AC Hall coefficient $R_{\rm H}(\omega) = \sigma_{xy}(\omega)/\sigma_{xx}^2(\omega)$ in YBCO [1–4], BSCCO [5], LSCO [6], and PCCO [7, 8]. They found that the ω-dependence of $R_{\rm H}(\omega)$ in HTSC shows amazing non-Fermi-liquid-like behaviors, which have been a big challenge for researchers for a long time. Here, we show that this crucial experimental constraint is well satisfied by the numerical study using the FLEX + CVC method.

In the RTA, both $\sigma_{xx}(\omega)$ and $\sigma_{xy}(\omega)$ in a single-band model follow the following "extended Drude forms":

$$\sigma_{xx}^{\rm RTA}(\omega) = \frac{\Omega_{xx}}{2\gamma_0(\omega) - iz^{-1}\omega}, \tag{7.1}$$

$$\sigma_{xy}^{\rm RTA}(\omega) = \frac{\Omega_{xy}}{(2\gamma_0(\omega) - iz^{-1}\omega)^2}, \tag{7.2}$$

where z^{-1} is the mass-enhancement factor and $\gamma_0(\omega)$ is the ω-dependent damping rate in the optical conductivity, which is approximately given by $\gamma_0(\omega) \approx (\gamma_{\rm cold}(\omega/2) + \gamma_{\rm cold}(-\omega/2))/2$ for small ω. According to the spin fluctuation theory [9], $\gamma_0(\omega) \propto \max\{\omega/2, \pi T\}$, which is observed by the optical conductivity measurements. The ω-dependence of z is important in heavy-fermion systems ($1/z \gg 1$ at $\omega = 0$), whereas it will not be so important in HTSC since $1/z$ is rather small. Expressions (7.1) and (7.2) are called the "extended Drude form". Within the RTA, the AC-Hall coefficient is independent of ω even if the ω-dependence of z is considered:

$$R_{\rm H}^{\rm RTA}(\omega) = \Omega_{xy}/\Omega_{xx}^2 \sim 1/ne. \tag{7.3}$$

H. Kontani, *Transport Phenomena in Strongly Correlated Fermi Liquids*,
Springer Tracts in Modern Physics 251, DOI: 10.1007/978-3-642-35365-9_7,

7.1 AC Hall Effect in Hole-Doped Systems

Very interestingly, Drew's group has revealed that $R_H(\omega)$ in HTSC decreases drastically with ω: as shown in Fig. 7.1, $\mathrm{Im}R_H(\omega)$ shows a peak at $\sim\omega_0 = 50\,\mathrm{cm}^{-1}$ in optimally-doped YBCO [4]. Moreover, $\mathrm{Im}R_H(\omega)$ is as large as $\mathrm{Re}R_H(\omega)$ for $\omega \gtrsim \omega_0$. Both $\mathrm{Re}R_H(\omega)$ and $\mathrm{Im}R_H(\omega)$ are connected by the Kramers-Kronig relation. Such a large ω-dependence of R_H cannot be explained by the RTA, even if one assume an arbitrary $(\mathbf{k},\omega)$-dependence of the quasiparticle damping rate $\gamma_{\mathbf{k}}(\omega)$. Therefore, the AC-Hall effect presents a very severe constraint on the theory of HTSCs.

Recently, we studied both $\sigma_{xx}(\omega)$ and $\sigma_{xy}(\omega)$ in HTSC using the FLEX + CVC method, by performing the analytic continuation of Eqs. (3.45) and (3.47) using the highly accurate Pade approximation introduced in Refs. [10, 11]. Since the ω-dependence of the CVC is correctly included, the obtained $\sigma_{xx}(\omega)$ and $\sigma_{xy}(\omega)$ satisfy the following f-sum rules very well:

$$\int_0^\infty \mathrm{Re}\sigma_{xx}(\omega)d\omega = \pi e^2 \sum_k (\partial^2 \epsilon^0_{\mathbf{k}}/\partial k_x^2) n_{\mathbf{k}}, \tag{7.4}$$

$$\int_0^\infty \mathrm{Re}\sigma_{xy}(\omega)d\omega = 0, \tag{7.5}$$

the relative error is less than 2.5 % [10]. A useful f-sum rule for the Hall angle has been derived in Ref. [12]. The obtained numerical results are shown in Fig. 7.2a–c.

In Fig. 7.2a, it is found that $\sigma_{xx}(\omega) \approx \sigma_{xx}^{\mathrm{RTA}}(\omega)$ is realized, indicating that the CVC is not so important for $\sigma_{xx}(\omega)$. The peak frequency of $\mathrm{Im}\sigma_{xx}(\omega)$ is $\omega_{xx} = 0.06$ at $T = 0.02$. It is verified that $\sigma_{xx}(\omega)$ is well reproduced by Eq. (7.1), by substituting

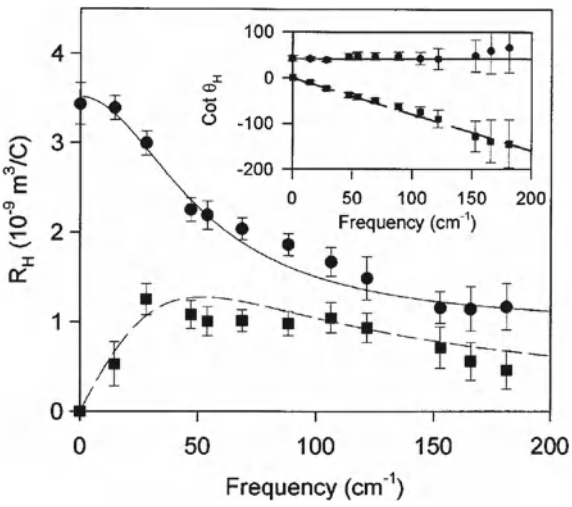

Fig. 7.1 $R_H(\omega)$ in optimally-doped YBCO at 95 K, derived from Faraday rotation. The *closed circles* and *squares* represent experimental values of $\mathrm{Re}R_H(\omega)$ and $\mathrm{Im}R_H(\omega)$, respectively. *Lines* are guides for eye [4]

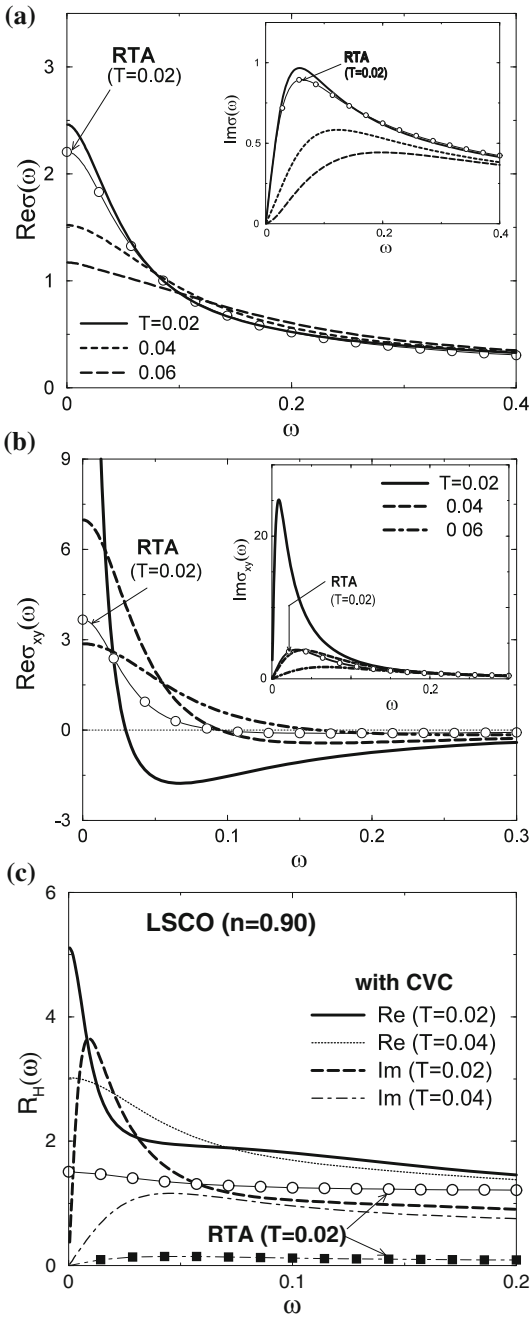

Fig. 7.2 **a** $\sigma_{xx}(\omega)$, **b** $\sigma_{xy}(\omega)$ and **c** $R_{\mathrm{H}}(\omega)$ for LSCO ($n = 0.9$, $U = 5$) given by the FLEX + CVC method. $\omega = 0.1$ corresponds to $\sim 300\,\mathrm{cm}^{-1}$. Because of the CVC, $\sigma_{xy}(\omega) \gg \sigma_{xy}^{\mathrm{RTA}}(\omega)$ at low frequencies [10]

$\gamma_0(\omega) = (\gamma_{\rm cold}(\omega/2) + \gamma_{\rm cold}(-\omega/2))/2$. However, $\sigma_{xx}^{\rm RTA}(\omega)$ do not satisfy the f-sum rule [10]. In Fig. 7.2b, $\sigma_{xy}(\omega)$ given by the FLEX + CVC method completely deviates from the RTA result $\sigma_{xy}^{\rm RTA}(\omega)$, meaning the significant role of the CVC for AC Hall effect. The peak frequency of ${\rm Im}\sigma_{xy}(\omega)$ is $\omega_{xy} = 0.01$, which is six times less than ω_{xx}, consistently with experiments. This fact cannot be explained by using the extended Drude form. The effect of CVC on $\sigma_{xy}(\omega)$ is important for very wide frequency range; $\omega \lesssim 0.3$ ($\sim$1000 cm^{-1}). In fact, $\sigma_{xy}^{\rm RTA}(\omega)$ do not satisfy the f-sum rule in Eq. (7.5), since the magnitude of ${\rm Re}\sigma_{xy}^{\rm RTA}(\omega)$ for $\omega > 0.1$, which takes negative values, is too small if the CVC is dropped. The significance of the CVC is well understood by studying the AC Hall coefficient shown in Fig. 7.2c: $R_{\rm H}(\omega)$ given by the FLEX + CVC method show striking ω-dependences, whereas $R_{\rm H}^{\rm RTA}(\omega)$ is a nearly real constant of the order $1/ne$. This fact means that the strong violation of the extended Drude rule $[\sigma_{xx}^{\rm RTA}(\omega)^2 \propto \sigma_{xy}^{\rm RTA}(\omega)]$ is caused by the strong ω-dependence of the CVC, which is very prominent at low frequencies $\omega \lesssim \omega_{\rm sf} \sim T$.

Here, we study the origin of the ω-dependence of $\sigma_{xy}(\omega)$ by considering the ω-dependence of the CVC. The Bethe–Salpeter equation for $\omega \neq 0$ is given by

$$\boldsymbol{J}_{\mathbf{k}}(\epsilon;\omega) = \boldsymbol{v}_{\mathbf{k}} + \int \frac{d\epsilon'}{4\pi i} \sum_{\mathbf{k}'\mathbf{q}} \mathcal{T}^{(0)}_{\mathbf{k},\mathbf{k}+\mathbf{q}}(\epsilon,\epsilon';\omega) \times G^R_{\mathbf{k}+\mathbf{q}}(\epsilon'+\omega/2) G^A_{\mathbf{k}+\mathbf{q}}(\epsilon'-\omega/2) \boldsymbol{J}_{\mathbf{k}+\mathbf{q}}(\epsilon';\omega), \tag{7.6}$$

which is equivalent to Eq. (3.63) when $\omega = 0$. A simplified Bethe–Salpeter equation for $\omega = 0$ is given in Eq. (3.81). Here, we extend Eq. (3.81), to the case of $\omega \neq 0$. By noticing the relationship $G^R_{\mathbf{k}+\mathbf{q}}(\epsilon'+\omega/2) G^A_{\mathbf{k}+\mathbf{q}}(\epsilon'-\omega/2) \approx \pi\rho_{\mathbf{k}}(\epsilon') \cdot 2/(2\gamma_{\mathbf{k}} - i\omega z^{-1})$, Eq. (7.6) is simplified for $|\omega| \ll \gamma$ as

$$\boldsymbol{J}_{\mathbf{k}}(\omega) = \boldsymbol{v}_{\mathbf{k}} + \frac{\alpha_{\mathbf{k}} \cdot 2\gamma_{\mathbf{k}}}{2\gamma_{\mathbf{k}} - i\omega z^{-1}} \boldsymbol{J}_{\mathbf{k}^*}(\omega), \tag{7.7}$$

where $(1-\alpha_{\mathbf{k}})^{-1} \propto \xi_{\rm AF}^2$. In deriving Eq. (7.7), we assumed that the ϵ-dependence of $\chi^s_{\mathbf{q}}(\epsilon + i\delta)$ is small for $|\epsilon| < \gamma$. The solution of Eq. (7.7) is given by

$$\boldsymbol{J}_{\mathbf{k}} = \frac{(2\gamma - i\omega z^{-1})^2}{(2\gamma - i\omega z^{-1})^2 - (\alpha_{\mathbf{k}} \cdot 2\gamma)^2} \left[\boldsymbol{v}_{\mathbf{k}} + \frac{\alpha_{\mathbf{k}} \cdot 2\gamma}{2\gamma - i\omega z^{-1}} \boldsymbol{v}_{\mathbf{k}^*} \right], \tag{7.8}$$

which is equivalent to Eq. (3.82), when $\omega = 0$. Similar to the derivation of Eq. (5.9), we get

$$\boldsymbol{J}_{\mathbf{k}} \times \frac{\partial \boldsymbol{J}_{\mathbf{k}}}{\partial k_\parallel} = \frac{(2\gamma - i\omega z^{-1})^2}{(2\gamma - i\omega z^{-1})^2 - (\alpha \cdot 2\gamma)^2} \cdot \boldsymbol{v}_{\mathbf{k}} \times \frac{\partial \boldsymbol{v}_{\mathbf{k}}}{\partial k_\parallel}. \tag{7.9}$$

As a result, $\sigma_{xy}(\omega)$ for $\omega \ll \gamma_0$ is approximately given by

$$\sigma_{xy}(\omega)/H_z = e^3 \oint_{\mathrm{FS}} \frac{dk_\parallel}{(2\pi)^2} \frac{1}{(2\gamma - i\omega z^{-1})^2} \left(\boldsymbol{J}_{\mathbf{k}} \times \frac{\partial \boldsymbol{J}_{\mathbf{k}}}{\partial k_\parallel} \right)_z$$
$$\approx \frac{\Omega_{xy}}{((1-\alpha_{\mathbf{k}})2\gamma_0 - i\omega z^{-1})((1+\alpha_{\mathbf{k}})2\gamma_0 - i\omega z^{-1})}. \tag{7.10}$$

If we omit the CVC (i.e., $\alpha_{\mathbf{k}} = 0$), Eq. (7.10) is equivalent to the extended Drude form in Eq. (7.2). According to Eq. (7.10), the solution of $\mathrm{Re}\sigma_{xy}(\omega_0) = 0$ is given by $\omega_0 = 2\sqrt{1-\alpha_{\mathbf{k}}^2}z\gamma$, which is much smaller than the solution obtained from the RTA; $\omega_0^{\mathrm{RTA}} = 2z\gamma$. This analytical result can be recognized in the numerical result shown in Fig. 7.2a, b. As a result, the striking ω-dependence of $R_{\mathrm{H}}(\omega)$ in HTSCs for $|\omega| < \gamma_0$ can be explained by including the CVC.

We explain that the effect of CVC is still large even for the infrared region $\omega \lesssim 0.3$ ($\sim$1000 cm^{-1}). This fact is required by the f-sum rule in Eq. (7.5) when the DC σ_{xy} is significantly enhanced by the CVC. Schmadel et al. [5] observed $\sigma_{xy}(\omega)$ in optimally doped BSCCO for a wide range of ω ($\leq 0.3 \sim$1000 cm^{-1}), and found that $\sigma_{xy}(\omega)$ follows a "simple Drude form"; $\sigma_{xy} \propto (2\gamma_{xy} - iz\omega)^{-2}$, where ω-dependence of γ_{xy} is much smaller than $\gamma_0(\omega)$ and $\gamma_{xy} \ll \gamma_0(0)$. In Fig. 7.3a, b, we show the experimental ω- and T-dependences of $\mathrm{Re}\sqrt{B/\sigma_{xy}}$ ($\propto \gamma_{xy}$) and $\mathrm{Im}\sqrt{B/\sigma_{xy}}$ ($\propto -z\omega$), together with the theoretical results by FLEX + CVC. In the infrared region where $T \ll \omega$ ($= 950\,\mathrm{cm}^{-1}$), it is experimentally found that (i) γ_{xy} depends on ω only weakly, whereas (ii) $\gamma_{xy} \propto T$ is realized below 300 K. This result is highly contradicts the RTA result, since $\gamma_0 \propto \max\{\omega, \pi T\}$ in nearly AF metals. This mysterious behavior is well reproduced by the FLEX + CVC method, as indicated by the solid dots in Fig. 7.3b. This result indicates that the effect of the ω-dependence of $\gamma_0(\omega)$ on the AC-Hall conductivity approximately cancels with that of the CVC.

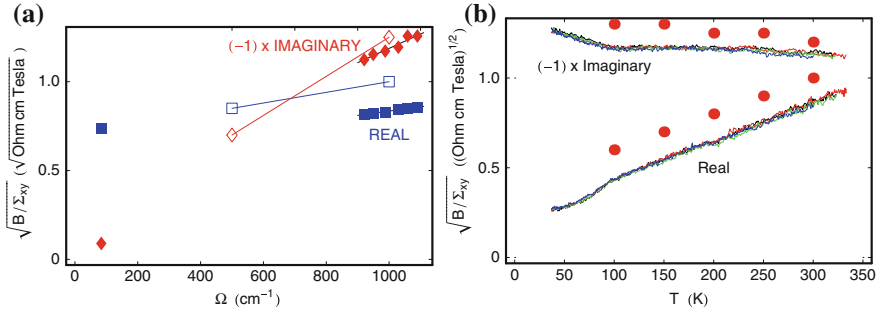

Fig. 7.3 **a** ω-dependence of $\sqrt{B/\sigma_{xy}}$ in BSCCO at 300 K. *Open squares* and *diamonds* represent real and imaginary part of theoretical result given by the FLEX + CVC method. **b** $\sqrt{B/\sigma_{xy}}$ in optimally-doped BSCCO at 950 cm^{-1}. The *solid dots* represent the result of the FLEX + CVC method [5]

Interestingly, the Hall angle $\theta_{\rm H}(\omega) = \sigma_{xy}(\omega)/\sigma_{xx}(\omega)$ follows an approximate simple Drude form in both YBCO [2] and LSCO [6]—$\theta_{\rm H}(\omega) \propto (2\gamma_{\rm H} - iz\omega)^{-1}$ with an ω-independent constant $\gamma_{\rm H} \propto T^{-n}$ ($n = 1.5 \sim 2$). (Exactly speaking, both σ_{xy} and $\theta_{\rm H}$ cannot follow the simple Drude forms at the same time when σ_{xx} exhibits an extended Drude form.) This experimental fact has also been theoretically reproduced [10]. Therefore, the anomalous (ω, T)-dependences of $\sigma_{xy}(\omega)$ and $R_{\rm H}(\omega)$ in HTSCs can be semiquantitatively explained by the FLEX + CVC method—a microscopic theory without any fitting parameters except for U. At the present stage, the FLEX + CVC method is the only theory that is able to explain the anomalous AC and DC transport coefficients in a unified way.

7.2 AC Hall Effect in Electron-Doped Systems

In this section, we study the AC-Hall effect of the electron doped cuprates using the FLEX + CVC method. Figure 7.4 shows the temperature and doping dependences of the Hall angle $\theta_{\rm H}(\omega) \equiv \dfrac{\sigma_{xy}(\omega)}{\sigma_{xx}(\omega)}$ on overdoped $Pr_{2-x}Ce_xCuO_4$ (PCCO) at THz frequencies $\lesssim$10 meV [8]. The Hall signals were found to be linear in field over the measured magnetic field range of $\pm$8 T. At finite frequencies near zero temperatures where inelastic scattering is still large, we observe a strong suppression of the Hall response which corresponds to electron-like contributions coming into $\sigma_{\rm xy}$, even at $T = 0$.

First, we discuss the DC Hall effect: In Fig. 7.4, the DC Hall angle $\theta_{\rm H}(0)$ for $x = 0.17$ is negative for 50 K $\lesssim T \lesssim$ 300 K, since DC Hall conductivity $\sigma_{xy}(0)$ is negative because of the CVC due to spin fluctuations, as discussed in Chap. 5. At higher temperatures ($T \gtrsim$ 300 K), $\sigma_{xy}(0)$ approaches to $\sigma_{xy}^{\rm RTA}(0) > 0$ since the CVC due to spin fluctuations become weak. The CVC is also less important at lower temperatures ($T \lesssim$ 50 K) in the presence of the residual elastic scattering $\gamma_{\rm imp}$, as we will discuss in Chap. 8: The CVC due to spin fluctuations is suppressed by $\gamma_{\rm imp}$ when the inelastic scattering rate is smaller than $\gamma_{\rm imp}$ at lower temperatures.

At finite frequencies, the temperature dependence of ${\rm Re}\theta_{\rm H}(\omega)$ becomes weaker and weaker as increasing ω. Especially, at $\omega = 10.5$ meV, ${\rm Re}\theta_{\rm H}(\omega)$ becomes positive for 75 K $< T <$ 150 K, at which the CVC is very important in DC Hall effect. This result indicates that the effect of the CVC becomes small with ω, as is the case with hole-doped systems. As for the imaginary part, ${\rm Im}\theta_{\rm H}(\omega) = 0$ at $\omega = 0$. At $\omega = 5.24$ meV, however, ${\rm Im}\theta_{\rm H}(\omega)$ is as large as the real part in magnitude, whereas its temperature dependence becomes moderate at $\omega = 10.5$ meV, indicating that the CVC becomes smaller at higher ω.

We should also stress that ${\rm Re}\theta_{\rm H}(\omega)$ at $\omega = 10.5$ meV starts to decrease below $\sim$60 K, and becomes negative below $\sim$20 K. These very complicated temperature and frequency dependences of AC Hall effect would indicate the important role of the CVC, which presents strong temperature and frequency dependences.

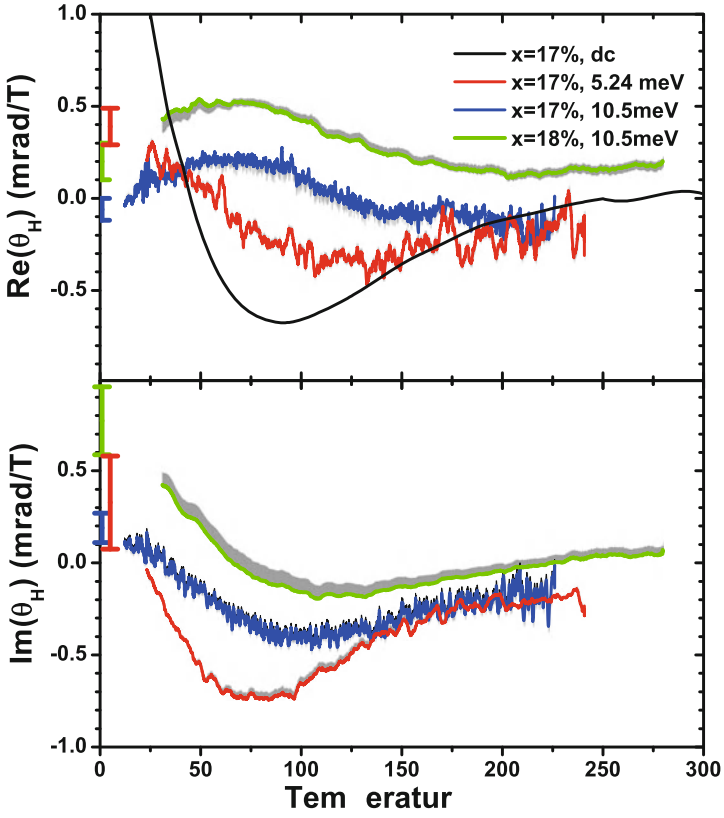

Fig. 7.4 The real and imaginary parts of the Hall angle measured at DC, 5.24, and 10.5 meV [8]. The negative value at finite temperature in both the real and imaginary parts of $\theta_{\rm H}(\omega)$ signify strong electron-like contributions which dominate the $\sigma_{\rm xy}$ response, a clear deviation from the simple hole-like Fermi surface observed by ARPES. Depicted in *grey* with each data set are error bars derived from the juxtaposition of uncertainties in thickness, $\sigma_{\rm xx}$, and $\theta_{\rm F}$

To examine the role of CVCs on the IR Hall response, we calculate the frequency and temperature dependent conductivity for overdoped PCCO within the FLEX + CVC approximation. The model parameters (t, t', t'') and U are the same as those for NCCO given in Chap. 5. The strong scattering process in nearly AF metals not only shortens the quasiparticle lifetime (i.e., hot-spot), but also changes the direction of electron motion: The former and the latter effects are described by the self-energy and the CVC, respectively. How the electron scattering due to spin fluctuations leads to strong CVC effects is illustrated in Fig. 3.7.

Figure 7.5 shows the AC Hall angle obtained by the FLEX + CVC approximation. The nearest neighbor hopping integral is taken as $t = 0.36\,$eV and the quasiparticle damping rate due to elastic scattering was set at $\gamma_{\rm imp} = 3.5\,$meV corresponding to $\rho_{\rm imp} \sim 5\,\mu\Omega\,$cm. In the RPA without the CVC, the Hall angle follows the simple

Drude formula: $\theta_{\rm H}^{\rm RPA}(\omega) = \dfrac{\Omega_{\rm H}}{2\gamma_0(\omega) - iz^{-1}\omega}$. As shown in the insets of Fig. 7.5, $\mathrm{Re}\theta_{\rm H}^{\rm RPA}(\omega)$ and $\mathrm{Im}\theta_{\rm H}^{\rm RPA}(\omega)$ are always positive, reflecting the large hole-like Fermi surface.

When the CVC are taken into account in Fig. 7.5, both $\mathrm{Re}\theta_{\rm H}$ and especially $\mathrm{Im}\theta_{\rm H}$ take on increasingly negative values as temperature is lowered from room temperature and the AF fluctuations become stronger. According to Eq. (7.7), the CVC is controlled by the parameter $\tilde{\alpha}_{\mathbf{k}} \equiv \alpha_{\mathbf{k}} \dfrac{\gamma_{\mathbf{k}}^{\rm AF}}{\gamma_{\mathbf{k}}} \cdot \dfrac{4\gamma_{\mathbf{k}}^2}{4\gamma_{\mathbf{k}}^2 + (\omega z^{-1})^2}$: The total current is written as $\boldsymbol{J}_{\mathbf{k}} \approx \dfrac{\boldsymbol{v}_{\mathbf{k}} + \tilde{\alpha}_{\mathbf{k}} \boldsymbol{v}_{\mathbf{k}^*}}{1 - \tilde{\alpha}_{\mathbf{k}}^2}$. Here, the damping rate $\gamma_{\mathbf{k}}$ is given by the sum of the inelastic damping rate due to AF fluctuations ($\gamma_{\mathbf{k}}^{\rm AF}$) and the elastic damping rate ($\gamma_{\rm imp}$). (The factor $\alpha_{\mathbf{k}}(\lesssim 1)$ in Eq. (7.7) is replaced with $\alpha_{\mathbf{k}}(\gamma_{\rm AF}/\gamma)$ as we will discuss in Chap. 8.) In optimally-doped cuprates, the damping rate due to AF fluctuations is approximately given as $\gamma_{\rm AF} \sim a \max\{\omega, \pi T\}$ and $a \sim O(1)$. Considering the function form of $\tilde{\alpha}_{\mathbf{k}}$, the CVC due to strong AF fluctuations ($\alpha_{\mathbf{k}} \sim 1$) is suppressed when (i) $\gamma_{\rm AF}/\gamma = \gamma_{\rm AF}/(\gamma_{\rm AF} + \gamma_{\rm imp}) \ll 1$, which will be satisfied at low T and low

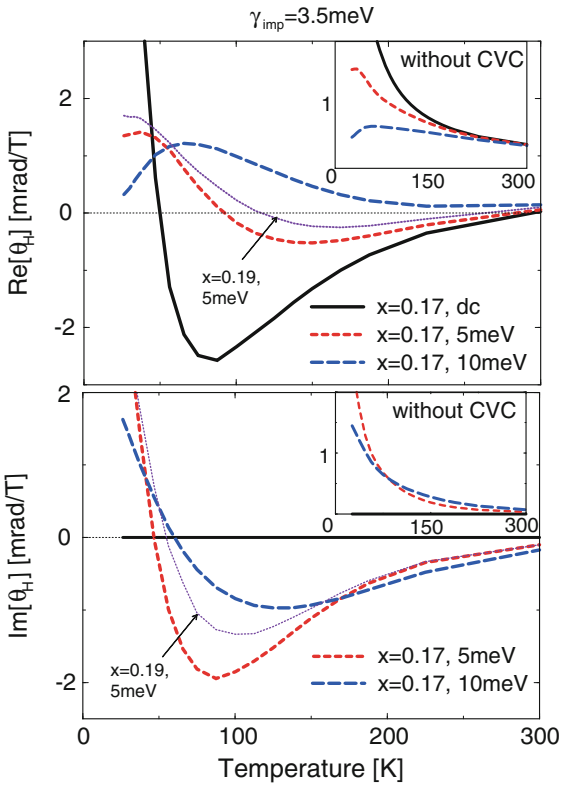

Fig. 7.5 Prediction of the real and imaginary part of the Hall angle by incorporating current-vertex corrections (CVCs) induced by magnon scattering. The Hall angle calculated in the FLEX approximation without including CVCs is shown in the *insets*

ω. [In fact, the CVC term in Eq. (3.78) vanishes if we replace $\gamma_{\mathbf{k}+\mathbf{q}}$ ($\propto T^2$) with $\gamma^{\rm imp} \neq 0$ at $T = 0$.] Also, the CVC becomes weaker in the (ii) collisionless regime $\omega \gg \gamma$.

In Fig. 7.5, at $\omega = 0$ and 5 meV, $\mathrm{Re}\theta_{\rm H}(\omega) < 0$ below 300 K due to the CVC. However, $\mathrm{Re}\theta_{\rm H}(\omega)$ changes to positive at $T = 50 \sim 100$ K because of the suppression of the CVC by impurities (reason (i)). At $\omega = 10$ meV, in contrast, $\mathrm{Re}\theta_{\rm H}(\omega)$ is positive below 300 K, since the effect of the CVC is small in the collisionless regime (reason (ii)). However, $\mathrm{Re}\theta_{\rm H}(\omega)$ starts to decrease below 70 K, indicating that the CVC becomes important at lower temperatures. In fact, the factor $\alpha_{\mathbf{k}} \approx 1 - c\xi_{\rm AF}^{-2}$ approaches to unity at low temperatures. (For $T = 0$ and $\gamma_{\rm imp} > 0$, the CVC due to spin fluctuations is absent at $\omega = 0$, whereas the CVC will be important for $\omega > 0$ since $\gamma_{\rm AF}/\gamma$ increases with ω.) Therefore, overall T- and ω-dependences of $\theta_{\rm H}$ in PCCO are well reproduced by taking the CVC into account. In addition, Fig. 7.5 shows the calculated results for two different doping levels which demonstrate the reduction of the CVC effects in the over-doped region.

In summary, strong and complex temperature and frequency dependences of the AC Hall conductivity in PCCO are naturally reproduced in the FLEX + CVC approximation. This result provides us a very strong indication that the electron-doped cuprates are well described by the Fermi liquid picture. The present study shows that the CVCs contribute significantly to the magnetotransport properties of PCCO and, by extension, suggest that CVC effects would also be the underlying mechanism causing the anomalous Hall transport in the hole-doped cuprate systems [13].

References

1. L.B. Rigal, D.C. Schmadel, H.D. Drew, B. Maiorov, E. Osquiguil, J.S. Preston, R. Hughes, G.D. Gu, Phys. Rev. Lett. **93**, 137002 (2004)
2. M. Grayson, L.B. Rigal, D.C. Schmadel, H.D. Drew, P.-J. Kung, Phys. Rev. Lett. **89**, 037003 (2002)
3. J. Cerne, M. Grayson, D.C. Schmadel, G.S. Jenkins, H.D. Drew, R. Hughes, A. Dabkowski, J.S. Preston, P.-J. Kung, Phys. Rev. Lett. **84**, 3418 (2000)
4. S.G. Kaplan, S. Wu, H.-T.S. Lihn, H.D. Drew, Q. Li, D.B. Fenner, J.M. Phillips, S.Y. Hou, Phys. Rev. Lett. **76**, 696 (1996)
5. D.C. Schmadel, G.S. Jenkins, J.J. Tu, G.D. Gu, H. Kontani, H.D. Drew, Phys. Rev. B **75**, 140506(R) (2007)
6. L. Shi, D. Schmadel, H.D. Drew, I. Tsukada, Y. Ando, cond-mat/0510794
7. A. Zimmers, L. Shi, D.C. Schmadel, W.M. Fisher, R.L. Greene, H.D. Drew, M. Houseknecht, G. Acbas, M.-H. Kim, M.-H. Yang, J. Cerne, J. Lin, A. Millis, Phys. Rev. B **76**, 064515 (2007)
8. G.S. Jenkins, D.C. Schmadel, P.L. Bach, R.L. Greene, X. Bechamp-Laganiere, G. Roberge, P. Fournier, H. Kontani, H.D. Drew, Phys. Rev. B **81**, 024508 (2010)
9. P. Monthoux, D. Pines, Phys. Rev. B **47**, 6069 (1993)
10. H. Kontani, J. Phys. Soc. Jpn. **75**, 013703 (2006)
11. H. Kontani, J. Phys. Soc. Jpn. **76**, 074707 (2007)
12. H.D. Drew, P. Coleman, Phys. Rev. Lett. **78**, 1572 (1997)
13. H. Kontani, Rep. Prog. Phys. **71**, 026501 (2008)

Chapter 8
Impurity Effects in Nearly AF Metals

In earlier sections, we studied the transport phenomena in nearly AF metals without randomness. By including CVCs, we succeeded in explaining the anomalous DC and AC transport phenomena in a unified way, in both hole- and electron-doped cuprate HTSCs. However, effects of impurity or disorder cannot be negligible in many compounds. In fact, the residual resistivity due to disorder increases drastically as the system approaches to the half-filling [1]. Moreover, STM/STS measurements revealed that the electronic states in under-doped HTSCs are highly inhomogeneous at the nanoscale, reflecting the random potential induced by the disordered atoms outside of the CuO_2 plane [2]. These experimental facts are reproduced by assuming that the SC pairing interaction (due to spin fluctuations) is strongly influenced by the impurity potential [3, 4].

Further, the anomalous transport phenomena near the AF QCP are sensitive to the randomness. For example, the hot/cold spot structure due to strong AF fluctuations would be smeared out by impurities, since the impurity-induced damping rate $\gamma^{\rm imp}$ is usually isotropic. Also, the CVC due to electron-electron interaction is suppressed when the impurity scattering is dominant: In fact, the CVC term in Eq. (3.78) vanishes if we replace $\gamma_{\mathbf{k}+\mathbf{q}}$ ($\propto T^2$) with $\gamma^{\rm imp} \neq 0$ at very low temperatures. Therefore, anomalous transport phenomena due to CVC are expected to be suppressed by impurities.

However, this naive expectation would be valid only when the impurity potential is weak, in which the Born approximation is applicable. When the impurity potential is strong, the cross term between the impurity potential and Coulomb interaction could modify the many-body electronic states of the host metal, and resulting in a new anomalous transport phenomena. In this chapter, we will show that a "strong" local impurity potential in under-doped HTSCs induces drastic and widespread changes in the electron-electron correlation around the impurity site. Thus, the impurity effect in HTSCs depends on the strength of the impurity potential. Hereafter, we study the nontrivial impurity effects in nearly AF Fermi liquids.

H. Kontani, *Transport Phenomena in Strongly Correlated Fermi Liquids*,
Springer Tracts in Modern Physics 251, DOI: 10.1007/978-3-642-35365-9_8,

8.1 Hall Coefficient in the Presence of "Weak" Local Impurities

First, we study the effect of "weak local impurities" on the transport phenomena within the Born approximation, where the quasiparticle damping rate due to impurity scattering is given by

$$\gamma^{\mathrm{imp}} = n_{\mathrm{imp}} I^2 \sum_{\mathbf{k}} \mathrm{Im} G_{\mathbf{k}}(-i\delta) = \pi n_{\mathrm{imp}} I^2 N(0), \tag{8.1}$$

where n_{imp} is the impurity density, I is the impurity potential, and $N(0)$ is the DOS at the chemical potential. Then, the total quasiparticle damping rate $\tilde{\gamma}_{\mathbf{k}}$ is given by

$$\tilde{\gamma}_{\mathbf{k}} = \gamma_{\mathbf{k}} + \gamma^{\mathrm{imp}}, \tag{8.2}$$

where $\gamma_{\mathbf{k}}$ represents the quasiparticle damping rate due to inelastic scattering, which is given by Eq. (3.71) in the Fermi liquid theory or by Eq. (2.23) in the FLEX approximation. (Here, we ignored the self-energy correction given by the cross terms between U and I. This simplification is not allowed for a large I, as we will show in Sect. 8.2.) Also, the CVC due to local impurities vanishes identically within the Born approximation. Therefore, in the case of $\gamma^{\mathrm{imp}} \neq 0$, the Bethe-Salpeter Equation (3.78) is modified as

$$\begin{aligned} \boldsymbol{J}_{\mathbf{k}} &= \boldsymbol{v}_{\mathbf{k}} + \sum_{\mathbf{q}} \frac{3U^2}{2} (\pi T)^2 \,\mathrm{Im}\dot{\chi}^s_{\mathbf{q}}(0) \frac{\rho_{\mathbf{k}+\mathbf{q}}(0)}{2\tilde{\gamma}_{\mathbf{k}+\mathbf{q}}} \boldsymbol{J}_{\mathbf{k}+\mathbf{q}} \\ &\approx \boldsymbol{v}_{\mathbf{k}} + \tilde{\alpha}_{\mathbf{k}} \boldsymbol{J}_{\mathbf{k}^*}, \end{aligned} \tag{8.3}$$

where $\tilde{\alpha}_{\mathbf{k}} = \alpha_{\mathbf{k}} \cdot (\gamma_{\mathbf{k}}/\tilde{\gamma}_{\mathbf{k}})$. Thus, an approximate solution of Eq. (8.3) is

$$\boldsymbol{J}_{\mathbf{k}} = \frac{1}{1 - \tilde{\alpha}^2_{\mathbf{k}}} \left(\boldsymbol{v}_{\mathbf{k}} + \tilde{\alpha}_{\mathbf{k}} \boldsymbol{v}_{\mathbf{k}^*} \right). \tag{8.4}$$

In the absence of impurities, $\boldsymbol{J}_{\mathbf{k}}$ exhibits singular $\mathbf{k}$-dependence since $\alpha_{\mathbf{k}} \lesssim 1$ near AF-QCP. In the case of $\gamma_{\mathbf{k}} \sim \gamma^{\mathrm{imp}}$, on the other hand, $\tilde{\alpha}_{\mathbf{k}} \ll \alpha_{\mathbf{k}} \lesssim 1$ and therefore $\boldsymbol{J}_{\mathbf{k}} \sim \boldsymbol{v}_{\mathbf{k}}$. As a result, the CVC is strongly suppressed by high density "weak local impurities", when the elastic scattering is stronger than the inelastic scattering due to AF fluctuations.

In Ref. [5], we have pointed out that the enhancement of R_{H} due to the CVC is suppressed by weak impurities [5]. Figure 8.1 shows the impurity effects on ρ and R_{H} obtained by the FLEX + CVC method for electron-doped systems. As expected, R_{H} is suppressed by a small amount of impurities, although the induced residual resistivity is small. (Note that $\rho = 1$ corresponds to 250 $\mu\Omega$ cm.) As a result, R_{H} changes from negative to positive at low temperatures in the presence of impurities,

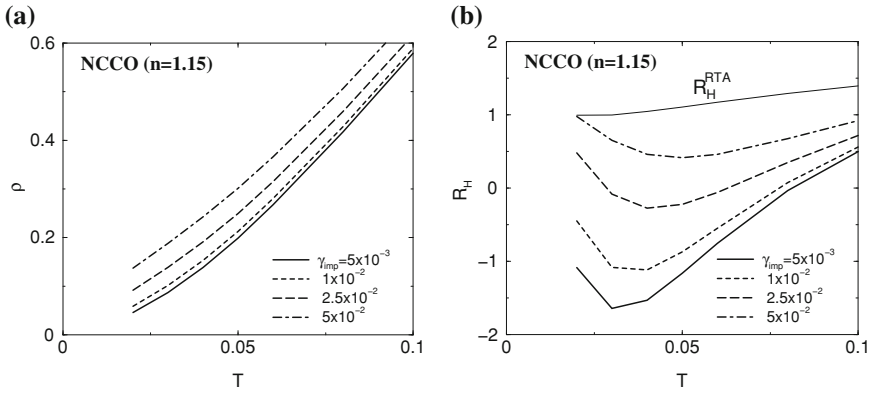

Fig. 8.1 Theoretically obtained T-dependence of (**a**) ρ and (**b**) $R_{\rm H}$ for NCCO in the presence of elastic scattering due to weak local impurities. In the case of $\gamma_{\rm imp} \neq 0$, $R_{\rm H}$ becomes positive at low temperatures since the CVC is reduced by the elastic scattering

which is consistent with the experimental behavior of $R_{\rm H}$ in PCCO for $\delta = 0.16 \sim 0.18$ [6]. Finally, we consider the case where the impurity potential is widespread (nonlocal). In this case, the impurity potential $I(\mathbf{q})$ is momentum-dependent, and the kernel of the Bethe-Salpeter equation in Eq. (8.3), $(3U^2/2)(\pi T)^2\,{\rm Im}\dot{\chi}^s_{\mathbf{q}}(0)$, is replaced with $n_{\rm imp}I^2(\mathbf{q}) + (3U^2/2)(\pi T)^2\,{\rm Im}\dot{\chi}^s_{\mathbf{q}}(0)$. When $I(\mathbf{q})$ is large only for $\mathbf{q} \sim 0$ (forward scattering), both the residual resistivity and the reduction in $R_{\rm H}$ due to the impurities will be small. In HTSCs, it is considered that impurities outside of the CuO_2 plane causes the forward impurity scattering [7].

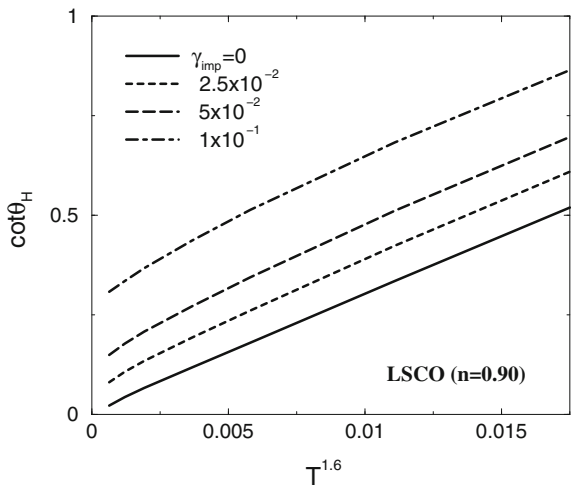

Fig. 8.2 Obtained T-dependence of $\cot\theta_{\rm H} = \rho/R_{\rm H}$ for LSCO for $0.01 \leq T \leq 0.08$. $\cot\theta_{\rm H} \propto T^{1.6} + c$ is realized well, and c is proportional to $\gamma_{\rm imp}$

Figure 8.2 shows the impurity effects on $\cot\theta_{\rm H} = \rho/R_{\rm H}$ obtained by the FLEX + CVC method for LSCO. The relationship $\cot\theta_{\rm H} \propto T^{1.6} + c$ holds well, and $c \propto \gamma_{\rm imp}$. Such a parallel shift of $\cot\theta_{\rm H}$ by impurity doping is actually observed in various hole-doped HTSCs [8].

8.2 Effect of "Strong" Local Impurities Near AF QCP

Now, we discuss the effect of "strong local impurities" in cuprate HTSCs, due to impurities on CuO_2-planes. According to a recent LDA study [9], a Zn atom introduced in the CuO_2 plane of HTSCs induces a large positive potential (less than 10 eV), and the potential radius is only ∼1 Angstrom. In HTSCs, however, Zn doping causes a nontrivial widespread change of the electronic states. In Zn-doped YBCO compounds, site-selective ^{89}Y NMR measurements revealed that both local spin susceptibility [10, 11] and staggered susceptibility [12] are drastically enhanced around the Zn site, within a radius of the AF correlation length $\xi_{\rm AF}$. The same result was obtained by the ^{7}Li Knight shift measurement in Li-doped YBCO compounds [13], and by the ^{63}Cu NMR measurement in Zn-doped YBCO compounds [14]. Moreover, a small concentration of Zn impurities induces a huge residual resistivity, which is significantly greater than the s-wave unitary scattering limit [1]. These nontrivial impurity effects were frequently considered as evidence for the breakdown of the Fermi liquid state in under-doped HTSCs.

Up to now, many theorists have studied this important issue. The single-impurity problem in a cluster t-J model has been studied by using the exact diagonalization method [15, 16]. When the number of holes is two, both AF correlations and electron density increase near the impurity site. This problem was also studied by using the extended Gutzwiller approximation [17]. Although these methods of calculation are founded, the available cluster size is rather small. Moreover, these studies are restricted to $T = 0$.

In this section, we study a single-impurity problem in a large size square lattice (say 64×64) Hubbard model based on the nearly AF Fermi liquid theory [18, 19]:

$$H = \sum_{i,j,\sigma} t_{ij} c^{\dagger}_{i\sigma} c_{j\sigma} + U \sum_{i} n_{i\uparrow} n_{i\downarrow} + I(n_{0\uparrow} + n_{0\downarrow}), \tag{8.5}$$

where I is the local impurity potential at site $i = 0$. It is a difficult problem since we have to consider two different types of strong interactions (U and I) on the same footing. Moreover, the absence of translational symmetry severely complicates the numerical analysis. To overcome these difficulties, we developed the GV^I method—a powerful method for calculating the electronic states in real space in the presence of impurities [18, 19]. The GV^I method is applicable for finite temperatures since the thermal fluctuation effect is taken into account appropriately. Based on the GV^I

method, nontrivial impurity effects in HTSCs are explained *in a unified way* without assuming any exotic mechanisms.

In the GV^I method, the real-space spin susceptibility $\hat{\chi}^{Is}(\omega_l)$ is given by

$$\hat{\chi}^{Is} = \hat{\Pi}^I \left(1 - U\hat{\Pi}^I\right)^{-1}, \tag{8.6}$$

$$\Pi^I(\mathbf{r}_i, \mathbf{r}_j; \omega_l) = -T \sum_{\epsilon_n} G^I(\mathbf{r}_i, \mathbf{r}_j; \epsilon_n + \omega_l) G^I(\mathbf{r}_j, \mathbf{r}_i; \epsilon_n). \tag{8.7}$$

Here, G^I is given by solving the following Dyson equation;

$$\hat{G}^I(\epsilon_n) = \hat{G}^0(\epsilon_n) + \hat{G}^0(\epsilon_n)\hat{I}\hat{G}^I(\epsilon_n), \tag{8.8}$$

where $(\hat{I})_{i,j} = I\delta_{i,0}\delta_{j,0}$, and $\hat{G}^0$ is the real-space Green function in the FLEX approximation without the impurity potential I. The solution of Eq. (8.8) is

$$G^I_{i,j} = G^0_{i,j} + I\frac{G^0_{i,0}G^0_{0,j}}{1 - IG^0_{0,0}}, \tag{8.9}$$

where the position of the impurity potential is $i = 0$.

In Fig. 8.3, we show the numerical results for spin susceptibilities, $\hat{\chi}^{Is}$, given by the GV^I method for $I = \infty$. Surprisingly, a nonmagnetic impurity induces a huge Curie-like component in the uniform susceptibility; $\Delta\chi \approx n_{\rm imp} \cdot \mu^2_{\rm eff}/3T$. This result explains the long-standing experimental problem [20–22]. The obtained

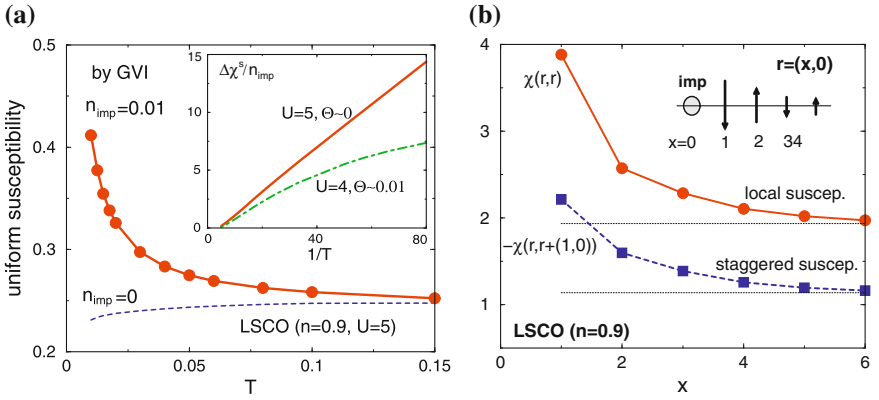

Fig. 8.3 **a** The uniform susceptibility given by the GV^I method in the presence of impurities ($n_{\rm imp} = 0.01$) for the impurity potential $I = \infty$. A single impurity induces a large Curie-term $\Delta\chi^s$, which is consistent with the experimental results. **b** The local susceptibility $\chi^s(\mathbf{r}, \mathbf{r})$ and staggered one $\chi^s(\mathbf{r}, \mathbf{r} + (1, 0))$ given by the GV^I method. The *inset* describes the state in which both local and staggered susceptibilities are enhanced around the impurity site

value of $\mu_{\rm eff}$ is $0.74\mu_{\rm B}$, which is close to the experimental value $\mu_{\rm eff} \sim 1\mu_{\rm B}$ in $YBa_2Cu_3O_{6.66}$ ($T_c \approx 60$ K) [20] and in LSCO ($\delta = 0.1$) [22]. In addition, both the local and staggered susceptibilities get enhanced around the impurity site within a radius of about $3\,(\sim \xi_{\rm AF})$ at $T = 0.02$. Here, we discuss the physical reason for this drastic impurity effect. In the FLEX approximation, the AF order (in the mean-field level) is suppressed by the self-energy effect, which represents the destruction of the long-range order due to thermal and quantum fluctuations. However, this self-energy effect in G^I is weaken near the impurity site, reflecting the reduction of thermal and quantum fluctuations. For this reason, the spin susceptibility given in Eq. (8.6), which is composed of G^Is, is strongly enhanced around the impurity site. Some examples of the cross terms between U and I for the susceptibility are shown in Fig. 8.4a. Consistently, quantum fluctuation is reduced near the vacant site in the $s = 1/2$ Heisenberg model [23]. Therefore, AF spin correlations are enhanced around a vacancy, due to the reduction in quantum fluctuations [23–28].

Before the study of GV^I method, the single impurity problem in the Hubbard model had been studied using the RPA [29–31], assuming a nonlocal impurity potential; V_0 for the on-site and V_1 for the site adjacent to the impurity atom. The obtained result strongly depends on the value of V_1: When $V_1 = 0$, the enhancement of susceptibility is tiny or absent although $V_1 \approx 0$ for the Zn impurity atom in the CuO_2-plane according to the LDA study [9]. On the other hand, in the GV^I method, strong enhancement of the susceptibility is realized even when $V_1 = 0$ (local impurity potential case), since χ_Q is renormalized by the self-energy correction in the FLEX approximation: Then, χ_Q is easily enhanced when the self-energy effect is reduced by introducing an impurity. Therefore, the GV^I method has a great advantage in the study of the impurity problem in HTSCs.

Next, we discuss the transport phenomena in the presence of dilute impurities according to the GV^I method [18, 19]. The impurity-induced enhanced susceptibilities cause the "additional self-energy correction $\delta\Sigma \equiv \Sigma^I - \Sigma^{I=0}$" around the impurity site. If the area of $\delta\Sigma \neq 0$ is large, a large residual resistivity will be induced by the non-s-wave scattering channels. In the GV^I method, $\delta\Sigma$ is given by

$$\delta\Sigma(\mathbf{r}_i, \mathbf{r}_j; \epsilon_n) = T\sum_l G(\mathbf{r}_i, \mathbf{r}_j; \omega_l + \epsilon_n) V^I(\mathbf{r}_i, \mathbf{r}_j; \omega_l) - \Sigma^0(\mathbf{r}_i - \mathbf{r}_j; \epsilon_n), \tag{8.10}$$

$$V^I(\mathbf{r}_i, \mathbf{r}_j; \omega_l) = U^2\left(\frac{3}{2}\chi^{Is}(\mathbf{r}_i, \mathbf{r}_j; \omega_l) + \frac{1}{2}\chi^{Ic}(\mathbf{r}_i, \mathbf{r}_j; \omega_l) - \Pi^I(\mathbf{r}_i, \mathbf{r}_j; \omega_l)\right), \tag{8.11}$$

where Σ^0 is the self-energy given by the FLEX approximation without the impurity potential ($I = 0$). The Green function $G(\mathbf{r}_i, \mathbf{r}_j; \epsilon_n)$ is given by solving the following Dyson equation in real space:

$$\hat{G}(\epsilon_n) = \hat{G}^I(\epsilon_n) + \hat{G}^I(\epsilon_n)\delta\hat{\Sigma}(\epsilon_n)\hat{G}(\epsilon_n). \tag{8.12}$$

In the GV^I method, we solve Eqs. (8.10) and (8.12) self-consistently. The local DOS given by the GV^I method in real space—$\rho(\mathbf{r}, \omega) = \mathrm{Im}G(\mathbf{r}, \omega - i\delta)/\pi$—is shown in Fig. 8.4b. The local DOS decreases around the impurity site within the radius of approximately $3a$ (a is the lattice spacing), since the quasiparticle lifetime is very short due to the large $\mathrm{Im}\delta\hat{\Sigma}$. We verified that the radius of $\mathrm{Im}\delta\hat{\Sigma}$ increases as the filling number n approaches to unity, in proportion to ξ_{AF}. As explained in Ref. [18, 19], we should not solve V^I in Eq. (8.11) self-consistently, since the feedback effect on V^I introduced by iteration is canceled by the vertex correction for V^I that is absent in the FLEX approximation.

To derive the resistivity in the presence of impurities, we have to obtain the t-matrix, $\hat{t}(\epsilon)$, which is defined as $\hat{G} = \hat{G}^0 + \hat{G}^0\hat{t}\hat{G}^0$. The expression of $\hat{t}(\epsilon)$ in the case of $n_{\mathrm{imp}} \ll 1$, which is composed of I, $\delta\hat{\Sigma}$ and $\hat{G}$, had been derived in Ref. [18, 19]. Using the obtained t-matrix, the quasiparticle damping rate due to the impurity is given by [32, 33]

$$\gamma_{\mathbf{k}}^{\mathrm{imp}}(\epsilon) = \frac{n_{\mathrm{imp}}}{N^2}\sum_l \mathrm{Im}T_l(\epsilon - i\delta)e^{i\mathbf{k}\cdot\mathbf{r}_l}, \tag{8.13}$$

where $T_l(\epsilon) = \sum_m t_{m,m+l}(\epsilon)$. n_{imp} is the density of the impurities. In the case of $n_{\mathrm{imp}} \neq 0$, the total quasiparticle damping rate is $\gamma_{\mathbf{k}}(\epsilon) = \gamma_{\mathbf{k}}^0(\epsilon) + \gamma_{\mathbf{k}}^{\mathrm{imp}}(\epsilon)$, where $\gamma_{\mathbf{k}}^0(\epsilon) = \mathrm{Im}\Sigma_{\mathbf{k}}^0(\epsilon - i\delta)$. The resistivity is approximately given by $\rho \propto \gamma_{\mathrm{cold}}$.

Figure 8.5a shows $\mathbf{k}$-dependences of $\gamma_{\mathbf{k}}^{\mathrm{imp}}$ ($n_{\mathrm{imp}} = 0.05$) and $\gamma_{\mathbf{k}}^0$. We emphasize that $\gamma_{\mathbf{k}}^{\mathrm{imp}}$ exhibits strong $\mathbf{k}$-dependence that is similar to the $\mathbf{k}$-dependence of $\gamma_{\mathbf{k}}^0$. This

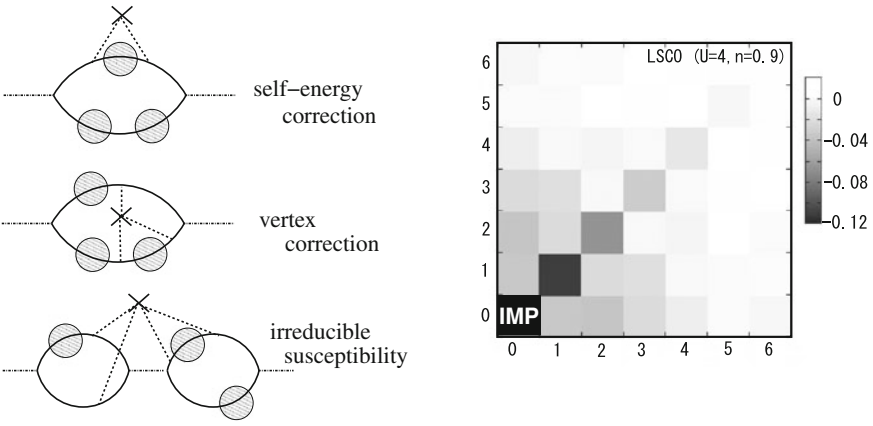

Fig. 8.4 **a** Examples of diagrams for $\hat{\chi}^{Is}$ in the presence of a single-impurity potential I in the Hubbard model. They are cross terms between I and U. The *cross* represents I, and the *large circle with the shadow* represents the self-energy given by the FLEX approximation for $I = 0$. **b** The local DOS given by the GV^I method: it is suppressed around the impurity site within the radius of about 3, due to the imaginary part of the "nonlocal effective impurity potential", $\delta\Sigma(\mathbf{r}, \mathbf{r}'; \epsilon = 0)$

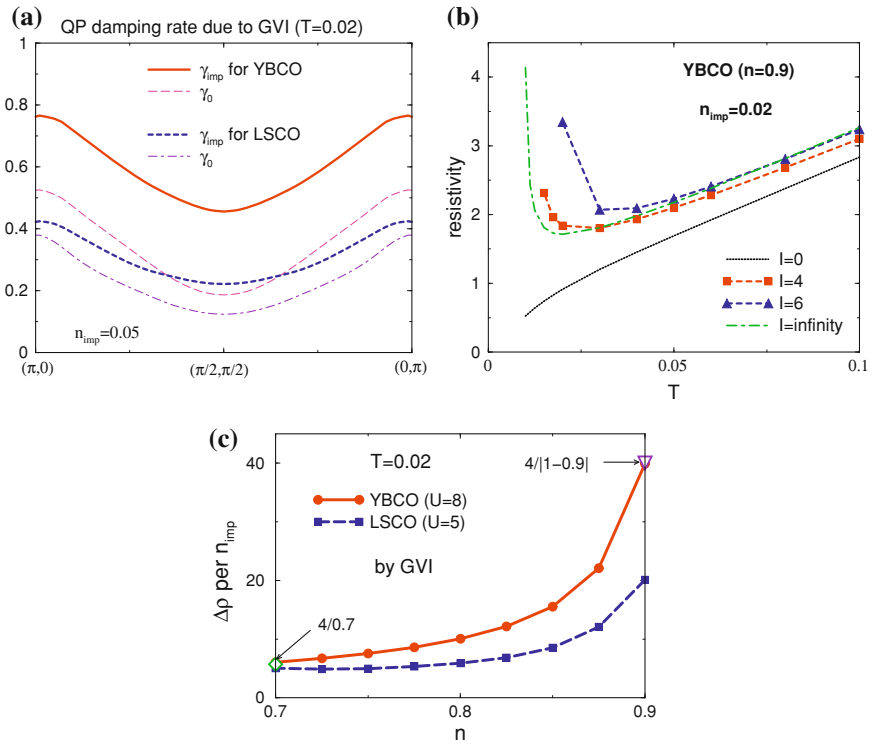

Fig. 8.5 **a** $\gamma_{\mathbf{k}}^{\text{imp}}$ for $n_{\text{imp}} = 0.05$ and $\gamma_{\mathbf{k}}^{0}$ for YBCO and LSCO at $T = 0.02$. Their **k**-dependences will be verified by the ARPES measurements. **b** ρ in YBCO ($n = 0.9$) for $n_{\text{imp}} = 0.02$ given by the GV^I method. At lower temperatures, an insulating behavior is observed in the close vicinity of the AF QCP. In HTSCs, $T = 0.1$ and $\rho = 1$ correspond to 400 K and 250 $\mu\Omega$cm, respectively. **c** The filling dependence of $\Delta\rho \equiv \rho_{\text{imp}} - \rho_0$ per n_{imp} at $T = 0.02$ given by the GV^I method. Note that $\Delta\rho = (4n_{\text{imp}}/n)$ $[\hbar/e^2]$ in a 2D electron-gas model due to strong local impurities

result means that the effective impurity potential $\delta\Sigma$ is nonlocal. For this reason, the structure of the "hot spot" and the "cold spot", is preserved even in the presence of strong local impurities, although it will be smeared out by the weak local impurities. This finding suggests that the enhancement of the Hall coefficient near the AF QCP, which is induced by the strong CVC around the cold spot [34, 35], is not suppressed by the strong local impurities. Moreover, the enhancement of χ_{AF} due to n_{imp} would also enhance R_{H}. Experimentally, R_{H} for under-doped YBCO and $Bi_2Sr_{2-x}La_xCuO_{6+\delta}$ are approximately independent of the doping of Zn and other non-magnetic impurities [36–38], whereas R_{H} for LSCO decreases with Zn doping [39, 40].

Figure 8.5b shows the resistivity ρ for YBCO with $n_{\text{imp}} = 0.02$ for $I = 0, 4, 6$, and ∞. The obtained impurity effect is the most prominent when $I = 6$. As T decreases, nonmagnetic impurities cause a "Kondo-like upturn" of ρ below $T_x \sim 0.02$, reflecting an extremely short quasiparticle lifetime around the

impurities. In other words, *the considerable residual resistivity is caused by the large scattering cross section of the "effective impurity potential* $\delta\hat{\Sigma}$" shown in Fig. 8.4b, whose radius is $\sim\xi_{\rm AF} \propto T^{-0.5}$ near AF-QCP. Note that T_x increases with $n_{\rm imp}$. This drastic result indicates that the insulating behavior of ρ observed in under-doped LSCO [41, 42] and NCCO [43] is caused by the residual disorder in the CuO_2 plane. As shown in Fig. 8.5c, the parallel shift of the resistivity at finite temperatures due to impurities ($\Delta\rho$) substantially increases in the under-doped region; $\Delta\rho$ exceeds the s-wave unitary scattering limit in the 2D electron gas model, $\Delta\rho = (\hbar/e^2)(4n_{\rm imp}/n)$. This result well explains the strong carrier-doping dependence of $\Delta\rho$ observed experimentally [1].

The enlarged residual resistivity near AF QCP is also observed in many heavy-fermion systems such as $CeAl_3$ [44] and $CeCu_5Au$ [45], and in the organic superconductor κ-(BEDT-TTF)$_4$Hg$_{2.89}$Br$_8$ [46]. In these compounds, $\Delta\rho$ quickly decreases with pressure, as increasing the distance from the AF QCP. In κ-(BEDT-TTF)$_4$Hg$_{2.89}$Br$_8$, $\Delta\rho$ under 2 GPa is six times smaller than the value at 0.5 GPa. Such a large change in $\Delta\rho$ is difficult to be explained by the pressure dependence of the DOS. In fact, according to the t-matrix approximation, $\gamma^{\rm imp} = (\pi I^2 N(0)/2)/(1 + (\pi I N(0)/2)^2)$. The residual resistivity in 2D free dispersion model ($\epsilon^0_{\mathbf{k}} = \mathbf{k}^2/2m$) is $\Delta\rho = 2\pi N(0)\gamma_{\rm imp}/e^2 n$. Therefore, $\Delta\rho$ is given by

$$\Delta\rho = \frac{\hbar}{e^2}\frac{4(\pi I N(0)/2)^2}{1 + (\pi I N(0)/2)^2}\frac{n_{\rm imp}}{n}, \tag{8.14}$$

in 2D free dispersion model. Note that the renormalization factor z does not appear in the expression of $\Delta\rho$. In case of $IN(0) \gg 1$, Eq. (8.14) gives the s-wave unitary scattering value; $\Delta\rho = (\hbar/e^2)4(n_{\rm imp}/n)$. In case of weak impurity scattering where $IN(0) \ll 1$ (Born limit), we obtain the relation $\Delta\rho \propto I^2 N^2(0)$, which will decrease under pressure since $N(0) \propto 1/W_{\rm band}$. However, pressure dependence of $\Delta\rho$ in κ-(BEDT-TTF)$_4$Hg$_{2.89}$Br$_8$ seems too strong to be explained by the Born approximation. We comment that the increment in $\Delta\rho$ due to valence fluctuations is discussed in some heavy-fermion systems [47, 48]. However, strong valence fluctuations would be inconsistent with the strong mass-enhancement $z^{-1} \ll 1$.

In summary, the present study revealed that a single impurity strongly influence the electronic states in a wide area around the impurity site in metals near AF QCP. Using the GV^I method, drastic impurity effects in under-doped HTSCs are successfully explained in a unified way, which strongly supports the Fermi liquid ground state in HTSCs. Similar novel impurity effects in other metals near AF QCP, such as heavy-fermion systems and organic metals, will also be explained by the GV^I method. The validity of the GV^I method is verified in Ref. [18, 19] based on the microscopic Fermi liquid theory.

References

1. Y. Fukuzumi, K. Mizuhashi, K. Takenaka, S. Uchida, Phys. Rev. Lett. **76**, 684 (1996)
2. K. McElroy, J. Lee, J.A. Slezak, D.-H. Lee, H. Eisaki, S. Uchida, J.C. Davis. Science **309**, 1048 (2005)
3. B.M. Andersen, A. Melikyan, T.S. Nunner, P.J. Hirschfeld, Phys. Rev. B **74**, 060501(R) (2006)
4. A.C. Fang, L. Capriotti, D.J. Scalapino, S.A. Kivelson, N. Kaneko, M. Greven, A. Kapitulnik, Phys. Rev. Lett. **96**, 017007 (2006)
5. K. Kanki, H. Kontani, J. Phys. Soc. Jpn. **68**, 1614 (1999)
6. Y. Dagan, M.M. Qazilbash, C.P. Hill, V.N. Kulkarni, R.L. Greene, Phys. Rev. Lett. **92**, 167001 (2004)
7. H. Eisaki, N. Kaneko, D.L. Feng, A. Damascelli, P.K. Mang, K.M. Shen, Z.-X. Shen, M. Greven, Phys. Rev. B **69**, 064512 (2004)
8. N.P. Ong, Phys. Rev. B **43**, 913 (1991)
9. L.-L. Wang, P.J. Hirschfeld, H.-P. Cheng, Phys. Rev. B **72**, 224516 (2005)
10. A.V. Mahajan, H. Alloul, G. Collin, J.F. Marucco, Phys. Rev. Lett. **72**, 3100 (1994)
11. W.A. MacFarlane, J. Bobroff, H. Alloul, P. Mendels, N. Blanchard, G. Collin, J.-F. Marucco, Phys. Rev. Lett. **85**, 1108 (2000)
12. A.V. Mahajan, H. Alloul, G. Collin, J.F. Marucco, G. Collin, J.-F. Marucco, Eur. Phys. J. B **13**, 457 (2000)
13. J. Bobroff, W.A. MacFarlane, H. Alloul, P. Mendels, N. Blanchard, G. Collin, J.-F. Marucco, Phys. Rev. Lett. **83**, 4381 (1999)
14. M.-H. Julien, T. Feher, M. Horvatic, C. Berthier, O.N. Bakharev, P. Segransan, G. Collin, J.-F. Marucco, Phys. Rev. Lett. **84**, 3422 (2000)
15. J. Riera, S. Koval, D. Poilblanc, F. Pantigny, Phys. Rev. B **54**, 4771 (1996)
16. T. Tohyama, M. Takahashi, S. Maekawa, Physica C **357–360**, 93 (2001)
17. H. Tsuchiura, Y. Tanaka, M. Ogata, and S. Kashiwaya: Phys. Rev. B 64 (2001) 140501(R).
18. H. Kontani, M. Ohno, Phys. Rev. B **74**, 014406 (2006)
19. H. Kontani, M. Ohno, J. Mag. Mag. Mat. **310**, 483 (2007)
20. P. Mendels, J. Bobroff, G. Collin, H. Alloul, M. Gabay, J.F. Marucco, N. Blanchard, B. Grenier, Europhys. Lett. **46**, 678 (1999)
21. K. Ishida, Y. Kitaoka, K. Yamazoe, K. Asayama, Y. Yamada, Phys. Rev. Lett. **76**, 531 (1996)
22. R.S. Islam, J.R. Cooper, J.W. Loram, S.H. Naqib, Phys. Rev. B **81**, 054511 (2010)
23. N. Bulut, D. Hone, D.J. Scalapino, E.Y. Loh, Phys. Rev. Lett. **62**, 2192 (1989)
24. A.W. Sandvik, E. Dagotto, D.J. Scalapino, Phys. Rev. B **56**, 11701 (1997)
25. G.B. Martins, M. Laukamp, J. Riera, E. Dagotto, Phys. Rev Lett. **78**, 3563 (1997)
26. M. Laukamp et al., Phys. Rev. B **57**, 10755 (1998)
27. M. Laukamp et al., Phys. Rev. Lett. **96**, 017204 (2006)
28. Fabrizio Anfuso, Sebastian Eggert, Phys. Rev. Lett. **96**, 017204 (2006)
29. N. Bulut, Physica C **363**, 260 (2001)
30. N. Bulut, Phys. Rev. B **61**, 9051 (2000)
31. Y. Ohashi, J. Phys. Soc. Jpn. **70**, 2054 (2001)
32. G.M. Eliashberg, Sov. Phys. JETP **14**, 886 (1962)
33. J.S. Langer, Phys. Rev. **120**, 714 (1960)
34. H. Kontani, K. Kanki, K. Ueda, Phys. Rev. B **59**, 14723 (1999)
35. H. Kontani, K. Yamada, J. Phy. Soc. Jpn. **74**, 155 (2005)
36. Y. Abe, K. Segawa, Y. Ando, Phys. Rev. B **60**, R15055 (1999)
37. Y. Hanaki, Y. Ando, S. Ono, J. Takeya, Phys. Rev. B **64**, 172514 (2001)
38. T.R. Chien, Z.Z. Wang, N.P. Ong, Phys. Rev. Lett. **67**, 2088 (1991)
39. G. Xiao, P. Xiong, M.Z. Cieplak, Phys. Rev. B **46**, 8687 (1992)
40. A. Malinowski, M.Z. Cieplak, S. Guha, Q. Wu, B. Kim, A. Krickser, A. Perali, K. Karpinska, M. Berkowski, C.H. Shang, P. Lindenfeld, Phys. Rev. B **66**, 104512 (2002)
41. Y. Ando, G.S. Boebinger, A. Passner, T. Kimura, K. Kishio, Phys. Rev. Lett. **75**, 4662 (1995)

42. G.S. Boebinger, Y. Ando, A. Passner, T. Kimura, M. Okuya, J. Shimoyama, K. Kishio, K. Tamasaku, N. Ichikawa, S. Uchida, Phys. Rev. Lett. **77**, 5417 (1996)
43. T. Sekitani, M. Naito, N. Miura, Phys. Rev. B **67**, 174503 (2003)
44. D. Jaccard, J. Sierro, Physica B **206-207**, 625 (1995)
45. H. Wilhelm, S. Raymond, D. Jaccard, O. Stockert, H.v. Lohneysen, A. Rosch, J. Phys.: Condens. Matter **13** L329 (2001)
46. H. Taniguchi, T. Okuhara, T. Nagai, K. Satoh, M. Mori, Y. himizu, M. Hedo, Y. Uwatoko, J. Phys. Soc. Jpn. **76**(11), Article number 103701 (2007)
47. K. Miyake, O. Narikiyo, J. Phys. Soc. Jpn. **71**, 867 (2002)
48. A.T. Holmes, D. Jaccard, K. Miyake, Phys. Rev. B **69**, 024508 (2004)

Chapter 9
Anomalous Transport Behaviors in Heavy Fermions and Organic Superconductors

Thus far, we have shown that the CVC due to strong AF + SC fluctuations induces various anomalous transport phenomena in cuprate HTSCs. To validate this idea, we have to study the various nearly AF systems other than HTSCs. In general, the electronic structure of heavy-fermion systems and organic metals are very sensitive to the pressure. Therefore, the distance from the AF QCP can be easily changed by applying the pressure, without introducing disorders or randomness. This is a great advantage with respect to investigating the intrinsic electronic states near the AF QCP, free from the disorder effects. A useful theoretical review for heavy-fermion systems near the AF QCP is given in Ref. [1]. Recently, detailed measurements of the transport phenomena under pressure have been performed in heavy-fermion superconductor CeMIn$_5$ (M=Co or Rh) and organic superconductor κ-(BEDT-TTF). They exhibit striking non-Fermi-liquid-like behaviors as observed in HTSCs—Eqs. (1.1)–(1.4). Hereafter, we explain the experimental and theoretical studies on the transport phenomena in these systems.

9.1 CeMIn$_5$ (M = Co, Rh, Ir)

CeMIn$_5$ is a quasi 2D heavy-fermion superconductor with $T_c = 2.3$ K. According to the angle-resolved measurements of thermal conductivity [3] and specific heat [4], the symmetry of the SC gap is the d-wave. Figure 9.1 shows the temperature dependence of R_H in CeCoIn$_5$ and CeRhIn$_5$ in the limit of $H_z \to 0$. In CeRhIn$_5$, the critical pressure for the AF QCP is $P_c \approx 2.01$ GPa. At $P = P_c$, $R_H(2.3\,\mathrm{K})/R_H(300\,\mathrm{K})$ reaches 50, whereas the magnitude of R_H rapidly decreases as the pressure is increased. A similar pressure dependence of R_H is observed in CeCoIn$_5$, where it is considered that P_c is slightly below the ambient pressure. In both these compounds, R_H is inversely proportional to T at higher temperatures. Moreover, as shown in Fig. 9.2, the modified Kohler's rule given in Eq. (5.19) is well satisfied in CeRhIn$_5$ [2] for over four orders of magnitude. Furthermore, this is well satisfied in CeCoIn$_5$ [2, 5] as well as CeIrIn$_5$ [6] Therefore, both R_H and $\Delta\rho/\rho_0$ in CeMIn$_5$ shows

H. Kontani, *Transport Phenomena in Strongly Correlated Fermi Liquids*,
Springer Tracts in Modern Physics 251, DOI: 10.1007/978-3-642-35365-9_9,

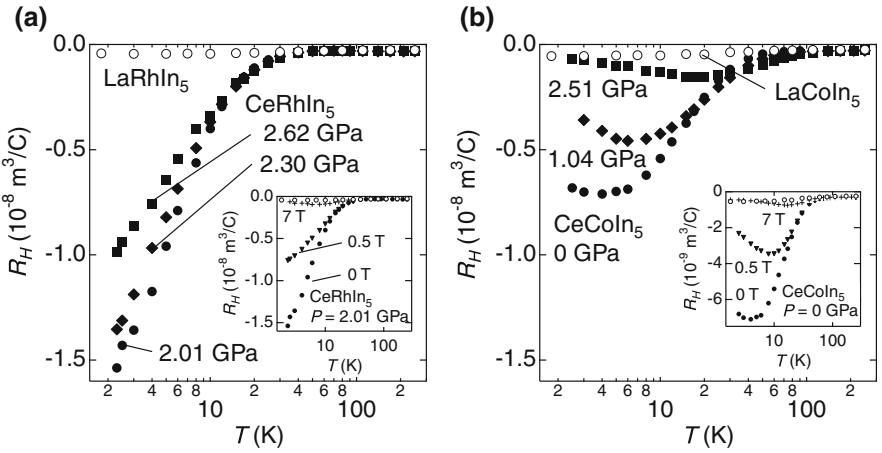

Fig. 9.1 Temperature dependence of R_{H} in **a** $CeRhIn_5$ for $P \geq P_{\mathrm{c}} = 2.01$ GPa, and in **b** $CeCoIn_5$ for $P \geq 0$. (Reference [2])

anomalous behaviors which are similar to HTSCs. This experimental fact strongly suggests that the CVC due to strong AF fluctuations is the origin of the anomalous transport phenomena.

Now, we discuss the magnetic field dependence of the transport coefficients. Interestingly, $R_{\mathrm{H}} \equiv d\rho_{\mathrm{H}}(H_z)/dH_z$ in $CeMIn_5$ near P_{c} is easily suppressed only by a small magnetic field, as shown in the inset of Fig. 9.1. At the same time, $(\Delta\rho/\rho_0)H_z^{-2}$ is also significantly suppressed. Therefore, the relationships $\sigma_{xy} \propto H_z$ and $\Delta\sigma_{xx} \propto H_z^2$ are satisfied only below ~0.1 T near the QCP [2, 5]. These behaviors cannot be attributed to the orbital effect (i.e., the cyclotron motion of conduction electrons) since $\omega_c^*\tau^* = (eH_z/m^*c)\tau^* \gtrsim 1$ is satisfied only when $H_z \gg H_{c2} = 5$ T and $T \ll 1$ K [7]. The condition $\omega_c^*\tau^* \ll 1$ is also recognized from the relationship $\Delta\rho/\rho_0 \lesssim 0.1$ for $T > 2$ K and $H < 3$ T, as shown in Fig. 9.2.

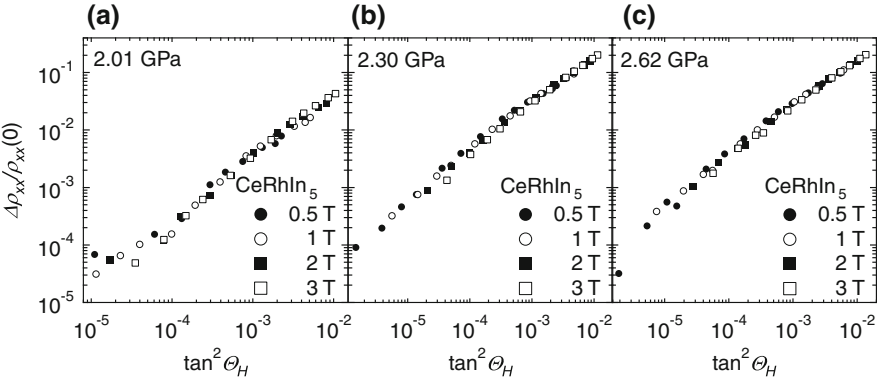

Fig. 9.2 $\Delta\rho/\rho_0$ plotted as a function of $\tan^2\Theta_{\mathrm{H}}$ for $CeRhIn_5$. [Reference [2]]

When $\omega_c^* \tau^* \ll 1$ is satisfied, we can safely expand Nakano-Kubo formula given in Eq. (3.34) with respect to the vector potential, as we did in Chaps. 5–8. Then, the following relationships derived in Chap. 5

$$\rho_{\rm H} \propto H_z \xi_{\rm AF}^2, \tag{9.1}$$

$$\Delta\rho/\rho_0 \propto H_z^2 \xi_{\rm AF}^4/\rho_0^2, \tag{9.2}$$

are expected to be valid for CeMIn$_5$. Here, the factors $\xi_{\rm AF}^2$ and $\xi_{\rm AF}^4$ in Eqs. (9.1) and (9.2), respectively, come from the CVCs. Therefore, experimental striking non-linear behaviors of $R_{\rm H}$ and $\Delta\rho/\rho_0$ with respect to H_z should originate from the field-dependence of $\chi_Q(0) \propto \xi_{\rm AF}^2$: The suppression of $\xi_{\rm AF}$ due to the magnetic field results in reducing both Eqs. (9.1) and (9.2). Since the correlation length is sensitive to the outer parameters in the vicinity of the QCP [8], the anomalous sensitivity of $\rho_{\rm H}$ and $\Delta\rho/\rho_0$ to the magnetic field in CeMIn$_5$ originates from the field-dependence of the CVC. Recently, $\rho_{\rm H}$ and $\Delta\rho/\rho_0$ in PCCO were measured in magnetic field up to 60 T, and it is found that both of them shows striking non-linear behaviors with respect to H_z [9]. Their behaviors would also be explained by the field-dependence of the CVC.

Even if the field dependence of CVC is strong, the modified Kohler's rule in Eq. (5.19) should be satisfied for a wide range of the magnetic field strength, since both $\Delta\rho/\rho_0$ and $\cot^2\theta_{\rm H}$ are proportional to $\xi_{\rm AF}^4\rho^{-2}$. This is a crucial test for the preset theory of the CVC. In fact, the modified Kohler's rule is well satisfied for $T = 2.5{-}30$ K and $0 < H_z \lesssim 3$ T in CeRhIn$_5$ as shown in Fig. 9.2, regardless of the fact that the conventional Kohler's rule is violated even for $H_Z \sim 0.1$ T. This fact strongly suggests that both σ_{xy} and $\Delta\sigma_{xx}$ are enhanced by the same origin, namely, the CVC due to AF fluctuations. Therefore, the anomalous transport phenomena in CeCoIn$_5$ are consistently described by the theory of CVC in nearly AF Fermi liquids.

The Nernst signal ν in CeCoIn$_5$ is also very anomalous [10].[1] Below 20 K, ν starts to increase approximately in proportion to T^{-1}, exhibiting anomalously large values ($\nu \sim 1\mu$V/KT) below 4 K. This behavior is very similar to that of ν in electron-doped HTSC, whose T-dependence and the magnitude are well reproduced by the FLEX + CVC theory, as the quasiparticle transport phenomena. It reaches $\sim 0.1\mu$V/KT in optimally-doped NCCO. Since ν is proportional to $\tau \propto \rho_0^{-1}$, the experimental relations $\nu_{\rm CeCoIn_5(4\,K)}/\nu_{\rm NCCO(100\,K)} \approx 1(\mu{\rm V/KT})/0.1(\mu{\rm V/KT}) = 10$ and $\rho_{\rm CeCoIn_5(4\,K)}/\rho_{\rm NCCO(100\,K)} \approx 5(\mu\Omega)/50(\mu\Omega) = 1/10$ indicates that the giant Nernst signal in CeCoIn$_5$ is caused by the CVC near AF QCP.

Although the spin susceptibility $\chi^s(\mathbf{q})$ in CeMIn$_5$ has a quasi 2D structure, the anisotropy of resistivity is only two ($\rho_c/\rho_{ab} \sim 2$) at low temperatures. In the dynamical-mean-field-theory (DMFT) [12, 13], which is believed to effectively describe the electronic properties in 3D systems, the CVC vanishes identically. Therefore, it is highly desired to confirm whether the CVC is really significant in 3D

[1] Note that the sign of ν in CeCoIn$_5$ is positive according to the definition of the present paper [Eq. (6.5)]. See also Ref. [11].

systems or not. Recently, we performed the numerical study of a 3D Hubbard model with the conduction electron spectrum is $\epsilon_{\mathbf{k}}^{3D} = \epsilon_{\mathbf{k}}^{0} + 2t_z \cos k_z$, where $\epsilon_{\mathbf{k}}^{0}$ is given in Eq. (2.5). The obtained ρ, R_H and ν in quasi 2D Hubbard model are shown in Fig. 9.3a–c. Since the unit cell lengths in CeMIn$_5$ are $a_a = a_b = 4.6$ Angstrom and $a_c = 7.6$ Angstrom, $\rho = 1$ and $R_H = 1$ correspond to 300 $\mu\Omega$cm and 1.0×10^{-9} m$^3/C$, respectively. We find that both R_H and ν are strikingly enhanced due to the CVC even if $t_z/t_0 \sim 1$. In CeCoIn$_5$, R_H starts to increase below $\sim$40 K, which corresponds to $T = 0.08$ in Fig. 9.3b. At $T = 0.02$ ($\sim$8 K for CeMIn$_5$), $R_H \sim 5$ for $t_z/t_0 = 0.8$. Then, the extrapolated value of R_H at 2 K is $5 \times (8\,\mathrm{K}/2\,\mathrm{K}) = 20$.

As shown in Fig. 9.3c, the obtained ν is drastically enhanced by the CVC, consistently with experiments. To discuss the absolute value of ν, we have to take account of the fact that ν is proportional to the mass-enhancement factor $1/z$. According to the de Haas-van Alphen measurement, $1/z = m^*/m_{\mathrm{band}} \sim 50$ in CeCoIn$_5$. Since the mass-enhancement factor in the present FLEX approximation is $1/z_{\mathrm{FLEX}} \sim 3$, we describe the experimental mass-enhancement factor as $1/z = 1/(z_{\mathrm{FLEX}} z^*)$, where $1/z^* = 50/3$ is the mass enhancement factor which cannot be described by the FLEX approximation in the Hubbard model. [Even in the FLEX approximation, relatively large $1/z_{\mathrm{FLEX}} \sim 10$ is obtained in the periodic Anderson model, which is an effective model for heavy fermion systems [14]. We will comment on this fact in Sect. 2.4.] We present $\nu = \nu_{\mathrm{FLEX}}/z^*$ in Fig. 9.3c, where ν_{FLEX} is given by the FLEX approximation, by using the relation $k_B a_a^2/\hbar = 28$ nV/KT. Recently, we extended the FLEX approximation to reproduce appropriate results under a finite magnetic field, and calculated the field dependence of R_H and ν. It was suggested that both these quantities were rapidly suppressed by the magnetic field near AF QCP, reflecting the reduction of AF fluctuations. The obtained result is in good agreement with experiments.

In CeCoIn$_5$, R_H exhibits a peak at $T_{R_H}^* \sim 4$ K at ambient pressure, and $T_{R_H}^*$ increases with pressure [see Fig. 9.1]. This is different from the pseudo-gap behavior in under-doped HTSCs, in which the pseudo-gap temperature T^* decreases as the doping increases. In addition, R_H of CeRhIn$_5$ at $P = P_c$ maintains its increasing trend with decreasing T just above T_c. These behaviors can be understood as the effect of the weak (local) residual disorders, as we have discussed in Sect. 8.1: As shown in Fig. 8.1b, $|R_H - R_H^{\mathrm{RTA}}|$ starts to decrease at lower temperatures when $\gamma_{\mathrm{imp}} > 0$, and its peak temperature $T_{R_H}^*$ increases with γ_{mp}. For a fixed γ_{imp}, $T_{R_H}^*$ increases as AF fluctuations decrease. In CeCoIn$_5$, the resistivity at $T_{R_H}^*$ is $\rho(T = T_{R_H}^*) \sim 6\,\mu\Omega$ cm [2] for $P = 0 \sim 2.5$ GPa. On the other hand, in CeRhIn$_5$ at $P = 2$ GPa, $\rho(T \gtrsim T_c) \approx 10\,\mu\Omega$ cm because of the large inelastic scattering. Since γ_{imp} is expect to be similar in both compounds, $\tilde{\alpha}_{\mathbf{k}} = \alpha_{\mathbf{k}} \cdot \gamma_{\mathbf{k}}/(\gamma_{\mathbf{k}} + \gamma_{\mathrm{imp}})$ in Eq. (8.4) will be smaller in CeCoIn$_5$. That is, the CVC is larger in CeRhIn$_5$. Therefore, we can explain the different behaviors of R_H in CeRhIn$_5$ and CeCoIn$_5$ at low temperatures as the effect of residual disorders.

One may ascribe the temperature dependence of R_H in CeMIn$_5$ to the multiband effect. For example, a sign change of R_H can occur if hole-like and electron-like Fermi surfaces coexist and their mean free paths have different T-dependences. Based on such a multiband model, however, it is very difficult to explain the relation

$|R_H| \gg 1/ne$. In fact, in order to explain the drastic pressure dependence of R_H in $CeCoIn_5$ within the RTA, one has to assume that a tiny Fermi pocket governs the transport phenomena at 0 GPa (near AF QCP), whereas a large Fermi surface changes to be important under 2.5 GPa. The same drastic change in the electronic states should occur by applying a magnetic field $H \sim 1$ T. This unnatural assumption is not true since the other transport coefficients cannot be explained, such as the elegant modified Kohler's rule plot for $CeRhIn_5$ shown in Fig. 9.2 *for over four orders of magnitude*. This is a strong evidence for the significance of the CVC in a single large Fermi surface composed of heavy quasiparticles. Since the enhancements of both R_H and $\Delta\rho/\rho_0$ originate from a small portion of the Fermi surface (i.e., the cold spot) as shown in Fig. 5.3b, the multiband effect is unimportant in CeMIn$_5$. In fact, the modified Kohler's rule is observed in other multiband systems, such as Fe-based superconductors [16].

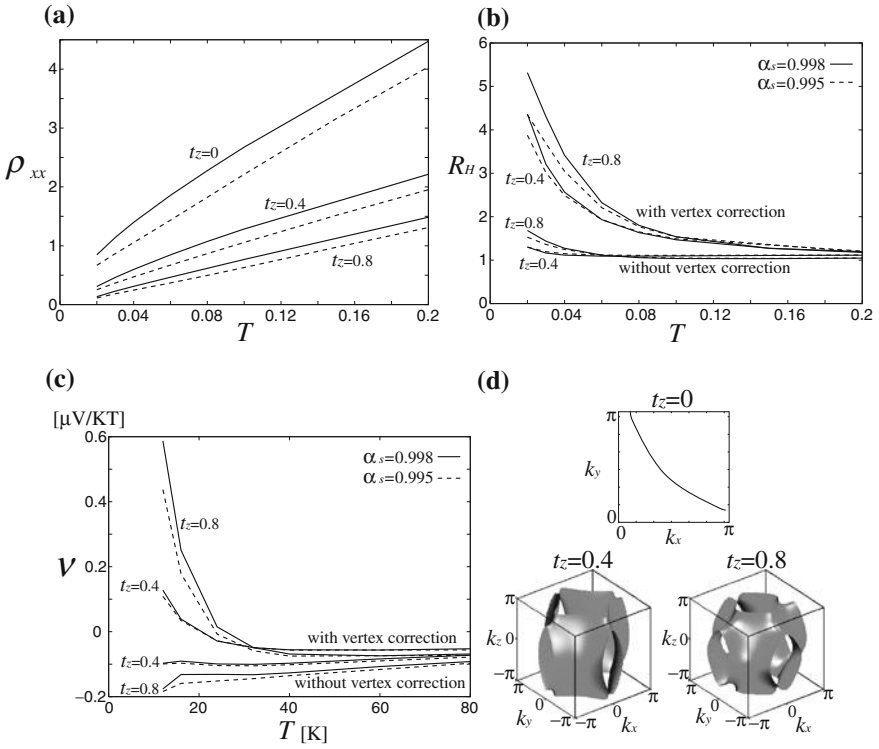

Fig. 9.3 **a** ρ, **b** R_H and **c** ν for the 3D Hubbard model ($t_z = 0.4,\ 0.8$) given by the FLEX + CVC method. *Broken lines* represent the numerical results for $U = 9.4$ ($t_z = 0$), $U = 6.2$ ($t_z = 0.4$) and $U = 5.4$ ($t_z = 0.8$). In these parameters, the Stoner factors α_S is 0.995 at $T = 0.02$. *Full lines* represents the numerical results for Us with which $\alpha_S = 0.998$ is satisfied at $T = 0.02$. **d** Fermi surfaces for $t_z = 0,\ 0.4,\ 0.8$. (Reference [15])

The Hall coefficient in heavy-fermion compounds is given by the summation of the normal Hall coefficient R_{H}^{n} and anomalous Hall coefficient $R_{\mathrm{H}}^{\mathrm{AHE}}$. The former originates from the Lorentz force, and the latter is caused by the angular velocity caused by momenta of f-orbitals, as we will discuss in Sect. 10.1. $R_{\mathrm{H}}^{\mathrm{AHE}}$ exhibits a Curie-like behavior above the coherent temperature T_0, whereas it decreases in proportion to ρ^2 below T_0.

In usual heavy-fermion compounds away from the AF-QCP, the relation $|R_{\mathrm{H}}^{\mathrm{AHE}}| \gg |R_{\mathrm{H}}^{n}|$ holds since R_{H}^{n} is small and temperature independent when the CVC is unimportant. In heavy-fermion compounds near the AF QCP, on the other hand, both R_{H}^{n} and $R_{\mathrm{H}}^{\mathrm{AHE}}$ would become important. Paschen et al. extracted R_{H}^{n} from the experimental Hall coefficient in $YbRh_2Si_2$, and discussed the critical behavior of R_{H}^{n} near AF QCP that is realized under the magnetic field [17]. In contrast, R_{H} in CeMIn$_5$ (M = Co, Rh) is almost constant above 50 K as shown in Fig. 9.1. Therefore, anomalous Hall effect in CeMIn$_5$ is very small and negligible, as explained in detail in Ref. [2, 5]. This fact is a great advantage in the study of anomalous T-dependence of the ordinary Hall effect in CeMIn$_5$.

In $CeCoIn_5$, novel kinds of critical behaviors are observed near $H_{c2} \sim 5$ T for $T \ll 1$ K, where drastic increment in the effective mass was observed. This phenomenon is referred to as a "field-induced QCP". One possible origin will be the field-induced SDW state that is hidden in the SC state. We will discuss this important future problem in Sect. 2.4 in more detail.

9.2 κ-(BEDT-TTF)

The measurements of R_{H} under pressure have been intensively performed in κ-(BEDT-TTF)$_2$X. Figure 9.4 shows the temperature dependence of R_{H} and $\cot\theta_{\mathrm{H}}$ for X = Cu(NCS)$_2$, which has two elliptical Fermi surfaces. Here, the AF correlations are the strongest at the lowest experimental pressure (0.19 GPa). As the pressure is increased, the AF fluctuations get reduced and a conventional Fermi liquid state is realized. At the same time, R_{H} is reduced and exhibits a constant value. Since the observed R_{H} is independent of pressure at room temperature, the origin of the increment in R_{H} below 100 K cannot be related to the pressure induced deformation of Fermi surfaces. Similar increment in R_{H} is observed in X = Cu[N(CN)$_2$]Cl, which has a single elliptical Fermi surface [19]. Because of the analogy of the study in cuprate HTSCs and CeMIn$_5$, the CVC is expected to play also a significant role in κ-(BEDT-TTF)$_2$X.

As discussed in Sect. 2.3, the resistivity in 2D systems in the presence of AF fluctuations is [20],

$$\rho \propto T^2 \xi_{\mathrm{AF}}^2. \tag{9.3}$$

This relationship is reliable when $\omega_{\mathrm{sf}} \gtrsim T$, which is satisfied in optimally- or over-doped HTSCs. The T-dependence of ω_{sf} is given in Eq. (2.3). We consider Eq. (9.3) is realized in X = Cu(NCS)$_2$ since the AF fluctuations are not so prominent.

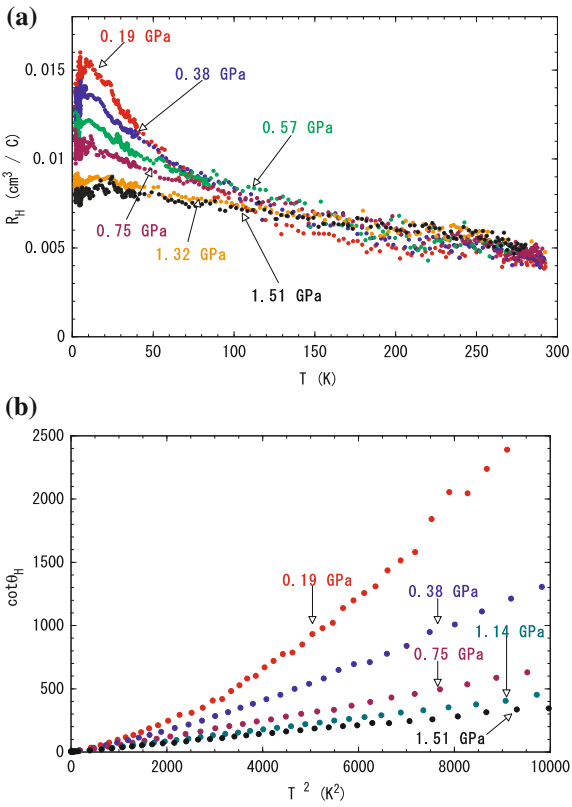

Fig. 9.4 Temperature dependences of **a** R_H and **b** $\cot\theta_H$ for κ-(BEDT-TTF)$_2$Cu(NCS)$_2$ under pressure. (Reference [18])

Since R_H is proportional to ξ_{AF}^2 as shown in Eq. (5.10), we obtain

$$\cot\theta_H = \rho/R_H \propto T^2. \tag{9.4}$$

Figure 9.4b shows that Eq. (9.4) is well satisfied below 80 K, except at $P = 0.19$ GPa. [Large thermal contraction of this organic superconductor might modify this relationship at the lowest pressure.] The observed scaling relationships (5.10), (9.3) and (9.4) is strong evidence that the enhancement of R_H in κ-(BEDT-TTF)$_2$X is caused by the CVC due to AF fluctuations.

In many κ-(BEDT-TTF)$_2$X compounds, the phase transition between the SDW and metallic phases is a weak first order. Since the AF-QCP is absent in these compounds, the AF fluctuations are not so strong even in the vicinity of the SDW phase. For this reason, the enhancement of R_H in κ-(BEDT-TTF)$_2$X is much smaller than that in CeMIn$_5$. On the contrary, carrier doped (11 % doping) κ-type superconductor κ-(BEDT-TTF)$_4$Hg$_{2.89}$Br$_8$ ($T_c = 4$ K at ambient pressure) exhibits very strong AF fluctuations, and therefore the critical pressures is expected to be slightly below 0 kbar. According to NMR measurement, $1/T_1T$ [$\propto \xi_{AF}^2$] increases with

decreasing temperature above ∼10 K, in proportion to $(T + \Theta)^{-1}$ with $\Theta = 13$ K [21]. The P-T phase diagram and transport properties of κ-(BEDT-TTF)$_4$Hg$_{2.89}$Br$_8$ are carefully measured by Taniguchi et al. [22]: It was found that T_c shows two-peak structure under pressure. Also, the power n in $\rho = \rho_0 + AT^n$ increases from 1 to 2 with increases pressure, which indicates that the AF fluctuations are monotonically suppressed by pressure.

Taniguchi et al. also measured the R_H in κ-(BEDT-TTF)$_4$Hg$_{2.89}$Br$_8$ under pressures, and found that R_H exhibits a Curie-Weiss temperature dependence; $R_H \propto (T - \Theta_{RH})^{-1}$ where $\Theta_{RH} < 0$ [18]. At 0.19 GPa where AF fluctuations are strong, $R_H(10\,K)/R_H(300\,K)$ reaches 10, whereas the enhancement of R_H is totally suppressed by 1 GPa. The behavior of R_H in κ-(BEDT-TTF)$_4$Hg$_{2.89}$Br$_8$ is very similar to the observation in CeMIn$_5$. Θ_{RH} decreases with pressure, and its extrapolated value to 0 GPa (−13 K) coincides with the Weiss temperature of $1/T_1T$ at ambient pressure. This is strong evidence that the Hall coefficient in κ-(BEDT-TTF)$_4$Hg$_{2.89}$Br$_8$ is proportional to ξ_{AF}^2, due to the CVC induced by AF fluctuations. It is noteworthy that the residual resistivity $\Delta\rho$ in κ-(BEDT-TTF)$_4$Hg$_{2.89}$Br$_8$ drastically decreases with pressure [22]. As we have discussed in Sect. 8.2, the large residual resistivity near 0 GPa is expected to be given by the enlarged effective impurity potential due to the many-body effect.

Note that R_H in κ-(BEDT-TTF)$_2$Cu[N(CN)$_2$]Br changes to negative under high pressures and low temperatures, when the electron-electron correlation becomes very weak. The origin of this observation is considered to be the lattice deformation with the long-period structure inherent in this compound [23].

Here, we analyzed the anisotropic triangular lattice Hubbard model at half-filling, which is a theoretical effective model for κ-(BEDT-TTF)$_2$X. Figure 9.5a shows the numerical results for the U-T phase diagram given by the FLEX approximation. Here, t_0 (> 0) and t_1 (> 0) are the nearest neighbor integrals of the triangular lattice; t_0 is for two of three axes and t_1 is for the remaining axis, respectively. In many

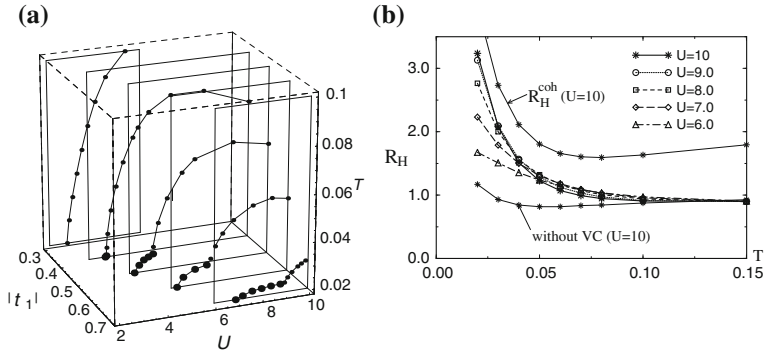

Fig. 9.5 **a** U-T phase diagram for the anisotropic *triangular* lattice Hubbard model [$t_1 = 0.3 \sim 0.7$] given by the FLEX approximation. The *large* (*small*) dots represent the d-wave T_c (T_N). **b** R_H given by the FLEX + CVC method. (References [24, 25])

κ-(BEDT-TTF)$_2$X compounds, $t_1/t_0 \approx 0.7$. Then, the corresponding Fermi surface is hole-like and ellipsoidal around the Γ-point. Hereafter, we substitute $t_0 = 1 \sim 600$ K. Then, the AF ordered state appears at $T_N \lesssim 0.04 \sim 24$ K when U is as large as the bandwidth ($\sim$10). As U decreases, T_N decreases and the $d_{x^2-y^2}$-wave SC appears next to the AF phase. The obtained U-T phase diagram well explains the experimental P-T phase diagram (Kanoda diagram [26]), since U/W_{band} decreases with increasing P. Figure 9.5b also shows the T-dependence of R_H for $t_1/t_0 = 0.7$. We see that R_H is enhanced by the CVC at low temperatures, and it becomes smaller as U decreases. At half-filling, obtained enhancement of R_H is not so large since the AF fluctuations in this model are rather weak due to the strong geometric frustration ($t_1/t_0 \sim 0.7$). Therefore, both the P-T phase diagram as well as the P-dependence of R_H are well understood based on the FLEX+CVC method.

References

1. P. Coleman, *Handbook of Magnetism and Advanced Magnetic Materials*, vol. 1 (Wiley, New York, 2007). cond-mat/0612006
2. Y. Nakajima, H. Shishido, H. Nakai, T. Shibauchi, K. Behnia, K. Izawa, M. Hedo, Y. Uwatoko, T. Matsumoto, R. Settai, Y. Onuki, H. Kontani, Y. Matsuda, J. Phys. Soc. Jpn. **76**, 027403 (2007)
3. K. Izawa, H. Yamaguchi, Y. Matsuda, H. Shishido, R. Settai, Y. Onuki, Phys. Rev. Lett. **87**, 057002 (2001)
4. H. Aoki, T. Sakakibara, H. Shishido, R. Settai, Y. Onuki, P. Miranovic, K. Machida, J. Phys. Condens. Matter **16**, L13 (2004)
5. Y. Nakajima, K. Izawa, Y. Matsuda, S. Uji, T. Terashima, H. Shishido, R. Settai, Y. Onuki, H. Kontani, J. Phys. Soc. Jpn. **73**, 5 (2004)
6. Y. Nakajima, H. Shishido, H. Nakai, T. Shibauchi, M. Hedo, Y. Uwatoko, T. Matsumoto, R. Settai, Y. Onuki, H. Kontani, Y. Matsuda, Phys. Rev. B **77**, 214504 (2008)
7. J. Paglione, M.A. Tanatar, D.G. Hawthorn, E. Boaknin, R.W. Hill, F. Ronning, M. Sutherland, L. Taillefer, C. Petrovic, P.C. Canfield, Phys. Rev. Lett. **91**, 246405 (2003)
8. K. Sakurazawa, H. Kontani, T. Saso, J. Phys. Soc. Jpn. **74**, 271 (2004)
9. P. Li, F.F. Balakirev, R.L. Greene, Phys. Rev. Lett. **99**, 047003 (2007)
10. R. Bel, K. Behnia, Y. Nakajima, K. Izawa, Y. Matsuda, H. Shishido, R. Settai, Y. Onuki, Phys. Rev. Lett. **92**, 217002 (2004)
11. K. Izawa, K. Behnia, Y. Matsuda, H. Shishido, R. Settai, Y. Onuki, J. Flouquet, Phys. Rev. Lett. **99**, 147005 (2007)
12. A. Georges, G. Kotliar, W. Krauth, M.J. Rozenberg, Rev. Mod. Phys. **68**, 13 (1996)
13. G. Kotliar, D. Vollhardt, Phys. Today **57**, 53 (2004)
14. S. Onari, H. Kontani, Y. Tanaka, J. Phys. Soc. Jpn. **77** (2008, to be published)
15. S. Onari, H. Kontani, Y. Tanaka, Phys. Rev. B **73**, 224434 (2006)
16. S. Kasahara, T. Shibauchi, K. Hashimoto, K. Ikada, S. Tonegawa, R. Okazaki, H. Shishido, H. Ikeda, H. Takeya, K. Hirata, T. Terashima, Y. Matsuda, Phys. Rev. B **81**, 184519 (2010)
17. S. Paschen, T. Luhmann, S. Wirth, P. Gegenwart, O. Trovarelli, C. Geibel, F. Steglich, P. Coleman, Q. Si, Nature **432**, 881 (2004)
18. H. Taniguchi, unpublished
19. H. Kino, H. Fukuyama, J. Phys. Soc. Jpn. **65**, 2158 (1996)
20. H. Kohno, K. Yamada, Prog. Theor. Phys. **85**, 13 (1991)
21. K. Miyagawa, H. Taniguchi, Private communication

22. H. Taniguchi, T. Okuhara, T. Nagai, K. Satoh, M. Mori, Y. himizu, M. Hedo, Y. Uwatoko, J. Phys. Soc. Jpn. **76**(11) (2007)
23. K. Katayama, T. Nagai, H. Taniguchi, K. Satoh, N. Tajima, R. Kato, J. Phys. Soc. Jpn. **76**(Suppl A), 194 (2007)
24. H. Kino, H. Kontani, J. Phys. Soc. Jpn. **67**, 3691 (1998)
25. H. Kontani, H. Kino, Phys. Rev. B **63**, 134524 (2001)
26. K. Kanoda, Physica C **282–287**, 299 (1997)

Chapter 10
Multiorbital Systems

In previous chapters, we have explained the significant role of the CVC in the presence of AF fluctuations. For example, $R_{\rm H}$ shows strong temperature dependence due to the CVC. This mechanism of non-Fermi-liquid-like behaviors occurs not only in single-band systems like cuprates, but also in multiband systems like $CeMIn_5$ $(M = Co, Rh, Ir)$.

In this chapter, we will study the electronic properties and transport phenomena in various multiband models, such as orbitally degenerate periodic Anderson model for heavy fermion systems and five-orbital tight-binding model for Fe-based superconductors. We present various transport phenomena and electronic states that are specific to multiband systems.

10.1 Heavy Fermion Systems: Grand Kadowaki-Woods Relation

Here, we introduce the model Hamiltonian for heavy-fermion systems. Bandstructure of Ce- and Yb-based heavy-fermion system is described by the following orbitally degenerate periodic Anderson model [1, 2]:

$$H = \sum_{\mathbf{k}\sigma} \epsilon_{\mathbf{k}} c^{\dagger}_{\mathbf{k}\sigma} c_{\mathbf{k}\sigma} + \sum_{\mathbf{k}M} E_{f,M} f^{\dagger}_{\mathbf{k}M} f_{\mathbf{k}M} + \sum_{\mathbf{k}M\sigma} (V^{*}_{\mathbf{k}M\sigma} f^{\dagger}_{\mathbf{k}M} c_{\mathbf{k}\sigma} + \text{h.c.}) + \frac{U}{2} \sum_{iM\neq M'} n^{i}_{M} n^{i}_{M'}, \tag{10.1}$$

where $c^{\dagger}_{\mathbf{k}\sigma}$ $(f^{\dagger}_{\mathbf{k}M})$ is the creation operator of the conduction electron (f-electron) with $\sigma = \pm 1$ $(M = J, J-1, \ldots, -J)$, and $n^{i}_{M} = f^{\dagger}_{iM} f_{iM}$ is the number of f-electrons on orbital M at site i. The f-orbital degeneracy is $N_f = 2J + 1$, and $\epsilon_{\mathbf{k}}$ $(E_{f,M})$ is the spectrum for conduction electrons (f electrons). In the case

H. Kontani, *Transport Phenomena in Strongly Correlated Fermi Liquids*,
Springer Tracts in Modern Physics 251, DOI: 10.1007/978-3-642-35365-9_10,

of Ce-compound ($J = 5/2$, $N_f = 1$), the complex c-f mixing potential is given by $V_{\mathbf{k}M\sigma} = \sigma V_0 \sqrt{4\pi/3}\sqrt{(7/2 - 2M\sigma)/7} Y_{l=3}^{M-\sigma}(\theta_k, \varphi_k)$, where $Y_{l=3}^{m}(\theta_k, \varphi_k)$ is the spherical harmonic function, In the case of Yb-compound ($J = 7/2$, $N_f = 13$), $V_{\mathbf{k}M\sigma} = V_0 \sqrt{\pi}\sqrt{(7/2 + 2M\sigma)/7} Y_{l=3}^{M-\sigma}(\theta_k, \varphi_k)$. Note that the relation $\sum_{M=-J}^{J} |V_{\mathrm{k}M\sigma}|^2 = V_0^2$ holds. The bandstructure of the orbitally degenerate periodic Anderson model is shown in Fig. 10.1.

Here, we derive the c-electron Green function $G_{\mathbf{k}}^{c}(\omega)$, given by the Fourier transformation of $G_{\mathbf{k}}^{c}(\tau) = -\langle T_\tau c_{\mathbf{k}}(\tau) c_{\mathbf{k}}^{\dagger}(0)\rangle$. Its Dyson equation is given as

$$G_{\mathbf{k}}^{c}(\omega) = G_{\mathbf{k}}^{c0}(\omega) + G_{\mathbf{k}}^{c0}(\omega) \cdot \sum_{M} V_{\mathbf{k}M\sigma} G_{M}^{f0}(\omega) V_{\mathbf{k}M\sigma}^{*} \cdot G_{\mathbf{k}}^{c}(\omega) \tag{10.2}$$

where $G_{\mathbf{k}}^{c0}(\omega) = (\omega + \mu - \epsilon_{\mathbf{k}})^{-1}$ and $G_{M}^{f0}(\omega) = (\omega + \mu - E_{f,M})^{-1}$ are free c- and f-electron Green functions without c-f hybridization. Equation (10.2) is expressed in Fig. 10.2a. If $E_{f,M}$ is independent of M, the self-energy due to c-f hybridization, $\sum_M V_{\mathbf{k}M\sigma} G_{M}^{f0}(\omega) V_{\mathbf{k}M\sigma}^{*}$, is simply given as $(V_0)^2 G^{f0}(\omega)$. Then, the Dyson equation is solved as [1, 2]

$$G_{\mathbf{k}}^{c}(\omega) = \left(\omega + \mu - \epsilon_{\mathbf{k}} - \frac{(V_0)^2}{\omega + \mu - E_f - \Sigma(\omega)}\right)^{-1} \tag{10.3}$$

where the f-electron self-energy due to Coulomb interaction, $\Sigma(\omega)$, is included. We assume that $\Sigma(\omega)$ is diagonal with respect to M. When $H = 0$, $G_{\mathbf{k}}^{c}(\omega)$ is diagonal with respect to σ because of the relation $\sum_M V_{\mathbf{k}M\sigma} V_{\mathbf{k}M-\sigma}^{*} = 0$ [2]. That

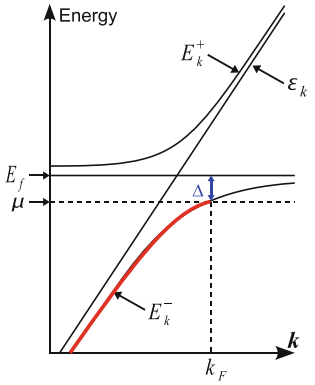

Fig. 10.1 The bandstructure of the PAM with f-orbital degeneracy $N_f = 2J + 1$. After the c-f hybridization, heavy quasiparticle bands $E_{\mathbf{k}}^{\pm}$ (degeneracy 2) and unhybridized f-electron bands E_f (degeneracy $N_f - 2$) are formed. This bandstructure is strongly renormalized by the factor $z = (1 - \partial \mathrm{Re}\Sigma(\omega)/\partial\omega)^{-1}|_{\omega=0} (\ll 1)$, where $\Sigma(\omega)$ is the f-electron self-energy. The relation $E_f > \mu$ holds in this figure, which corresponds to Ce-based compounds ($J = 5/2$, $N_f = 1$). The opposite relation $E_f < \mu$ holds in Yb-based compounds ($J = 7/2$, $N_f = 13$)

is, the c-electron spin is conserved for $H = 0$, irrespective of the strong spin-orbit interaction of f-electrons when levels of $J = 5/2$ and $J = 7/2$ states are well separated.

Using $G^c_{\mathbf{k}}(\omega)$, the f-electron Green function is expressed as

$$G^f_{\mathbf{k}MM'}(\omega) = G^{f0}(\omega)\delta_{M,M'} + G^{f0}(\omega)\sum_{\sigma} V^*_{\mathbf{k}M\sigma} G^c_{\mathbf{k}}(\omega) V_{\mathbf{k}M'\sigma} \cdot G^{f0}(\omega) \tag{10.4}$$

which is expressed in Fig. 10.2b.

In the presence of the self-energy, the approximate expression of $G^c_{\mathbf{k}}(\omega)$ is

$$G^c_{\mathbf{k}}(\omega) \approx \left(\omega + \mu - \epsilon_{\mathbf{k}} - \frac{(V_0^*)^2}{\omega - \tilde{E}_f - i\gamma^*} \right)^{-1} \tag{10.5}$$

where $V_0^* = \sqrt{z}V_0$, $\tilde{E}_f = z(E_f + \mathrm{Re}\Sigma(0) - \mu)$, $\gamma^* = z\mathrm{Im}\Sigma(0)$, and $z = (1 - \partial \mathrm{Re}\Sigma(\omega)/\partial\omega)^{-1}|_{\omega=0}$ is the renormalization factor. $z \ll 1$ in heavy-fermion systems.

The quasiparticle energy $E^*_{\mathbf{k}}$ is given by the solution of $\mathrm{Re}\{1/G^c_{\mathbf{k}}(E^*_{\mathbf{k}})\} = 0$. Below T_{coh}, where γ^* is negligible near the Fermi level, the quasiparticle energy is given as

$$E^*_{\mathbf{k}\pm} = \frac{1}{2}\left(\epsilon_{\mathbf{k}} - \mu + \tilde{E}_f \pm \sqrt{(\epsilon_{\mathbf{k}} - \mu - \tilde{E}_f)^2 + 4(V_0^*)^2} \right), \tag{10.6}$$

where $E^*_{\mathbf{k}-}$ ($E^*_{\mathbf{k}+}$) represents the lower (upper) quasiparticles band. γ^* grows monotonically as temperature increases, and $|\tilde{E}_f| \sim \gamma^*$ at the coherent temperature T_{coh}. When $T \gg T_{\mathrm{coh}}$, the c-f hybridization is prohibited by $\gamma^* \gg |\tilde{E}_f|$.

We summarize the electronic states in heavy-fermion systems: (i) Below T_{coh}, Fermi liquid state with heavy quasiparticles is realized due to c-f hybridization. Mass enhancement factor z^{-1} and uniform susceptibility $\chi \propto z^{-1}$ are constant. The heavy quasiparticle bandwidth, W_{HF}, is approximately given by $W_{\mathrm{HF}} \sim \min\{E^*_{\mathbf{k}+} - E^*_{\mathbf{k}-}\} \sim (V_0^*)^2/W_c \sim |\tilde{E}_f|$, where W_c is the c-electron bandwidth.

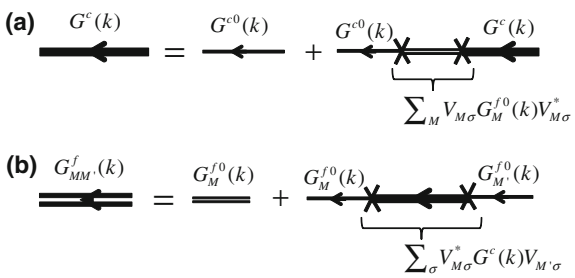

Fig. 10.2 **a** The Dyson equation for c-electron Green function $G^c_{\mathbf{k}}(\omega)$. **b** f-electron Green function $G^f_{\mathbf{k}MM'}(\omega)$

(ii) Above $T_{\rm coh}$, c-f hybridization ceases, and localized f-electrons causes Curie-Weiss susceptibility. Experimentally, the temperature of maximum resistivity T_ρ^* is larger than $T_{\rm coh}$.

Hereafter, we discuss the multiorbital effect on the Kadowaki-Woods (KW) ratio $A\gamma_{\rm sp}^{-2}$, where A is the coefficient of the T^2 term in the resistivity, and $\gamma_{\rm sp}$ is the coefficient of the T-linear term of the electric specific heat. Experimentally, the KW ratio in Ce- and U-based heavy-fermion compounds shows an approximate universal value $A\gamma_{\rm sp}^{-2} \approx 10^{-5}$ [$\mu\Omega$ cm (mol$\cdot$K/mJ)^2], which is known as the KW relation [3]. Although it was believed to be universal in heavy-fermion systems for a long time, recent experimental activities have revealed that the KW relation is strongly violated in many Yb-based compounds. Recently, the author had derived a generalized KW relation that is applicable for systems with general f-orbital degeneracy N_f for Ce- and Yb-based compounds [4] and for Sm- and Er-based compounds [5]. By considering the material dependence of N_f, the failure of the KW relation was resolved.

Here, we analyze the KW ratio in terms of the DMFT ($d = \infty$-limit) [6, 7], which is useful in heavy-fermion systems that is not close to the AF-QCP. In DMFT, the self-energy and irreducible vertex correction are constructed of local f-electron Green function, $g(\omega) \equiv \sum_{\mathbf{k}} G^f_{\mathbf{k}MM}(\omega)$, which is diagonal and independent of M in the present model. It is given as [4]

$$g(\omega) = g^f(\omega) + \left(1 - \frac{2}{N_f}\right) G^{f0}(\omega), \tag{10.7}$$

$$g^f(\omega) = \frac{2}{N_f} \sum_{\mathbf{k}} \left(\{G^{f0}(\omega)\}^{-1} - \frac{V_0^2}{\omega + \mu - \epsilon_{\mathbf{k}}} \right)^{-1}. \tag{10.8}$$

where $G^{f0}(\omega) = (\omega + \mu - E_f - \Sigma(\omega))^{-1}$, and $\mathrm{Im}G^{f0}(-i\delta) = 0$. Then, the f-electron DOS at the Fermi level per channel is

$$\rho^f(0) = \frac{2}{\pi} \mathrm{Im} g(-i\delta) = \frac{1}{N_f} \frac{V_0^2}{(\mu - E_f - \Sigma(0))^2} \rho^c(0), \tag{10.9}$$

where $\rho^c(0) = \sum_{\mathbf{k}} \delta(\mu - \epsilon_{\mathbf{k}})$ is the c-electron DOS per spin without hybridization. $N_f \rho^f(0)$ is the total DOS at the Fermi level. Hereafter, we show several beautiful scaling relations for general $N_f \geq 2$.

By using the DMFT, we can utilize the strong-coupling Fermi liquid theory for the impurity Anderson model developed by many authors [8–12]: First, we analyze $\gamma_{\rm sp}$ and $\mathrm{Im}\Sigma(0)$ in the present PAM. As for $\mathrm{Im}\Sigma(0)$, the second-order term due to the Coulomb interaction $\frac{U}{2} \sum_{i, M \neq M'} n^i_M n^i_{M'}$ is

$$\mathrm{Im}\Sigma^{\rm 2nd}_M(0) = U^2 \frac{\pi^3 (k_{\rm B}T)^2}{2} \cdot \rho^f_M(0) \cdot \left(\sum_{M'} \rho^f_{M'}(0)^2 - \rho^f_M(0)^2 \right) \tag{10.10}$$

since the local f-Green function is diagonal with respect to M. It is expressed in Fig. 10.3a or b. When $E_{f,M}$ is independent of M, we can neglect the Pauli principle in the Coulomb interaction by adding the M-independent potential term $\frac{U}{2}\sum_{i,M}(n^i_M)^2 = \frac{U}{2}\sum_{i,M} n^i_M$ to the Hamiltonian. Then, the general expression for $\mathrm{Im}\,\Sigma_M(0)$ is

$$\mathrm{Im}\,\Sigma(0) = \frac{\pi^3(k_\mathrm{B}T)^2}{2}(N_f-1)\Gamma^2_{\mathrm{loc}}(0,0)\rho^f(0)^3, \tag{10.11}$$

which is shown in Fig. 10.3c. Here, $\Gamma_{\mathrm{loc}}(0,0)$ the asymmetric local four-point vertex introduced in Ref. [4].

We also discuss the specific heat coefficient γ_{sp} given by

$$\gamma_{\mathrm{sp}} = N_\mathrm{A}k^2_\mathrm{B}\frac{\pi^2}{3}N_f\rho^f(0)\cdot\frac{1}{z}, \tag{10.12}$$

where $N_\mathrm{A} = 6.02\times10^{23}$ is the Avogadro constant, and $z^{-1} = 1-\partial\Sigma(\omega)/\partial\omega|_{\omega=0}$ is the mass-enhancement factor. By using the relation of the non-interacting Green function at $T=0$, $dg^f(\omega)/d\omega = dg^f(\omega)/d\mu - 2\pi i\rho^f(0)\delta(\omega)$, and shifting the frequencies of every closed loop by ω, we obtain the following Ward identity:

$$\left.\frac{\partial\Sigma(\omega)}{\partial\omega}\right|_{\omega=0} = \frac{\partial\Sigma(0)}{\partial\mu} + (N_f-1)\Gamma_{\mathrm{loc}}(0,0)\rho^f(0) \tag{10.13}$$

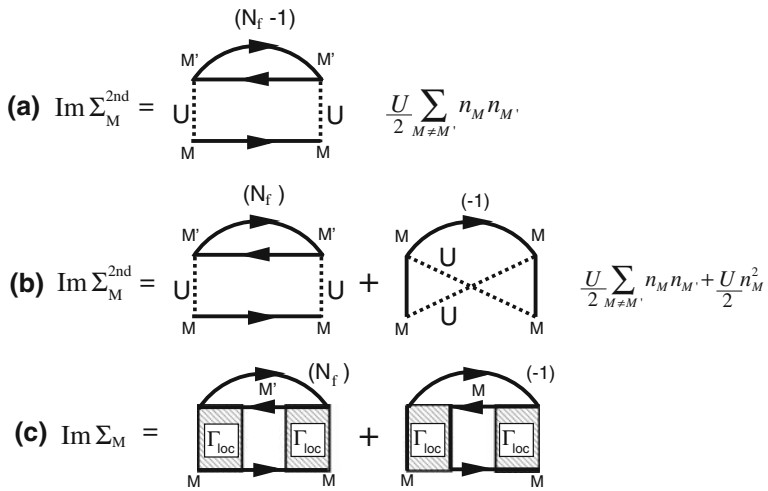

Fig. 10.3 The expression for $\mathrm{Im}\,\Sigma^{2\mathrm{nd}}_M(0)$ within the DMFT. The *solid lines* represent the local f-electron Green functions. In **a**, we consider the Pauli principle of the Coulomb interaction, and the closed loop presents the factor N_f-1. In **b**, we drop the Pauli principle by adding $\frac{U}{2}n^2_M = \frac{U}{2}n_M$, and the obtained result is the same as **a** when $E_{f,M}$ is independent of M

where the factor N_f (-1) originates from the derivative of closed loops (the line connecting two outer points). In the Kondo limit ($U \gg W_{\rm band}$), $z^{-1} = m^*/m \gg 1$ whereas the charge susceptibility enhancement factor $z_\mu^{-1} \equiv 1 - \partial\Sigma(0)/\partial\mu$ is suppressed since the *f*-electron is almost localized [4].[1] Thus, the factor $\partial\Sigma(0)/\partial\mu$ in the right-hand-side of Eq. (10.13) is negligible.

When $\epsilon_{\mathbf{k}}$ in Eq. (10.1) is a free dispersion, the conductivity at low temperatures is given by

$$\begin{aligned}\sigma_{xx} &= \frac{e^2}{\pi}\sum_{\mathbf{k}} |G^c_{\mathbf{k}}(0)|^2 v^2_{\mathbf{k}x} \\ &= \frac{e^2}{h}\frac{(3/\pi)^{1/3} n^{4/3} a^3}{N_f \rho^f(0)\cdot {\rm Im}\,\Sigma(0)},\end{aligned} \tag{10.14}$$

where $n(= k_{\rm F}^3/3\pi^2)$ is the density of quasiparticles that form the conduction band, and a is the unit cell length. According to Eqs. (10.11)–(10.14), we find the scaling properties $\gamma_{\rm sp} \propto N_f(N_f-1)\Gamma_{\rm loc}{\rho^f}^2$ and $A \propto N_f(N_f-1)\Gamma_{\rm loc}^2{\rho^f}^4$. Therefore, we obtain the "grand KW relation" that is valid for any N_f (≥ 2) [4, 5, 13]:

$$\begin{aligned}A\gamma_{\rm sp}^{-2} &\approx \frac{h}{e^2 k_{\rm B}^2}\frac{9(3\pi)^{-1/3}}{4n^{4/3}a^3 N_{\rm A}^2}\frac{1}{\frac{1}{2}N_f(N_f-1)} \\ &\approx \frac{1\times 10^{-5}}{\frac{1}{2}N_f(N_f-1)}\quad [\mu\Omega\,{\rm cm}({\rm mol}\cdot{\rm K/mJ})^2].\end{aligned} \tag{10.15}$$

where we put $h/e^2 = 2.6\times 10^4\,\Omega$, $k_{\rm B} = 1.38\times 10^{-23}\,{\rm JK}^{-1}$, and we assumed $1/n^{4/3}a^3 \approx 4\times 10^{-8}\,{\rm cm}$.

Without crystal field splitting of the *f*-level, $N_f = 2J+1 = 6$ for Ce^{3+} and Sm^{3+} ions, and $N_f = 8$ for Yb^{3+} and Er^{2+} ions. Therefore, the previous KW relation turned out to be valid only when $N_f = 2$ (Kramers doublet case due to strong crystal field splitting). A similar universal relation $\lim_{T\to 0} eS/T\gamma_{\rm sp} \approx \pm 1$ (S is the Seebeck coefficient) was recently found [14, 15]. The characteristics of the electronic state in heavy-fermion systems are (i) large mass-enhancement and (ii) small charge susceptibility since the *f*-electron is almost localized. The grand KW relation (10.15) is derived only by imposing these constraints on the microscopic Fermi liquid theory. This fact illustrates a remarkable advantage of the Fermi liquid theory for the analysis of strongly correlated systems.

Figure 10.4a shows the experimental verification of Eq. (10.15) for various heavy-fermion compounds, where N_f in each compound was determined by the temperature dependence of χ and the inelastic neutron scattering [13]. Tsujii's study confirmed

[1] In Refs. [4, 5], we put $= (\pi T)^2/6\cdot N_f\rho^f(0)$ by mistake; the correct relation is $\gamma = (\pi T)^2/3\cdot N_f\rho^f(0)$. For this reason, Eq. (10.13) is two times Eq. (8) in Ref. [4]. Since the author of Ref. [4] assumed $1/n^{4/3}a^3 \approx 1\times 10^{-8}\,{\rm cm}$, the grand-KW relation in Ref. [4] is equal to Eq. (10.15) in the present paper.

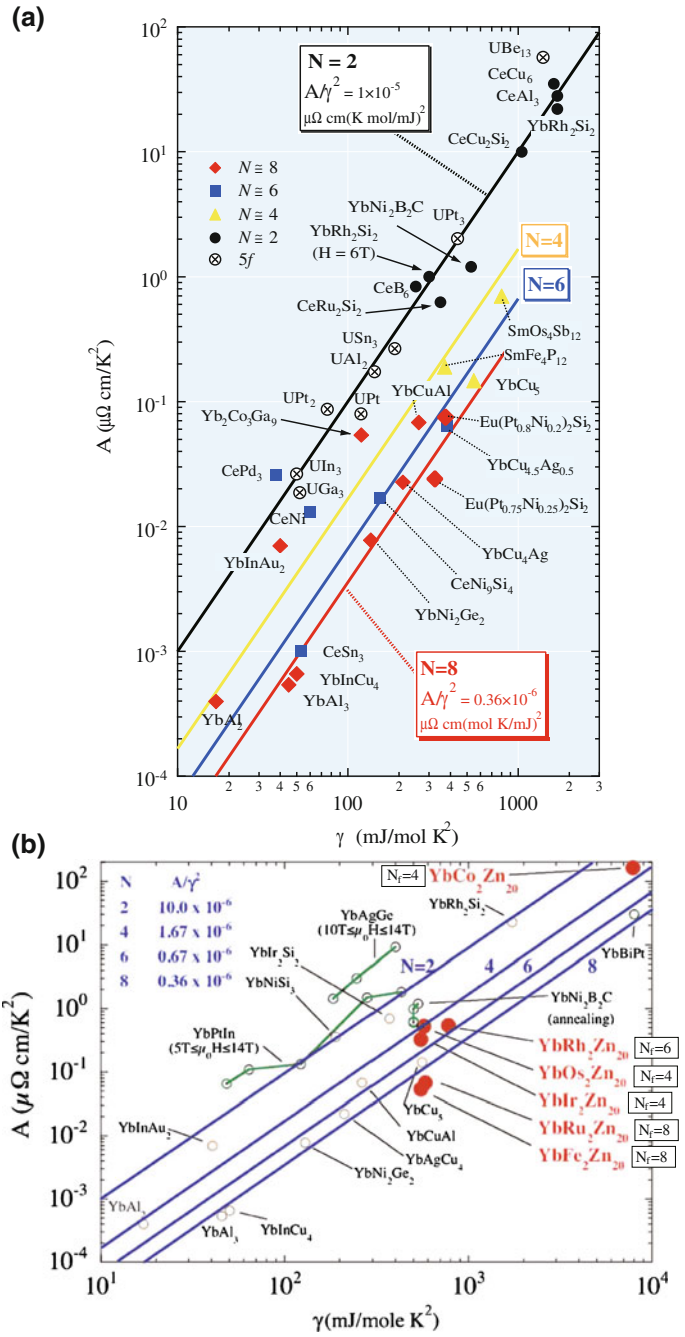

Fig. 10.4 **a** Kadowaki-Woods plot for various heavy-fermion systems $N_f = 2 \sim 8$ in Ref. [13]. **b** Kadowaki-Woods plot for YbT_2Zn_{20} (Ref. [16]: Copyright (2007) National Academy of Sciences, U.S.A.)

that $N_f \sim 2$ in many Ce-based compounds, where crystal-field splitting is larger than the renormalized Fermi energy $W_{\rm HF}$. On the other hand, $N_f \sim 8$ in many Yb-based ones, where crystal-field splitting is smaller than $W_{\rm HF}$. Torikachvili et al. also found that other Yb-based heavy-fermion systems YbT_2Zn_{20} (T = Fe, Co, Ru, Rh, Os, or Ir) follows the grand KW relation shown in Eq. (10.15) [16]. Their experimental results are shown in Fig. 10.4b.

We shortly discuss the "multiband effect" on the KW relation: In a usual heavy-fermion compound, there are one or two main large Fermi surfaces composed of heavy quasiparticles, and several minor small Fermi surfaces composed of light-quasiparticles. In the presence of impurities, $AT^2 \propto \langle \gamma_{\mathbf{k}} \rangle_{\rm FS}$ as explained in Eq. (2.32). Therefore, heavy quasiparticles on the large Fermi surfaces give the dominant contribution to both the specific heat and the A-term. As a result, the grand-KW relation is universally realized. We note that $|R_{\rm H}^n| \sim 1/ne$ is realized in many heavy-fermions away from AF-QCPs. This fact means that heavy quasiparticles on the large Fermi surfaces give the dominant contribution to the conductivity, since $|R_{\rm H}^n| \gg 1/ne$ should be realized when small Fermi surfaces are the most conductive.

Finally, we discuss the Wilson ratio $R \equiv (\chi/\chi^0)/(\gamma_{\rm sp}/\gamma_{\rm sp}^0) \equiv z_H^{-1}/z^{-1}$ for general N_f in the strong coupling limit ($z^{-1} \gg 1$). Here, χ^0 and $\gamma_{\rm sp}^0$ represent the non-interacting values. The magnetic susceptibility enhancement factor z_H^{-1} is given as $\dfrac{1}{z_H} \equiv 1 + \dfrac{\partial \Sigma_M(0)}{\partial HM}$.

By using the relation of the non-interacting Green function at $T = 0$, $dg^f(\omega)/d\omega = dg_M^f(\omega)/dHM - 2\pi i \rho^f(0)\delta(\omega)$, and the fact that H-derivative of every closed loop vanishes identically after the summation of f-orbital angular momentum, we obtain the following Ward identity:

$$\left.\frac{\partial \Sigma(\omega)}{\partial \omega}\right|_{\omega=0} = \frac{\partial \Sigma_M(0)}{\partial HM} - 1 \times \Gamma_{\rm loc}(0,0)\rho^f(0) \tag{10.16}$$

By eliminating the left-hand-side using Eq. (10.13), we obtain

$$\frac{\partial \Sigma_M(0)}{\partial HM} = \frac{\partial \Sigma(0)}{\partial \mu} + N_f \Gamma_{\rm loc}(0,0)\rho^f(0) \tag{10.17}$$

Therefore, the Wilson ratio in the Kondo regime is obtained as

$$R = \frac{z_H^{-1}}{z^{-1}} = \frac{N_f}{N_f - 1} \tag{10.18}$$

[11, 17, 18]. We stress that the universality of the grand-KW relation and the Wilson ratio in heavy-fermion systems ensures the smallness of valence fluctuations in usual compounds.

10.2 Fe-Based Superconductors

Iron-based high-T_c superconductors had been discovered by Kamiahara et al. in 2008 [19], and the highest T_c at present reaches 56 K in F-doped SmFeAsO. The structure of mother compounds is orthorhombic, and the tetragonal structure transition is realized by carrier or chemical doping. In $Ba(Fe, Co)_2As_2$, the highest SC transition temperature T_c is realized next to the non-SC orthorhombic phase, and the structure transition at $T = T_S$ is second-order [20]. Very large softening of shear modulus C_{66} suggests the existence of strong orbital (quadrupole) fluctuations [21–23]. Moreover, the spin-density-wave (SDW) state with $\mathbf{Q} \approx (\pi, 0)$ occurs in the orthorhombic phase, that is, T_N is close to but always lower than T_S. These experimental facts suggest a close relation between the mechanism of superconductivity and structure/orbital/SDW transitions.

Near the structure or magnetic QCP, high-T_c superconductivity as well as the non-Fermi liquid transport phenomena similar to cuprates are frequently observed. For example, T-linear resistivity is observed below 200 K in optimally-doped $Ba(Fe, Co)_2As_2$ and $BaFe_2(As, P)_2$ with $T_c \sim 25$ K. Also, Curie-Weiss behavior of R_H as well as the modified Kohler's rule (1.4) are also observed, although conventional Kohler's rule is violated [24]. These anomalous transport phenomena are expected to be realized by CVC due to strong orbital and/or spin fluctuations.

As for the pairing mechanism, based on the spin fluctuation theories, fully-gapped sign-reversing s-wave ($s_\pm$-wave) state had been predicted [25–28]. The origin of the spin fluctuations is the intra-orbital nesting between hole- and electron-pockets. However, the robustness of T_c against randomness in iron pnictides indicates the absence of sign-reversal in the superconducting (SC) gap [29–34]. Later, orbital-fluctuation-mediated s-wave state without sign reversal (s_{++}-wave) had been proposed [35–38]. The orbital fluctuations mainly originate from the inter-orbital Fermi surface nesting and the inter-orbital (quadrupole) interaction: The quadrupole interaction is caused by the vertex correction due to Coulomb interaction [39] in addition to the electron-phonon (e-ph) interaction [35].

Now, we introduce the model Hamiltonian. The band structure of Fe-based superconductors is well described by the five orbital square lattice tight-binding model [26]:

$$H_0 = \sum_{i,j,\mu,\nu,\sigma} t_{i,j}^{\mu,\nu} c_{i,\mu\sigma}^\dagger c_{j,\nu\sigma} \tag{10.19}$$

where i, j represent the Fe-sites, and μ, ν represent the five d-orbitals, $3z^2 - r^2$, xz, yz, xy and $x^2 - y^2$. For $i \neq j$, $t_{i,j}^{\mu,\nu}$ is the hopping integral between different sites, and $t_{i,i}^{\mu,\nu} = E_\mu \delta_{\mu,\nu}$ is the on-site energy level [26]. The Fermi surfaces are composed of three hole-pockets (α_1, α_2, γ) and two electron-pockets (β_1, β_2), as shown in Fig. 10.5a.

The total Hamiltonian is given by $H_0 + H_{int}$, where H_{int} is the interaction term. H_{int} contains the multiorbital on-site Coulomb interaction term:

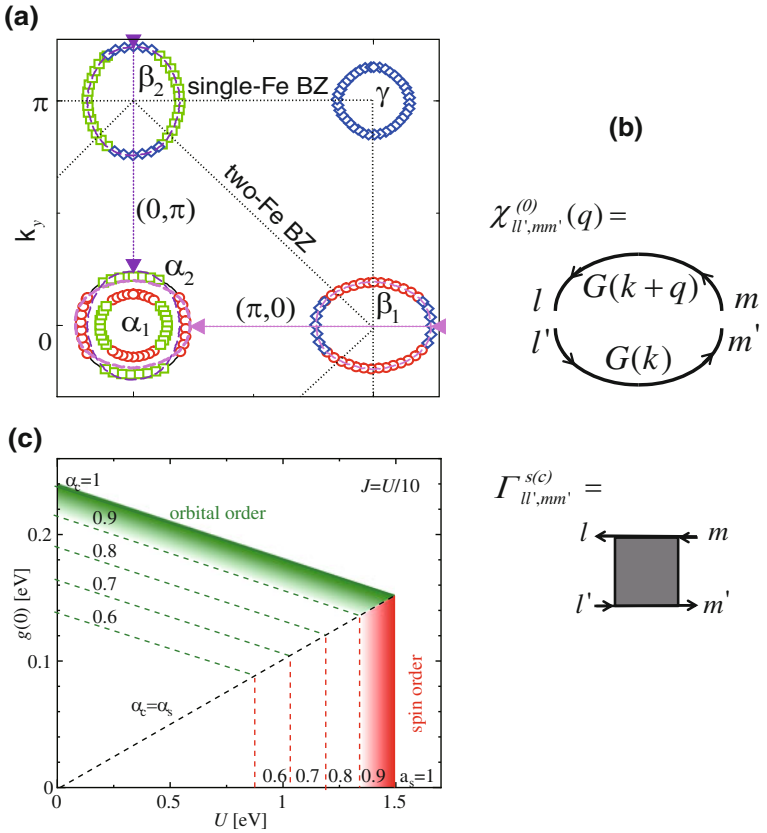

Fig. 10.5 **a** Fermi surfaces of Fe-based superconductors in the one-forth of the first Brillouin zone. **b** Bare bubble $\chi^0_{ll',mm'}(q)$ and bare vertex functions $\Gamma^{s(c)}_{ll',mm'}$. **c** The U-g phase diagram given by the RPA

$$
\begin{aligned}
H_{\mathrm{C}} = U \sum_{i,l} n_{i,l,\uparrow} n_{i,l,\downarrow} + \frac{U'}{2} \sum_{i,l \neq m} n_{i,l} n_{i,m} \\
+ \frac{J}{2} \sum_{i,l \neq m,\sigma,\sigma'} c^{\dagger}_{i,l,\sigma} c_{i,m,\sigma} c^{\dagger}_{i,m,\sigma'} c_{i,l,\sigma'} \\
+ \frac{J}{2} \sum_{i,l \neq m,\sigma} (c^{\dagger}_{i,l,\sigma} c_{i,m,\sigma} c^{\dagger}_{i,l,-\sigma} c_{i,m,-\sigma} + \mathrm{H.c.})
\end{aligned}
\tag{10.20}
$$

where U (U') is the intra-orbital (inter-orbital) Coulomb repulsion, $J(>0)$ is the exchange interaction, and the relation $U = U' + 2J$ holds. We also introduce the following quadrupole–quadrupole interaction in H_{int}:

$$H_{\rm quad} = -g \sum_i \sum_{\Gamma}^{xz,yz,xy} \hat{O}^i_\Gamma \hat{O}^i_\Gamma \tag{10.21}$$

where $\hat{O}_{\Gamma,i} = \sum_{\mu,\nu,\sigma} o^{\mu,\nu}_\Gamma c^\dagger_{i,\mu\sigma} c_{i,\nu\sigma}$ is the quadrupole operator for channel Γ at site i introduced in Ref. [35], and $-g$ is the coupling constant. (Note that $o^{\mu\nu}_{xz} = \langle\mu|\hat{x}\hat{z}|\nu\rangle$.) Here, we set $\langle xz|\hat{O}_{yz}|xy\rangle = \langle yz|\hat{O}_{xy}|xz\rangle = \langle xy|\hat{O}_{xz}|yz\rangle = 1$ by multiplying a constant. Recently, we have found that Eq. (10.21) is also caused by the vertex correction due to Coulomb interaction that is neglected in the RPA [39].

First, we study the total Hamiltonian $H_{\rm tot} = H_0 + H_{\rm C} + H_{\rm quad}$ based on the RPA: The RPA for multiorbital system was first performed in Ref. [40]. Here, the irreducible susceptibility is given by

$$\chi^0_{ll',mm'}(q) = -\frac{T}{N} \sum_k G^0_{lm}(k+q) G^0_{m'l'}(k), \tag{10.22}$$

where $\hat{G}^0(k) = [i\epsilon_n + \mu - \hat{H}^0_{\mathbf{k}}]^{-1}$ is the Green function in the orbital basis: $q = (\mathbf{q}, \omega_l)$, $k = (\mathbf{k}, \epsilon_n)$, and $\epsilon_n = (2n+1)\pi T$ is the fermion Matsubara frequency. μ is the chemical potential, and $\hat{H}^0_{\mathbf{k}}$ is the kinetic term in Eq. (10.19). Then, the susceptibilities for spin and charge sectors in the RPA are given as

$$\hat{\chi}^{s(c)}(q) = \hat{\chi}^0(q)[1 - \hat{\Gamma}^{s(c)}\hat{\chi}^0(q)]^{-1}. \tag{10.23}$$

The bare vertex for the spin and charge channels are respectively given as [40]

$$\Gamma^s_{l_1l_2,l_3l_4} = \begin{cases} U, & l_1 = l_2 = l_3 = l_4 \\ U', & l_1 = l_3 \neq l_2 = l_4 \\ J, & l_1 = l_2 \neq l_3 = l_4 \\ J', & l_1 = l_4 \neq l_2 = l_3 \end{cases} \tag{10.24}$$

$$\hat{\Gamma}^c(\omega_l) = -\hat{C} - 2\hat{V}(\omega_l), \tag{10.25}$$

$$C_{l_1l_2,l_3l_4} = \begin{cases} U, & l_1 = l_2 = l_3 = l_4 \\ -U' + 2J, & l_1 = l_3 \neq l_2 = l_4 \\ 2U' - J, & l_1 = l_2 \neq l_3 = l_4 \\ J', & l_1 = l_4 \neq l_2 = l_3 \end{cases} \tag{10.26}$$

$\hat{V}$ is given by Eq. (10.21), by neglect the ladder diagram contribution [35]. The bare bubble $\chi^0_{ll',mm'}(q)$ and bare vertex functions are schematically shown in Fig. 10.5b.

Figure 10.5c shows the U-g phase diagram obtained by the RPA (mean-field approximation) for the electron filling $n = 6.1$ and $J = U/10$. Here, α_c (α_s) is the charge (spin) Stoner factor, which is given by the maximum eigenvalue of $\hat{\Gamma}^{s(c)}\hat{\chi}^0(\mathbf{q}, 0)$. Then, the enhancement factor for $\chi^{\rm s(c)}$ is $(1 - \alpha_{\rm s(c)})^{-1}$, and $\alpha_{\rm s(c)} = 1$ gives the spin (orbital) order boundary. By solving the SC gap equation,

spin-fluctuation-mediated $s_{\pm}$-wave state is realized for $g = 0$ [26]. On the other hand, we obtain the s_{++}-wave state when the orbital fluctuations caused by g dominate over spin fluctuations [35].

Hereafter, we perform the FLEX approximation for the five-orbital model. The self-energy is given as

$$\Sigma_{l_1 l_3}(k) = \frac{T}{N} \sum_{q} \sum_{l_2 l_4} V_{l_1 l_2, l_3 l_4}(q) G_{l_2 l_4}(k - q), \tag{10.27}$$

$$\hat{V}(q) = \frac{3}{2} \hat{\Gamma}^s \hat{\chi}^s(q) \hat{\Gamma}^s + \frac{1}{2} \hat{\Gamma}^c \hat{\chi}^c(q) \hat{\Gamma}^c - \frac{1}{4} (\hat{\Gamma}^s - \hat{\Gamma}^c) \hat{\chi}^{\mathrm{irr}}(q) (\hat{\Gamma}^s - \hat{\Gamma}^c) + \frac{3}{2} \hat{\Gamma}^s + \frac{1}{2} \hat{\Gamma}^c, \tag{10.28}$$

where $k = (\mathbf{k}, \epsilon_n)$ with fermion Matsubara frequency $\epsilon_n = (2n + 1)\pi T$, and $q = (\mathbf{q}, \omega_n)$ with boson Matsubara frequency $\omega_n = 2n\pi T$. Then, the quasiparticle damping on the αth band is given by

$$\gamma_{\mathbf{k},\alpha} = \frac{1}{2} \sum_{lm} U^{\dagger}_{\mathbf{k},l\alpha} \mathrm{Im} \left\{ \Sigma^R_{lm}(\mathbf{k}, 0) - \Sigma^A_{lm}(\mathbf{k}, 0) \right\} U_{\mathbf{k},m\alpha}, \tag{10.29}$$

where $\Sigma_{lm}(\mathbf{k}, \omega)^{R(A)}$ is the retarded (advanced) self-energy given by the analytic continuation of Eq. (10.27), and $U_{\mathbf{k},m\alpha}$ is the unitary matrix introduced in Eq. (4.26). Figure 10.6a shows the quasiparticle damping on each Fermi surfaces due to spin (orbital) fluctuations, $\gamma^{s(c)}_{\mathbf{k}}$, for $T = 0.015$ and $U = 1.8$, given by substituting $\hat{V}$ in Eq. (10.27) with $[\frac{3}{2} \hat{\Gamma}^s \hat{\chi}^s \hat{\Gamma}^s + \frac{3}{2} \hat{\Gamma}^s]$ $([\frac{1}{2} \hat{\Gamma}^c \hat{\chi}^c \hat{\Gamma}^c + \frac{1}{2} \hat{\Gamma}^c])$.

In Fig. 10.6a, the relation $\gamma^s \gg \gamma^c$ holds for $g = 0$, and the momentum dependence of $\gamma^s_{\mathbf{k}}$ on each FS is small although the AF spin correlation is well developed. The value of γ^c increases with g, and the relation $\gamma^c \gg \gamma^s$ is satisfied for $g = 0.3$. Then, $\gamma^c_{\mathbf{k}}$ on FS4 (e-pocket) is anisotropic due to the momentum and orbital dependencies of $\chi^{s,c}_{ll',mm'}(\mathbf{q})$. Since the cold spot is on the e-pocket, the Hall coefficient R_{H} and thermoelectric poser S will be negative, consistently with experiments [41–43].

In Fig. 10.6b, we show the temperature dependence of the spin (orbital) susceptibility enhancement factor $S_{s(c)} = (1 - \alpha_{s(c)})^{-1}$, where $\alpha_{s(c)}$ is the Stoner factor. In the case of $U = 1.8$ and $g = 0$, large S_s ($\gtrsim 10$) is realized at $\mathbf{q} \approx \mathbf{Q} \equiv (\pi, 0)$ (i.e., $\chi^s(\mathbf{Q}, 0) \propto S_s$). S_s gradually increases as T drops, which is a typical critical behavior near the AF magnetic QCP [44]. When $g > 0$, $\chi^c(\mathbf{q}, 0)$ is enhanced at $\mathbf{q} = \mathbf{0}$ and $\mathbf{q} = \mathbf{Q}$ almost equivalently [36]. At $g = 0.3$, large S_c ($\gg 10$) is produced at $\mathbf{q} \approx \mathbf{Q}$ or $\mathbf{0}$, and it increases approximately proportional to T^{-1}.

Figure 10.6c, d show the obtained resistivity $\rho = 1/\sigma_{xx}$ for $U = 1.2$ and 1.8, given by neglecting the CVC: In case of $U = 1.2$, ρ shows a conventional sub-linear (concave) T-dependence at $g = 0$. ρ increases with g due to the orbital fluctuations, and almost T-linear resistivity is realized at $g = 0.22$. At $g = 0.25$, ρ shows a super-linear (convex) T-dependence. In case of $U = 1.8$, ρ is linear-in-T at $g = 0$,

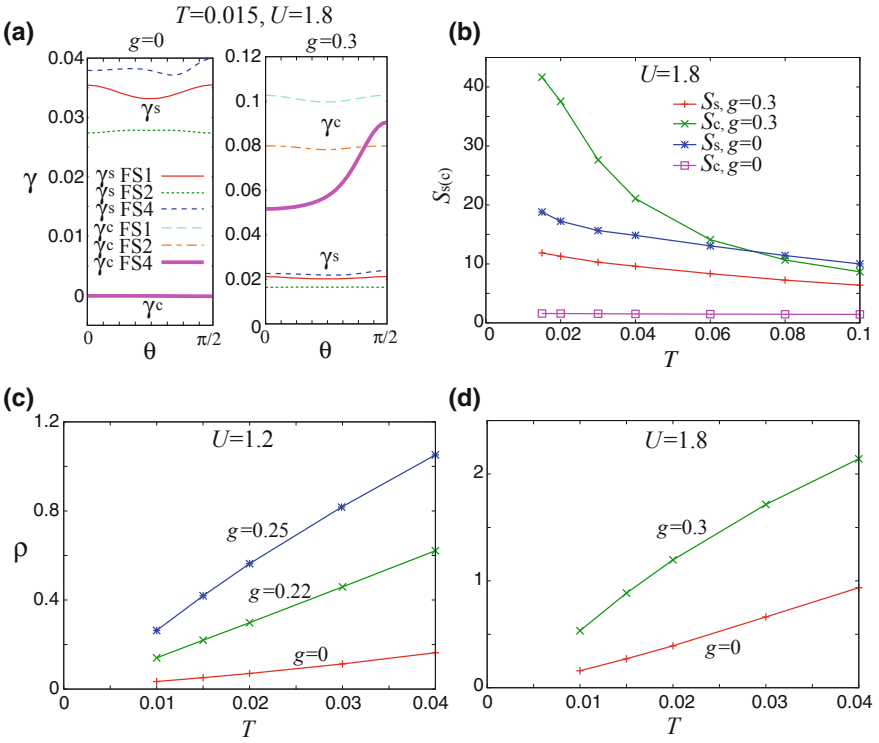

Fig. 10.6 **a** $\gamma_{\mathbf{k}}^{s(c)}$ on the Fermi surfaces. FS1,2,3,4 corresponds to FSα_1,α_2,β_1,β_2 in Fig. 10.5a. The angle θ represents the position on the Fermi surfaces: $\theta = \tan^{-1}(\tilde{k}_y/\tilde{k}_x)$, and the origin of $\tilde{\mathbf{k}}$ is the center of each Fermi surface. **b** Spin (charge) susceptibility enhancement $S_{s(c)} = (1 - \alpha_{s(c)})^{-1}$. **c**, **d** Resistivities given by the FLEX approximation

whereas it shows a clear super-linear T-dependence at $g = 0.3$. Thus, non-Fermi-liquid resistivity in Fe-based superconductors is produced by the combination of orbital and spin fluctuations.

We also study the thermo-electric power S based on the FLEX approximation. According to experimental results [45–49], S in e-doped systems is negative below the room temperature, and $|S|$ develops inversely proportional to the temperature till $T^* \sim 100\,\mathrm{K}$. In optimum doped $Ba(Fe_{1-x}Co_x)_2As_2$ peak value of $|S| \sim 50\,\mu\mathrm{V/K}$ and $T^* \sim 130\,\mathrm{K}$ are observed [49]. The obtained T-dependence of S is presented in Fig. 10.7. In the case of $U = 1.2$ shown in Fig. 10.7a, Fermi-liquid behavior ($S \propto T$) is obtained for $g = 0$, where both the spin and orbital fluctuations are weak. For $g = 0.25$, where the orbital fluctuation is strong, $|S|$ becomes larger than that for $g = 0$, and the deviation from the Fermi-liquid-like behavior is realized.

In the case of $U = 1.8$ shown in Fig. 10.7b, where spin fluctuations are strong, non-Fermi-liquid-like behavior becomes more prominent. For $g = 0$, the value of $|S|$ is small and almost independent of T. On the other hand, $|S|$ is drastically enhanced,

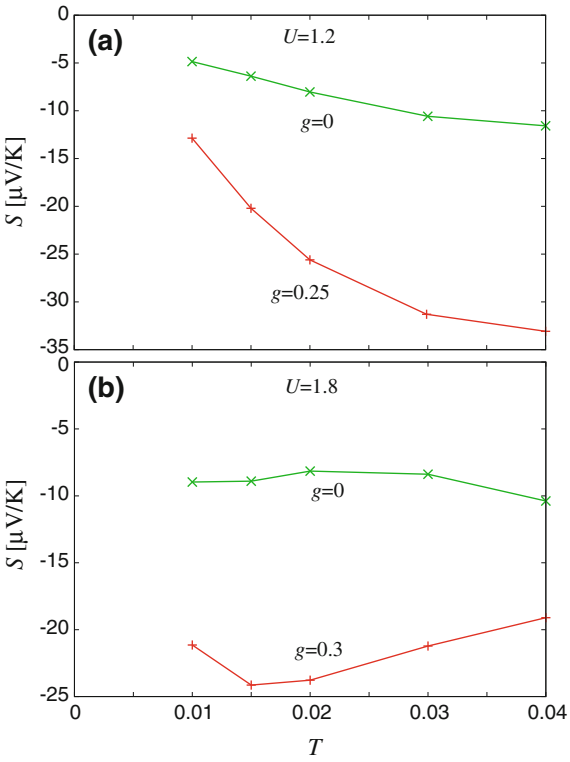

Fig. 10.7 Thermoelectric power given by the FLEX approximation

and shows the peak at $T^* \sim 150\,\mathrm{K}$ for $g = 0.3$, where both the spin and orbital fluctuations are strong. The obtained result for $U = 1.8$ and $g = 0.3$ is consistent with experiments [45–49], meaning the cooperative development of orbital and spin fluctuations in Fe-based superconductors.

In the following, we explain why the absolute value of S becomes large for $g \sim 0.3$. Since $v_{\alpha,\mathbf{k}} \sim 1/N_\alpha(\omega)$ at $\omega = \varepsilon^\alpha_{\mathbf{k}}$, where N_α and $\varepsilon^\alpha_{\mathbf{k}}$ are the density of state and the dispersion on band α, respectively, S is rewritten as

$$\begin{aligned} S &\propto \frac{e}{\sigma_{xx} T} \sum_\alpha \int_{-\infty}^{\infty} d\omega \frac{z_\alpha \omega}{N_\alpha(\omega)\gamma_a(\omega)} \left(-\frac{\partial f(\omega)}{\partial \omega}\right) \\ &\propto \frac{-eT}{\sigma_{xx}} \sum_\alpha z_\alpha \frac{\partial}{\partial \omega} \left(\frac{1}{N_\alpha(\omega)\gamma_\alpha(\omega)}\right)_{\omega=0}, \end{aligned} \tag{10.30}$$

where z_α and γ_α are the renormalization factor and the quasiparticle damping on band α, respectively. In the presence of strong orbital fluctuation with large value of g, the absolute value of S is strongly enhanced due to the large value of $\frac{\partial}{\partial \omega}\gamma_\alpha > 0$ at the cold

spots on e-pocket (see Fig. 10.6a). Thus, the orbital fluctuation plays an important role in various anomalous transport phenomena in Fe-based superconductors.

Within the RPA, the condition $J \leq 0$ is required for the development of orbital fluctuations ($\alpha_c \lesssim 1$) in multiorbital Hubbard models (without g) under the constraint $U = U' + 2J$. Taking this fact into account, we have introduced small quadrupole interaction g, and shown that strong orbital fluctuations are induced even for finite J. The interaction g could be derived from not only the e-ph interaction, but also the "Coulomb interaction" due to the vertex correction, which describes the many-body effect beyond the RPA.

Actually, we have recently studied the mechanism of orbital/spin fluctuations due to multiorbital Coulomb interaction ($U = U' + 2J$) going beyond the RPA. For this purpose, we develop a self-consistent vertex correction (SC-VC) method, and find that both orbital and spin fluctuations are strongly emphasized by the VC, even if $g = 0$ [39]. It is found that both the antiferro-orbital and ferro-orbital fluctuations simultaneously develop for $J/U \sim 0.1$, both of which contribute to the s-wave superconductivity. Especially, the ferro-orbital fluctuations give the orthorhombic structure transition as well as the softening of shear modulus C_{66}.

In the SC-VC method, the susceptibility for the charge (spin) channel is given by

$$\hat{\chi}^{c(s)}(q) = \hat{\chi}^{\mathrm{irr},c(s)}(q)(1 - \hat{\Gamma}^{c(s)}\hat{\chi}^{\mathrm{irr},c(s)}(q))^{-1}, \tag{10.31}$$

where the irreducible susceptibility is given as

$$\hat{\chi}^{\mathrm{irr},c(s)}(q) = \hat{\chi}^{0}(q) + \hat{X}^{c(s)}(q), \tag{10.32}$$

where $\chi^0_{ll',mm'}(q) = -T\sum_p G_{lm}(p+q)G_{m'l'}(p)$ is the bare bubble, and the second term is the VC that is neglected in both RPA and FLEX approximation. In the present discussion, it is convenient to consider the quadrupole susceptibilities:

$$\begin{aligned}\chi^c_\gamma(q) &\equiv \sum_{ll',mm'} O^{l,l'}_\gamma \chi^c_{ll',mm'}(q) O^{m',m}_\gamma \\ &= \mathrm{Tr}\{\hat{O}_\gamma \hat{\chi}^c(q)\hat{O}_\gamma\}.\end{aligned} \tag{10.33}$$

Non-zero matrix elements of the quadrupole operators for the t_{2g}-orbital $2 = xz$, $3 = yz$, $4 = xy$ are $O^{3,4}_{xz} = O^{2,4}_{yz} = O^{2,2}_{x^2-y^2} = -O^{3,3}_{x^2-y^2} = 1$ [50]. Here, the charge (spin) Stoner factor $\alpha^{c(s)}_{\mathbf{q}}$ is given by the largest eigenvalue of $\hat{\Gamma}^{c(s)}\hat{\chi}^{\mathrm{irr},c(s)}(\mathbf{q})$ at $\omega_l = 0$.

Here, we study the role of VC due to the Maki-Thompson (MT) and Aslamazov-Larkin (AL) terms in Fig. 10.8a, which become important near the QCPs [44, 51]. Here, $\hat{X}^{c(s)}(q) \equiv \hat{X}^{\uparrow,\uparrow}(q) + (-)\hat{X}^{\uparrow,\downarrow}(q)$, and wavy lines represent $\chi^{s,c}$. The AL term (AL1 + AL2) for the charge sector is given as

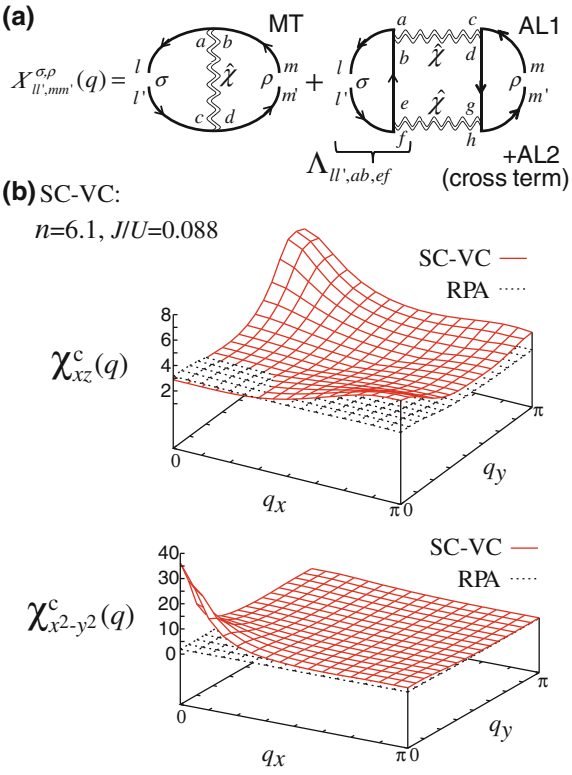

Fig. 10.8 **a** The MT and AL terms: The wavy and *solid lines* are susceptibilities and electron Green functions, respectively. **b** $\chi^c_{xz}(\mathbf{q})$ and $\chi^c_{x^2-y^2}(\mathbf{q})$ given by the SC-VC method for $n = 6.1$ and $J/U = 0.088$. $\alpha^s_{\max} = \alpha^c_{\mathbf{0}} = 0.97$ and $\alpha^c_{\mathbf{Q}} = 0.86$

$$X^{\mathrm{AL},c}_{ll',mm'}(q) = \frac{T}{2}\sum_k \sum_{a\sim h} \Lambda_{ll',ab,ef}(q;k)\{V^c_{ab,cd}(k+q)V^c_{ef,gh}(-k) + 3V^s_{ab,cd}(k+q)V^s_{ef,gh}(-k)\}\Lambda'_{mm',cd,gh}(q;k), \tag{10.34}$$

where $\hat{V}^{s,c}(q) \equiv \hat{\Gamma}^{s,c} + \hat{\Gamma}^{s,c}\hat{\chi}^{s,c}(q)\hat{\Gamma}^{s,c}$, $\hat{\Lambda}(q;k)$ is the three-point vertex made of three Green functions in Fig. 10.8a [50], and $\Lambda'_{mm',cd,gh}(q;k) \equiv \Lambda_{ch,mg,dm'}(q;k) + \Lambda_{gd,mc,hm'}(q;-k-q)$. According to Eq. (10.34) and Ref. [50], $X^{\mathrm{AL},c}_{x^2-y^2}(\mathbf{0}) \sim \Lambda^2 U^4 T\sum_q\{\chi^s(q)\}^2$ when $\alpha_s \lesssim 1$, and it grows in proportion to $T\chi^s(\mathbf{Q})$ [$\log\{\chi^s(\mathbf{Q})\}^2$] at high [low] temperatures. We include all U^2-terms, which are important for reliable results.

In the SC-VC method, we perform a self-consistent calculation of the VC as well as spin/orbital fluctuations. Then, $\hat{\chi}^c(q)$ is strongly enhanced by $X^{\mathrm{AL},c}$ in Eq. (10.34), which is relevant when either $\hat{\chi}^c$ or $\hat{\chi}^s$ is large. On the other hand, $\hat{X}^s \sim T\sum \Lambda \cdot V^s V^c \cdot \Lambda$ is less important, as explained in Refs. [39, 52]. Therefore, we drop $\hat{X}^s(q)$ to simplify the argument. Figure 10.8b show $\chi^c_\gamma(\mathbf{q})$ given by the SC-VC method for $n = 6.1$, $J/U = 0.088$ and $U = 1.53$; the Stoner factors are $\alpha^s_{\max} = \alpha^c_{\mathbf{0}} = 0.97$ and

$\alpha^c_{\mathbf{Q}} = 0.86$. Compared to the RPA, both $\chi^c_{x^2-y^2}(\mathbf{q})$ and $\chi^c_{xz}(\mathbf{q})$ are strongly enhanced by the charge AL term, $\hat{X}^{\mathrm{AL},c}$, since the results are essentially unchanged even if MT term is dropped. In the SC-VC method, the enhancements of other charge multipole susceptibilities are small. Especially, the density susceptibility $\sum_{l,m} \hat{\chi}^c_{ll,mm}(\mathbf{q})$ is suppressed in the SC-VC method.

Here, we make comparison between the present SC-VC method with other theoretical methods. The present multi-fluctuation mechanism is not correctly described by the dynamical-mean-field theory (DMFT), since the irreducible VC is treated as *local*. Also, the local density approximation (LDA), in which the VC is neglected, does not reproduce the nonmagnetic orthorhombic phase.

We discuss the physical meaning of the VC in the strong-coupling regime ($t/U \gg 1$): Due to the Kugel-Khomskii (KK) type spin-orbital exchange coupling $\sim (t^2/U)(\mathbf{s}_i \cdot \mathbf{s}_j)(O^i_{x^2-y^2} \cdot O^j_{x^2-y^2})$, the antiferro-spin order induces the ferro-orbital order, and vise versa. Such spin-orbital coupling should be finite even in the metallic state ($t \sim U$), and it is actually described by the AL-type VC. For this reason, cooperative development of spin and orbital fluctuations is obtained in the SC-VC analysis. [The RPA is insufficient in multiorbital Hubbard models in that it fails to reproduce the KK-type spin-orbital coupling.] Especially, non-magnetic orbital nematic order can be realized since the scalar order parameter $O_{x^2-y^2}$ is more stable than the vector order parameter $\mathbf{s}$ against the quantum and thermal fluctuations.

In summary, we developed the SC-VC method, and obtained the Coulomb-interaction-driven nematic and AF-orbital fluctuations due to the multimode (orbitons + magnons) interference effect [50] that is overlooked in the RPA. For $J/U \lesssim (J/U)_c$, the structure transition ($\alpha^c_{\mathbf{0}} \approx 1$) occurs prior to the magnetic transition ($\alpha^s_{\mathbf{Q}} \approx 1$), consistently with experiments. When $\alpha^s_{\max} \sim \alpha^c_{\max}$, both s_{++}- and $s_{\pm}$-states could be realized, depending on model parameters like the impurity concentration n_{imp} [35]. We expect that orbital-fluctuation-mediated superconductivity and structure transition are realized in many iron-based superconductors due to the cooperation of the Coulomb and e-ph interactions.

Recently, the SC-VC method had been applied to the (d_{xz}, d_{yz})-orbital Hubbard model introduced in Sect. 4.2. It was revealed that the ferro-quadrupole susceptibility $\chi^c_{x^2-y^2}(\mathbf{0})$ develops divergently near the magnetic QCP due to the AL-type VC [52]. This result would explain the "electronic nematic order" in a double-layer Ru-oxide, $Sr_3Ru_2O_7$, realized near the field-induced magnetic QCP [53]. It is noteworthy that the renormalization group (RG) method had been applied to this model, and the development of $\chi^c_{x^2-y^2}(\mathbf{0})$ had been confirmed [54]. The RG method is known as an unbiased and reliable theoretical method, whereas perturbation methods calculate only selected Feynman diagrams. Therefore, the mechanism of orbital nematic fluctuation due to AL-type VC had been confirmed by several reliable theoretical methods.

References

1. K. Hanzawa, K. Yosida, K. Yamada, Prog. Theor. Phys. **81**, 960 (1989)
2. H. Kontani, K. Yamada, J. Phys. Soc. Jpn. **63**, 2627 (1994)
3. K. Kadowaki, S.B. Woods, Solid State Commun. **58**, 507 (1986)
4. H. Kontani, J. Phys. Soc. Jpn. **73**, 515 (2004)
5. H. Kontani, Phys. B. **359–361**, 202 (2005)
6. A. Georges, G. Kotliar, W. Krauth, M.J. Rozenberg, Rev. Mod. Phys. **68**, 13 (1996)
7. G. Kotliar, D. Vollhardt, Phys. Today **57**, 53 (2004)
8. K. Yamada, Prog. Theor. Phys. **53**, 970 (1975)
9. K. Yamada, K. Yosida, Prog. Theor. Phys. **53**, 1286 (1975)
10. K. Yamada, K. Yosida, Prog. Theor. Phys. **54**, 316 (1975)
11. A. Yoshimori, Prog. Theor. Phys. **55**, 67 (1976)
12. H. Shiba, Prog. Theor. Phys. **54**, 967 (1975)
13. N. Tsujii, H. Kontani, K. Yoshimura, Phys. Rev. Lett. **94**, 057201 (2005)
14. K. Behnia, D. Jaccard, J. Flouquet, J. Phys. Condens. Matter. **16**, 5187 (2004)
15. K. Miyake, H. Kohno, J. Phys. Soc. Jpn. **74**, 254 (2005)
16. M.S. Torikachvili, S. Jia, E.D. Mun, S.T. Hannahs, R.C. Black, W.K. Neils, D. Martien, S.L. Bud'ko, P.C. Canfield, Proc. Natl. Acad. Sci. U. S. A. **104**, 9960 (2007)
17. H. Kontani, K. Yamada, J. Phys. Soc. Jpn. **65**, 172 (1996)
18. H. Kontani, K. Yamada, J. Phys. Soc. Jpn. **66**, 2232 (1997)
19. Y. Kamihara, T. Watanabe, M. Hirano, H. Hosono, J. Am. Chem. Soc. **130**, 3296 (2008)
20. C.R. Rotundu1, R.J. Birgeneau, arXiv:1106.5761
21. M. Yoshizawa et al., Private communication
22. T. Goto, R. Kurihara, K. Araki, K. Mitsumoto, M. Akatsu, Y. Nemoto, S. Tatematsu, M. Sato, J. Phys. Soc. Jpn. **80**, 073702 (2011)
23. T. Goto et al., (unpublised)
24. S. Kasahara, T. Shibauchi, K. Hashimoto, K. Ikada, S. Tonegawa, R. Okazaki, H. Ikeda, H. Takeya, K. Hirata, T. Terashima, Y. Matsuda, Phys. Rev. B **81**, 184519 (2010)
25. I.I. Mazin, D.J. Singh, M.D. Johannes, M.H. Du, Phys. Rev. Lett. **101**, 057003 (2008)
26. K. Kuroki, R. Arita, H. Aoki, Phys. Rev. B **60**, 9850 (1999)
27. S. Graser, G.R. Boyd, C. Cao, H.-P. Cheng, P.J. Hirschfeld, D.J. Scalapino, Phys. Rev. B **77**, 180514(R) (2008)
28. A.V. Chubukov, D.V. Efremov, I. Eremin, Phys. Rev. B **78**, 134512 (2008)
29. S. Onari, H. Kontani, Phys. Rev. Lett. **103**, 177001 (2009)
30. A. Kawabata, S.C. Lee, T. Moyoshi, Y. Kobayashi, M. Sato, J. Phys. Soc. Jpn. **77** (2008) Suppl. C 103704
31. M. Sato, Y. Kobayashi, S.C. Lee, H. Takahashi, E. Satomi, Y. Miura, J. Phys. Soc. Jpn. **79**, 014710 (2009)
32. S.C. Lee, E. Satomi, Y. Kobayashi, M. Sato, J. Phys. Soc. Jpn. **79**, 023702 (2010)
33. Y. Nakajima, T. Taen, Y. Tsuchiya, T. Tamegai, H. Kitamura, T. Murakami, Phys. Rev. B **82**, 220504 (2010)
34. J. Li, Y. Guo, S. Zhang, S. Yu, Y. Tsujimoto, H. Kontani, K. Yamaura, E. Takayama-Muromachi, Phys. Rev. B **84**, 020513(R) (2011)
35. H. Kontani, S. Onari, Phys. Rev. Lett. **104**, 157001 (2010)
36. T. Saito, S. Onari, H. Kontani, Phys. Rev. B **82**, 144510 (2010)
37. S. Onari, H. Kontani, arXiv:1009.3882
38. S. Onari, H. Kontani, Phys. Rev. B **85**, 134507 (2012)
39. S. Onari, H. Kontani, Phys. Rev. Lett. **109**, 137001 (2012)
40. T. Takimoto et al., J. Phys. Condens. Matter. **14**, L369 (2002)
41. S.C. Lee, A. Kawabata, T. Moyoshi, Y. Kobayashi, M. Sato, J. Phys. Soc. Jpn. **78**, 043703 (2009)
42. R.H. Liu, G. Wu, T. Wu, D.F. Fang, H. Chen, S.Y. Li, K. Liu, Y.L. Xie, X.F. Wang, R.L. Yang, L. Ding, C. He, D.L. Feng, X.H. Chen, Phys. Rev. Lett. **101**, 087001 (2008)

43. S. Kasahara, T. Shibauchi, K. Hashimoto, K. Ikada, S. Tonegawa, R. Okazaki, H. Shishido, H. Ikeda, H. Takeya, K. Hirata, T. Terashima, Y. Matsuda, Phys. Rev. B **81**, 184519 (2010)
44. T. Moriya, K. Ueda, Adv. Phys. **49**, 555 (2000)
45. M.A. McGuire et al., Phys. Rev. B **78**, 094517 (2008)
46. M. Tropeano, C. Fanciulli, C. Ferdeghini, D. Marre, A.S. Siri, M. Putti, A. Martinelli, M. Ferretti, A. Palenzona, M.R. Cimberle, C. Mirri, S. Lupi, R. Sopracase, P. Calvani, A. Perucchi, Supercond. Sci. Technol. **22**, 034004 (2009)
47. S.J. Singh, J. Prakash, S. Patnaik, A.K. Ganguli, Supercond. Sci. Technol. **22**, 045017 (2009)
48. V.P.S. Awana, R.S. Meena, A. Pal, A. Vajpayee, K.V.R. Rao, H. Kishan, Eur. Phys. J. B **79**, 139 (2011)
49. E.D. Mun, S.L. Bud'ko, N. Ni, A.N. Thaler, P.C. Canfield, Phys. Rev. B **80**, 054517 (2009)
50. H. Kontani, T. Saito, S. Onari, Phys. Rev. B **84**, 024528 (2011)
51. N.E. Bickers, S.R. White, Phys. Rev. B **43**, 8044 (1991)
52. Y. Ohno, M. Tsuchiizu, S. Onari, H. Kontani, J. Phys. Soc. Jpn. **82**, 013707 (2013)
53. A.P. Mackenzie, J.A.N. Bruin, R.A. Borzi, A.W. Rost, S.A. Grigera, Phys. C **481**, 207 (2012)
54. M. Tsuchiizu, S. Onari, H. Kontani, arXiv:1209.3664

Chapter 11
AHE and SHE in Multiorbital Systems

In previous chapters, we studied transport phenomena single-band models, and showed that the CVC induces various striking non-Fermi-liquid-like behaviors in the presence of AF fluctuations. For example, $R_{\rm H}$ shows strong temperature dependence due to the CVC. In multiband systems, however, $R_{\rm H}$ can exhibit temperature dependence or sign change within the RTA, if a hole-like Fermi surface and an electron-like Fermi surface coexist and their relaxation times have different T-dependences. There are many such examples even in conventional metals. However, $|R_{\rm H}|$ is as small as $\sim 1/ne$ in this multiband mechanism. Thus, the RTA+multiband mechanism is impossible to explain the huge $|R_{\rm H}| \gg 1/ne$ observed in various systems near the AF QCP.

On the other hand, as discussed in Chap. 4, the intrinsic AHE and SHE are the transport phenomena that are inherent in multiband systems. In the presence of the spin-orbit interaction (SOI), the Bloch electron acquires the trajectory- and spin-dependent Berry phase, which works as the spin-dependent outer magnetic field. These transport phenomena in various d- and f-electron systems are now attracting growing attentions. In this chapter, we explain resent development of the intrinsic AHE and SHE in multiorbital models in the presence of SOI. To analyze these quantum transport phenomena, we have to use the linear response theory. We will show that the huge SHE and AHE in various d- and f-electron systems originates from the "spin-dependent Berry phase" induced by the atomic orbital angular momentum.

11.1 SHE in Transition Metals

In this section, we study the intrinsic SHC in various $5d$-transition metals (Ta, W, Re, Os, Ir, Pt, and Au) and $4d$-transition metals (Nb, Mo, Tc, Ru, Rh, Pd, and Ag) based on realistic multiorbital tight-binding models, which enables us to perform quantitatively reliable analysis. In each metal, the obtained intrinsic SHC is independent of resistivity in the low resistive regime ($\rho < 50\,\mu\Omega\,$cm) whereas it decreases in

H. Kontani, *Transport Phenomena in Strongly Correlated Fermi Liquids*,
Springer Tracts in Modern Physics 251, DOI: 10.1007/978-3-642-35365-9_11,

proportion to ρ^{-2} in the high resistive regime. In the low resistive regime, the SHC takes a large positive value in Pt and Pd, both of which have approximately nine d-electrons per ion ($n_d = 9$). On the other hand, the SHC takes a large negative value in Ta, Nb, W, and Mo where $n_d < 5$. The origin of the SHE is the spin-dependent Aharonov-Bohm phase factor discussed in the previous section.

After the theory of Karplus-Luttinger, theories of the intrinsic SHE have been developed based on several specific theoretical models [1–9]. In the present study, we employ the Naval Research Laboratory tight-binding (NRL-TB) model developed by Papaconstantopoulos et al. [10, 11], which enables us to construct nine-orbital ($s + p + d$) tight binding models for each transition metal. This is a non-orthogonal Slater-Koster (SK) model. To describe the electronic state in $4d$ ($5d$) metals, we consider $5s$, $5p$, and $4d$ ($6s$, $6p$, and $5d$) orbitals, that is, we consider nine orbitals per atom.

Table 11.1 shows the crystal structure, electron number per atom, and the coupling constant λ of SOI $\lambda \sum_i \hat{l}_i \hat{s}_i$ ($i = x, y, z$) for various $4d$- and $5d$-transition metals. ($m_d d^{n_d} m_s s^{n_s}$) represent the electronic configuration of an isolated atom, where m_d and m_s is the main quantum number, and n_s and n_d is the number of electrons on s- and d-orbital. In this table, we put $\lambda = 0.03$ Ry for $5d$ electron in Pt and $\lambda = 0.013$ Ry for $4d$ electron in Pd, according to optical spectroscopy [12]. For other $4d$- and $5d$- transition metals, we used Herman-Skillman atomic spin-orbit parameters [13]: These parameters had been calculated by using the self-consistent Hartree-Fock-Slater atomic functions. Here, we consider only the d-orbital SOI, and neglect other SOI terms which may be **k**-dependent. In this section, we set the unit of energy Ry; 1 Ry = 13.6 eV.

Table 11.1 The crystal structure, electron number per atom, and the coupling constant λ of SOI for various transition metals

Metals	Structure	Electron number	SOI (Ry)
Nb	bcc	5 ($4d^4 5s^1$)	0.006
Mo	bcc	6 ($4d^5 5s^1$)	0.007
Tc	hcp	7 ($4d^6 5s^1$)	0.009
Ru	hcp	8 ($4d^7 5s^1$)	0.01
Rh	fcc	9 ($4d^8 5s^1$)	0.011
Pd	fcc	10 ($4d^{10} 5s^0$)	0.013
Ag	fcc	11 ($4d^{10} 5s^1$)	0.019
Ta	bcc	5 ($5d^3 6s^2$)	0.023
W	bcc	6 ($5d^4 6s^2$)	0.027
Re	hcp	7 ($5d^5 6s^2$)	0.025
Os	hcp	8 ($5d^6 6s^2$)	0.025
Ir	fcc	9 ($5d^9 6s^0$)	0.025
Pt	fcc	10 ($5d^9 6s^1$)	0.03
Au	fcc	11 ($5d^{10} 6s^1$)	0.03

($m_d d^{n_d} m_s s^{n_s}$) represent the electronic configuration of an isolated atom. Here, m_d and m_s is the main quantum number, and n_s and n_d is the number of electrons on s- and d-orbital. Bcc, hcp and fcc represents a body-centered cubic, hexagonal closed packed and face-centered cubic, respectively

In the presence of SOI for $4d$ or $5d$ electrons, the total Hamiltonian is given by

$$\hat{H} = \begin{pmatrix} \hat{H}_0 + \lambda \hat{l}_z/2 & \lambda(\hat{l}_x - i\hat{l}_y)/2 \\ \lambda(\hat{l}_x + i\hat{l}_y)/2 & \hat{H}_0 - \lambda \hat{l}_z/2 \end{pmatrix}, \tag{11.1}$$

here the first and the second rows (columns) correspond to $s_z = +\hbar/2$ ($\uparrow$-spin) and $s_z = -\hbar/2$ ($\downarrow$-spin). $\hat{H}_0$ is 9×9 matrix given by NRL-TB model for bcc and fcc structure, whereas it is 18×18 matrix for hpc structure since a unit cell contains two atoms. The matrix elements of $\mathbf{l}$ for d-orbital are given by [12]

$$l_x = \begin{pmatrix} 0 & 0 & -i & 0 & 0 \\ 0 & 0 & 0 & -i & -i\sqrt{3} \\ i & 0 & 0 & 0 & 0 \\ 0 & i & 0 & 0 & 0 \\ 0 & i\sqrt{3} & 0 & 0 & 0 \end{pmatrix}, \tag{11.2}$$

$$l_y = \begin{pmatrix} 0 & i & 0 & 0 & 0 \\ -i & 0 & 0 & 0 & 0 \\ 0 & 0 & 0 & -i & i\sqrt{3} \\ 0 & 0 & i & 0 & 0 \\ 0 & 0 & -i\sqrt{3} & 0 & 0 \end{pmatrix}, \tag{11.3}$$

$$l_z = \begin{pmatrix} 0 & 0 & 0 & 2i & 0 \\ 0 & 0 & i & 0 & 0 \\ 0 & -i & 0 & 0 & 0 \\ -2i & 0 & 0 & 0 & 0 \\ 0 & 0 & 0 & 0 & 0 \end{pmatrix}. \tag{11.4}$$

where the first to the fifth rows (columns) correspond to d-orbitals xy, yz, zx, $x^2 - y^2$, and $3z^2 - r^2$, respectively.

In NRL-TB model, we use the non-orthogonal basis since the atomic wave functions of different sites are not orthogonal:

$$\int d\mathbf{r} \phi_\alpha^*(\mathbf{r} - \mathbf{R}_i)\phi_\beta(\mathbf{r} - \mathbf{R}_{i'}) = O_{\alpha\beta}(\mathbf{R}_i - \mathbf{R}_{i'}), \tag{11.5}$$

where $\phi_\alpha(\mathbf{r} - \mathbf{R}_i)$ represents the atomic wave function at the ith site and α, β is orbital state indices, and $O_{\alpha\beta}(\mathbf{R}_i - \mathbf{R}_{i'})$ represents the overlap integral between different sites. The band structures obtained for the present model in Au and Ta are shown in Fig. 11.1. Near the Fermi level, the obtained band structures are in good agreement with the results of the relativistic first-principles calculations [14, 15].

In this case, creation and annihilation operators $c^\dagger_{\mathbf{k}\alpha}$, $c_{\mathbf{k}\alpha}$ do not satisfy the canonical anticommutation relations, but instead satisfy [16]

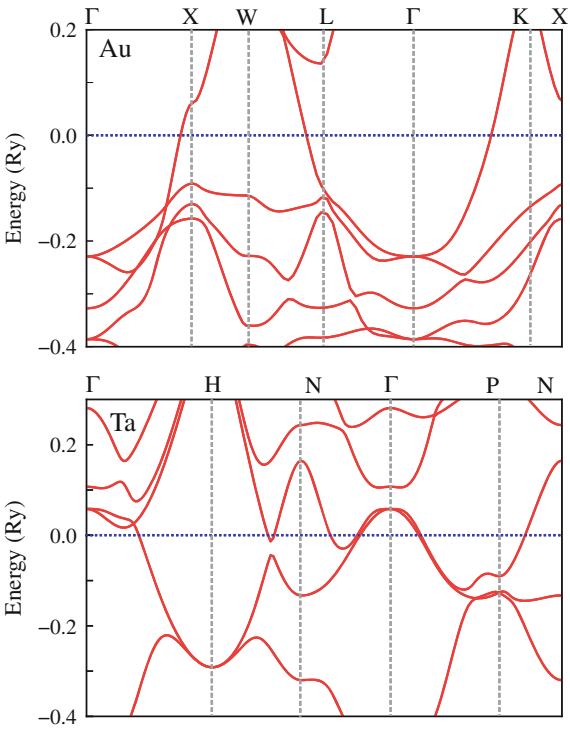

Fig. 11.1 (*upper panel*) Band structure of Au. Here, $\Gamma = (0, 0, 0)$, $\mathrm{X} = (\pi, 0, 0)$, $\mathrm{W} = (\pi, \pi/2, 0)$, $\mathrm{L} = (\pi/2, \pi/2, \pi/2)$, and $\mathrm{K} = (3\pi/4, 3\pi/4, 0)$. (*lower panel*) Band structure of Ta. Here, $\Gamma = (0, 0, 0)$, $\mathrm{H} = (\pi, 0, 0)$, $\mathrm{N} = (\pi/2, \pi/2, 0)$, $\mathrm{P} = (\pi/2, \pi/2, \pi/2)$. Near the Fermi level, we see that the band structures obtained in the present model agree well with the result of the relativistic first-principles calculation in Refs. [14, 15]

$$\{c_{\mathbf{k}\alpha}, c^{\dagger}_{\mathbf{k}'\beta}\} = \delta_{\mathbf{k}\mathbf{k}'} O^{-1}_{\alpha\beta}(\mathbf{k}). \tag{11.6}$$

Since matrix $\hat{O}(\mathbf{k})$ is positive definite Hermitian matrix, we can introduce a matrix $\hat{S}(\mathbf{k})$ that transforms $\hat{O}(\mathbf{k})$ into the unit matrix:

$$\hat{S}^{\dagger}(\mathbf{k})\hat{O}(\mathbf{k})\hat{S}(\mathbf{k}) = 1. \tag{11.7}$$

We note that matrix $\hat{S}(\mathbf{k})$ cannot be determined uniquely: Using an arbitrary unitary matrix $\hat{X}$, $\hat{S}' = \hat{S}\hat{X}$ also satisfies Eq. (11.7). Here, we introduce the following new basis $(\bar{c}_{\mathbf{k}\alpha}, \bar{c}^{\dagger}_{\mathbf{k}\alpha})$ using $\hat{S}(\mathbf{k})$:

$$\bar{c}_{\mathbf{k}\alpha} = \sum_{\beta} S^{-1}_{\alpha\beta}(\mathbf{k}) c_{\mathbf{k}\beta}. \tag{11.8}$$

We can easily verify that these operators $(\bar{c}_{\mathbf{k}\alpha}, \bar{c}^{\dagger}_{\mathbf{k}\alpha})$ satisfy the canonical anticommutation relations $\{\bar{c}_{\mathbf{k}\alpha}, \bar{c}^{\dagger}_{\mathbf{k}'\beta}\} = \delta_{\mathbf{k}\mathbf{k}'}\delta_{\alpha\beta}$. In this basis, the Hamiltonian is rewritten as

$$\hat{H}_0 = \sum_{\mathbf{k},\alpha,\beta} \bar{c}^{\dagger}_{\mathbf{k}\alpha} \left[\bar{h}_{\alpha\beta}(\mathbf{k}) - \mu\delta_{\alpha\beta} \right] \bar{c}_{\mathbf{k}\beta}, \tag{11.9}$$

where $\bar{h}_{\alpha\beta}(\mathbf{k}) = (\hat{S}^{\dagger}(\mathbf{k})\hat{h}(\mathbf{k})\hat{S}(\mathbf{k}))^{\alpha\beta} \equiv (\hat{\bar{h}}(\mathbf{k}))^{\alpha\beta}$. Therefore, the Green function in the $(\bar{c}_{\mathbf{k}\alpha}, \bar{c}^{\dagger}_{\mathbf{k}\alpha})$ basis is given by

$$\hat{\bar{G}}(\mathbf{k}, \omega) = \left(\omega + \mu - \hat{\bar{h}}(\mathbf{k}) \right)^{-1}. \tag{11.10}$$

As shown in Ref. [17], based on the continuity equation, the current operator in the $(c_{\mathbf{k}\alpha}, c^{\dagger}_{\mathbf{k}\alpha})$ basis is given by

$$\hat{v}_x(\mathbf{k}) = \frac{\partial \hat{h}(\mathbf{k})}{\partial k_x} + \frac{1}{2}\hat{h}(\mathbf{k})\hat{D}_x(\mathbf{k}) + \frac{1}{2}\hat{D}^{\dagger}_x(\mathbf{k})\hat{h}(\mathbf{k}), \tag{11.11}$$

where $D_x(\mathbf{k})$ is given by

$$\hat{D}_x(\mathbf{k}) = \left\{ \frac{\partial}{\partial k_x} \hat{O}^{-1}(\mathbf{k}) \right\} \hat{O}(\mathbf{k}) = -\hat{O}^{-1}(\mathbf{k}) \frac{\partial}{\partial k_x} \hat{O}(\mathbf{k}). \tag{11.12}$$

Apparently, $\hat{D}_x(\mathbf{k}) = 0$ in an orthogonal basis. In the $(\bar{c}_{\mathbf{k}\alpha}, \bar{c}^{\dagger}_{\mathbf{k}\alpha})$ basis, the velocity $\hat{\bar{v}}_x(\mathbf{k})$ is given by

$$\hat{\bar{v}}_x(\mathbf{k}) = \hat{S}^{\dagger}(\mathbf{k})\hat{\bar{v}}_x(\mathbf{k})\hat{S}(\mathbf{k}). \tag{11.13}$$

Therefore, even when the overlap integrals between different sites exist, we can calculate the SHC and AHC in the basis $(\bar{c}_{\mathbf{k}\alpha}, \bar{c}^{\dagger}_{\mathbf{k}\alpha})$ using the matrix $\hat{S}(\mathbf{k})$.

Then, the SHC (σ^s_{xy}) is derived from the general expression of the AHC (σ^a_{xy}) in Eqs. (4.28), (4.30) and (4.31), with the definition of the spin velocity in Eq. (4.33). In the present model, we have to replace $v_{\mathbf{k},\mu}$, $v^s_{\mathbf{k},\mu}$ and $G(k)$ with $\bar{v}_{\mathbf{k},\mu}$, $\bar{v}^s_{\mathbf{k},\mu}$ and $\bar{G}(k)$ in the basis $(\bar{c}_{\mathbf{k}\alpha}, \bar{c}^{\dagger}_{\mathbf{k}\alpha})$.

Figure 11.2 shows the electron number n-dependence of the SHC, where $n = n_s + n_d$. The crystal structure of various transition metals is shown in Table 11.1. The SHC obtained in the present model for the quasiparticle damping $\gamma = 0.002$ Ry is shown in Fig. 11.2a, and for $\gamma = 0.02$ Ry and 0.2 Ry in Fig. 11.2b. The SHC is negative for $n = 5, 6$, and positive for $n = 9 \sim 11$: The SHC changes its sign around $n = 7$ and 8. The magnitude of SHC is largest in Pt for $\gamma = 0.002$ Ry and 0.02 Ry, where the corresponding resistivities are $\sim$8 and $\sim$64 $\mu\Omega$ cm in Pt, respectively. When $\gamma = 0.2$, however, the absolute value of SHC in Ta and W becomes larger than that of Pt, where $\rho \sim 220$ (250) $\mu\Omega$ cm in Pt (Ta and W). Therefore, large negative values of SHC in Ta and W will be observed even in high resistive samples. For comparison, we also calculated the SHC for $n = 5 \sim 9$ using the band structure of Pt, which is represented as the open symbols in Fig. 11.2a. Interestingly, the obtained SHC is positive (negative) in metals with more than (less than) half-filling.

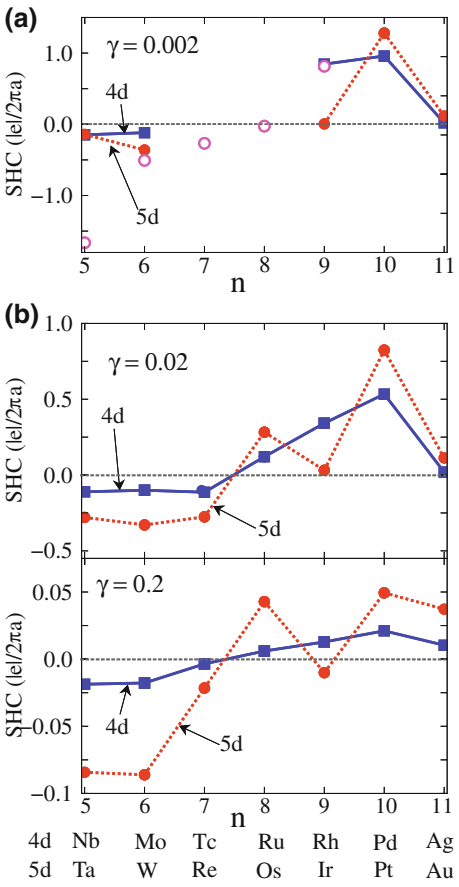

Fig. 11.2 n-dependence of SHC for $\gamma = 0.002$, 0.02 and 0.2 Ry. In **a**, we see that Pt shows the largest SHC in magnitude for $\gamma = 0.002$ Ry. The *open symbols* represents the SHC in Pt for $n = 5 \sim 9$. In **b**, the SHCs obtained in the present model for $n = 7, 8$ (hcp structure) are also shown. SHC in W takes the largest value for $\gamma = 0.2$

This result had been recently confirmed experimentally by Otani's group [18]: Fig. 11.3 shows the experimentally obtained SHCs for Nb, Ta, Mo, Pd and Pt, together with the theoretically calculated intrinsic SHC by using γ that reproduces the resistivity of the sample. In most cases, the experimental results are quantitatively consistent with the calculated ones within a factor of 2. This fact strongly suggests that the SHEs in 4*d* and 5*d* transition metals are mainly caused by the intrinsic mechanism.

Based on the periodic Anderson model, the following relationship had been derived in Ref. [19]:

$$\sigma_{xy} \approx \frac{2R}{3L^2} \cdot O^z_{xy}, \tag{11.14}$$

where $L = 2$ is the d-orbital angular momentum, $R \equiv \langle \mathbf{l} \cdot \mathbf{s} \rangle_{\mathrm{FS}}$ is the spin-orbit polarization ratio due to the SOI at the Fermi level, and $O^z_{xy} \equiv j^O_x / E_y \sim +eL^2$ is the orbital Hall conductivity. Since $O^z_{xy} > 0$, the sign of σ_{xy} is equal to the sign

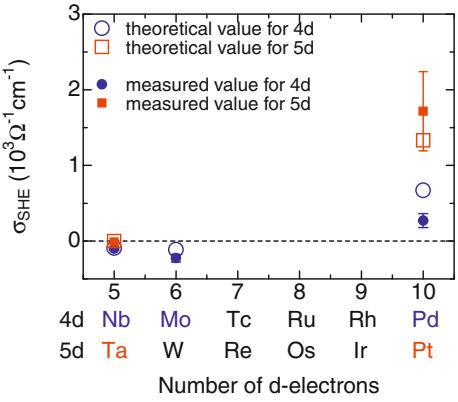

Fig. 11.3 Experimentally measured (*closed symbols*) and theoretically calculated (*open symbols*) spin Hall conductivities as a function of the number of d electrons for 4d (*circle*) and 5d (*square*) transition metals (Reference [18])

of R. We have calculated R based on the NRL-TB model, and found that R is positive (negative) in metals with more than (less than) half-filling, consistently with Hund's rule. Therefore, the n_d-dependence of the SHC in Fig. 11.2 can be understood in terms of the spin-orbit polarization (Hund's rule).

Recently, the intrinsic SHC in several Fe-based superconductors had been studied based on the realistic 10 orbital models [20]. Although the SOI in Fe is small, it was found that the SHC in heavily hole-doped compound KFe_2As_2 becomes comparable to the SHC in Pt, due to the Dirac cone bandstructure near the Fermi level.

11.2 AHE in Transition Metals

Mechanism of the AHE in transition metals has been a well studied, yet controversial subject. Originally, Karplus and Luttinger (KL) [21] first explained the AHE in transition metals as the intrinsic mechanism, which predicts $\sigma^a_{xy} \propto \rho^0$ ($\rho_H \propto \rho^2$). Soon after KL, Smit proposed an impurity-induced extrinsic mechanism, skew scattering mechanism, for the AHE [22]. Due to the spin-orbit interaction, conduction electrons are scattered by impurities asymmetrically depending on the direction of spin. This "skew scattering" gives the AHC in proportion to ρ^{-1} ($\rho_H \propto \rho$). Furthermore, Berger found another extrinsic mechanism, side-jump mechanism, which predicts $\sigma^a_{xy} \propto \rho^0$ ($\rho_H \propto \rho^2$) [23].

In spite of much effort, the interpretation of the AHE has been controversial so far. However, the theory of KL had been developed intensively, and the order of magnitude and sign of the results agree with experimental findings, thus giving much credibility to the intrinsic mechanism of the AHE. For example, quantitative studies based on realistic models have recently been performed for f-electron systems [24, 25], d-electron systems [26–29], and two-dimensional Rashba electron gas model [4, 30]. The origin of giant AHE realized in $d(f)$ electron systems is the "orbital Aharonov-Bohm (AB) effect", in which the complex phase factor arises

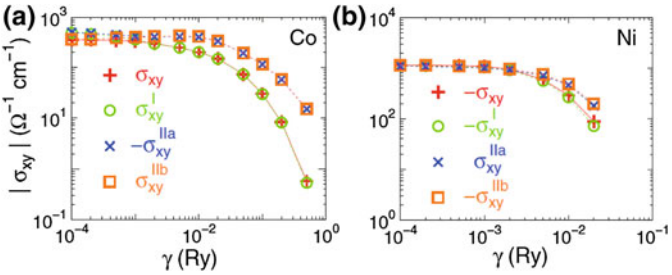

Fig. 11.4 γ-dependence of the AHCs for Co and Ni obtained by the NRL-TB model. The AHC is positive (negative) in Co (Ni)

from the $d(f)$ angular momentum that is revived by the strong atomic spin-orbit interaction (SOI) [8, 17, 19, 24, 29].

Recently, Naito et al. studied the intrinsic AHE in ferromagnetic 3d transition metals (Fe, Co, and Ni) using realistic NRL-TB models, to investigate the mechanism of the AHE in detail [31]. In previous studies for transition metals [27, 28], the AHC is expressed as an integral of the Berry curvature, which is expressed as σ_{xy}^{IIb} is this textbook. However, using the linear-response theory, it was found that additional terms, σ_{xy}^{I} and σ_{xy}^{IIa}, appear in the expression of the AHC. Figure 11.4 shows the obtained AHC (σ_{xy}) for Co and Ni, together with σ_{xy}^{I}, σ_{xy}^{IIa} and σ_{xy}^{IIb}. The obtained AHC for Co (Ni) is 341 $[(\Omega\text{cm})^{-1}]$ (-1078), which are close to the experimental value $\sim$205 $[(\Omega\text{cm})^{-1}]$ (~ -646). As recognized in Fig. 11.4, the most appropriate expression for the AHC in a wide range of damping rate γ is not the Berry curvature term, but the Fermi surface term σ_{xy}^{I}. The origin of the intrinsic AHE is the "orbital Berry phase" depicted in Fig. 4.7.

11.3 Spin-Structure-Driven AHE in Pyrochlore Compounds

The AHE due to nontrivial spin structure attracts increasing attention, in accordance with the recent development of the study of frustrated systems. The AHE induced by the Berry phase associated with spin chirality had been discussed for Mn-oxides [32], pyrochlore compounds (kagome lattice) [33, 34], and in spin glass systems [35]. Metallic pyrochlore $Nd_2Mo_2O_7$ would be the most famous experimental candidate [36–40]: Below $T_c = 93$ K, Mo $4d$ electrons is in the ferromagnetic state. Below $T_N \approx 30$ K, localized Nd $4f$ electrons form non-coplanar spin-ice magnetic order, and the tilting of Mo moment θ is induced by d-f exchange interaction, as shown in Fig. 11.5. The chirality-driven anomalous Hall conductivity (AHC) is proportional to $\mathbf{s}_A \cdot (\mathbf{s}_B \times \mathbf{s}_C) \propto \theta^2$ in the weak exchange coupling near half filling [33, 34]. However, the neutron diffraction experiments [37] had shown that $\theta^2 \ll 10^{-3}$, suggesting that

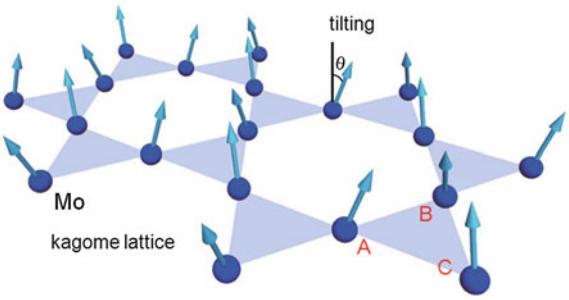

Fig. 11.5 Tilted spin structure of the Mo-ion kagome lattice realized in $Nd_2Mo_2O_7$ below 30 K, induced by the spin-ice order of Nd-ions. Experimentally, $\theta^2 \ll 10^{-3}$

the chirality-driven AHC is very small. Moreover, the field dependences of the AHC and θ^2 are quite different [37].

Authors in Refs. [32–34] studied the spin structure driven AHE in various s-orbital models. However, it is natural to expect a significant role of the orbital degree of freedom on the spin structure-driven AHE, as in the case of the conventional KL-type AHE in d-electron systems [8, 17, 19, 24, 29].

In this section, we explain that the Berry phase is induced by the complex d-orbital wavefunction in tilted ferromagnetic metals, and it causes a prominent spin structure-driven AHE [41, 42]. In $Nd_2Mo_2O_7$, the AHE due to orbital Berry phase is much larger than the chirality driven AHE, since the former is *linear in* θ consistently with experiments. In contrast, both the conventional KL term in simple ferromagnets ($\propto M_z \propto \cos\theta$) and the spin chirality term cannot have θ-linear terms. The present orbital mechanism will be realized in various geometrically frustrated metals.

Here, we construct the t_{2g}-orbital tight-binding model for Mo $4d$ electrons. For this purpose, we consider the spinel structure (XMo_2O_4) instead of pyrochlore structure ($X_2Mo_2O_7$). In both structures, Mo atoms form the same pyrochlore lattice. The location of O atoms in spinel is rather easy to treat theoretically, and the difference is not essential for later study, as we discuss later. Figure 11.6a represents the Mo atoms (black circles) and O atoms (white circles) in the spinel structure. The [111] Mo layer and the surrounding O atoms in the spinel structure is extracted in Fig. 11.6b, where the white (gray) circles represent the O atoms above (below) the Mo layer. We study this kagome lattice t_{2g}-orbital tight binding model, where the principal axis for the Mo d-orbital is fixed by the surrounding O_6 octahedron. A vector (n_x, n_y, n_z) in the xyz-coordinate in Fig. 11.6a is transformed into $[n_X, n_Y, n_Z]$ in the XYZ-coordinate in Fig. 11.6b as $(n_x, n_y, n_z) = [n_X, n_Y, n_Z]\hat{O}$, where the coordinate transform matrix $\hat{O}$ is given by

$$\hat{O} = \frac{1}{\sqrt{6}} \begin{pmatrix} -\sqrt{3} & \sqrt{3} & 0 \\ -1 & -1 & 2 \\ \sqrt{2} & \sqrt{2} & \sqrt{2} \end{pmatrix}, \tag{11.15}$$

Arrows in Fig. 11.6c represents the local effective magnetic (exchange) field at Mo sites, which is composed of the ferromagnetic exchange field from Mo $3d$ electrons

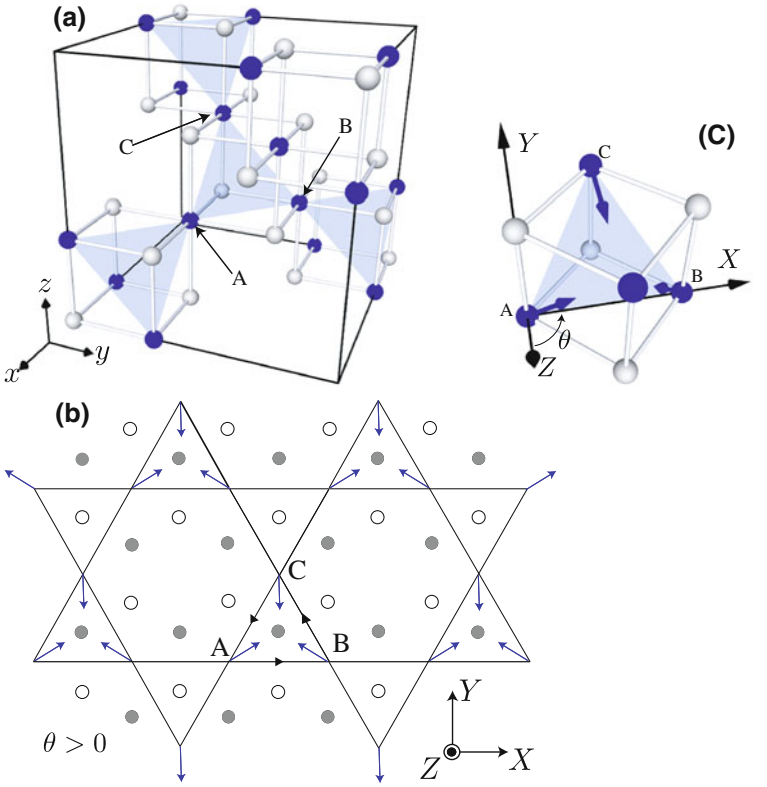

Fig. 11.6 **a** Spinel crystal structure. *Blue* (*white*) *circles* are Mo (O) ions. The Mo ions on the [111] plane form the kagome lattice. **b** Kagome lattice made of Mo ions. *White* (*gray*) *circles* are O ions *above* (*below*) the Mo layer. A unit cell contains sites A, B, C. **c** Umbrella like local exchange field at Mo sites represented by *arrows*

and the exchange field from Nd $4f$ electrons. Under the magnetic field parallel to (1, 1, 1) direction, below the Néel temperature of Nd sites, the directions of the local exchange fields at sites A, B and C in the XYZ-coordinate are $(\phi_{\mathrm{A}} = \pi/6, \theta)$, $(\phi_{\mathrm{B}} = 5\pi/6, \theta)$ and $(\phi_{\mathrm{C}} = 3\pi/2, \theta)$, respectively [36–39]. The tilting angle θ changes from $-1.5°$ ($H \to +0$ T) to $+1.5°$ ($H \sim 6$ T) in $Nd_2Mo_2O_7$, corresponding to the change in the spin-ice state at Nd sites [37].

Here, we present a discussion of symmetry. If we rotate the lattice by π around the site C in Fig. 11.6b, the local exchange field is changed from $\theta = \theta_0 > 0$ to $-\theta_0$. Since the conductivity tensor is unchanged by the π rotation, the AHC due to spin chirality mechanism is an even function of θ [33, 34]. However, O sites in Fig. 11.6b are changed by the π rotation around C, which means that the Mo $3d$ orbital state is changed. For this reason, the AHC in pyrochlore compounds due to orbital AB phase can have a θ-linear term.

The t_{2g}-orbital kagome lattice model is given by

$$H = \sum_{i\alpha,j\beta,\sigma} t_{i\alpha,j\beta} c^{\dagger}_{i\alpha,\sigma} c_{j\beta,\sigma} - \sum_{i\alpha,\sigma\sigma'} \mathbf{h}_i \cdot [\mu_e]_{\sigma,\sigma'} c^{\dagger}_{i\alpha,\sigma} c_{i\alpha,\sigma'} + \lambda \sum_{i\alpha\beta,\sigma\sigma'} [\mathbf{l}]_{\alpha,\beta} \cdot [\mathbf{s}]_{\sigma,\sigma'} c^{\dagger}_{i\alpha,\sigma} c_{i\beta,\sigma'} \tag{11.16}$$

where i, j represent the sites, α, β represent the t_{2g}-orbitals (xy, yz, zx), and σ, $\sigma' = \pm 1$. $t_{i\alpha,j\beta}$ is the hopping integrals between (i, α) and (j, β). The direct d-d hopping integrals are given by the Slater-Koster (SK) parameters $(dd\sigma)$, $(dd\pi)$ and $(dd\delta)$. The third term in Eq. (11.16) represents the SOI, where λ is the coupling constant, and $\mathbf{l}$ and $\mathbf{s}$ are the spin and d-orbital operators: Their matrix elements are given in Ref. [17]. For convenience in calculating the AHC, we take the Z-axis for the spin quantization axis, where $[s_X, s_Y, s_Z] \times 2$ becomes the Pauli matrix vector. Then, $(s_x, s_y, s_z) = [s_X, s_Y, s_Z]\hat{O}$. The second term in Eq. (11.16) represents the Zeeman term, where $\mathbf{h}_i$ is the local exchange field at site i. $\mu_e \equiv -2\mathbf{s}$ is the magnetic moment of an electron.

Before the numerical calculations, we explain an intuitive reason why prominent AHE is induced by the non-collinearity of the local exchange field $\mathbf{h}_i$. For this purpose, we assume the strong coupling limit where the Zeeman energy is much larger than Fermi energy E_{F} and the SOI. Since $\mu_e = -2\mathbf{s}$, the SOI term at site i is replaced with $(-\lambda/2)\mathbf{l} \cdot \mathbf{n}_i$, where $\mathbf{n}_i \equiv \mathbf{h}_i/|\mathbf{h}_i|$. Its eigenenergies in the t_{2g} space are 0 and $\pm\lambda/2$, as shown in Fig. 11.7a. The eigenstate for $E = -\lambda/2$ is given by

$$|\mathbf{n}\rangle = \frac{1}{\sqrt{2(n_x^2 + n_y^2)}}[-(n_x n_z - i n_y)|xy\rangle + (n_y^2 + n_z^2)|yz\rangle - (n_x n_y + i n_z)|zx\rangle] \tag{11.17}$$

where $\mathbf{n} = (n_x, n_y, n_z)$ in the xyz-coordinate: $\mathbf{n}_{\Xi}$ (Ξ =A,B,C) in the xyz-coordinate is given by $[\sin\theta\cos\phi_{\Xi}, \sin\theta\cos\phi_{\Xi}, \cos\theta]\hat{O}$. When $\theta = 0$ ($n_{x,y,z} = 1/\sqrt{3}$), Eq. (11.17) becomes $[\omega|xy\rangle + |yz\rangle + \omega^*|zx\rangle]/\sqrt{3}$, where $\omega = \exp(i2\pi/3)$. Considering that $|\theta| \sim 0.01$ in $Nd_2Mo_2O_7$ [37], we expand Eq. (11.17) up to the first order in θ. For site C, it is given as $|\mathrm{C}\rangle = [(1 + \frac{\theta}{\sqrt{2}})\omega e^{-i\frac{1}{2}\sqrt{\frac{3}{2}}\theta}|xy\rangle + (1 - \frac{\theta}{2\sqrt{2}})|yz\rangle + (1 - \frac{\theta}{2\sqrt{2}})\omega^* e^{-i\sqrt{\frac{3}{2}}\theta}|zx\rangle]/\sqrt{3}$. Table 11.2 shows the phases for $|\alpha\rangle$ orbital at site Ξ in the eigenstate in Eq. (11.17), ψ_{α}^{Ξ}, up to $O(\theta)$.

Here, we explain that a moving electron acquires the "orbital AB phase", which gives rise to the prominent AHE that is sensitively controlled by the tilting angle θ. Figure 11.7b shows the motion of an electron that enter into site C via yz orbital and exit via zx orbital. When the electron is in the eigenstate $|\mathrm{C}\rangle$, the electron acquires the phase difference between yz and zx orbitals, $\exp(i(\psi_{zx}^{\mathrm{C}} - \psi_{yz}^{\mathrm{C}})) = \omega^* e^{-i\sqrt{3/2}\theta}$, which is the orbital AB phase that is controlled by θ. The total orbital AB phase

Table 11.2 Phases for t_{2g} orbitals in Eq. (11.17) up to $O(\theta)$

	ψ^{Ξ}_{xy}	ψ^{Ξ}_{yz}	ψ^{Ξ}_{zx}
Ξ =A	$\frac{2\pi}{3} - \frac{1}{2}\sqrt{\frac{3}{2}}\theta$	0	$-\frac{2\pi}{3} + \frac{1}{2}\sqrt{\frac{3}{2}}\theta$
Ξ =B	$\frac{2\pi}{3} + \sqrt{\frac{3}{2}}\theta$	0	$-\frac{2\pi}{3} + \frac{1}{2}\sqrt{\frac{3}{2}}\theta$
Ξ =C	$\frac{2\pi}{3} - \frac{1}{2}\sqrt{\frac{3}{2}}\theta$	0	$-\frac{2\pi}{3} - \sqrt{\frac{3}{2}}\theta$

factor for the triangle path along A→B→C→A in Fig. 11.7b is given by the phase of the following amplitude:

$$T_{\rm orb} = \langle {\rm A}|H_0|{\rm C}\rangle\langle {\rm C}|H_0|{\rm B}\rangle\langle {\rm B}|H_0|{\rm A}\rangle \tag{11.18}$$

where H_0 is the kinetic term. Here, we take only the most largest SK parameter $(dd\sigma)$, and neglect $(dd\pi)$ and $(dd\delta)$ to simplify the discussion. In this case, only the following intraorbital hoppings exist: $\langle {\rm B}; xy|H_0|{\rm A}; xy\rangle = \langle {\rm C}; yz|H_0|{\rm B}; yz\rangle = \langle {\rm A}; zx|H_0|{\rm C}; zx\rangle = t$. By concentrating only on the phase given in Table 11.2, we obtain

$$\begin{aligned} T_{\rm orb} &\sim (t^3/27)e^{i(\psi^{\rm C}_{zx}-\psi^{\rm C}_{yz})+i(\psi^{\rm B}_{yz}-\psi^{\rm B}_{xy})+i(\psi^{\rm A}_{xy}-\psi^{\rm A}_{zx})} \\ &= (t^3/27)\exp(-i3\sqrt{3/2}\theta) + O(\theta^2). \end{aligned} \tag{11.19}$$

$T_{\rm orb}$ is also expressed as $T_{\rm orb} = |T_{\rm orb}|e^{-i2\pi\Phi_{\rm orb}/\Phi_0}$, where $\Phi_0 = 2\pi\hbar/|e|$ is the flux quantum, and $\Phi_{\rm orb}$ is the "fictitious magnetic flux" due to the orbital AB effect. Therefore, $\Phi_{\rm orb} = (3/2\pi)\sqrt{3/2}\theta\cdot\Phi_0$ up to $O(\theta)$. Since the relation $\Phi_{\rm orb}\propto\theta$ also holds in pyrochlore compounds, the orbital AB flux should give rise to the AHE that is linear in θ in $Nd_2Mo_2O_7$. The line (i) in Fig. 11.7c represents $\Phi_{\rm orb}$ for $|\theta|\le\pi/2$, which is given by using Eq. (11.18) and the relationship $-(\Phi_0/2\pi){\rm Im}\ln(T_{\rm orb}/|T_{\rm orb}|)$. At $\theta = \pm\pi/2$, the obtained $\Phi_{\rm orb}$ is not an integer multiple of $\Phi_0/2$. This fact means that the AHC is finite even in the case of coplanar order.

In the above discussion, we have neglected interorbital hoppings integrals for simplicity. If we include them, the AHC is finite even if $\theta = 0$ since the orbital AB phase is nonzero, as discussed in Refs. [8, 29]. Thus, interorbital hoppings integrals are necessary to realize the AHE for $\theta = 0$ (conventional KL type AHE).

We also discuss the fictitious magnetic flux due to the spin chirality, which comes from the Berry phase accompanied with the spin rotation due to the electron hopping [33]. The line (ii) in Fig. 11.7c represents the fictitious magnetic flux due to the spin chirality $\Phi_{\rm spin}$: Geometrically, $-4\pi\Phi_{\rm spin}$ corresponds to the solid angle subtended by $\mathbf{n}_{\rm A}$, $\mathbf{n}_{\rm B}$ and $\mathbf{n}_{\rm C}$. Since $\Phi_{\rm spin}\propto\theta^2$ for $\theta\ll 1$, spin chirality mechanism is negligible in $Nd_2Mo_2O_7$ [37]. The line (iii) shows the total flux $\Phi_{\rm tot} = \Phi_{\rm orb} + \Phi_{\rm spin}$.

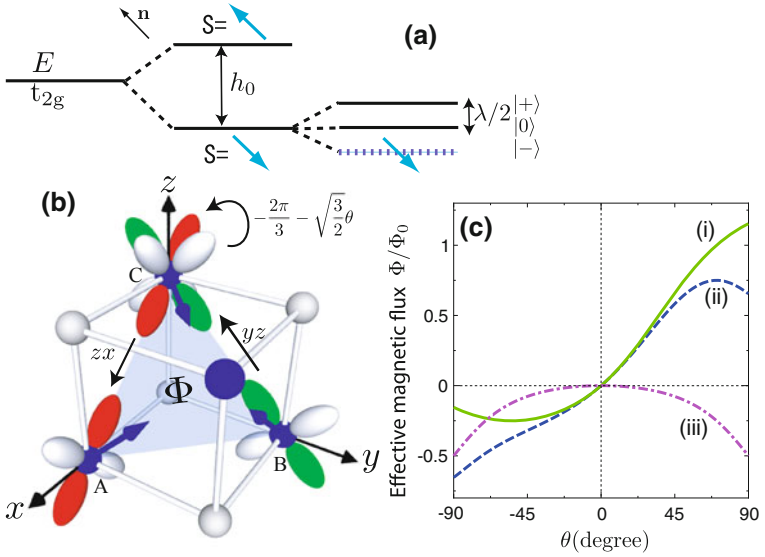

Fig. 11.7 **a** Eigenenergies for t_{2g} electron under the exchange field **h** and the SOI $(-\lambda/2)\mathbf{n}\cdot\mathbf{l}$. **b** Orbital AB phase given by the complex t_{2g} orbital wavefunction at site C. **c** Fictitious magnetic flux due to orbital AB effect (i), due to spin chirality (ii), and the total flux (iii)

Thus, all the upward and downward ABC triangles in Fig. 11.6b are penetrated by $\Phi_{\rm tot}$. However, the total flux in the unit cell cancels out since the hexagons are penetrated by $-2\Phi_{\rm tot}$. Nonetheless, the AHC becomes finite [33, 43] since the contribution from the triangle path, which is the third order of the hopping integrals, would be the most important. The main features of the AHE due to orbital AB effect, $\sigma_{\rm AH}^{\rm orb}$, are the following: (a) $\sigma_{\rm AH}^{\rm orb}$ dominates the spin chirality AHE for $\theta \ll 1$. (b) $\sigma_{\rm AH}^{\rm orb}$ exists even if $\theta = \pi/2$ (coplanar order), whereas spin chirality AHE vanishes since $\Phi_{\rm spin}(\theta = \pi/2) = \Phi_0/2$.

From now on, we perform numerical calculation for the AHC based on the general expression of the AHC in Eqs. (4.28), (4.30) and (4.31). Then, the contributions from both $\Phi_{\rm orb}$ and $\Phi_{\rm spin}$ are automatically contained, and we can verify that the concept of orbital AB effect is still appropriate even in the weak coupling regime where $|\mathbf{h}_i| \ll E_{\rm F}$. Here, we put the SK parameters between the nearest neighbor Mo sites as $(dd\sigma) = -1.0$, $(dd\pi) = 0.6$, and $(dd\delta) = -0.1$. $|(dd\sigma)|$ corresponds to 2000 K. The spin-orbit coupling constant for Mo $4d$ electron is $\lambda = 0.5$ [17]. The number of electrons per site is $n = 2$ (1/3-filling) for $Nd_2Mo_2O_7$ since the valence of Mo ion is 4+. To reproduce the magnetization of Mo ion $1.3\mu_{\rm B}$ in $Nd_2Mo_2O_7$, we set $|\mathbf{h}_i| = 0.9$. We also put the damping rate $\gamma = 0.2 \sim 0.5$ to reproduce the resistivity $\sim$1 mΩcm in a single crystal [38, 39].

Figure 11.8a shows the μ-dependence of the AHC for $\theta = -1.5°$ ($\sim$0 T), $\theta = 0$ ($\sim$3 T), and $\theta = 1.5°$ ($\sim$6 T). The AHC for $\theta = 0$ is given by the conventional KL mechanism. Since the present spin structure-driven AHE is linear in θ, a very small

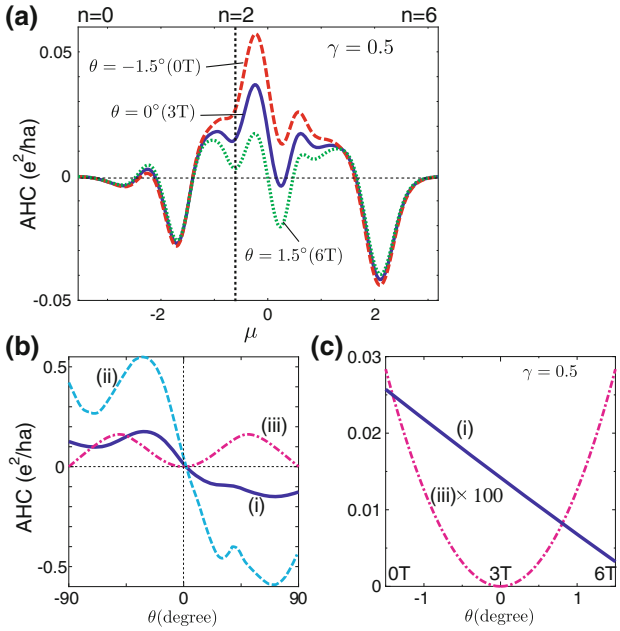

Fig. 11.8 **a** AHC for $\theta = 0$ and $\pm 1.5°$ as function of μ. **b** AHC in the present t_{2g}-orbital model for (i) $\gamma = 0.5$ and (ii) $\gamma = 0.2$. (iii) shows the AHC in the s-orbital model for $\gamma = 0.5$. **c** (i) and (iii) for $|\theta| \leq 1.5°$

θ causes a prominent change in the AHC for $1.3 > \mu > -1.3$ ($4.7 > n > 1.0$). Since $e^2/ha = 10^3\ \Omega^{-1}\mathrm{cm}^{-1}$ for $a = 4$ Angstrom (a is the interlayer spacing), the AHC for $n = 2$ and $\theta = 1.5°$ corresponds to 30 $\Omega^{-1}\mathrm{cm}^{-1}$, which is consistent with experiments.

Here, we analyze the θ-dependence of the AHC in detail, by ignoring the experimental constraint $|\theta| \leq 1.5°$. Figure 11.8b shows the AHCs as functions of θ. The lines (i) and (ii) represent the total AHC in the present model for $\gamma = 0.5$ and 0.2, respectively. Their overall functional forms are approximately odd with respect to θ, and it takes a large value even if $\theta = \pm\pi/2$ (coplanar order). These results are consistent with the AHE induced by the orbital AB effect discussed in Fig. 4.7. Note that $\gamma > 0.2$ corresponds to "high-resistivity regime" where the intrinsic AHC follows an approximate scaling relation $\sigma_{\mathrm{AH}} \propto \rho^2$ [24, 29]. The line (iii) in Fig. 11.8b shows the AHC in the s-orbital model studied in Ref. [34]. We put the nearest neighbor hopping $t = -0.8$, $\gamma = 0.5$, and $|\mathbf{h}| = 0.9$. We also put $n = 2.5/3 = 0.83$ since $n = 2/3$ (1/3-filling) corresponds to band insulating state [34]. Although the obtained AHC takes a large value for $\theta \sim 50°$, it is 100 times smaller than the AHC in the t_{2g} model (i) for $|\theta| \leq 1.5°$, as shown in Fig. 11.8c.

Here, we make comparison with the theory and experiments for $Nd_2Mo_2O_7$: Under $\mathbf{H} \parallel (1, 1, 1)$ below T_{N}, σ_{AH} decreases with H monotonically from $H \to 0$ T ($\theta \approx -1.5°$) to 6 T ($\theta \approx 1.5°$). This experimental result is consistent with the AHE

due to the orbital AB effect that is linear in θ. The present study also reproduces the experimental phenomenological equation $\rho_{\rm H}^{\rm AHE} = 4\pi R_s M_Z^{\rm Mo} + 4\pi R_s' M_Z^{\rm Nd}$: The first term is the conventional KL term ($\theta = 0$), and the second term is the θ-linear term since $\theta \propto \sqrt{h_X^2 + h_Y^2}$ and $\sqrt{h_X^2 + h_Y^2} \propto M_Z^{\rm Nd}$ due to non-coplanar magnetic order of Nd moments [37].

The realization condition for the spin-structure-driven AHE in the present t_{2g} model is much more general than that in the s-orbital model. For example, the AHC is finite even in the coplanar spin state ($M_z = 0$), in high contrast to the chirality-driven AHE. Moreover, according to Eq. (11.19), orbital AB phase emerges if only one of $\theta_{\rm A}, \theta_{\rm B}, \theta_{\rm C}$ is nonzero. Therefore, in the present t_{2g} model, prominent AHE due to non-collinearity is realized unless $\mathbf{n}_{\rm A} \parallel \mathbf{n}_{\rm B} \parallel \mathbf{n}_{\rm C}$, with the aid of the orbital AB effect and the SOI.

In summary, we studied the spin-structure-driven AHE in the t_{2g}-orbital model in the presence of non-collinear magnetic configurations. Thanks to the SOI, local exchange field modifies the complex d-orbital wavefunction, and the resultant Berry phase induces prominent AHE that is much larger than the chirality-driven AHE. Since the derived AHC is linear in the tilting angle of Mo moment, θ, experimental large field dependence in $Nd_2Mo_2O_7$ is reproduced.

11.4 AHE and SHE in Heavy Fermion Systems

In this section, we discuss the AHE and SHE in heavy fermion systems. In paramagnetic systems, the observed Hall coefficient is given by

$$R_H^{\rm HF} = R_H^n + R_H^{\rm AHE}, \tag{11.20}$$

where $R_{\rm H}^{\rm AHE} = R_{\rm H}^a \cdot \chi$ and $\chi = M/B$ is the uniform magnetic susceptibility. In heavy-fermion systems, the AHE due to the second term takes large value since the uniform susceptibility $M/B = \chi$ is widely enhanced due to the strong Coulomb interaction. Due to the AHE, $R_H^{\rm HF}$ starts to increase with increasing temperature from 0 K, and it turns to decrease after exhibiting its maximum value around the coherent temperature $T_{\rm coh}$. The maximum value of $|R_H^{\rm HF}|$ is more than one order of magnitude greater than $1/|ne| \sim 1.0 \times 10^{-9}$ m^3/C. The AHE cannot be derived from the RTA since the interband hopping of electrons is important. [In the AHE, the effect of CVC is not expected to be crucial.] Experimentally, $R_H^{\rm a}$ is positive in usual Ce and U based heavy-fermion systems [44, 45].

In paramagnetic heavy-fermion systems, the Hall coefficients takes huge values due to the AHE [44–46]. In the early stage, Coleman et al. [47] and Fert and Levy [48] developed theories of extrinsic AHE: they studied the extrinsic mechanism based on the f-electron impurity Anderson models with d-orbital channels, and predicted the relation $R_{\rm H}^{\rm AHE} \propto \chi\rho$ above $T_{\rm coh}$ when the d-orbital phase-shift is finite.

On the other hand, Kontani and Yamada studied the intrinsic AHE due to multi-band effect based on the $J = 5/2$ periodic Anderson model in Eq. (10.1), which a the model in the strong limit of spin-orbit interaction [24, 25]. In this model, the anomalous velocity originates from the angular momentum of the localized f-electrons. That is, the AHE originates from the phase factor of the c-f mixing potential $V_{\mathbf{k}M\sigma} \propto e^{i(M-\sigma/2)\phi_{\mathbf{k}}}$, where $\phi_{\mathbf{k}} = \tan^{-1}(k_x/k_y)$, due to the f-orbital degree of freedom and the SOI. By the same reason, we have shown that the heavy-fermion systems exhibit large intrinsic SHE, based on the study of the periodic Anderson models.

Here, we calculate the intrinsic Hall effects in this model. The charge current operator is given by $\hat{J}^C_\mu = -e\hat{v}_{\mathbf{k}\mu}$, where $-e$ ($e > 0$) is the electron charge and $\hat{v}_{\mathbf{k}\mu} \equiv \partial\hat{H}_{\mathbf{k}}/\partial k_\mu$ is the velocity. According to Eq. (10.1),

$$\hat{v}_{\mathbf{k}\mu} = \sum_\sigma \frac{\partial}{\partial k_\mu}\epsilon_{\mathbf{k}} c^\dagger_{\mathbf{k}\sigma} c_{\mathbf{k}\sigma} \sum_{\sigma M} \left\{ \frac{\partial}{\partial k_\mu} V_{\mathbf{k}M\sigma} c^\dagger_{\mathbf{k}\sigma} f_{\mathbf{k}M} + \text{h.c} \right\}. \tag{11.21}$$

Next, we explain the s_z-spin current operator $\hat{J}^S_\mu$. In the present model, $\hat{s}_z$ is given by

$$\hat{s}_z = \sum_\sigma \frac{\sigma}{2} c^\dagger_{\mathbf{k}\sigma} c_{\mathbf{k}\sigma} + \sum_M S_M f^\dagger_{M\mathbf{k}} f_{M\mathbf{k}}, \tag{11.22}$$

where $S_M = \sum_{m\sigma} \frac{\sigma}{2} \left[a^M_{m\sigma}\right]^2$. It is straight forward to show that $S_M = -\frac{M}{7}$ ($\frac{M}{7}$) for $J = 5/2$ ($J = 7/2$). Then, the spin current $\hat{J}^S_\mu \equiv \left\{\hat{v}_{\mathbf{k}\mu}, \hat{s}_z\right\}/2$ is given by

$$\begin{aligned} \hat{J}^S_\mu =& \sum_\sigma \frac{\sigma}{2} \frac{\partial \epsilon_{\mathbf{k}}}{\partial k_\mu} c^\dagger_{\mathbf{k}\sigma} c_{\mathbf{k}\sigma} \\ &+ \sum_{\sigma M} \left\{ \frac{1}{2} \left(\frac{\sigma}{2} + S_M \right) \frac{\partial V_{\mathbf{k}M\sigma}}{\partial k_\mu} c^\dagger_{\mathbf{k}\sigma} f_{\mathbf{k}M} + \text{h.c} \right\}. \end{aligned} \tag{11.23}$$

Here, the velocity due to the c-f mixing potential $V_{\mathbf{k}M\sigma}$ is [24]

$$\begin{aligned} \frac{\partial V_{\mathbf{k}M\sigma}}{\partial k_x} =& -i \left(M - \frac{\sigma}{2} \right) \frac{k_y}{k_x^2 + k_y^2} V_{\mathbf{k}M\sigma} \\ &+ \frac{\partial}{\partial k_x} \left(V_{\mathbf{k}M\sigma} \alpha^*_{M,\sigma} \right) \alpha_{M,\sigma} \\ \equiv& v^a_{\mathbf{k}M\sigma,x} + v^n_{\mathbf{k}M\sigma,x} \end{aligned} \tag{11.24}$$

Here, v^a_x is the anomalous velocity given by k_x-derivative of the phase factor $\alpha_{M,\sigma} = \exp\left\{ i \left(M - \frac{\sigma}{2} \right) \phi_k \right\}$ in $V_{\mathbf{k}M\sigma}$. Figure 11.9 is a schematic view of the anomalous velocity $v^a \propto \nabla_k \phi_k$. Since $v^a_x \propto k_y$ and thus $\sum_{\mathbf{k}} v^a_x (\partial\epsilon_{\mathbf{k}}/\partial k_y) \neq 0$, the anomalous velocity gives rise to the large SHE and AHE in heavy fermion systems. Hereafter,

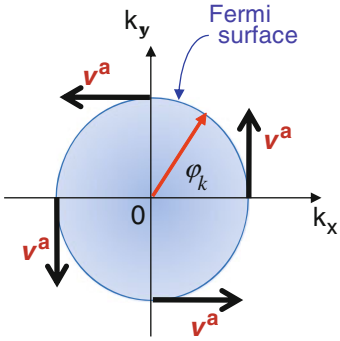

Fig. 11.9 A schematic view of the anomalous velocity v^a

we drop the normal velocity $v_x^n \propto k_x$ since it is less important for the intrinsic Hall effects [49].

First, we study the SHC since the theoretical analysis is easier. We calculate σ_{xy}^s due to the Fermi surface term, given by the correlation function between J_y^C and J_x^S. Figure 11.10 shows the diagrammatic expression for σ_{xy}^s with neglecting v_μ^n in both $\hat{J}_x^S$ and $\hat{J}_y^C$. Its mathematical expression at zero temperature is

$$\sigma_{xy}^s = \frac{-e}{2\pi N}\sum_{\mathbf{k}M\sigma}\frac{1}{2}\left(\frac{3\sigma}{2}+S_M\right) \times\left[v^a_{\mathbf{k}M\sigma,x}\frac{\partial\epsilon_{\mathbf{k}}}{\partial k_y}V^*_{\mathbf{k}M\sigma}|G^{cR}_{\mathbf{k}}(0)|^2G^{0fR}(0)+\text{c.c.}\right], \tag{11.25}$$

where $G^c_{\mathbf{k}}(0)$ is given in Eq. (10.3), and $G^{f0R}(0) = (\mu - E_f - i\gamma)^{-1}$ with $\gamma = \text{Im}\,\Sigma^f(0+i\delta)$. Here, we confine ourselves to the case $J = 5/2$ state corresponding to Ce $^{3+}$-ion, and use the following relationships

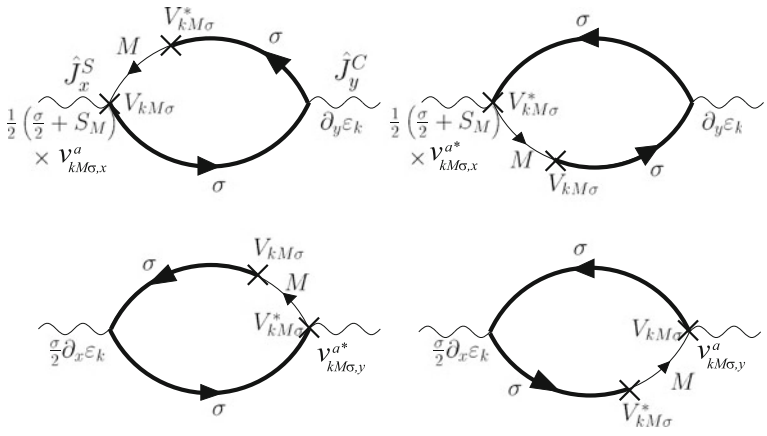

Fig. 11.10 The diagrammatic expressions for σ_{xy}^s

$$\sum_{M\sigma} M^2 |V_{\mathbf{k}M\sigma}|^2 = \frac{|V_0|^2}{2}\left(1 + 16\sin^2\theta_{\mathbf{k}}\right), \tag{11.26}$$

$$\sum_{M\sigma} M\sigma |V_{\mathbf{k}M\sigma}|^2 = |V_0|^2\left(1 - 4\sin^2\theta_{\mathbf{k}}\right), \tag{11.27}$$

and $\dfrac{\partial\epsilon_{\mathbf{k}}}{\partial k_y} = \dfrac{\partial\epsilon_{\mathbf{k}}}{\partial k}\dfrac{k_y}{|\mathbf{k}|}$. Assuming a spherical Fermi surface, Eq. (11.25) is transformed as follows [49]:

$$\sigma^s_{xy} = \frac{-e}{2\pi N}\frac{52}{7}|V_0|^2 \sum_k \frac{1}{|\mathbf{k}|}\frac{\partial\epsilon_{\mathbf{k}}}{\partial k}|G^{cR}_{\mathbf{k}}(0)|^2 \cdot \mathrm{Im}G^{f0R}(0). \tag{11.28}$$

When γ is small enough, $\mathrm{Im}G^{f0R}(0) = \gamma(\mu - E_f)^{-2}$ and $|G^{cR}_{\mathbf{k}}(0)|^2$ can be approximated as

$$\begin{aligned} |G^{cR}_{\mathbf{k}}(0)|^2 &= \frac{1}{(\tilde{\epsilon}_{\mathbf{k}} - \mu)^2 + \Gamma_c^2} \\ &\simeq \frac{\pi}{\Gamma_c}\delta(\tilde{\epsilon}_{\mathbf{k}} - \mu), \end{aligned} \tag{11.29}$$

where $\tilde{\epsilon}_{\mathbf{k}} = \epsilon_{\mathbf{k}} + \dfrac{|V_0|^2}{\mu - E^f}$ and $\Gamma_c = \dfrac{|V_0|^2}{(\mu - E^f)^2}\gamma$. Then, Eq. (11.28) is simplified for small γ as:

$$\sigma^s_{xy} = \frac{-e}{2\pi N}\frac{52}{21}\sum_{\mathbf{k}} \frac{1}{|\mathbf{k}|}\frac{\partial\epsilon_{\mathbf{k}}}{\partial k}\delta(\tilde{\epsilon}_{\mathbf{k}} - \mu). \tag{11.30}$$

Moreover, we introduce the approximation $\epsilon_{\mathbf{k}} = k^2/2m$. Then, σ^s_{xy} for $J = 5/2$ is simplified as [49]

$$\begin{aligned} \sigma^s_{xy} &= -e\frac{26}{21}\frac{k_F}{2\pi^2} \\ &= -\frac{e}{2\pi a}\frac{26}{21}, \end{aligned} \tag{11.31}$$

where a is the lattice spacing. The first line in Eq. (11.31) means that the SHC depends only on the density of conduction electron $n_{\mathrm{c}} = k_{\mathrm{F}}^3/3\pi^2$. This result suggests that SHCs in Ce-compound heavy fermion systems take similar large negative values. The second line in Eq. (11.31) is obtained by putting $k_{\mathrm{F}} = \pi/a$. When $a = 4$ Angstrom, then $e/2\pi a \approx 1000\,\hbar e^{-1}\Omega^{-1}\mathrm{cm}$, which corresponds to $\sigma_{xy} \sim 1000\,\hbar e^{-1}\Omega^{-1}\mathrm{cm}^{-1}$ for Ce-compound system. Interestingly, σ^s_{xy} is independent of the strength of the c-f mixing potential.

In the case of $J = 7/2$ (Yb-compounds), σ^s_{xy} is obtained as

$$\begin{aligned}\sigma^s_{xy} &= e\frac{15}{14}\frac{k_{\rm F}}{2\pi^2} \\ &= \frac{e}{2\pi a}\frac{15}{14}.\end{aligned} \tag{11.32}$$

The second line in Eq. (11.32) is obtained by putting $k_{\rm F} = \pi/a$. This result means that SHCs in Yb-compound heavy fermion systems take similar large positive values.

Next, we calculate the AHC σ^a_{xy} due to the Fermi surface term, given by the correlation function between J^C_y and J^C_x. Since we are interested in the AHE in the paramagnetic heavy fermions systems under the magnetic field, we introduce the Zeeman term to the f-level as $E_f + g\mu_{\rm B}MH$, and extract the H-linear term of the AHC. That is, we calculate $\sigma^a_{xy}/H|_{H=0}$ that given by the triangle diagram with respect to J^C_y, J^C_x and $g\mu_{\rm B}M$. The method of calculation is explained in Ref. [24] in detail. The procedure is rather complex but similar to the derivation of the SHC explained above. By neglecting $\hat{v}^n$ in Eq. (11.24) and assuming a spherical Fermi surface, we obtain the AHC for $J = 5/2$ as [24]

$$\begin{aligned}\frac{\sigma^a_{xy}}{H} &= 2e^2\sum_{\mathbf{k}}\sum_{MM'\sigma}\frac{\partial\epsilon_{\mathbf{k}}}{\partial k_y}v_{\mathbf{k}MM',x} \\ &\quad\times g\mu_{\rm B}(M-M')V_{kM\sigma}V^*_{\mathbf{k}M'\sigma}|G^{cR}_{\mathbf{k}}(0)|^2 i{\rm Im}G^{f0R}(0) \\ &= \frac{8}{3}\cdot\frac{e^2 g\mu_{\rm B}}{E_f-\mu}\sum_{\mathbf{k}}\frac{1}{|\mathbf{k}|}\frac{\partial\epsilon_{\mathbf{k}}}{\partial k},\end{aligned} \tag{11.33}$$

where $v_{\mathbf{k}MM',x} \equiv \dfrac{\partial\sum_\sigma V^*_{\mathbf{k}M\sigma}V_{\mathbf{k}M'\sigma}}{\partial k_x}\dfrac{|G^{f0R}(0)|^2}{\mu-\epsilon_{\mathbf{k}}}$. The last equation in Eq. (11.33) is obtained by performing the surface integration on the Fermi surface. For $J = 7/2$, the coefficient $\dfrac{8}{3}$ in the last line of Eq. (11.33) is replaced with 5. Inserting some physical constants ($\mu_{\rm B} = 9.27\times10^{-24}$[JT], $e = 1.60\times10^{-19}$[C], $\hbar = 1.05\times10^{-34}$[JS] and $k_{\rm B} = 1.38\times10^{-23}$[JK^{-1}]) into Eq. (11.33), and taking the mass renormalization discussed in Sect. 10.1, we obtain

$$\frac{\sigma^a_{xy}}{H}[(\Omega\ {\rm cm\ Gauss})^{-1}] = \frac{5.8\times10^{-9}(n[{\rm cm}]^{-3})^{1/3}}{\tilde{E}_f[{\rm K}]} \tag{11.34}$$

for $J = 5/2$ ($g = 6/7$). $\tilde{E}_f$ is the renormalized f-level measured from the Fermi energy, and $|\tilde{E}_f|$ gives approximate quasiparticle bandwidth. The present study predicts that $R^{\rm AHE}_{\rm H} > 0$ (< 0) in Ce (Yb) based heavy-fermion systems since $\tilde{E}_f > 0$ (< 0). This prediction for Ce- and Yb-compounds is consistent with the

experimental results [44, 45]. If we substitute $\tilde{E}_f = 10$ K and $n = 10^{22}\text{cm}^{-3}$, $\sigma^a_{xy}/H = 1.3 \times 10^2$[1/Ω cm Gauss], which is a typical experimental value.

In heavy fermion systems $\gamma = \text{Im}\Sigma(0)$ increases at finite temperatures, and $\gamma \sim |\mu - E_f|$ is expected at $T \sim T_{\text{K}}$. As revealed in Ref. [24], the expression of the AHC valid for finite γ is obtained by replacing $\dfrac{1}{\mu - E_f}$ in Eq. (11.33) with $\text{Re}\dfrac{1}{\mu - E_f + i\gamma}$. That is, $R_H^{\text{AHE}} = (\sigma^{\text{a}}_{xy}/H)\rho^2$ behaves as $R_H^{\text{AHE}} \propto \chi \cdot \dfrac{\gamma^{*2}}{\tilde{E}_f^2 + \gamma^{*2}}$, where $\gamma^* \equiv z\gamma$ [24]. Therefore, R_H^{AHE} shows the following cross-over behavior:

$$R_H^{\text{AHE}} \propto \chi\rho^2 \ [\sim \rho^2] \quad : \text{below } T_{\text{coh}}(\gamma^* < |\tilde{E}_f|), \tag{11.35}$$

$$R_H^{\text{AHE}} \propto \chi \ [\sim 1/T] \quad : \text{above } T_{\text{coh}}(\gamma^* > |\tilde{E}_f|). \tag{11.36}$$

In typical Ce-based heavy-fermion systems, $1/z \sim 100$ and $|\tilde{E}_f| \sim 10$ K. Below T_{coh}, Eq. (11.35) is proportional to ρ^2 since χ is constant for $T < T_{\text{coh}}$. Figure 11.11 shows the R_{H} in $U_3Ni_3Sn_4$ ($\gamma = 380$ mJ/K^2), where the relation $R_{\text{H}}^{\text{AHE}} = R_{\text{H}}^{\text{HF}} - R_{\text{H}}^n \propto \rho^2$ holds well below $\sim 0.3T_{\text{coh}} \sim 25$ K. Note that the extrinsic type AHE [47, 48] and the intrinsic type AHE [24] can coexist. However, the relation $R_{\text{H}}^{\text{AHE}} \propto \rho^2$ suggests that the intrinsic-type AHE is dominant at least below T_{coh}. Above T_{coh}, the AHE due to interband transition is suppressed when c-f mixing is prohibited. Therefore, Eq. (11.36) is independent of ρ. This *coherent-incoherent crossover of intrinsic AHE* was first theoretically derived in Ref. [24]. This crossover behavior is not restricted to heavy-fermions systems, but also observed in various transition ferromagnets [50].

In heavy-fermion systems near the AF QCP, R_{H}^n shows strong temperature dependence due to the CVC. To extract R_{H}^n from the observed Hall coefficient, we have to seriously consider the T-dependence of $R_{\text{H}}^{\text{AHE}}$. Very fortunately, AHE is vanishingly small in CeMIn$_5$ [51, 52]. Therefore, we could perform reliable analysis of the ordinary Hall effect in CeMIn$_5$ as discussed in Sect. 9.1, without the necessity of subtracting the AHE. Note that the AHE vanishes when the crystal-field splitting of the f-levels is much larger than T_{coh}. This may be the reason for the small AHE in CeMIn$_5$.

11.5 Summary of This Chapter

We have explained the recent progress on the theoretical study of the intrinsic AHE and SHE in multiorbital systems. The existence of these intrinsic Hall effects was predicted by Karplus and Luttinger (KL) [21] in 1954. However, intrinsic Hall effects had been underestimated for a long time because of the absence of quantitative calculation based on an established model Hamiltonian. In 1994, we have calculated the intrinsic AHE in heavy fermion systems based on the periodic Anderson model:

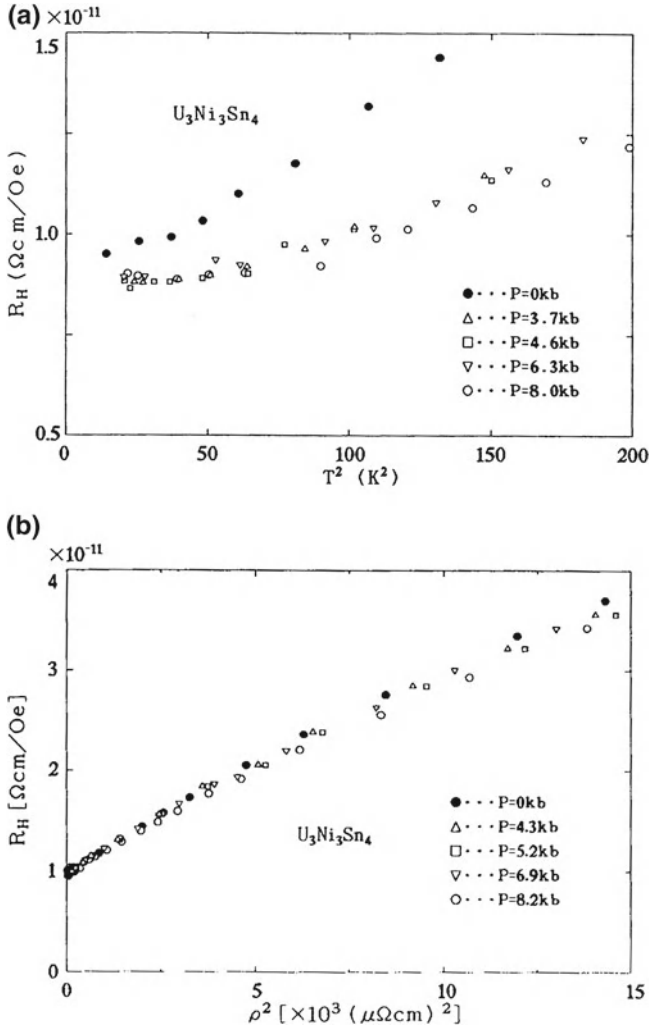

Fig. 11.11 R_{H} in $U_3Ni_3Sn_4$ plotted as functions of **a** T^2 and **b** ρ^2. The relation $R_{\mathrm{H}}^{\mathrm{HF}} - R_{\mathrm{H}}^{n} \propto \rho^2$ is satisfied well, as predicted by the theory of AHE [24] (Reference [46])

Is was shown that the large AHE in heavy fermion systems is well explained in terms of the intrinsic mechanism. It was also found the significant role of the orbital degree of freedoms in these intrinsic Hall effects. The spin structure driven AHE in ferromagnetic Pyrochlore oxides is also understood in terms of the intrinsic mechanism [41, 42].

We have also studied the intrinsic SHE in 4*d* and 5*d* transition metals based on the realistic nine orbital tight-binding models. It was found that the spin-dependent Berry phase due to orbital degree of freedoms, which is understood as the orbital

Berry phase shown in Fig. 4.7, is the main origin of large SHE in transition metals [17]. Recently, significant role of orbital degree of freedoms in the extrinsic SHE had been understood [53].

In metals with low resistivity, the intrinsic Hall conductivities are independent of the quasiparticle damping rate γ. This fact means that the intrinsic Hall effects are quantum transport phenomena, which cannot be explained by a conventional Boltzmann transport theory. For this reason, we have used the Nakano-Kubo formula in the present study. However, it is noteworthy that Sundaram and Niu had constructed a semiclassical transport theory that can explain the intrinsic Hall effects [54]. They had derived the following equation of motion for the wavepacket $(\mathbf{r}, \mathbf{k})$ in multiband systems:

$$\dot{\mathbf{r}} = \frac{\partial \epsilon_{n\mathbf{k}}}{\partial \mathbf{k}} - \dot{\mathbf{k}} \times \Omega_n(\mathbf{k}), \tag{11.37}$$

$$\dot{\mathbf{k}} = (-e) \cdot (-\nabla \phi(\mathbf{r})) \tag{11.38}$$

where $\phi(\mathbf{r})$ is the potential, and $\Omega^n_{\mathbf{k}} = (\nabla \times \mathbf{A}^n_{\mathbf{k}})_z$ is the Berry curvature of band n. $\mathbf{A}^n_{\mathbf{k}} = i\langle \mathbf{k}, n|\nabla|\mathbf{k}, n\rangle$ is the Berry connection, where $|u_n(\mathbf{k})\rangle$ being the periodic part of the Bloch wave.

Neglecting the normal Hall effect due to Lorentz force, the AHC is given by the summation of the Berry curvature below the Fermi level:

$$\begin{aligned}\sigma_{xy} &= -e \sum_{\mathbf{k},n} [\dot{\mathbf{r}}]_x f(\epsilon_{n\mathbf{k}})/E_y = e^2 \sum_{n,\mathbf{k}} [\mathbf{E}_y \times \mathbf{\Omega}_n(\mathbf{k})]_x f(\epsilon_{n\mathbf{k}})/E_y \\ &= e^2 \sum_{\mathbf{k},n} f(\epsilon_{n\mathbf{k}}) \, [\mathbf{\Omega}_n(\mathbf{k})]_z \end{aligned} \tag{11.39}$$

which is mathematically equivalent to σ^{IIb}_{xy} in Eq. (4.31). Thus, the AHC is simply determined by the topological nature of the Bloch electrons, independently of the scattering process of electrons. In band insulators, the integration in Eq. (11.39) is quantized due to the Stokes' theorem [55].

However, this simple statement is true only in metals with low resistivity. When the lifetime of quasiparticle $\tau = 2/\gamma$ is shorter than the lifetime of inter-band excitation $\tau_{\text{inter}} = 1/\Delta$ (Δ being the minimum band-splitting), the SHC decreases in proportion to $\tau^2 \propto \rho^{-2}$. This crossover phenomenon of the intrinsic AHE and SHE, which was first pointed out in Ref. [24], can be described by the exact expression in Eqs. (4.10) and (4.11), not by Eq. (11.39). At present, many body effect on the SHE and AHE, especially the role of the CVC on these effects, is not well understood. This is a very important future issue.

References

1. M.I. Dyakonov, V.I. Perel, Sov. Phys. JETP Lett. **13**, 467 (1971)
2. M.I. Dyakonov, V.I. Perel, Phys. Lett. **83**, 1834 (1971)
3. S. Murakami, N. Nagaosa, S.C. Zhang, Phys. Rev. B **69**, 235206 (2004)
4. J. Sinova, D. Culcer, Q. Niu, N.A. Sinitsyn, T. Jungwirth, A.H. MacDonald, Phys. Rev. Lett. **92**, 126603 (2004)
5. J. Inoue, G.E.W. Bauer, L.W. Molenkamp, Phys. Rev. B **70**, 041303(R) (2004)
6. R. Raimondi, P. Schwab, Phys. Rev. B **71**, 033311 (2005)
7. E.I. Rashba, Phys. Rev. B 70, 201309(R) (2004).
8. H. Kontani, T. Tanaka, D.S. Hirashima, K. Yamada, J. Inoue. Phys. Rev. Lett. **100**, 096601 (2008)
9. H. Kontani, M. Naito, D.S. Hirashima, K. Yamada, J. Inoue, J. Phys. Soc. Jpn. **76**, 103702 (2007)
10. M.J. Mehl, D.A. Papaconstantopoulos, Phys. Rev. B **54**, 4519 (1996)
11. D.A. Papaconstantopoulos, M.J. Mehl, J. Phys. Condens. Matter **15**, R413 (2003)
12. J. Friedel, P. Lenglart, G. Leman, J. Phys. Chem. Solids **25**, 781 (1964)
13. F. Herman, S. Skillman, *Atomic Structure Calculations* (Prentice-Hall, Englewood Cliffs, 1963)
14. L.F. Mattheiss, R.E. Watson, Phys. Rev. Lett. **13**, 526 (1964)
15. S.B. der Kellen, A.J. Freemann, Phys. Rev. B **54**, 11187 (1996)
16. M. Naito, D.S. Hirashima, J. Phys. Soc. Jpn. **76**, 044703 (2007)
17. T. Tanaka, H. Kontani, M. Naito, T. Naito, D.S. Hirashima, K. Yamada, J. Inoue, Phys. Rev. B **77**, 165117 (2008)
18. M. Morota, Y. Niimi, K. Ohnishi, T. Tanaka, H. Kontani, T. Kimura, Y. Otani, Phys. Rev. B **83**, 174405 (2011)
19. H. Kontani, T. Tanaka, D.S. Hirashima, K. Yamada, J. Inoue Phys, Rev. Lett. **102**, 016601 (2009)
20. S. Pandey, H. Kontani, D.S. Hirashima, R. Arita, H. Aoki, Phys. Rev. B **86**, 060507(R) (2012)
21. R. Karplus, J.M. Luttinger, Phys. Rev. **95**, 1154 (1954)
22. J. Smit, Physica **24**, 39 (1958)
23. L. Berger, Phys. Rev. B **2**, 4559 (1970)
24. H. Kontani, K. Yamada, J. Phys. Soc. Jpn. **63**, 2627 (1994)
25. H. Kontani, K. Yamada, J. Phys. Soc. Jpn. **66**, 2252 (1997)
26. M. Miyazawa, H. Kontani, K. Yamada, J. Phys. Soc. Jpn. **68**, 1625 (1999)
27. Y. Yao, L. Kleinman, A.H. MacDonald, J. Sinova, T. Jungwirth, D. Wang, E. Wang, Q. Niu, Phys. Rev. Lett. **92**, 037204 (2004)
28. Z. Fang et al., Science **302**, 92 (2003)
29. H. Kontani, T. Tanaka, K. Yamada, Phys. Rev. B **75**, 184416 (2007)
30. J. Inoue et al., Phys. Rev. Lett. **97**, 046604 (2006)
31. T. Naito, D.S. Hirashima, H. Kontani, Phys. Rev. B **81**, 195111 (2010)
32. J. Ye et al., Phys. Rev. Lett. **83**, 3737 (1999)
33. K. Ohgushi et al., Phys. Rev. B **62**, R6065 (2000)
34. M. Taillefumier et al., Phys. Rev. B **74**, 085105 (2006)
35. G. Tatara, H. Kawamura, J. Phys. Soc. Jpn. **71**, 2613 (2002)
36. S. Yoshii et al., J. Phys. Soc. Jpn. **69**, 3777 (2000)
37. Y. Yasui et al., J. Phys. Soc. Jpn. **75**, 084711 (2006)
38. Y. Taguchi et al., Science **291**, 2573 (2001)
39. Y. Taguchi et al., Phys. Rev. Lett. **90**, 257202 (2003)
40. Y. Machida et al., Phys. Rev. Lett. **98**, 057203 (2007)
41. T. Tomizawa, H. Kontani, Phys. Rev. B **80**, 100401(R) (2009)
42. T. Tomizawa, H. Kontani, Phys. Rev. B **82**, 104412 (2010)
43. F.D.M. Haldane, Phys. Rev. Lett. **61**, 2015 (1988)
44. Y. Ōnuki, T. Yamayoshi, I. Ukon, T. Komatsubara, A. Umezawa, W.K. Kwok, G.W. Crabtree, D.G. Hinks, J. Phys. Soc. Jpn. **58**, 2119 (1989)

45. Y. Ōnuki, T. Yamayoshi, T. Omi, I. Ukon, A. Kobori, T. Komatsubara, J. Phys. Soc. Jpn. **58**, 2126 (1989)
46. T. Hiraoka, T. Sada, T. Takabatake, H. Fujii, Physica B **186–188**, 7603 (1993)
47. P. Coleman, P.W. Anderson, T.V. Ramakrishman, Phys. Rev. Lett. **55**, 414 (1985)
48. A. Fert, P.M. Levy, Phys. Rev. B **36**, 1907 (1987)
49. T. Tanaka, H. Kontani, Phys. Rev. B **81**, 224401 (2010)
50. T. Miyasato, N. Abe, T. Fujii, A. Asamitsu, S. Onoda, Y. Onose, N. Nagaosa, Y. Tokura, Phys. Rev. Lett. **99**, 086602 (2007)
51. Y. Nakajima, K. Izawa, Y. Matsuda, S. Uji, T. Terashima, H. Shishido, R. Settai, Y. Onuki, H. Kontani, J. Phys. Soc. Jpn. **73**, 5 (2004)
52. Y. Nakajima, H. Shishido, H. Nakai, T. Shibauchi, K. Behnia, K. Izawa, M. Hedo, Y. Uwatoko, T. Matsumoto, R. Settai, Y. Onuki, H. Kontani, Y. Matsuda, J. Phys. Soc. Jpn. **76**, 027403 (2007)
53. T. Tanaka, H. Kontani, New J. Phys. **11**, 013023 (2009)
54. G. Sundaram, Q. Niu, Phys. Rev. B **59**, 14915 (1999)
55. D. Thouless, M. Kohmoto, M. Nightingale, M. den Nijs, Phys. Rev. Lett. **49**, 405 (1982)

Appendix A
Proof of Variational Formula

In this appendix, we prove the variational principle for the resistivity expressed in Eq. (3.22), by following the Ziman's textbook [1]. First, we calculate the following inner product for a trial function $\Psi_{\mathbf{k}}$:

$$\langle \Psi, P\Psi \rangle = \frac{1}{T} \sum_{\mathbf{k},\mathbf{k}',\mathbf{q}} \tilde{I}(\mathbf{k}, \mathbf{k}'; \mathbf{q}) \Psi_{\mathbf{k}} \left\{ \Psi_{\mathbf{k}} + \Psi_{\mathbf{k}'} - \Psi_{\mathbf{k}+\mathbf{q}} - \Psi_{\mathbf{k}'-\mathbf{q}} \right\} \tag{A.1}$$

where the operator P appears in the right-hand-side of Eq. (3.21), which represents the scattering process. Because of the self-adjoint nature of the operator P, Eq. (A.1) is rewritten as

$$\begin{aligned} \langle \Psi, P\Psi \rangle &= \frac{1}{4T} \sum_{\mathbf{k},\mathbf{k}',\mathbf{q}} \tilde{I}(\mathbf{k}, \mathbf{k}'; \mathbf{q}) \left\{ \Psi_{\mathbf{k}} + \Psi_{\mathbf{k}'} - \Psi_{\mathbf{k}+\mathbf{q}} - \Psi_{\mathbf{k}'-\mathbf{q}} \right\}^2 \\ &\geq 0 \end{aligned} \tag{A.2}$$

Therefore, P is positive definite.

Here, we assume $\Phi_{\mathbf{k}}$ is the solution of $X = -P\Phi$, and consider a trial flection $\Psi_{\mathbf{k}}$ that satisfies the normalization condition $\langle \Psi, X \rangle = -\langle \Psi, P\Psi \rangle$. Starting from the relationship

$$\langle (\Phi - \Psi), P(\Phi - \Psi) \rangle \geq 0 \tag{A.3}$$

and using the self-adjoint nature of P, it is easy to derive the following relationship

$$\langle \Phi, P\Phi \rangle \geq \langle \Psi, P\Psi \rangle \tag{A.4}$$

For general $\Psi_{\mathbf{k}}$, the normalization condition is satisfied by replacing $\Psi_{\mathbf{k}}$ with $\Psi_{\mathbf{k}} \cdot \langle \Psi, X \rangle / \langle \Psi, P\Psi \rangle$. Therefore, Eq. (A.4) is rewritten as

$$\frac{\langle \Phi, P\Phi \rangle}{\langle \Phi, X \rangle^2} \leq \frac{\langle \Psi, P\Psi \rangle}{\langle \Psi, X \rangle^2} \tag{A.5}$$

H. Kontani, *Transport Phenomena in Strongly Correlated Fermi Liquids*,
Springer Tracts in Modern Physics 251, DOI: 10.1007/978-3-642-35365-9,

which is valid for general $\Psi_{\mathbf{k}}$.

Using $\Phi_{\mathbf{k}}$, the conductivity is given as

$$\sigma = -2e\sum_{\mathbf{k}} v_{\mathbf{k}x}\frac{\Phi_{\mathbf{k}}}{E}\left(-\frac{\partial f^0}{\partial \epsilon}\right) = -2\langle X(E=1), \Phi\rangle$$
$$= 2\frac{\langle X(E=1), \Phi\rangle^2}{\langle \Phi, P\Phi\rangle} \tag{A.6}$$

By inputting Eq. (A.5) into Eq. (A.6), the variational formula for the resistivity is obtained as

$$\rho \leq \frac{\langle \Psi, P\Psi\rangle}{2\langle X(E=1), \Psi\rangle^2} \tag{A.7}$$

where the equal sign is realized when the trial function $\Psi_{\mathbf{k}}$ is the exact solution $\Phi_{\mathbf{k}}$. The physical meaning of this variational formula is that the current in the nonequilibrium steady state under E is realized so as to maximize the production of entropy due to scattering processes (= Joule heat E^2/ρ) [1].

Appendix B
Expression of $\mathcal{T}^{i,j}(\epsilon, \epsilon'; \omega)$

In Eq. (3.54), we performed the analytic continuation of of $\Lambda^{n;l}_{\mathbf{k}x} = \Lambda_{\mathbf{k}x}(i\epsilon_n, \omega_l)$ from region i shown in Fig. 3.1a to real frequencies. Then, we encountered the four-point vertex $\Gamma^{i,j;X}(\epsilon, \epsilon'; \omega)$ with real frequencies, which was first performed by Eliashberg in Ref. [2]. Here, we shortly explain its derivation: We consider the function $\Gamma(\epsilon, \epsilon'; \omega)$ given by the analytic continuation of the Matsubara frequency function $\Gamma(i\epsilon_n, i\epsilon_m; i\omega_l)$. In Fig. B.1a, singularities of $\Gamma(\epsilon, \epsilon'; \omega)$ are plotted in the $(\mathrm{Im}\epsilon, \mathrm{Im}\epsilon')$ plane.

Here, we perform the m-summation in

$$T\sum_n \Gamma(i\epsilon_n, i\epsilon_m; i\omega_l)G(i\epsilon_m + i\omega_l)G(i\epsilon_m)$$
$$= \int_C \frac{dz'}{4\pi i}\mathrm{th}\frac{z'}{2T}\Gamma(i\epsilon_n, z'; i\omega_l)G(z' + i\omega_l)G(z') \tag{B.1}$$

where the path of integration C is shown in Fig. 3.1a, and the cuts of the integrand are given by $\mathrm{Im}z' = \epsilon_n, 0, -\omega_l, -\omega_l - \epsilon_n$ as shown in Fig. B.1a. Hereafter, we consider the case $\epsilon_n > 0$ (regin 1). Then, considering the relation $\epsilon_n > 0 > -\omega_l > -\omega_l - \epsilon_n$, the path C can be deformed as Fig. B.1b. Then, Eq. (B.1) is expressed as

$$\int_{-\infty}^{\infty}\frac{dx}{4\pi i}\Big(\mathrm{cth}\frac{x}{2T}\{\Gamma^{II}_{1,1}(i\epsilon_n, x + i\epsilon_n; i\omega_l) - \Gamma^{I}_{1,1}(i\epsilon_n, x + i\epsilon_n; i\omega_l)\}$$
$$\times G^R(x + i\epsilon_n + i\omega_l)G^R(x + i\epsilon_n)$$
$$+ \mathrm{th}\frac{x}{2T}\{\Gamma^{I}_{1,1}(i\epsilon_n, x; i\omega_l)G^R(x + i\omega_l)G^R(x)$$
$$- \Gamma_{1,2}(i\epsilon_n, x; i\omega_l)G^R(x + i\omega_l)G^A(x)\}$$
$$+ \mathrm{th}\frac{x}{2T}\{\Gamma_{1,2}(i\epsilon_n, x - i\omega_l; i\omega_l)G^R(x)G^A(x - i\omega_l)$$
$$- \Gamma^{I}_{1,3}(i\epsilon_n, x - i\omega_l; i\omega_l)G^A(x)G^A(x - i\omega_l)\}$$

H. Kontani, *Transport Phenomena in Strongly Correlated Fermi Liquids*,
Springer Tracts in Modern Physics 251, DOI: 10.1007/978-3-642-35365-9,

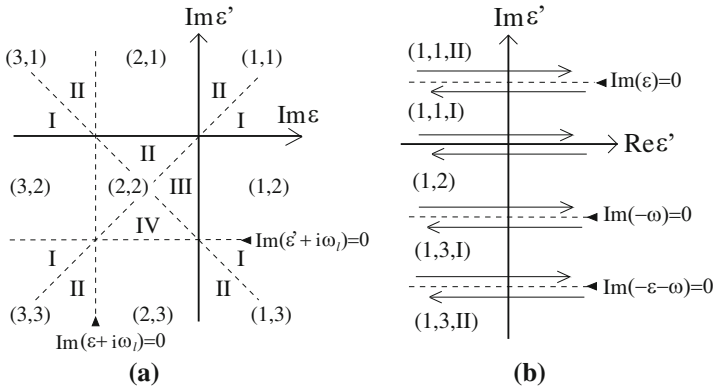

Fig. B.1 **a** Singularity lines of $\Gamma(\epsilon, \epsilon'; \omega)$, which is given by the analytic continuation of $\Gamma(i\epsilon_n, i\epsilon_m; i\omega_l)$ for $\omega_l > 0$. This plane is divided into 16 regions, each of which is analytic in that region in any of its arguments. The analytic continuation from each region to real frequencies present the function $\Gamma^{i,j;X}(\epsilon, \epsilon'; \omega)$, where $X = I \sim IV$ and $i, j = 1 \sim 3$. **b** The path C for $\epsilon_n > 0$

$$+ \mathrm{cth}\frac{x}{2T}\{\Gamma^{I}_{1,3}(i\epsilon_n, x - i\epsilon_n - i\omega_l; i\omega_l) - \Gamma^{II}_{1,3}(i\epsilon_n, x - i\epsilon_n - i\omega_l; i\omega_l)\}$$
$$\times G^A(x - i\epsilon_n)G^A(x - i\epsilon_n - i\omega_l)\Big) \tag{B.2}$$

By taking the analytic continuation of $i\epsilon_n$ and $i\omega_l$ of Eq. (B.2) to real frequencies, we obtain

$$\int_{-\infty}^{\infty}\frac{dx}{4\pi i}\Big(\mathrm{cth}\frac{x-\epsilon}{2T}\{\Gamma^{II}_{1,1}(\epsilon, x; \omega) - \Gamma^{I}_{1,1}(\epsilon, x; \omega)\}G^R(x+\omega)G^R(x)$$
$$+ \mathrm{th}\frac{x}{2T}\{\Gamma^{I}_{1,1}(\epsilon, x; \omega)G^R(x+\omega)G^R(x) - \Gamma_{1,2}(\epsilon, x; \omega)G^R(x+\omega)G^A(x)\}$$
$$+ \mathrm{th}\frac{x+\omega}{2T}\{\Gamma_{1,2}(\epsilon, x; \omega)G^R(x+\omega)G^A(x) - \Gamma^{I}_{1,3}(\epsilon, x; \omega)G^A(x+\omega)G^A(x)\}$$
$$+\mathrm{cth}\frac{x+\epsilon+\omega}{2T}\{\Gamma^{I}_{1,3}(\epsilon, x; \omega) - \Gamma^{II}_{1,3}(\epsilon, x; \omega)\}G^A(x+\omega)G^A(x)\Big) \tag{B.3}$$

We can repeat similar calculations for regions 2 and 3 of the variable $i\epsilon_n$.

Finally, by using the relation $\Gamma^{I}_{2,2} = \Gamma^{II}_{2,2} - \Gamma^{III}_{2,2} + \Gamma^{IV}_{2,2}$, we obtain the following expression:

$$\mathcal{T}^{1,1}(\epsilon, \epsilon'; \omega) = \mathrm{th}\frac{\epsilon'}{2T}\Gamma^{I}_{1,1} + \mathrm{cth}\frac{\epsilon'-\epsilon}{2T}\Big[\Gamma^{II}_{1,1} - \Gamma^{I}_{1,1}\Big], \tag{B.4}$$

$$\mathcal{T}^{1,2}(\epsilon, \epsilon'; \omega) = \left(\mathrm{th}\frac{\epsilon'+\omega}{2T} - \mathrm{th}\frac{\epsilon'}{2T}\right)\Gamma_{1,2}, \tag{B.5}$$

$$\mathcal{T}^{1,3}(\epsilon, \epsilon'; \omega) = -\mathrm{th}\frac{\epsilon' + \omega}{2T}\Gamma^{I}_{1,3} - \mathrm{cth}\frac{\epsilon' + \epsilon + \omega}{2T}\left[\Gamma^{II}_{1,3} - \Gamma^{I}_{1,3}\right], \tag{B.6}$$

$$\mathcal{T}^{2,1}(\epsilon, \epsilon'; \omega) = \mathrm{th}\frac{\epsilon'}{2T}\Gamma_{2,1}, \tag{B.7}$$

$$\begin{aligned}\mathcal{T}^{2,2}(\epsilon, \epsilon'; \omega) = &\left(\mathrm{cth}\frac{\epsilon' - \epsilon}{2T} - \mathrm{th}\frac{\epsilon'}{2T}\right)\Gamma^{II}_{2,2} \\ &+ \left(\mathrm{cth}\frac{\epsilon' + \epsilon + \omega}{2T} - \mathrm{cth}\frac{\epsilon' - \epsilon}{2T}\right)\Gamma^{III}_{2,2} \\ &+ \left(\mathrm{th}\frac{\epsilon' + \omega}{2T} - \mathrm{cth}\frac{\epsilon' + \epsilon + \omega}{2T}\right)\Gamma^{IV}_{2,2},\end{aligned} \tag{B.8}$$

$$\mathcal{T}^{2,3}(\epsilon, \epsilon'; \omega) = -\mathrm{th}\frac{\epsilon' + \omega}{2T}\Gamma_{2,3}, \tag{B.9}$$

$$\mathcal{T}^{3,1}(\epsilon, \epsilon'; \omega) = \mathrm{th}\frac{\epsilon'}{2T}\Gamma^{I}_{3,1} + \mathrm{cth}\frac{\epsilon' + \epsilon + \omega}{2T}\left[\Gamma^{II}_{3,1} - \Gamma^{I}_{3,1}\right], \tag{B.10}$$

$$\mathcal{T}^{3,2}(\epsilon, \epsilon'; \omega) = \left(\mathrm{th}\frac{\epsilon' + \omega}{2T} - \mathrm{th}\frac{\epsilon'}{2T}\right)\Gamma_{3,2}, \tag{B.11}$$

$$\mathcal{T}^{3,3}(\epsilon, \epsilon'; \omega) = -\mathrm{th}\frac{\epsilon' + \omega}{2T}\Gamma^{I}_{3,3} - \mathrm{cth}\frac{\epsilon' - \epsilon}{2T}\left[\Gamma^{II}_{3,3} - \Gamma^{I}_{3,3}\right], \tag{B.12}$$

where variables $(\epsilon, \epsilon'; \omega)$ for $\Gamma^{X}_{i,j}$ in the right-hand-sides are neglected for simplicity. They are given in Eq. (12) of Ref. [2].

References

1. H.M. Ziman, *Electrons and Phonons: The Theory of Transport Phenomena in Solids* (Oxford Classic Texts in the Physical Sciences, Oxford, 1960)
2. G.M. Eliashberg, Sov. Phys. JETP **14**, 886 (1962)